Controlled Modulation of Short- and Long-range Microscale Biogenic Replicas

A Dissertation

Presented to

The Academic Faculty

by

William Brandon Goodwin

In Partial Fulfillment

Of the Requirements for the Degree

Doctor of Philosophy in Materials Science and Engineering

Georgia Institute of Technology

May, 2015

Controlled Modulation of Short- and Long-range Adhesion of Microscale Biogenic Replicas

Approved by:

Dr. Kenneth H. Sandhage, Advisor
School of Materials Science
and Engineering
Georgia Institute of Technology

Dr. J. Carson Meredith
School of Chemical and
Biomolecular Engineering
Georgia Institute of Technology

Dr. Meilin Liu
School of Materials Science
and Engineering
Georgia Institute of Technology

Dr. Z. John Zhang
School of Chemistry & Biochemistry
Georgia Institute of Technology

Dr. Christopher Summers
School of Materials Science
and Engineering
Georgia Institute of Technology

Date Approved: October 27th 2014

To my granddads,

Prof. Emeritus William Albert Goodwin, P.E., R.L.S.,

And

Dr. Clarence Harold Buurman,

may my life as a scientist, engineer and humanitarian follow in your footsteps

Acknowledgements

As I wrap up the twenty and half grade, thankfully my final school year, I think it would be impossible to name all of those who have guided me to this point in my life. However, I will do my best to acknowledge all of those responsible for making this document possible.

Prof. Sandhage, I am glad you made me go deeper and spend the time to learn and understand the mechanistic work of this dissertation. I feel that I have learned more in the past few months trying to understand the reduction mechanism than I have during the rest of my duration in my lab. Overall, I am grateful for your passion for research, your consistency, your patience, and your ethics. Prof. Liu, Prof. Summers, Prof. Meredith, and Prof. Zhang, thank you for serving on my dissertation reading committee. Your time spent, your guidance, and your approval will not be forgotten.

The skills imparted to me by my professional mentors Prof. Chuck Melcher, Dr. Merry Koschan, Dr. Jon Vernon, Dr. Dan Berrigan, and Prof. Ken Sandhage have been invaluable. Thank you to all of the phenomenal collaborators with whom I have had the pleasure to work with: Dr. Ye Cai, Dr. Craig Cameron, Dr. Dimitri Deheyn, Dr. Yunnan Fang, Dr. Ismael Gomez, Dr. Dan Sabo, Dr. Cai, Dr. Yunshu Zhang, Phil Brooks, Ben DeGlee and Donglee Shin,

Thank you to all of my past and present peers in the Sandhage group and co-workers in the material science department for providing not only helpful conversations and patient instruction, but also such enjoyable work environments. I would especially like to thank Dan Berrigan and Jon Vernon for their friendship, problem solving skills, and guidance. I do not think I would have been able to graduate without your support.

Prof. Claudia Rawn, thank you for your instruction, mentorship, and teaching. Your influence sparked my interest in material science which molded my decision to become a life-long student of Materials Science and Engineering and peruse my Ph.D.

Thank you Dr. Kevin Pharris, Dr. Gabe Wardi, Dr. Julian Villiar, Barret Barns, Paul Rowland, Laurent Hugonet and Ryan Leatham, for being amazing roommates throughout my years at Georgia Tech. Your friendships have provided the much needed balance between work and life and have created some of my fondest and most memorable experiences. I would also like to thank Justin Lamb, Brian Booke, James Compagnoni, Brad Newcomb, and Kevin Lyons for providing many needed breaks from research and superb NASCAR trips.

Most importantly, I acknowledge my Mom and Dad. The two of you have inspired me, taught me, and supported me in ways I still cannot appreciate. I know as I grow older my understanding of what you have done for me will only continue to grow. To Benjamin, Lauren, and Merrill: thank you for being amazing siblings that have graciously put up with me for the past quarter century. I would also like to thank my wife Erin for supporting me the past few years. Not everyone would want to start a marriage with someone finishing their dissertation in another state. Your love and support has helped me tremendously in the past few months.

Table of Contents

List of Tables

List of Figures

List of Symbols and Abbreviations

ACS	Average Crystallite Size
AFM	Atomic Force Microscopy
3-D	Three-Dimensional
DI	Deionized
EDS	Energy Dispersive X-ray Spectroscopy
EELS	electron energy loss spectroscopy
h	hour(s)
HRTEM	High Resolution Transmission Electron Microscopy
HTXRD	High Temperature X-Ray Diffraction
IPA	Anhydrous Isopropyl Alcohol
ICP-MS	Inductively-coupled Plasma Mass Spectrometry
λ	Wavelength (nm)
LbL	Layer-by-Layer
μm	Micrometer
MSP	Microspectrophotometry
MWHT	Microwave Hydrothermal
nm	nanometer(s)
QCM	Quartz Crystal Microbalance
RBS	Rutherford backscattering spectrometry
RT	Room Temperature
SE	Secondary Electron
SEM	Scanning Electron Microscopy
SIMS	secondary ion mass spectrometry
SSG	Surface Sol Gel
SQUID	superconducting quantum interference device
TEM	Transmission Electron Microscopy
TG	Thermogravimetric
ToF	time of flight
VDW	van der Waals
XPS	X-ray photoelectron spectroscopy
XRD	X-ray Diffraction

Summary

The generation of nanostructured microscale assemblies with complex, three-dimensional (3-D) morphologies possessing multicomponent inorganic compositions tailored for adhesion is of considerable scientific and technological interest. This dissertation demonstrates that self-assembled 3-D organic templates of biogenic origin can be converted into replicas comprised of numerous other functional nanocrystalline inorganic materials and, further, how such replicas can tailored for adhesion. Nature provides a spectacular variety of biologically-assembled 3-D organic structures with intricate, hierarchical (macro-to-micro-to-nanoscale) morphologies designed for particle adhesion. The conformal coating of such structurally-complex biotemplates with synthetic materials provides a framework for chemical transformation of other, complex synthetic organic templates and the basis to study imparted adhesion properties.

Three specific research thrusts are detailed in this document. First, freestanding magnetite (Fe_3O_4) replicas of bio-organic templates are synthesized via a layer-by-layer (LbL) wet chemical deposition process and subsequent morphology-preserving thermal treatments to allow for structures with tailorable long-range magnetic adhesion. Second, freestanding spinel ferrite replicas of bio-organic templates are synthesized (via LbL coating and thermal treatment) for grain size controlled long-range magnetic adhesion and short range van der Waals adhesion. The final research thrust focuses on the use of a low temperature ($\leq 250°C$) wet-chemical based process to convert bioorganic templates into magnetically-coated structures retaining both the size and morphology of the template. The rate-limiting kinetic mechanism(s) of the partial reduction of the inorganic coatings have been examined via quartz crystal microbalance analysis. The effects of the

coating micro/nanostructure on magnetic behavior and on surface adhesion, have been investigated.

CHAPTER 1 **: Summary and Motivation**

1.1. ***Summary and Motivation***

The ability to adhere to a variety of surfaces using select modes of adhesion (e.g., entanglement, magnetic, and electrostatic) is important for many security applications including those associated with defense [1] and anti-counterfeiting.[2] To date, the syntheses of large volumes of reproducible and complex-shaped particles, with both nano and micro scale features, and chemistries tailored for adhesion has not been investigated. Using biological systems (such as diatoms,[3] butterflies,[4, 5] beetles,[5] and pollen grains[6]) as model templates is advantageous because nature has demonstrated unmatched proficiency in mass-producing complex three-dimensional (3-D) structures with features on both the nanometer and micrometer scales. Such complex biological structures often have beneficial structural/physical properties (e.g., high surface area,[7] unique optical properties,[8] and adhesion[9]), that are difficult to replicate synthetically. The native chemical compositions of such structures have limited uses and often cannot be used for engineering applications due to thermal and/or chemical instability. By applying conformal coatings to bioorganic templates, such as pollen, and subjecting such coated templates to morphology preserving chemical reactions, the structure may be maintained with careful selection of processing conditions, and adhesion properties can be improved/tailored by adjusting the selection of replica material chemistry (e.g., with magnetic materials [10]). Developing coating and reaction processes capable of replicating synthetic and bioorganic templates with functional materials for tuning particle adhesion is the primary focus of this research.

Synthesizing selectively-adhesive particles with controlled 3-D structures in the nano and micro range which are comprised of functional materials (magnetic[10]), with tunable adhesion properties had not previously been investigated. In addition, the study of how surface adhesion of macro scale particles is affected by magnetic forces has not been researched previously. With the use of a biogenic structure replication process that takes advantage of a LbL deposition method, it is possible to impart adhesion related material properties (magnetic) on intricate and massively reproducible biological structures. Pollen structures are of interest due to the wide range of species-specific morphologies (size, shape, and surface features) and the resulting adhesive properties from van der Waals (VDW) and other forces. Further understanding of how magnetic forces can couple with VDW forces to impart or enhance functional adhesion is an area that requires experimental proof and validation with theoretical modeling.

To investigate dual adhesion mechanisms (VDW and magnetic), a layer-by-layer (LbL) surface sol-gel (SSG) coating process has been used to coat pollen templates with ferromagnetic hematite (α-Fe_2O_3), and ferrimagnetic magnetite (Fe_3O_4), cobalt ferrite ($CoFe_2O_4$), and γ-Fe_2O_3 (maghemite). Hematite, magnetite, maghemite, and cobalt ferrite have well-known magnetic properties that will be used to demonstrate magnetic and VDW synergy.

The generally spherical pollen grains studied have a range of morphologies, from relatively smooth surfaces for low structural adhesion to rough surfaces covered with echini (spines) for significant structural adhesion (Figure 1).[11] Pollen with small echini radii allow for multiple contact points between the pollen grain and the substrate whereas smooth pollen and larger spined pollen possess increased single contact surface area for

enhanced VDW attraction. Spines may also improve adhesion due to entanglement, though this may be difficult to quantify. The SSG process has been used to apply conformal 3-D coatings to hydroxyl-rich pollen in a controlled manner while preserving morphological feature sizes of approximately 10 nm. Shape preservation is vital in maintaining the structural adhesion from VDW forces of the starting template while allowing for comparison of secondary adhesion based on magnetic attraction forces. Thus, developing a low temperature, chemical reduction process (>250°C) that can convert Fe-O bearing coatings into magnetite without distorting the pollen template or changing the VDW adhesion can be quite attractive.[12] The remanent magnetization,

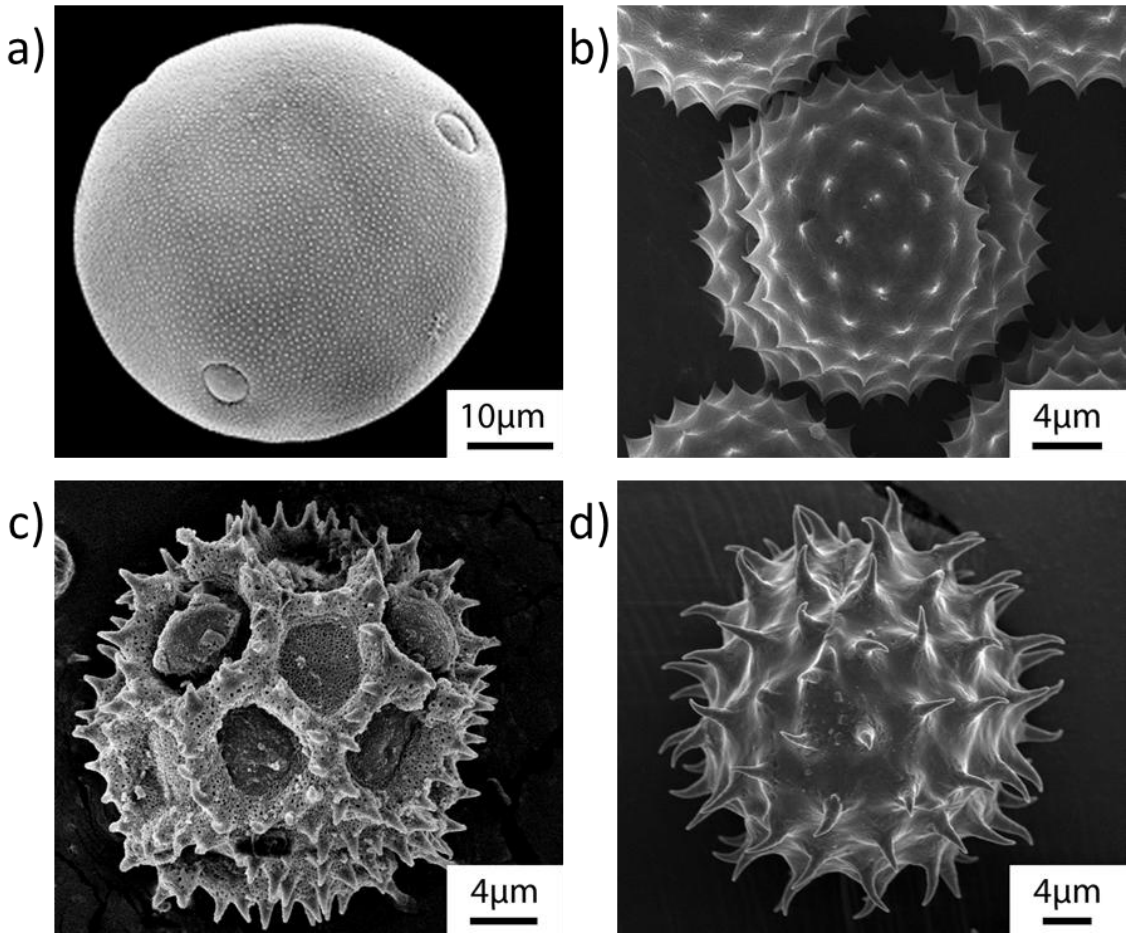

Figure 1: Secondary electron (SE) micrographs showing pollen with different surface morphologies, a) *C. illinoinensis* (Pecan pollen) with a smooth surface, b) *A. artemisiifolia* (Ragweed pollen) with small echini, c) *T. officinale* (Dandelion pollen) with a reticulated surface and medium sized echini, and d) *H. annuus* (Sunflower pollen) with large echini.

coercivity, and magnetic saturation can then be tuned by (i) controlling the thickness of the coatings, which can increase the remanent magnetization, coercivity, and magnetic saturation on a per particle basis, or (ii) controlling the grain size of the magnetic coating (larger grains can yield higher coercivity, remanent magnetization, and magnetic saturation values [13]). A novel aspect of this work is combining the structural based van der Waals adhesion of 3-D native pollen grains with a SSG LbL coating process to couple magnetic and VDW forces in a controlled manner.

1.2. *Introduction*

1.2.1. Organic Templates

Prior work with bio templates has focused on adding new material properties (e.g. optical, chemical, and magnetic) via surface coatings and chemical reactions to biological structures (such as diatoms,[3] butterflies,[4, 5] beetles,[5] and pollen grains[6]) for applications such as anti-counterfeiting,[14] catalysis,[15] and chemical filtration.[3] Recently, 3-D diatom microshells have been used as templates to create highly-porous Si and C replicas.[15] The carbon replicas displayed hierarchical porosity that stemmed from the diatom microshell structure (macro porosity) and the replica conversion process (meso and micro porosity) which enhanced the specific surface area from 1.65 to 1370 m^2/g.[15] However, little effort has been made to replicate biogenic templates that provide advantages due to synergy between the adhesive properties of the template structure and the material properties of the replica.

Pollen is a desirable template due to the multitude of unique pollen grain morphologies, with each pollinating species having a unique structure, shape, and

size.[16] It is inexpensive, readily available, globally abundant in a wide variety of morphologies, and naturally designed to stick to various surfaces. The complex structure and composition of the pollen outer wall, or exine, is composed of dicarboxylic acids and fatty acids that form a network of cross-linked polymers.[17] The two types of acids both contain hydroxyl groups that are necessary for a conformal coating to be deposited in LbL fashion via SSG processing. A variety of pollen species have been cataloged online (paldat.org) based on optical and secondary electron (SE) images. Pollen species have been then analyzed to determine how different morphologies, porosities and exine chemistries, vary within a single family and how they compare to other families.[16-19] Pollen grains that pollinate via wind (anemophilous pollination) have a smooth exine, while grains used in insect pollination (entomophilous pollination) have larger echini or spines.[11] Hence, depending on the pollination mechanism, pollen can be an ideal natural adhesive template. With current pollen databases (*www.paldat.org*), it is possible to browse through hundreds of species to find templates whose structural features (e.g., echini, porosity, and size) may prove beneficial for a given application (e.g., for selective adhesion, sensors, or anti-counterfeiting).

Several groups have utilized pollen as an organic template. Hall, *et al.* developed methods to fabricate hollow SiO_2, $CaCO_3$, and calcium phosphate pollen replicas by soaking pollen in precursor-bearing solutions (e.g., silicic acid) followed by a firing step to remove the organic components [7, 20]). The pollen replicas were then used in drug delivery or photocatalytic applications. Liu, *et al.* created amorphous TiO_2 inorganic replicas of pollen with the use of a supercritical fluid process by incubating cole pollen grains in titanium isopropoxide under 12 MPa of CO_2 followed by pyrolysis at

600°C.[21] This work is aimed at developing inorganic replicas (maghemite, magnetite, and cobalt ferrite) of pollen with the purpose of tailoring particle adhesion to various surfaces through new modes of adhesion (i.e., magnetic).

1.2.2. Surface Sol-gel Processing

The layer-by-layer (LbL) surface sol-gel (SSG) coating technique is a method used to apply sub-nanometer metal oxide layers onto hydroxyl-rich surfaces.[22] The SSG process can take advantage of a wide range of commercially available precursors and high-purity solutions, and allows for stoichiometric control of precursors in solution. The LbL can process benefit from surface-limited reactions allowing for conformal coatings on intricate 3-D structures. The process involves the surface limited chemisorptions of alkoxide precursors with template-bound hydroxyl or carboxyl groups. The substrate is then rinsed with anhydrous solvent to remove any excess precursors. The pendant alkoxide groups are then hydroxylated by incubating in water. Prior QCM (quartz crystal microbalance) analyses by Ichinose, et al.[22, 23] have shown that surface sol-gel deposition of oxide coatings (Al-O, Ti-O, Zr-O) on hydroxyl-rich (mercaptoethanol-modified) gold-on-quartz substrates occurred in a layer-by-layer fashion at a linear rate; that is, a similar amount of new material was deposited with each successive surface sol-gel deposition cycle. The LbL SSG process can be repeated in a controlled fashion to obtain a desired coating thickness.

A range of different chemistries can be applied with the SSG process to create thin, conformal coatings on complex inorganic or organic templates. Recently, coatings of TiO_2, SnO_2, $Sn_xTi_{1-x}O_2$, and Fe_3O_4 have been directly deposited onto butterfly or diatom templates[3, 4, 24, 25] Doping TiO_2 with SnO_2 has been used to induce the

formation of rutile TiO_2 at low temperatures (450^oC).[24] To date, the SSG process has been used to form single oxide or doped oxide replicas of various templates. The SSG process has not been used to directly synthesize binary or higher order oxide compound replicas of organic templates.

1.2.3. Magnetite

Magnetite (Fe_3O_4) is a naturally occurring mineral and is the first magnetic material known to man.[26] Magnetite is part of a group of magnetic ceramics, called ferrites, with a general formula of $MO{\cdot}Fe_2O_3$, where M = Fe, Ni, Co, Mn, or Cu.[27] Ferrites are designated as normal spinel, inverse spinel, or mixed spinel compounds depending on the location of cations on particular lattice sites. For a normal spinel structure, AB_2O_4, the divalent cations are located at the tetrahedral sites while the trivalent iron ions are located at the octahedral sites. For the inverse structure, $B(AB)O_4$, as in the case of magnetite, both the divalent cation and trivalent iron ions randomly occupy the octahedral sites, while only the trivalent iron ions occupy the tetrahedral sites. For mixed spinels, both types of cations are distributed across the octahedral and tetrahedral sites.

The general structure of a spinel compound consists of a face-centered-cubic-like (FCC-like) array of oxygen with 8 tetrahedral sites and 16 octahedral sites per unit cell. Each unit cell consists of 8 formula units. A schematic of the general crystal structure is shown in Figure 2. Magnetite has an inverse-spinel cubic structure; i.e., octahedral sites (of the FCC-like oxygen sub lattice) are half occupied by Fe^{2+} cations, with the other half occupied by Fe^{3+} cations, and the tetrahedral sites are occupied by Fe^{3+} ions and can be described by the following:[28]

$$(Fe^{3+})_8[Fe^{3+}Fe^{2+}]_8O_{32}^{2-} \quad (1.1)$$

where the brackets ( ) and [ ] designate occupied tetrahedral and octahedral sites, respectively, corresponding to 8a and 16d Wyckoff positions in space group F*d3m*.[29] Magnetite is ferrimagnetic as result of the alignment and population of the metal cation sites.[30] Cations in the octahedral and tetrahedral sites oppose one another, with the Fe^{3+} spins cancelling and a net spin created due to the Fe^{2+} atoms. Each magnetite formula unit has a net moment of 4 μB (Bohr magneton) or 32 μB per unit cell.[27, 30]

Magnetite can be an important material for various applications (e.g., batteries [31, 32] and arsenic removal devices [3, 33]). However, due to its bulk density of 4.9-5.2 g/cm^3, magnetite has limited utility in uses that require low density materials, such as for

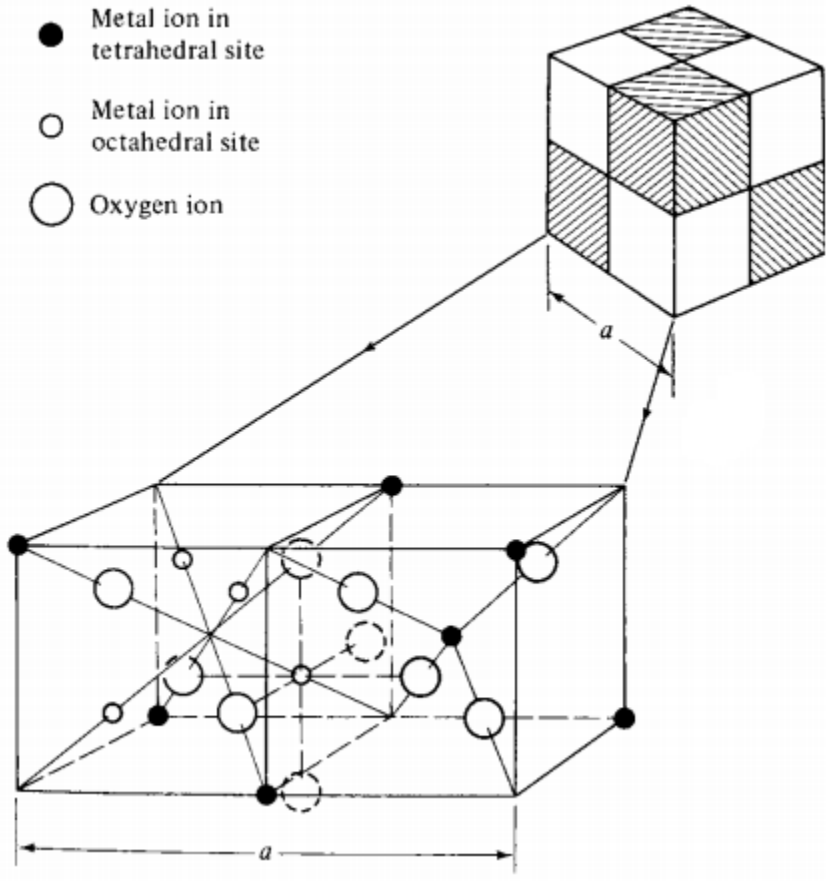

Figure 2: Crystal structure of a cubic ferrite or spinel ferrite.[30]

certain microwave absorption applications[34]. The microwave absorption properties of nano powders are influenced by irregularities in shape and by agglomeration of particles.[35] To circumvent density and size limitations, researchers have coated glass microspheres with magnetite[36] and $CoFe_2O_4$[37], creating lower density composite materials; that is, these composites take advantage of the low density of the glass microsphere templates and the microwave absorption properties of the coatings. Using pollen grains as a template would allow for the syntheses of hollow magnetite particles for the previously-mentioned applications.

Magnetite can be synthesized by the partial reduction of Fe^{3+} in hematite to Fe^{2+}, in a 1:2 stoichiometric ratio of Fe^{2+} and Fe^{3+}. The inverse spinel structure enables magnetite to be ferrimagnetic.[38] A number of methods have been reported for the syntheses of magnetite powders, such as reduction of hematite particles by CO/CO_2 or H_2, co-precipitation from a solution of mixed ferrous/ferric oxide salts, and low-temperature chemical reduction processes.[39] Using a sufficiently low temperature process, it may be possible to preserve an organic template while crystallizing an oxide coating. Chemical reducing agents, such as NH_2NH_2 (hydrazine), have been used to reduce FeOOH nano rods into magnetite.[40] Solution-based chemical reduction processes can involve precipitating and partially reducing Fe^{3+} cations from solution directly into $(Fe^{2+})(Fe^{3+})_2O_4$ (magnetite). For sol-gel coatings, the deposition of an oxide of single iron valence state (Fe^{3+}) may be followed by partial reduction into magnetite. With a low-temperature conversion process, it may be possible to better preserve the template morphology by using thermal conditions that do not pyrolyze or otherwise degrade the pollen template. With minimal template size change, it would be possible to

compare how the remanent magnetization of a magnetic coating and VDW forces affect particle adhesion. The magnetic properties, H_c and M_r, involve relatively weak but long-range interactions.[10] The length scale over which magnetic interactions operate is on the same order of magnitude for micro and nano-grain materials. The grain boundaries in a ferrimagnetic material can affect the extrinsic properties of the material. For magnetite, the remanent magnetization (M_r), magnetic saturation (M_s), and coercivity (H_c) all have grain size dependences.[13] Hence, by controlling the grain size of a coated pollen particle, the remanent magnetization, coercivity, and magnetic saturation can be modulated for the desired magnetic behavior. As the gain size approaches ~150 nm, the remanent magnetization, coercivity, and magnetic saturation start to approach the values of bulk magnetite.[13]

1.2.4. Maghemite

Maghemite (γ-Fe_2O_3) is a naturally-occurring mineral and second most stable polymorph of iron oxide after hematite (α-Fe_2O_3).[41] It is found in soil as a weathering product of magnetite (Fe_3O_4).[26] Maghemite exhibits a spinel-like crystal structure, similar to that of magnetite, with an array of oxygen vacancies. Maghemite's structure can be obtained from in a cubic spinel structure by introducing 8/3 vacancies out of the 16 octahedral sites Fe sites. The structure of maghemite is similar to that of magnetite and can be approximated as a cubic unit cell with F*d3m* space group by the following equation:

$$(Fe^{3+})_8\left[Fe^{3+}_{5/6} \quad {}_{1/6}\right]_{16} O^{2-}_{32} \tag{1.2}$$

The position and location of the octahedral vacancies has been investigated for several decades leading to a wide range of space groups used to describe the crystal

system.[42] Randomly-distributed cation vacancies over the octahedral sites, as was initially assumed, lead to the cubic spinel structure with the space group F*d3m* which is the same as magnetite.[43, 44] A long range superstructure was first noticed in 1939 when extra reflection peaks were detected in the powder diffraction pattern of maghemite prepared by oxidizing magnetite.[45]. The extra peaks were not consistent with an F*d3m* symmetry, so that a larger lattice and different space group were needed to describe maghemite. Lithium ferrite ($LiFe_5O_8$), which possess a spinel unit cell, was found to exhibit the same superstructure as maghemite with both materials having either ordered vacancies, in the case of maghemite, or Li ions, in the case of $LiFe_5O_8$.[46] The $LiFe_5O_8$ formula is given below.

$$(Fe^{3+})_8\left[Fe^{3+}_{3/4}Li^{1+}_{1/4}\right]_{16}O^{2-}_{32} \tag{1.3}$$

Lithium ferrite has a space group of P4_332 in which there are two types of octahedral sites, one with multiplicity 12 occupied by Fe^{3+}, and the other with multiplicity 4 occupied by Li. In maghemite, the same symmetry exists if the Fe vacancies are constrained to the Wyckoff 4b sites, as opposed to being randomly distributed.

Maghemite was then theorized to have a super structure in which all the vacancies are ordered, as opposed to being locally disordered, on the Wyckoff 4b sites and with a spinel tetragonal superstructure with c/a = 3.[47] The super structure was confirmed with a neutron diffraction study and found to have a higher degree of ordering then expected by the cubic P4_332 structure and the spinel tetragonal superstructure.[48] The positions of the vacancies in the fully ordered maghemite structure were obtained using synchrotron X-ray diffraction, and the maghemite structure was found to satisfy a tetragonal space group P4_12_12 with a = 8.347 Å and c = 25.042 Å or a spinel cubic cell tripled along the C

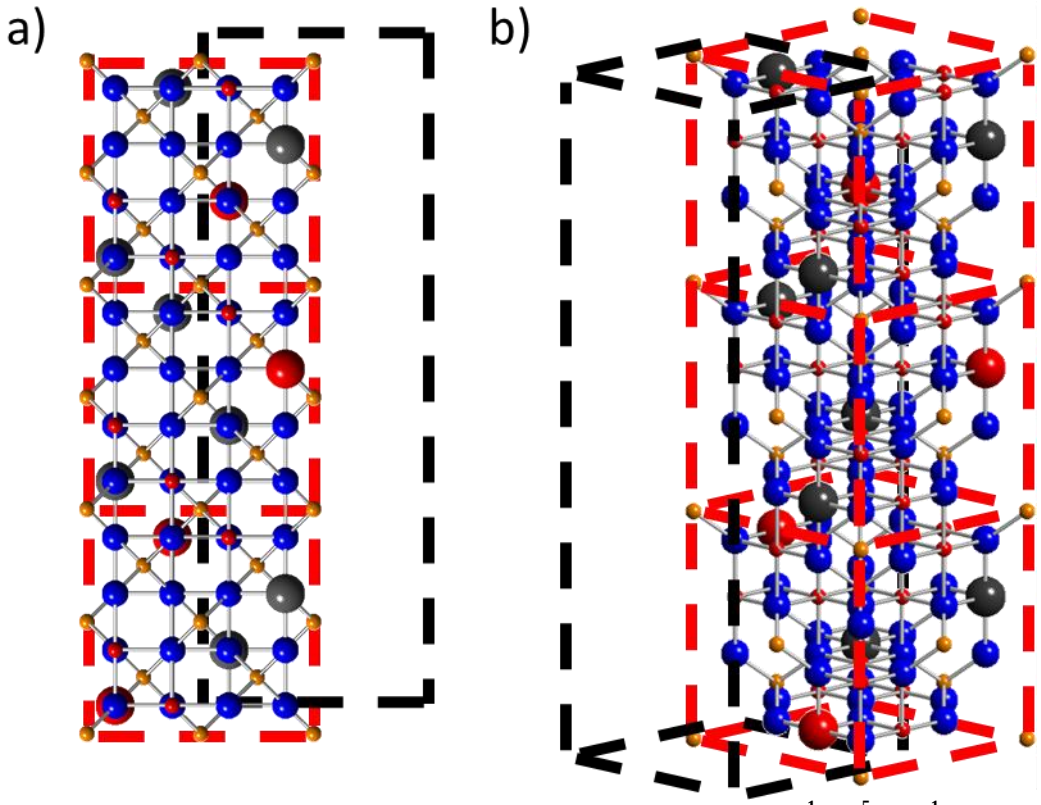

Figure 3: a) (100) and b) (111) orientation a maghemite unit cell offset by ($a^1/_2$, $b^5/_{24}$, $-c^1/_{24}$) from the origin. The black box represents the initial unit cell dimensions for the P4_12_12 space group, red boxes represent unit cell for the FCC-like spinel structure with an Fd3m symmetry. The blue spheres represent oxygen atoms, orange spheres are iron atoms at tetrahedral sites, small red spheres are iron atoms at octahedral sites, large red and grey spheres represent octahedral sites with ordered iron atoms and vacancies, respectively, located at the Wyckoff 4b sites.

axis.[49, 50] The crystal structure of maghemite can be seen in Figure 3 demonstrating the tripled spinel structure and location of the ordered octahedral vacancies. The unit cell is shifted from the origin to match that of the spinel structure. (note: the spinel structure is not immediately apparent with a unit cell generated from (000) for the P4_12_12 space group, so the unit cell was shifted ($a^1/_2$, $b^5/_{24}$, $-c^1/_{24}$) to resemble that of the spinel.)

While the structure for maghemite has been determined, the vacancy ordering in the lattice is not yet fully understood and it is unclear under which conditions vacancy disordering occurs. The degree of ordering has been shown to be effected by grain size with the superstructure reflections not visible in very small particles of maghemite.[26,

41, 51] Using density functional theory (DFT), it has been shown that the configuration with space group P4_12_12 is the most stable form and deviations from this state are associated with metastable growth.[42] Maghemite is expected to be fully ordered when in equilibrium. In the case of small nanoparticles it contains extended anti-site defects and surface effects which can lead to variations of the vacancy defects.

Contrasting with antiferromagnetic hematite (α-Fe_2O_3), maghemite exhibits ferrimagnetic ordering, similar to magnetite (4.0 μB per formula units) with a net magnetic moment slightly lower (2.5 μB per formula units) and a relatively high Neel temperature (~950 K). With its thermal stability compared to magnetite and low cost, maghemite has been used as a magnetic pigment in electronic recording media since the late 1940s.[41] Maghemite nanoparticles are also widely used in medicine due to being relatively biocompatible.[52, 53] In addition, γ-Fe_2O_3 has found use in the field of spintronics, where it acts as a tunneling barrier for room-temperature, spin-filter devices. [54, 55]

1.2.5. Van der Waals Forces

The adhesion and attractive forces between pollen and various surfaces have previously been investigated by Meredith, *et al*.[9] The short range van der Waals (VDW) adhesion forces were studied between *A. artemisiifolia (*Ragweed) and various synthetic surfaces, such as polystyrene and polyvinyl alcohol. Understanding how different pollen structures adhere to specific surfaces is vital in selecting a template for adhesion purposes. The adhesive force of pollen particles can be measured by using an atomic force microscope (AFM). Previous work has indicated that the reported VDW force for ragweed pollen grains can be quantitatively modeled using the average spine tip

radius and a Hamaker model.[56] The VDW force (F_{VDW}) can then be calculated using equation (1.4):

$$F_{VDW} = \frac{A_{132}R}{6D^2} \quad (1.4)$$

where A_{132} is the non-retarded Hamaker constant of material 1 and 2 interacting across a medium 3, R is the pollen spike tip radius, and D is the cut off separation distance for van der Waals interaction (0.165 nm). This model assumes that the contact substrate surface is infinitely flat and that the contact point of the particle can be modeled with a hemisphere. The Hamaker constant is estimated by combining the contributions of each medium in equation (1.5):

$$A_{132} \approx \left(\sqrt{A_{11}} - \sqrt{A_{33}}\right)\left(\sqrt{A_{22}} - \sqrt{A_{33}}\right) \quad (1.5)$$

where A_{11} is the Hamaker constant of the adhesive particle, in this case pollen or pollen replicas, A_{22} is the Hamaker constant of the substrate, and A_{33} is the Hamaker constant of air or other surrounding atmosphere. Approximate A_{132} values for sunflower pollen on the Si, PVA, PVAc, and PS substrates have been calculated from appropriate A_{11} and A_{22} values available in the literature[56-61]; and with the assumption that $A_{33} \approx 0$ via equation (1.6)

$$A_{132} \approx \sqrt{A_{11}}\sqrt{A_{22}} \quad (1.6)$$

The simplified expression in equation 1.6 is not applicable, however, to media with high dielectric constants. Therefore, interactions involving hematite, magnetite, Ni, or Ni–Nd were calculated on the basis of the Lifshitz theory[62] via equation. (1.7)

$$A_{132} \approx \frac{3}{4}kT\left(\frac{\varepsilon_1-\varepsilon_3}{\varepsilon_1+\varepsilon_3}\right)\left(\frac{\varepsilon_2-\varepsilon_3}{\varepsilon_2+\varepsilon_3}\right) + \frac{3h\nu_e}{8\sqrt{2}}\frac{(n_1^2-n_3^2)(n_2^2-n_3^2)}{(n_1^2+n_3^2)^{1/2}(n_2^2+n_3^2)^{1/2}\left\{(n_1^2+n_3^2)^{1/2}+(n_2^2+n_3^2)^{1/2}\right\}} \quad (1.7)$$

where k is Boltzmann's constant, T is temperature, h is Planck's constant, ν_e is the media absorption frequency, ε_1 and ε_2 are dielectric constants, and n_1 and n_2 are refractive indices. A_{132} values for sunflower pollen on the Ni or Ni–Nd substrates, as well as for hematite or magnetite replicas on all substrates, were calculated from equation 1.7 using appropriate ε_1, ε_2, n_1, and n_2 values available in the literature,[63-69] with the assumption that the absorption frequencies of all media are the same. Lacking a literature value for sporopollenin, the ε_1 value for sporopollenin was assumed to be the average of the values for PS, PVAc, and PVA. This assumption was consistent with the organic content of sporopollenin and produced A_{132} values of the expected magnitude. If the substrate is assumed to be flat, then R in equation 1.4 refers to the contact radius of the spine tip from the probe particle.

The Hamaker constant has been measured to be 0.83×10^{-19} J for a Sunflower particle adhering to a Si substrate in air.[56] For hematite and magnetite particles adhering to a Si substrate in air, the Hamaker constant was found to be 1.23-1.43 x 10^{-19} J and 1.17-1.36 x 10^{-19} J, respectively.[58, 70] With known values for the Hamaker constants, theoretical adhesion force values based on VDW attraction can be calculated by measuring the radius of curvature of the contact point. Using SE images, the spike tip radii of the pollen grains and pollen replicas can be measured and then used to calculate the expected van der Waals adhesion force.

VDW forces can also be measured experimentally by using AFM. For this work the pollen grains and pollen grain replicas have been attached to an AFM cantilever tip with a known spring constant. The measured deflection of the tip from the particle adhering to the substrate was then used to calculate the adhesion force. A schematic of a

typical short range adhesion plot can be seen in Figure 4. From location 1, the tip descends towards the surface. At location 2, the tip is pulled down by surface attraction. The tip is then pressed into the surface as the cantilever bends (location 3). As the tip is pulled away from the substrate surface, the upward force cancels out with the surface attraction (location 4). The cantilever then bends as the surface attraction holds the tip to the surface (location 5). The lift force eventually becomes stronger then the surface adhesion and the tip break free from the surface (location 6). As the tip is further removed it returns to the initial starting point (location 1). The force measured between locations 5 and 6 represents the VDW force between the particle and substrate. The calculated force (using contact radii values from SEM observation) can then be compared to the experimental values from AFM force curves to determine if VDW adhesion is the primary attraction force and to determine how magnetic and electrostatic forces also affect adhesion to substrates.

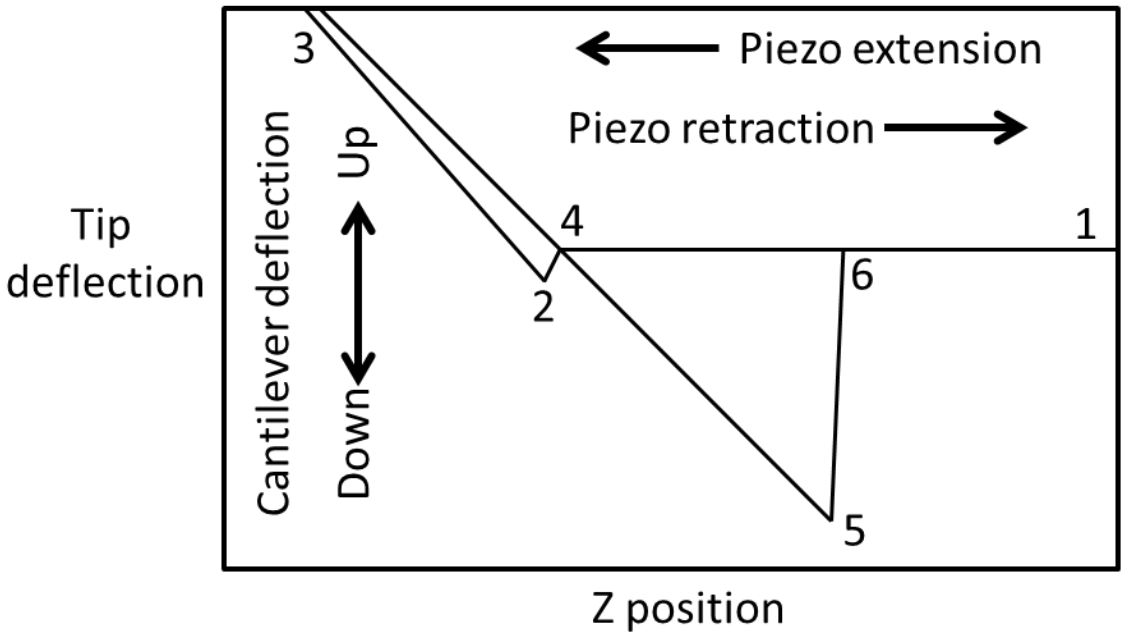

Figure 4: Schematic of a typical AFM-derived force curve for a sample with strong adhesion to a surface.

1.2.6. Magnetic Interactions

A magnetic model is needed to validate experimental long range attraction data measured using an AFM. By fitting experimental data to such a model, the magnetic volume of a single magnetic pollen sample can be determined. The force acting on a magnetic particle (F_m) interacting with a magnetic field gradient associated with a permanent magnet may be expressed as:[71]

$$F_m = \mu_o V_m M \nabla H \tag{1.8}$$

where μ_o (4π x 10^{-7} N A^{-2}) is the permeability of free space, V_m (m^3/particle) is the solid volume of magnetic material within the particle, M (A m^{-1}) is the magnetization, and ∇H (A m^{-2}) is the gradient in the magnetic field strength. Because the Fe_3O_4 sunflower replicas were anchored to tipless cantilevers, the direction of particle motion was restricted to the direction of cantilever deflection (herein referred to as the z direction). Therefore, the magnetic force acting on the Fe_3O_4 particle/cantilever assembly interacting with the permanent magnet can be expressed as:

$$F_m = \mu_o V_m M \frac{\partial H}{\partial z} \hat{z} \tag{1.9}$$

where $\partial H/\partial z$ is the gradient of the magnetic field in the z-direction and $\hat{z}$ is the unit vector parallel to the z direction. In order to utilize equation (1.9), $\partial H/\partial z$ needed to be evaluated.

The spatial dependence of the magnetostatic potential, Φ (A), of a disk-shaped permanent magnet may be expressed in cylindrical coordinates as:[72]

$$\nabla^2 \Phi = \frac{\partial^2 \Phi}{\partial r^2} + \frac{1}{r}\frac{\partial \Phi}{\partial r} + \frac{\partial^2 \Phi}{\partial z^2} = 0 \tag{1.10}$$

where Φ and H are related by:

$$H = -\nabla \Phi \tag{1.11}$$

The magnetostatic potential and magnetic field associated with the Ni-Nd disk-shaped substrate were modeled by applying a finite difference approach described elsewhere[72] to equations (1.10) and (1.11). The finite difference model was coded in FORTRAN77 and numerically evaluated using NAG Fortran Builder 5.2 software. This simulation was conducted using a 50 mm x 50 mm grid and a 50 μm step size for the disk-shaped Ni-Nd substrate of 1.5 mm diameter and 5 mm thickness. Values of $\partial H/\partial z$ were then calculated and, using equation (1.9), F_m values were determined as a function of position for a magnetic particle interacting with the field of the permanent magnet disk. Note: the derivations in Section 1.2.6. were developed and performed in collaboration with Ismael Gomez (Georgia Institute of Technology, Atlanta, GA,USA)

1.3. *References*

[1] A. Coxa and E. Garcia, "Three-Dimensional LIGA Structures for the Use in Tagging," *SPIE,* vol. 3673, pp. 122-126, March 1999.

[2] G. K. Phillips, "Combining Nanocharacter Printing, Digital Watermarking and UV Coded Taggents for Optimal Machine-Readable Security," *SPIE,* vol. 4677, pp. 150-158, 2002.

[3] G. Wang, Y. Fang, P. Kim, A. Hayek, M. R. Weatherspoon, J. W. Perry, *et al.*, "Layer-By-Layer Dendritic Growth of Hyperbranched Thin Films for Surface Sol-Gel Syntheses of Conformal, Functional, Nanocrystalline Oxide Coatings on Complex 3D (Bio)silica Templates," *Advanced Functional Materials,* vol. 19, pp. 2768-2776, 2009.

[4] M. R. Weatherspoon, Y. Cai, M. Crne, M. Srinivasarao, and K. H. Sandhage, "3D rutile titania-based structures with morpho butterfly wing scale morphologies," *Angew Chem Int Ed Engl,* vol. 47, pp. 7921-7923, 2008.

[5] M. Srinivasarao, "Nano-Optics in the Biological World: Beetles, Butterflies, Birds, and Moths," *Chem. Rev.,* vol. 99, pp. 1935-1961, 1999.

[6] F. Cao and D. X. Li, "Morphology-controlled synthesis of SiO_2 hollow microspheres using pollen grain as a biotemplate," *Biomed Mater,* vol. 4, pp. 1-6, Apr 2009.

[7] S. R. Hall, H. Bolger, and S. Mann, "Morphosynthesis of complex inorganic forms using pollen grain templates," *ChemComm,* pp. 2784-2785, 2003.

[8] W. Peng, S. Zhu, W. Wang, W. Zhang, J. Gu, X. Hu, *et al.*, "3D Network Magnetophotonic Crystals Fabricated on Morpho Butterfly Wing Templates," *Advanced Functional Materials,* vol. 22, pp. 2072-2080, 2012.

[9] B. J. R. Thio, J.-H. Lee, and J. C. Meredith, "Characterization of Ragweed Pollen Adhesion to Polyamides and Polystyrene Using Atomic Force Microscopy," *Environ. Sci. Technol.,* vol. 43, pp. 4308-4313, 2009.

[10] R. Skomski, "Nanomagnetics," *J. Phys.: Condens. Matter,* vol. 15, pp. R841–R896, 2003.

[11] N. Tanaka, K. Uehara, and J. Murata, "Correlation between pollen morphology and pollination mechanisms in the Hydrocharitaceae," *J Plant Res,* vol. 117, pp. 265-276, Aug 2004.

[12] R. Ghosh, A. D'Rozario, and S. Bera, "Can palynomorphs occur in burnt ancient potsherds? An experimental proof," *Journal of Archaeological Science,* vol. 33, pp. 1445-1451, 2006.

[13] G. Goya, T. Berquo, F. Fonseca, and M. Morales, "Static and dynamic magnetic properties of spherical magnetite nanoparticles," *Journal of Applied Physics,* vol. 94, pp. 3520-3528, 2003.

[14] J. P. Vernon, N. Hobbs, Y. Cai, A. Lethbridge, P. Vukusic, D. D. Deheyn, *et al.*, "3D photoluminescent lanthanide-doped barium titanate structures synthesized by coating and shape-preserving reaction of complex-shaped bioorganic templates," *Journal of Materials Chemistry,* vol. 22, pp. 10365-10940, 2012.

[15] Z. Bao, M.-K. Song, S. C. Davis, Y. Cai, M. Liu, and K. H. Sandhage, "High surface area, micro/mesoporous carbon particles with selectable 3-D biogenic morphologies for tailored catalysis, filtration, or adsorption," *Energy & Environmental Science,* vol. 4, pp. 3980-3984, 2011.

[16] S. Rosenfeldt and B. G. Galati, "Pollen morphology of Oxalis species from Buenos Aires province (Argentina)," *BIOCELL,* vol. 31, pp. 13-21, 2007.

[17] E. Domínguez, J. A. Mercado, M. A. Quesada, and A. Heredia, "Pollen sporopollenin: degradation and structural elucidation," *Sex Plant Reprod,* vol. 12, pp. 171-178, 1999.

[18] P. Xie and D. Zhang, "Pollen morphology supports the transfer of Wendlandia (Rubiaceae) out of Rondeletieae," *Botanical Journal of the Linnean Society,* vol. 164, pp. 128-141, 2010.

[19] N. Shaheen, Mir Ajab Khan, M. Q. Hayat, and G. Yasmin, "Pollen morphology of 14 species of Abutilon and Hibiscus of the family Malvaceae (sensu stricto)," *Journal of Medicinal Plants Research,* vol. 3, pp. 921-929, 2009.

[20] S. R. Hall, V. M. Swinerd, F. N. Newby, A. M. Collins, and S. Mann, "Fabrication of Porous Titania (Brookite) Microparticles with Complex Morphology by Sol-Gel Replication of Pollen Grains," *Chem. Mater.*, vol. 18, pp. 598-600, 2006.

[21] Y. Wang, Z. Liu, B. Han, Z. Sun, J. Du, J. Zhang, *et al.*, "Replication of biological organizations through a supercritical fluid route," *ChemComm,* pp. 2948-2950, Jun 21 2005.

[22] I. Ichinose, H. Senzu, and T. Kunitake, "A Surface Sol-Gel Process of TiO_2 and Other Metal Oxide Films with Molecular Precision," *Chem. Mater.*, vol. 9, pp. 1296-1298, 1997.

[23] I. Ichinose, H. Senzu, and T. Kunitake, "Stepwise Adsorption of Metal Alkoxides on Hydrolyzed Surfaces: A Surface Sol-Gel Process," *Chem. Lett.*, vol. 10, p. 831, 1996.

[24] M. R. Weatherspoon, M. B. Dickerson, G. Wang, Y. Cai, S. Shian, S. C. Jones, *et al.*, "Thin, conformal, and continuous SnO_2 coatings on three-dimensional biosilica templates through hydroxy-group amplification and layer-by-layer alkoxide deposition," *Angew Chem Int Ed Engl,* vol. 46, pp. 5724-5727, 2007.

[25] J. P. Vernon, Y. Fang, Y. Cai, and K. H. Sandhage, "Morphology-preserving conversion of a 3D bioorganic template into a nanocrystalline multicomponent oxide compound," *Angew Chem Int Ed Engl,* vol. 49, pp. 7765-7768, Oct 11 2010.

[26] R. M. Cornell and U. Schwertmann, *The Iron Oxides*: Weinheim: VCH Verlagsgesellschaft, 1996.

[27] J. Smit and H. P. J. Wijn, *Ferrites*: Philips Technical Library, 1959.

[28] C. Gleitzer, "Electrical Properties of Anhydrous Iron Oxides," *Key Engineering Materials,* vol. 125-126, pp. 355-0, 1997.

[29] F. Bourgeois, P. Gergaud, H. Renevier, C. Leclere, and G. Feuillet, "Low temperature oxidation mechanisms of nanocrystalline magnetite thin film," *Journal of Applied Physics,* vol. 113, pp. -, 2013.

[30] B. D. Cullity and C. D. Graham, *Introduction to Magnetic Materials 2ed*: A. john Wiley & Sons, Inc., 2009.

[31] X. Huang, X. Zhou, K. Qian, D. Zhao, Z. Liu, and C. Yu, "A magnetite nanocrystal/graphene composite as high performance anode for lithium-ion batteries," *Journal of Alloys and Compounds,* vol. 514, pp. 76-80, 2012.

[32] S. Ito, K. Nakaoka, M. Kawamura, K. Ui, K. Fujimoto, and N. Koura, "Lithium battery having a large capacity using Fe_3O_4 as a cathode material," *Journal of Power Sources,* vol. 146, pp. 319-322, 2005.

[33] B. J. Thio, K. K. Clark, and A. A. Keller, "Magnetic pollen grains as sorbents for facile removal of organic pollutants in aqueous media," *J Hazard Mater,* vol. 194, pp. 53-61, Oct 30 2011.

[34] Z. Y. Ma, D. Dosev, M. Nichkova, S. J. Gee, B. D. Hammock, and I. M. Kennedy, "Synthesis and bio-functionalization of multifunctional magnetic Fe_3O_4-Y_2O_3:Eu nanocomposites," *J. Mater. Chem.,* vol. 19, pp. 4695-4700, Jan 1 2009.

[35] S. Ni, S. Lin, Q. Pan, F. Yang, K. Huang, and D. He, "Hydrothermal synthesis and microwave absorption properties of Fe_3O_4nanocrystals," *Journal of Physics D: Applied Physics,* vol. 42, p. 055004, 2009.

[36] X. Li, H. Yang, W. Fu, C. Wu, S. Liu, H. Zhu, *et al.*, "Preparation of low-density superparamagnetic microspheres by coating glass microballoons with magnetite nanoparticles," *Materials Science and Engineering: B,* vol. 135, pp. 38-43, 2006.

[37] W. Fu, S. Liu, W. Fan, H. Yang, X. Pang, J. Xu, *et al.*, "Hollow glass microspheres coated with $CoFe_2O_4$ and its microwave absorption property," *Journal of Magnetism and Magnetic Materials,* vol. 316, pp. 54-58, 2007.

[38] A. J. Moulson and J. M. Herbert, *Electroceramics 2nd edition, materials properties applications* John Wiley & Sons Ltd, 2003.

[39] Y. B. Khollam, S. R. Dhage, H. S. Potdar, S. B. Deshpande, P. P. Bakare, S. D. Kulkarni, *et al.*, "Microwave hydrothermal preparation of submicron-sized spherical magnetite (Fe_3O_4) powders," *Materials Letters,* vol. 56, pp. 571-577, 10// 2002.

[40] I. Milosevic, H. Jouni, C. David, F. Warmont, D. Bonnin, and L. Motte, "Facile Microwave Process in Water for the Fabrication of Magnetic Nanorods," *The Journal of Physical Chemistry C,* vol. 115, pp. 18999-19004, 2011.

[41] R. Dronskowski, "The Little Maghemite Story A Classic Functional Material," *Adv. Funct. Mater.,* vol. 11, 2001.

[42] R. Grau-Crespo, A. Y. Al-Baitai, I. Saadoune, and N. H. D. Leeuw, "Vacancy ordering and electronic structure of γ-Fe_2O_3 (maghemite): a theoretical investigation," 2008.

[43] H. G, *Z. Phys. Chem. B,* vol. 29, 1935.

[44] V. E. J. W, *Z. Kristallogr. A,* vol. 91, 1935.

[45] R. Haul and T. Schoon, *J. Phys. Chem. B,* vol. 44, 1939.

[46] P. B. Braun, "A super structure in spinels," *Nature,* 1952.

[47] G. W. van Oosterhout and C. J. M. Rooijmans, "A new superstructure in γ-ferric oxide," *Nature,* vol. 181, p. 44, 1958.

[48] C. Greaves, "A Powder Neutron Diffraction Investigation of Vacancy Ordering and Covalence in γ-Fe_2O_3," *Journal of Solid State Chemistry,* vol. 49, pp. 358-333, 1983.

[49] A. N. Shmakov, G. N. Krvukova, S. V. Tsvbulva, A. L. Chuvilin, and L. P. Solovveva, "Vacancy Ordering in γ-Fe_2O_3 Synchrotron X-ray Powder Diffraction and High Resolution Electron Microscopy Studies," *J. Appl. Cryst,* vol. 28, pp. 141-145, 1995.

[50] J.-E. Jørgensen, L. Mosegaard, L. E. Thomsen, T. R. Jensen, and J. C. Hanson, "Formation of γ-Fe_2O_3 nanoparticles and vacancy ordering: An in situ X-ray powder diffraction study," *Journal of Solid State Chemistry,* vol. 180, pp. 180-185, 2007.

[51] T. J. Bastow, A. Trinchi, M. R. Hill, R. Harris, and T. H. Muster, "Vacancy ordering in γ-Fe_2O_3 nanocrystals observed by ^{57}Fe NMR," *Journal of Magnetism and Magnetic Materials,* vol. 321, pp. 2677-2681, 2009.

[52] Q. A. Pankhurst, J. Connolly, S. K. SKJones, and J. Dobson, "Applications of magnetic nanoparticles in biomedicine," *J. Phys. D: Appl. Phys,* vol. 36, pp. R167-R181, 2003.

[53] M. Levy, C. Wilhelm, J. M. Siaugue, O. Horner, J. C. Bacri, and F. Gazeau, "Magnetically induced hyperthermia: size-dependent heating power of gamma-Fe_2O_3 nanoparticles," *J Phys Condens Matter,* vol. 20, p. 204133, May 21 2008.

[54] J. A. Wiemann, E. E. Carpenter, J. Wiggins, W. Zhou, J. Tang, S. Li, *et al.*, "Magnetoresistance of a (γ-Fe_2O_3)$_{80}$$Ag_{20}$ nanocomposite prepared in reverse micelles," *Journal of Applied Physics,* vol. 87, p. 7001, 2000.

[55] H. Yanagihara, M. Hasegawa, E. Kita, Y. Wakabayashi, H. Sawa, and K. Siratori, "Iron Vacancy Ordered γ-Fe_2O_3(001) Epitaxial Films: The Crystal Structure and Electrical Resistivity," *J. Phys. Soc. Jpn.*, vol. 75, 2006.

[56] H. Lin, I. Gomez, and J. C. Meredith, "Pollenkitt wetting mechanism enables species-specific tunable pollen adhesion," *Langmuir,* vol. 29, pp. 3012-3023, Mar 5 2013.

[57] A. S. Dunn and L. C. H. Chong, "Application of the theory of colloid stability to the problem of particle formation in aqueous solutions of vinyl acetate," *Br. Polym. J.*, vol. 2, p. 49, 1970.

[58] J. Visser, "On Hamaker constants: A comparison between Hamaker constants and Lifshitz-van der Waals constants," *Advances in Colloid and Interface Science*, vol. 3, pp. 331-363, 12// 1972.

[59] N. F. Martinez, S. Patil, J. R. Lozano, and R. Garcia, "Enhanced compositional sensitivity in atomic force microscopy by the excitation of the first two flexural modes," *Appl. Phys. Lett.*, vol. 89, p. 153115, 2006.

[60] Y. Huang, D. Guo, X. Lu, and J. Luo, "Effects of the ultrasonic flexural vibration on the interaction between the abrasive particles; pad and sapphire substrate during chemical mechanical polishing (CMP)," *Appl. Surf. Sci.*, vol. 257, p. 3055, 2011.

[61] C. He, Y. Hao, H. Zeng, T. Tang, J. Xing, and J. Chen, "A new purification method for carbon nanotubes and associated atomic force microscope force–distance curve analysis," *Sep. Purif. Technol.*, vol. 81, pp. 174-183, 2011.

[62] J. Israelachvili, *Intermolecular and Surface Forces*, 1992.

[63] R. J. Nussbaumer, W. R. Caseri, P. Smith, and T. Tervoort, "Polymer-TiO_2 Nanocomposites: A Route Towards Visually Transparent Broadband UV Filters and High Refractive Index Materials," *Macromol. Mater. Eng.*, vol. 288, p. 44, 2003.

[64] H. Daoust and M. Rinfret, "On ionic copolymerization," *J. Colloid Sci.*, vol. 7, p. 11, 1952.

[65] C. U. Devi, A. K. Sharma, and V. V. R. N. Rao, "Electrical and optical properties of pure and silver nitrate-doped polyvinyl alcohol films," *Mater. Lett.*, vol. 56, p. 167, 2002.

[66] M. H. Chiu, J. Y. Lee, and D. C. Su, "Complex refractive-index measurement based on Fresnel's equations and the uses of heterodyne interferometry," *Appl. Opt.*, vol. 38, p. 4047, 1999.

[67] J. L. Rosenholtz and D. T. Smith, *Am. Mineral.*, vol. 21, p. 115, 1936.

[68] S. L. Atkin, S. Barrier, Z. Cui, P. D. I. Fletcher, G. Mackenzie, V. Panel, *et al.*, "UV and visible light screening by individual sporopollenin exines derived from Lycopodium clavatum (club moss) and Ambrosia trifida (giant ragweed)," *J. Photochem. Photobiol. B, Biol.*, vol. 102, p. 209, 2011.

[69] D. R. Lide, *CRC Handbook of Chemistry and Physics*, 2005.

[70] J. C. Meredith, A. P. Smith, A. Karim, and E. J. Amis, "Combinatorial Materials Science for Polymer Thin-Film Dewetting," *Macromolecules,* vol. 33, pp. 9747-9756, 2000.

[71] E. M. Pugh and E. W. Pugh, *Principles of electricity and magnetism*. Reading, Mass.,: Addison-Wesley Pub. Co., 1960.

[72] N. Leventis and X. Gao, "Magnetohydrodynamic electrochemistry in the field of Nd-Fe-B magnets. Theory, experiment, and application in self-powered flow delivery systems," *Analytical Chemistry,* vol. 73, pp. 3981-3992, 2001.

CHAPTER 2 **: Conversion of Pollen Particles into Three-Dimensional Ceramic Replicas with Tailorable and Predictable Multimodal Adhesion**

Discussions in this chapter are distinct from, and expand upon, the research presented in: W. Brandon Goodwin, Ismael J. Gomez, Yunnan Fang, J. Carson Meredith, and Kenneth H. Sandhage "Conversion of Pollen Particles into Three-Dimensional Ceramic Replicas Tailored for Multimodal Adhesion," *Chem. Mater.*, 2013, 25 (22), pp 4529–4536.

And

Ismael J. Gomez, W. Brandon Goodwin, Dan Sabo, Z. John Zhang, Kenneth H. Sandhage and J. Carson Meredith "Three-dimensional magnetite replicas of pollen particles with tailorable and predictable multimodal adhesion," *J. Mater. Chem. C.*, accepted fall 2014

2.1. ***Summary***

The ability to synthesize large quantities of 3-D microparticles with tunable adhesion is critically important for a variety of mature and emerging technologies, such as for paints, inks, chemical/water purification, drug delivery, cell manipulation, and assembly of hierarchical structures. Nature provides impressive examples of sustainable, complex-shaped microparticles with chemistries and structures tailored for adhesion, among the most common of which are pollen grains. For the first time, 3-D nanocrystalline all-oxide, replicas of pollen microparticles have been synthesized with tailored multimodal (bioenabled and synthetic) adhesion via use of a scalable, highly conformal surface sol–gel (SSG) coating process. High-fidelity replication allowed the pollen-shaped oxide microparticles to be utilized for adhesion via tailorable short-range (~10 nm) van der Waals (VDW) attraction. Analyses with a simple Hamaker model indicated that VDW adhesion of the oxide replicas was governed by the contact of oxide nanocrystals located on the spine tips (as opposed to the curvature of the entire spine tip).

Conversion of the pollen into ferrimagnetic (Fe_3O_4) microparticle replicas allowed the use of magnetic attraction at short and long ranges (up to ~1 mm).

In addition, the layer-by-layer SSG process has been used to carefully adjust the amount of iron oxide deposited onto the pollen grains. Modifying the number of deposition cycles (10, 20, 30, 40, and 50) is a potential design tool for tuning the short-range adhesion and long-range magnetic attraction of pollen replicas. Varying the coating layers allows for evaluating pollen replicas' capability to preserve the size and shape of natural pollen features. Controlled-atmosphere thermal treatments then yielded freestanding replicas with tailored hematite (α-Fe_2O_3) or magnetite (Fe_3O_4) contents. The 3-D morphology of the starting pollen was well-preserved in the all-oxide replicas, and the shrinkage upon firing could be controlled by increasing the number of Fe-O-bearing layers deposited on the pollen. While the short-range van der Waals (VDW) adhesion of the oxide replicas to a variety of surfaces was lower than for the larger starting pollen grains, this difference was not due to shrinkage of the replicas. The magnitude of such VDW-based adhesion was influenced by the nanoscale topography of surface features retained by the replicas.

The longer-range attraction to a magnetic substrate could be tailored independently of the short-range VDW attraction by controlling the magnetite content of the replicas, and a simple and effective model for describing such magnetic attraction was developed. This work demonstrates that sustainable pollen microparticles, with particular surface features, can be converted into high-fidelity 3-D oxide replicas with predictable and tailorable multimodal adhesion.

2.2. *Introduction*

Adhesion by or on microparticles plays a critical role in a wide range of developing and mature technologies, including drug delivery, catalysis, water/chemical purification, sensing, anti-fouling coatings and membranes, semiconductor device processing, composite processing, paints, printing, and xerography.[1-10] The ability to synthesis microparticles with tunable magnetic attraction is a key factor for magnetorheological fluids (e.g., for vibration damping), magnetophoretic separations, biological cell isolation and manipulation, microfluidics, targeted drug delivery, magnetic self-assembly of hierarchical structures, and the magnetic-field enabled tailoring of composite microstructures.[11-19]The coupling of other modes of attraction/adhesion with tunable magnetic forces could also provide new avenues for tailoring of the interactions of microparticles with surfaces.

While predominant models and mechanistic experimental studies for under-standing adhesion have been based on smooth, spherical particles,[20-26] microparticles with rough surfaces and non-spherical shapes are desired for a number of such technologies. However, the scalable fabrication of micro-particles with well-controlled surface asperities, in a variety of three-dimensional (3-D) morphologies, and with tailorable chemistries to allow for tunable adhesion remains a difficult synthetic challenge. Additionally, coupling long-range magnetic attractions with controlled short-range van der Waals (VDW) adhesion may present new avenues for microparticle research

Inspiration for the development of adhesive, structurally-complex microparticles can be found in nature. For example, diatoms (unicellular algae) and flowering plants

produce silica-bearing frustules and sporopollenin-bearing pollen grains, respectively, in great quantities throughout the world and in a tremendous variety of 3-D morphologies.[27-38] The surface chemistries and morphologies of these biogenic microparticles allow for selective and strong adhesion to natural and man-made surfaces.[39-41] Given their complex and diverse morphologies and sustainable (biological) production, these 3-D microparticles have attracted significant interest in recent years as templates for chemical conversion into replicas comprised of synthetic (non-biologically-derived) materials.[42-51] Pollen particles come in a wide variety of 3-D shapes and surface topographies,[27-30, 52, 53] and are produced in large and increasing quantities worldwide by plants.[31, 32, 54-59] Atomic force microscopy (AFM) based adhesion measurements have recently[60] shown that the van der Waals (VDW) attraction of pollen particles to various inorganic and organic surfaces scales directly with the contact radii of asperities on the pollen surface; that is, the selection of pollen particles with particular surface structural features may be used to affect such VDW-based adhesion.

The purpose of this chapter are: i) to show, for the first time, how such pollen particles may be converted into 3-D ceramic replicas endowed with tunable multi-modal adhesion, ii) to investigate the effect of the number of SSG cycles on size and morphology retention of the ceramic replicas, iii) to examine the tailorability of adhesion of 3-D iron oxide replicas of sunflower pollen particles to various surfaces through the use of the layer-by-layer (LbL) SSG process, and iv) to evaluate the applicability of simple models for describing short-range and long-range attractive forces acting on such chemically-tailored, complex-shaped replicas.

In the ensuing pages, native pollen particles have been converted, via use of a highly-conformal surface sol-gel (SSG) coating process,[61-63] into 3-D replicas comprised of ferromagnetic hematite (α-Fe_2O_3) or ferrimagnetic magnetite (Fe_3O_4). The nanoscale surface topography, and the magnetic oxide content, of such high-fidelity replicas can provide for multimodal attraction to surfaces via both short-range VDW and short-to-long-range magnetic forces. The replicas maintained the morphology of the native pollen creating complex, hollow, 3-D structures. Native, hematite (α-Fe_2O_3), and magnetite (Fe_3O_4) sunflower pollen exhibited short-range VDW adhesion that was dependent on spike tip radius for native pollen and crystallite size for α-Fe_2O_3, and Fe_3O_4 replicas. Fe_3O_4 replicas were found to possess an additional long-range magnetic attraction to a permanent magnet. Although other authors have used coating or infiltration methods to chemically modify/transform pollen[43, 46, 48, 51, 64-67] and other biological microparticles[44, 45, 49, 68-74] for desired (bio)chemical, optical, electrical, structural, or fluidynamic properties, this work is the first time the conversion of sustainable biogenic particles (like pollen) into all-inorganic 3-D replicas for the purpose of achieving tunable multimodal adhesion has been reported.

2.3. *Experimental Procedures*

2.3.1. Template

Pollen is a desirable type of microparticle template to use due to its biological replicability (i.e., sustainability), ready availability, abundance, low cost, and wide range of features in both the micro- and nanometer range. Pollen templates will be chosen based on the overall size and shape from different plant species. The exine (outer layer)

of pollen grains are composed of sporopollenin, a complex polymer consisting of carboxylic acids cross-linked with aliphatic chains (e.g. HOOC-$(CH_2)_n$-COOH).[75] The carboxylic acids provide an abundant amount of functional groups needed for the reaction with the isopropoxide precursors used in the SSG process. These surface groups can eliminate the need for surface modification in order to obtain conformal coatings. The initial templates chosen to demonstrate inorganic replication and nano-feature retention are Sunflower (*Helianthus annuus*) pollen grains, as shown in Figure 1 d (section 1.2.1).

2.3.2. Demineralization of Pollen Grains

Pollen grains obtained from Greer Laboratories, Lenoir, NC USA were cleaned, to remove pollenkitt, by immersion in a mixture of chloroform and methanol (3:1 volume ratio)[76] for 24 h, followed by deposition onto filter paper (P5, Fisher Scientific, Pittsburgh, PA USA) and drying under vacuum at 60^0C for 12 h. A second immersion was conducted in 1 M hydrochloric acid (VWR, Suwanee, GA USA) for 1 h to remove residual inorganic material, followed by rinsing three times with de-ionized water and drying by vacuum aspiration at room temperature for 5 min.

2.3.3. SSG Coating of Pollen Grains Process

Fe-O-bearing coatings were applied to cleaned, dematerialized pollen grains via a computer-automated, layer-by-layer (LbL) SSG deposition process by:[77-80] i) immersing pollen grains for 10 min, with stirring, in a solution of 0.0125 M Fe(III) isopropoxide (Alfa Aesar, Ward Hill, MA USA) in anhydrous 2-propanol (>99.8% purity, Acros Organics, Geel, Belgium), to allow for the chemisorption of a Fe-O-bearing layer, ii) rinsing three times with anhydrous 2-propanol followed by vacuum filtration,

iii) immersion in de-ionized water (DIW), with stirring, for 5 min, to allow for hydrolysis of the chemisorbed alkoxide layer, iv) rinsing three times with anhydrous 2-propanol followed by vacuum filtration, and v) and drying by vacuum aspiration for 5 min. This process (alkoxide exposure, 2-propanol rinsing, DIW exposure, 2-propanol rinsing, drying) was repeated for a total of 2, 10, 20, 30, 40, 50 and 70 cycles to build up a Fe-O-bearing coating. A schematic for the SSG process can be seen in Figure 5. (Note: the SSG coating process was conducted at room temperature in a N_2 atmosphere glove box with a relative humidity maintained between 0-2%. The relative humidity was monitored using an Omega RH32 sensor, OMEGA Engineering, INC. Stamford, Connecticut)

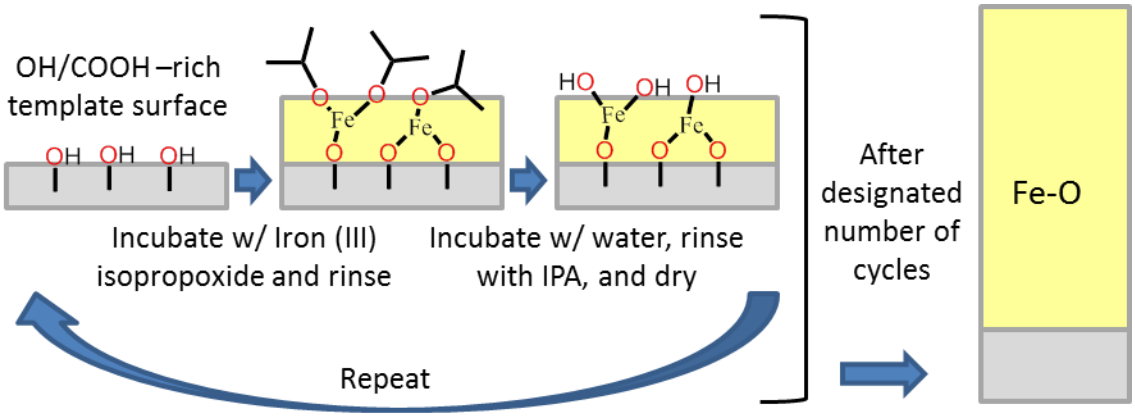

Figure 5: A schematic representation of the surface sol-gel process utilizing iron (III) isopropoxide as model metal alkoxide.

2.3.4. Organic Pyrolysis and Conversion to Magnetite and Iron

The SSG-coated pollen particles were prepared for pyrolysis in the following manner: i) SSG-coated pollen particles suspending in IPA and then dispersed onto nickel foil (25.4 µm thick, McMaster-Carr, Cleveland, OH, USA) using a pipette, ii) SSG-coated pollen particles suspending in IPA and then dispersed onto silicon wafers (Wafernet, Inc., San Jose, CA, USA) using a pipette, and iii) SSG-coated pollen particles also placed in an MgO crucible (96.6% MgO, 2% Y_2O_3, 1.6% other, Ozark Technical

Ceramics, Inc, Webb City, MO). Samples were fired in air using a tube furnace (Lindberg / Blue M, NC, USA,) with a ramp rate of 0.5°C min^{-1} to 200°C, 300°C, 400°C, or 600°C and held at this temperature for 4 h to allow for organic pyrolysis and oxide crystallization in air. For select samples the ramp rate was changed to either 0.5°C min^{-1}, 1°C min^{-1}, or 5.0°C min^{-1} to 600°C and held at this temperature for 4 h to allow for organic pyrolysis and oxide crystallization. Additionally samples were also heated in a sealed steel tube furnace in which the atmosphere was: i) vacuumed, and replaced with a 2%H_2/98%Ar gas mixture 3 times and ii) exposed to a flowing 2%H_2/98%Ar gas mixture for the duration of the thermal treatment. The thermal treatment in the reducing atmosphere were conducted in a tube furnace (Lindberg / Blue M, NC, USA,) with a ramp rate of 0.5°C min^{-1} to 200°C, 300°C, 400°C, and 600°C and held at this temperature for 4 h to allow oxide crystallization. The pyrolysis process was also studied using thermogravimetric analysis (TGA) (Netzsch STA 449C, Wolverhampton, UK). Thermogravimetric (TG) analysis measurements were performed with the as received pollen and as coated pollen grains (10-50 layers) at a heating rate of 0.5 and 5 ºC min^{-1} up to 1000 ºC in flowing synthetic air gas mixture. The residual mass was used to evaluate the mass of replica oxide coatings (10-50 layers) relative to the mass of native organic pollen. The sample mass was ~ 0.5 g for all measurements.

The resulting α-Fe_2O_3 hematite replicas were converted into magnetite via thermal treatment with a Rhines pack[81] powder mixture of Fe (99% purity, Acros Organics) and Fe_3O_4 (99.95% purity, Alfa Aesar). For the Rhines pack setup an 8 in. DOM steel (0.6 max wt.% Mn, 0.04 max wt.% P, 0.05 max wt.% S) tube (1 in. dia.) was clamped and welded shut at one end. The dispersed hematite replicas were placed in a Ni boat and

hematite pollen replicas in the MgO crucible were removed and placed in Ni foil crucible. A nickel boat filled with 2 g of Fe and 0.5 g of Fe_3O_4 was then placed in the welded end of the tube. This amount of Fe and Fe_3O_4 powder was well in excess of that needed to partially reduce the Fe_2O_3 replicas into Fe_3O_4. 0.1 g hematite pollen replicas were placed with the Fe/Fe_3O_4 powder mixture ($Fe:Fe_3O_4:Fe_2O_3$ replica mole ratio = 14:14:1) inside a mild steel ampoule. The remaining open end was then clamped and welded shut in air. The sealed samples were then heated at 3°C min^{-1} to 550°C and held at this temperature for 2 h. After cooling to room temperature, the ampoules were cut open and the magnetite pollen replicas were extracted. The Rhines pack setup is illustrated in Figure 6.

For conversion into iron, the magnetite pollen replicas were placed in a sealed steel tube furnace in which the atmosphere was: i) vacuumed, and replaced with a 2%H_2/98%Ar gas mixture 3 times and ii) exposed to a flowing 2%H_2/98%Ar gas mixture for the duration of the thermal treatment. The samples were then heated at 3°C min^{-1} to 550°C and held at this temperature for 2 h to reduce the magnetite replicas into iron replicas.

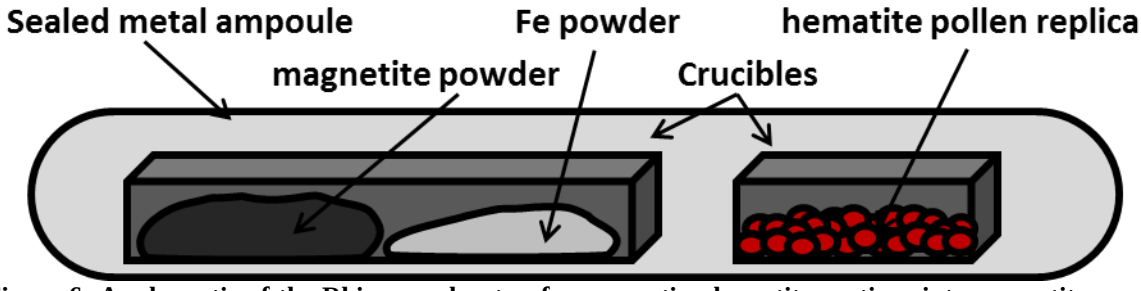

Figure 6: A schematic of the Rhines pack setup for converting hematite coatings into magnetite can be seen above. Hematite pollen replicas are placed in a sealed steal ampoule with excess Fe and magnetite powered in a 1:1 mol ratio. The sealed chamber allows for the hematite to be reduced and Fe to be oxidized until the pollen grains are converted in to magnetite.

2.3.5. Shape, Size, and Morphology Analyses

The morphologies of the native pollen grains, SSG-coated grains, the pyrolyzed grains, magnetite replicas, and iron replicas were evaluated with a field emission scanning electron microscope (1530 FEG SEM, LEO / Carl Zeiss SMT, Ltd., Thornwood, NY USA).

The change in pollen size before and after thermal treatments pollen were determined by imaging the same individual pollen grains before and after each thermal treatment in the following manner: Nickel foil substrates were stamped with distinctive patterns, such as "X" patterns. A pipette was used to place a droplet, consisting of a mixture of coated pollen particles in anhydrous 2-propanol, onto the nickel foil and the alcohol was allowed to evaporate. Low and high magnification SE images were used to identify particular particles (as well as particular surface features on a given particle) and their locations relative to a given stamped pattern. After pyrolysis and additional thermal treatments, similar SE images were again obtained to help locate particular individual grains and to evaluate the quality of replication (e.g., higher magnification SE images were used to identify whether particular surface features on a particular pollen grain replica were retained). Many of the pollen grains remained in the same location after pyrolysis (see the grains marked 1, 2, and 3 in Figure 7 a and b), which allowed for unambiguous evaluation of the shape and feature retention upon pyrolysis of these grains. The SSG coated pollen and pollen replica diameters were determined by fitting a circle around the pollen grain echini and measuring the diameter of the circle, as shown in Figure 8. The diameters of the same pollen grains were compared to each other before and after each thermal treatment. The average spine tip radii of cleaned sunflower pollen

particles, and of oxide replicas of sun-flower pollen particles, were obtained from secondary electron (SE) images of particles attached to cantilever probes (described below in section 2.3.7). For each particle-bearing probe, 5 spine tips located closest to the position where the particle made contact to the substrates were evaluated (for a total of 15 analyzed spine tips for all 3 similar types of particle-bearing probes).

Fracture cross-sections were obtained by grinding pollen grain replicas with a motor and pestle and placing the ground samples on carbon tape. Focused ion beam (FIB) milling (Nova Nanolab 200 FIB/SEM, FEI, Hillsboro, OR, USA) cross-sectional images of specimens were also obtained with the assistance of Dr. Ye Cai. FIB cross-sectional SE images of SSG coated sunflower pollen and the sunflower hematite replicas were generated by cutting(via FIB milling) an initial trench ~30 µm x 1µm and then milling sequential 200 nm thick slices ("cleaning cross-sections") away from the face of the trench being imaged.

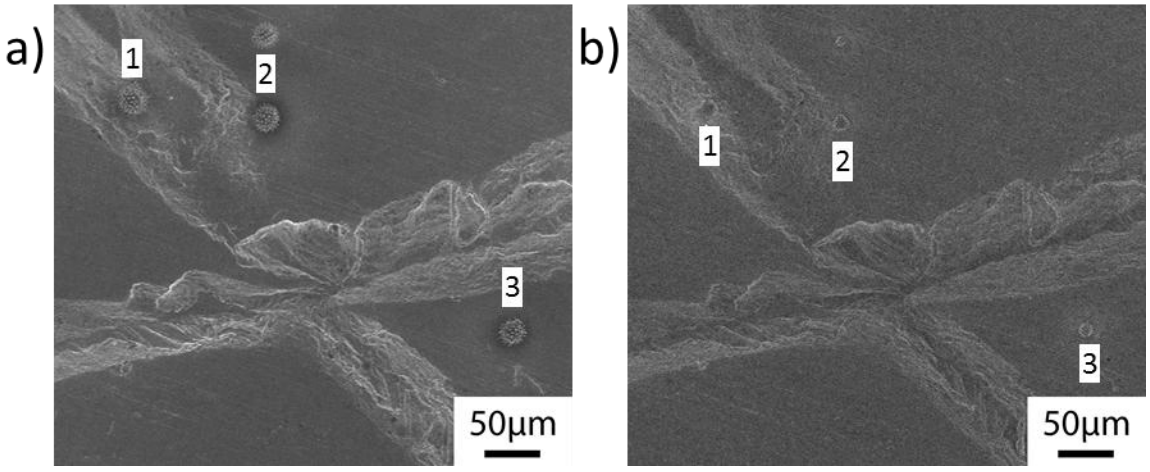

Figure 7: SE images of Fe-O-coated pollen grains on nickel foil: a) before thermal treatment (after 30 SSG cycles and drying) and b) after thermal conversion (at 600°C, 4 h, air) into α-Fe_2O_3 sunflower pollen replicas.

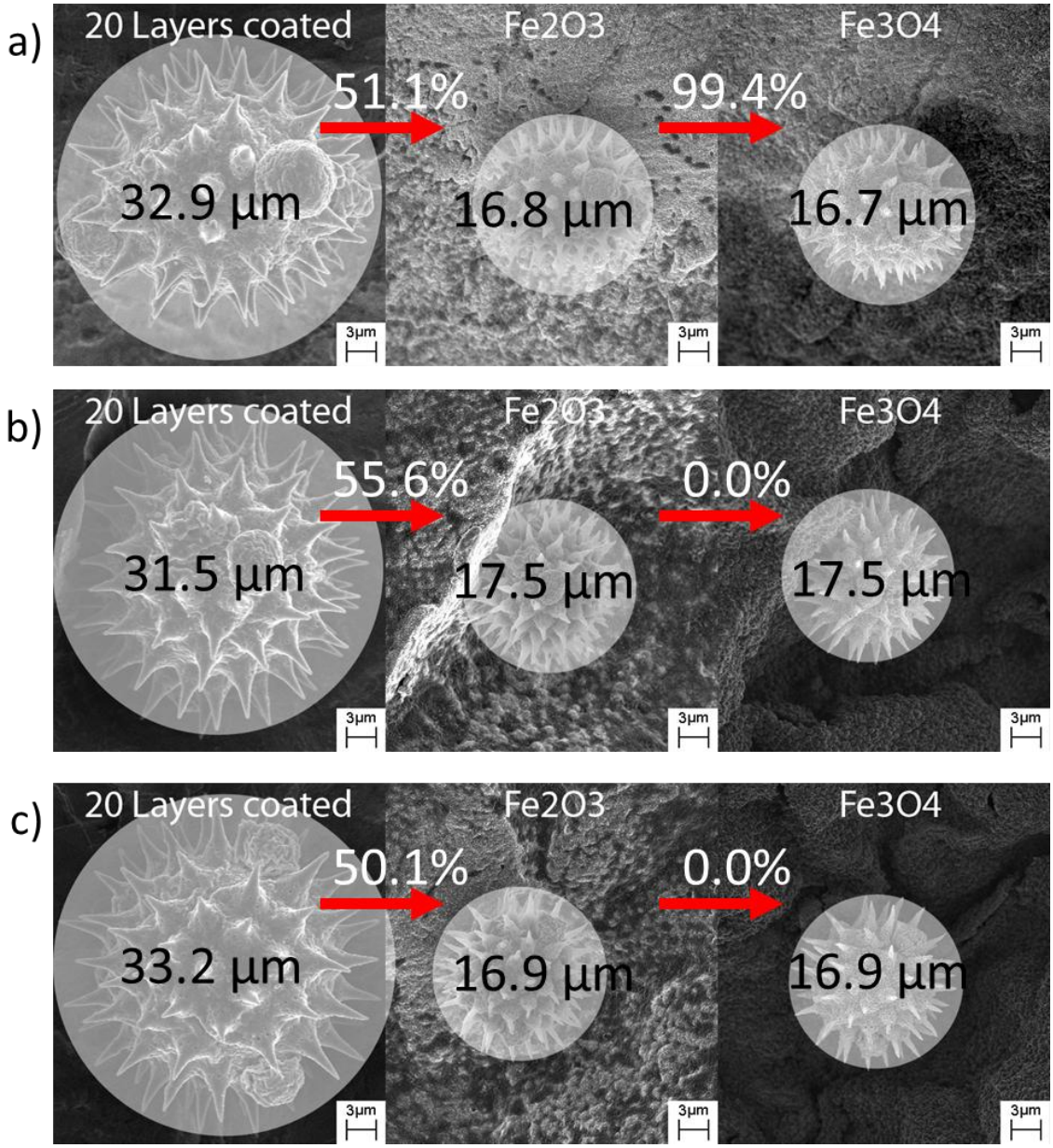

Figure 8: SE images demonstrating how the pollen and pollen replica diameters are calculated for 3 samples coated with 20 layers of Fe-O, converted into an α-Fe_2O_3 replica and converted into Fe_3O_4 replica. The translucent circles are fitted to the pollen grains and diameters are then measured to determine pollen size.

2.3.6. Phase, Grain Size, and Chemical Analysis

The phase identification for the fired pollen replicas were evaluated at room temperature using X-ray diffraction (XRD) analyses. XRD analyses were conducted on a diffractometer (X'Pert Pro Alpha-1, PANalytical B.V., ALMELO, Netherlands) with $Cu_{K\alpha 1}$(1.5405980 Å) radiation emanating from a 1.8 kW ceramic X-ray tube with a

copper anode (45 kV, 40 mA) through an incident beam Johannson monochromator (PANalytical) and detected by an X'Celerator detector. The incident beam optics were outfitted with 0.04 rad soller slits, a 1° fixed anti-scatter slit, a ½° programmable divergence slit, and a 10 mm mask. The diffracted beam optics was outfitted with a 5.5 mm anti-scatter slit and 0.04 rad soller slits placed before the X'Celerator detector. Each pattern was produced with a summation of 9 identical 30 minute scans conducted with Bragg-Brentano geometry and a step size of 0.004° 2θ ranging from 20° to 90° 2θ. Diffraction specimens were dispersed on quartz cut 6° from (0001) low background specimen support (GEM dugout, PA, USA) via pipetting an aliquot of IPA/powder slurry onto specimen support and allowing the IPA to evaporate. Phase identification and average crystallite size (ACS) were determined using the JADE software (Materials Data, Inc., Livermore, CA) based on the XRD peaks by using Scherrer's formula. The Scherrer's formula, given below, can be used to determine the average crystallite size, up to 100 nm in diameter, for powdered samples.[82]

$$t = \frac{k\gamma}{B\cos\theta} \tag{2.1}$$

were t = crystallite size, k = 0.89, λ= 1.54 Å ($Cu_{K\alpha 1}$), θ = peak position, and B = effective full width half maximum (FWHM) of the measured peak.

Elemental analysis determined by using an energy dispersive X-ray spectrometer (EDS) (INCA Model 7426, Oxford Instruments, Bucks, UK) equipped to a scanning electron microscope (1530 FEG SEM, LEO / Carl Zeiss SMT, Ltd., Thorn-wood, NY USA.

2.3.7. Substrate preparation and adhesion measurements

To study the short-range (VDW) and long range (magnetic) adhesion six types of substrates were utilize: silicon (Si), polyvinyl alcohol (PVA), polyvinyl acetate (PVAc), polystyrene (PS), nickel (Ni), and a nickel-coated neodymium (Ni-Nd) alloy. The Si substrates (Silicon, Inc., Boise, ID USA) were piranha-etched using a solution of 75 vol.% sulfuric acid (97% purity, BDH Chemicals Ltd., Radnor, PA USA) and 25 vol.% hydrogen peroxide (30 wt.%, BDH Chemicals Ltd.) at 80°C for 1 h. The polymer substrates (PVA, PVAc, PS) consisted of blade-cast polymer films on the cleaned Si substrates. For blade casting, solutions comprised of 15 wt% PS (MW = 100,000, Avocado Research Chemicals, Lancashire UK) in toluene (Sigma Aldrich, St. Louis, MO USA), 20 wt% PVAc (MW = 50,000, Alfa Aesar) in tetrahydrofuran (THF, BDH Chemicals Ltd.), or 3 wt% PVA (MW = 89,000-98,000, Sigma-Aldrich) in hexafluoroisopropanol (HFIP, TCI America, Portland, OR USA) were used. Blade casting (3540 Bird Film Applicator, Elcometer, Rochester Hills, MI USA) was conducted using a gap height of 1.2 mm, followed by slow drying under a saturated solvent environment for 2 days at 23°C. The films were then air-dried for 2 days at 23°C, followed by annealing in a vacuum oven for 1 day at 100°C. The resulting polymer films possessed thicknesses ranging from 20 to 100 μm and completely covered the underlying Si substrate. Ni substrates were prepared by polishing (PM5 System, Logitech Ltd., Glasgow, Scotland UK) nickel foil (0.150 mm thickness, grade 200, 99.5% purity, Shop-aid, Inc., Woburn, MA USA) to a surface finish of 0.06 μm using a colloidal SiO_2 suspension (Metlab Corp., Niagara Falls, NY USA). The Ni-Nd substrate consisted of an axially-poled, neodymium-iron-boron alloy permanent magnet disk (ND022N-35, 5 mm

diameter, 1.5 mm thick, Master Magnetics, Inc., Castle Rock, CO USA) onto which was attached the polished nickel foil.

The surface roughness of each type of substrate was evaluated with a scanning probe microscope (Dimension 3100 SPM equipped with a Nanoscope V Controller, Veeco Instruments, Inc., Plainview, NY USA) operated in tap-ping mode at 200-400 Hz using a pyramidal tip silicon cantilever (Applied NanoStructures, Inc., Santa Clara, CA USA). For each particular substrate, 3 randomly-located scans (10 μm x 10 μm) were conducted, with each scan area split into 4 sectors. The average roughness value for a given substrate was obtained from analysis of these 12 sectors.

To perform the adhesion measurements, single particle (a native sunflower pollen particle or oxide replica particle) were attached to an atomic force microscope (AFM) cantilever. A small amount of epoxy resin (Epoxy Marine, Loctite, Westlake, OH USA) was used to attach a given particle to a tipless silicon AFM cantilever (FORT-TL, Applied NanoStructures, Inc.). For each type of pollen-shaped particle (cleaned sunflower pollen, α-Fe_2O_3 replica, or Fe_3O_4 replica), and number of SSG coating cycles used (10, 20, 30, 40, and 50 layers) 3 single-particle-bearing cantilever probes were prepared (for a total of 63 particle/cantilever probes). The spring constants, as determined with the scanning probe microscope, of the sunflower pollen-bearing, α-Fe_2O_3 replica-bearing, and Fe_3O_4 replica-bearing cantilever probes fell in the ranges listed in Table 1. The adhesion force between an individual sunflower pollen particle, or oxide replica particle, and a particular substrate was evaluated with the scanning probe microscope operated in contact mode. For each particular particle/cantilever probe and particular substrate, 20 separate force-distance scans were randomly obtained, and the depth of

Table 1: Range of cantilever probe spring constants (N/m) used in this study.

Coatings	0	10	20	30	40	50
Cleaned	1.84-2.34	--	--	--	--	--
α-Fe_2O_3	--	1.44-2.26	1.08-1.66	1.19-1.91	0.81-1.53	1.60-3.10
Fe_3O_4	--	1.92-2.30	1.15-2.05	1.63-1.69	0.91-1.67	1.37-1.61

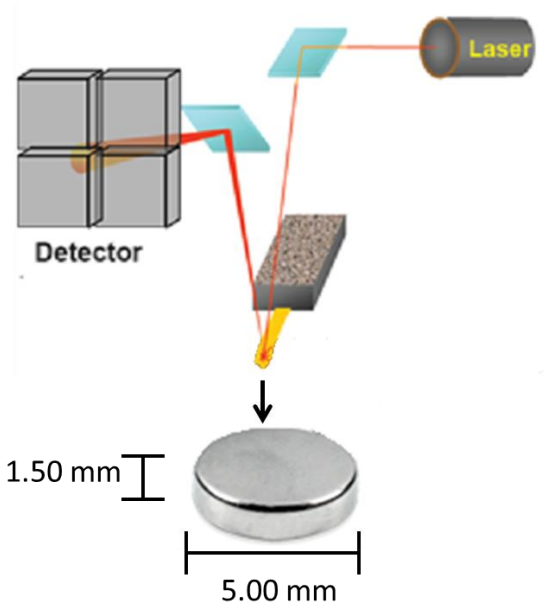

Figure 9: Experimental setup for long range magnetic adhesion measurements

adhesion wells upon retraction were aver-aged. The load force applied during the contact adhesion measurements was 2.5 nN. The longer-range magnetic forces acting between particle/cantilever probes and the axially magnetized permanent magnet Ni–Nd substrate were evaluated by scanning the probes across the diameter of this disk-shaped substrate at a fixed height of 140 μm above the substrate surface in order to locate the area of highest magnetic field. The pollen/cantilever probes were scanned from a height of 2000 μm to 50 μm with cantilever deflection measured at 50 μm intervals. The magnetic interaction setup can be seen in Figure 9. The ambient relative humidity in the laboratory during the adhesion measurements ranged from 30 to 35%. Note: the procedure described

in Section 2.3.7. was developed and performed by Ismael Gomez (Georgia Institute of Technology, Atlanta, GA, USA).

2.3.8. Magnetic property measurements

Magnetic property measurements were studied using a superconducting quantum interference device (SQUID) magnetometer (Quantum Design MPMS-5S, San Diego, CA USA). The instrument sensitivity is such that it can measure changes in magnetic response up to 10^{-11}G. For sample preparation, powder samples are weighed out and recorded to the nearest tenth of a milligram. The sample is then transferred to a 0.5 mm by 1.5 mm gelatin capsule (Quantum Design, San Diego, CA USA) and immobilized by eicosane ($C_{20}H_{42}$, Arcos Organic). The sample capsule is then sealed with Kapton tape and inserted in a plastic straw (Quantum Design, San Diego, CA USA). The sample container is then taped to the end of the sample rod and inserted into the sample chamber. The Magnetic Hysteresis measurements are performed at 300 K with magnetic field going up to 5 T. When the values are plotted, magnetic saturation, remanent magnetization, and coercivity can be determined. Magnetic responses are given in units of Am^2/Kg and the coercivity field in units of T.

2.3.9. Magnetic Force Measurements

The magnetic force of an individual oxide replica particle was probed with an axially-poled, neodymium-iron-boron alloy permanent magnet disk (ND022N-35, 5 mm diameter, 1.5 mm thick, Master Magnetics, Inc., Castle Rock, CO USA) onto which was attached a polished nickel foil (Ni-Nd). The Ni-Nd disk magnet possessed a residual induction of 12,300 G. For each particular particle/cantilever probe and Ni-Nd substrate,

20 separate force-distance scans were obtained at the edge of the Ni-Nd magnet (where the gradient of the magnetic field is highest). The difference in the non-contact forces at the surface of the Ni-Nd magnet and at maximum retraction from the Ni-Nd magnet is the magnitude of the magnetic force. Additionally, t-tests were performed to determine the overall statistical significance ($\alpha = 0.05$) of the change in calculated contact radii with the number of coating layers.

Magnetic force-distance curves between an individual oxide replica particle and the Ni-Nd substrate were obtained by recording the change in cantilever deflection relative to the cantilever deflection at maximum retraction upon approaching the edge of the Ni-Nd magnet. As a model standard, magnetic force-distance curves of a 10.4 μm diameter ferromagnetic chromium dioxide-coated polystyrene (CrO_2-PS) microsphere (M_r = 6.3 emu g^{-1}, 20 vol.% CrO_2, Spherotech, Inc., Lake Forest, IL USA) approaching the Ni-Nd disk magnet were measured. The ambient relative humidity in the laboratory during the magnetic force measurements ranged from 30 to 35%.

2.4. *Results & Discussion*

2.4.1. Acid Wash Treatments

Initial thermogravimetric (TG) analyses was conducted to determine the thermal conditions needed to completely pyrolyze the pollen particles (to allow for complete template removal for conversion of SSG-coated particles into freestanding, all-oxide replicas) indicated that the as-received defatted ragweed pollen contained a modest amount (~3%) of non-pyrolyzable inorganic material (ash), even after firing up to 1000°C (Figure 10 Black curve). TG analyses also indicated that all the organic content

could be pyrolyzed at a lower temperature of 600°C (Figure 10 blue curve). A 600°C minimum temperature was used for all pyrolysis conditions to insure all the organic content for the pollen replicas were removed. EDX analysis, of the residual pollen ash, indicated the presence of Ca, Si, and P, with lesser amounts of Mg and S, in the native pollen (Figure 11). X-ray diffraction (XRD) analysis of the ash generated by firing at 600^{o}C for 4 h in air yielded distinct diffraction peaks (Figure 12). To avoid undesired chemical interactions during the generation of oxide replicas of pollen particles (resulting from the reaction of native mineral constituents in the pollen with oxide coatings placed on the pollen), acid treatment (e.g., 1 M HCl) of the as-received pollen was examined for selective removal of the native mineral content based pervious work on demineralization on chitin.[83] Pyrolysis of such acid-treated particles (600°C, 4 h, air) yielded significant less ash and proved applicable to more than one type of pollen species, as TGA results indicates for both ragweed and sunflower pollen (Figure 13). Such acid demineralization was then adopted as a standard procedure prior to SSG coating of the pollen

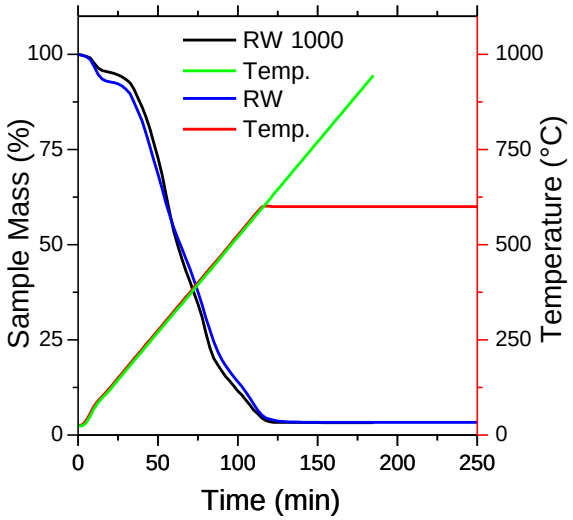

Figure 10: TG analyses of ragweed pollen upon heating in air at 5°C/min continuously to 1000°C, or to 600°C and holding at this temperature (the two TG traces are overlaid on top of each other)

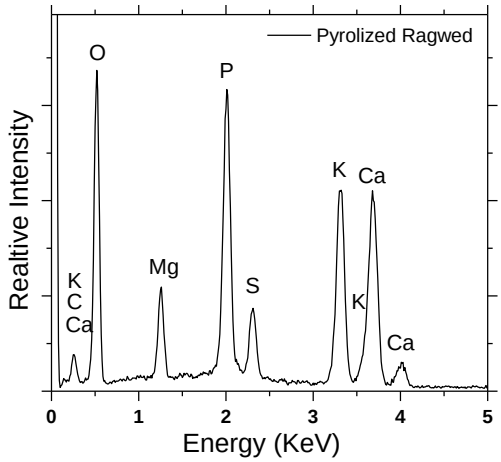

Figure 11: EDS analyses of ragweed pollen after pyrolysis in air at 600°C for 4 h.

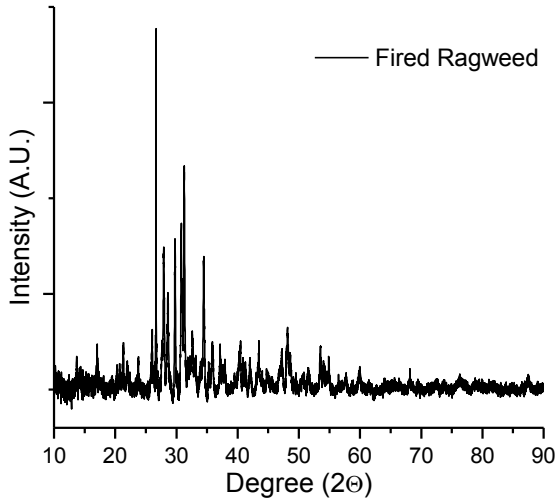

Figure 12: XRD analyses of ragweed pollen after pyrolysis in air at 600°C for 4 h.

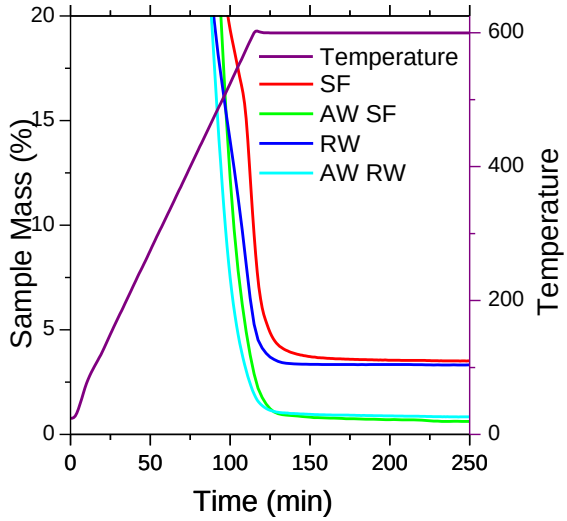

Figure 13: TG analyses of ragweed (RW) and Sunflower (SF) pollen upon heating in air at 5°C/min continuously to 600°C and holding at this temperature and TGA analyses of acid washed (AW) pollen grains showing a reduction in residual mass (ash) as a result of the acid treatment.

2.4.2. Hematite Pollen Replicas

Ragweed, dandelion, and sunflower pollen particles were converted into iron oxide replicas via use of a computer-automated LbL SSG coating process,[77-80] as described in section 2.3.3., without stirring, followed by pyrolysis at 600°C. Because the exine (outer layer) of such pollen grains is comprised of sporopollenin (a complex polymer consisting of carboxylic acids and aromatic moieties cross-linked with aliphatic chains[75]), the pollen surfaces were enriched with hydroxyl groups that provided an abundance of reaction sites for the chemisorption of alkoxide precursors during the SSG coating process.[61, 62] Repeated, alternating exposure of the pollen particles to an iron (III) isopropoxide precursor and to water allowed for the LbL buildup of a conformal Fe-O-bearing coating on the pollen grains. However, the pollen grains became clumped together after multiple coating cycles and a visual difference was noticed with the pollen grains at the center of the clumps compared to the edge. The pollen grains in the center retained more of the native yellow color compared to the much as the darker and brown pollen grains on the outside of the clumps. Initial SE results of the fired samples showed non-uniform results with significant differences in sunflower pollen replicas size. Certain pollen replicas were over 3.5 times the size as other grains as seen in Figure 14. An automated stirring mechanism was added to the SSG coating process to improve the pollen to pollen coating uniformity provide uniformity by preventing pollen grains to cluster together during incubation. Ragweed, dandelion, and sunflower pollen grains were coated with 30 layers of Fe-O and sequentially fired at 600°C. Secondary electron (SE) images of a starting, cleaned pollen grain are shown in Figure 15 a, c, and e and SE

image of the fired replicas can be seen in Figure 15 c, d, and f for Ragweed, dandelion, and sunflower pollen grains respectively.

Replicas of all three types of pollen grains were able to be synthesized demonstrating that the SSG process is not species dependent and that shape preserving replicas are able to be generated from each species of pollen. X-ray diffraction (XRD) analysis (Figure 16) indicated that these fired particles were comprised of phase-pure, nanocrystalline hematite (α-Fe_2O_3).

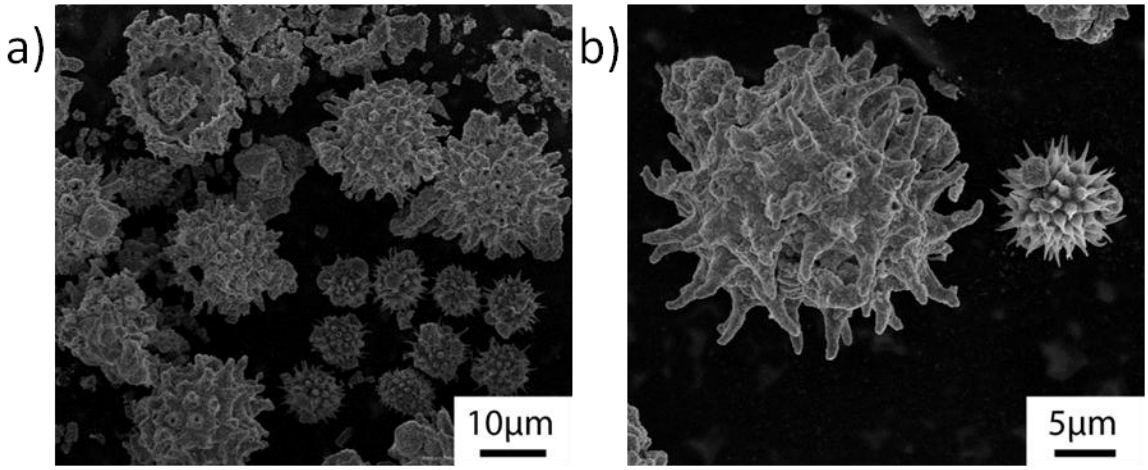

Figure 14: SE images of Hematite sunflower after coating with 30 Fe-O SSG deposition cycles without a stir bar and pyrolysis at 600^{o}C for 4 h in air.

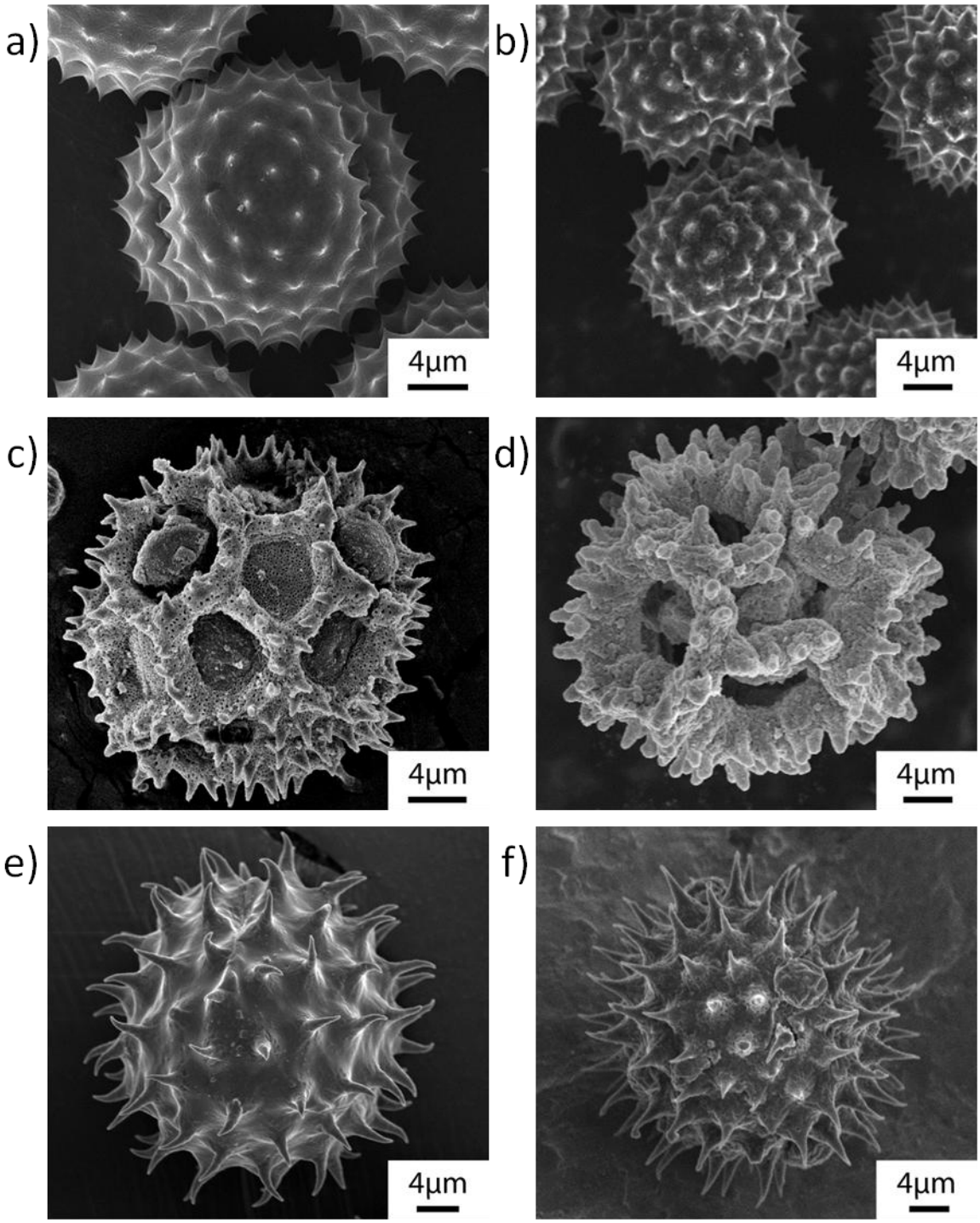

Figure 15: SE images of (a) native ragweed pollen, (c) native dandelion pollen, and (e) native sunflower pollen along with (b) ragweed pollen, (d) dandelion pollen, and (f) sunflower pollen α-Fe_2O_3 replica generated after 30 layers of Fe-O SSG deposition cycles and pyrolysis at 600°C for 4 h in air.

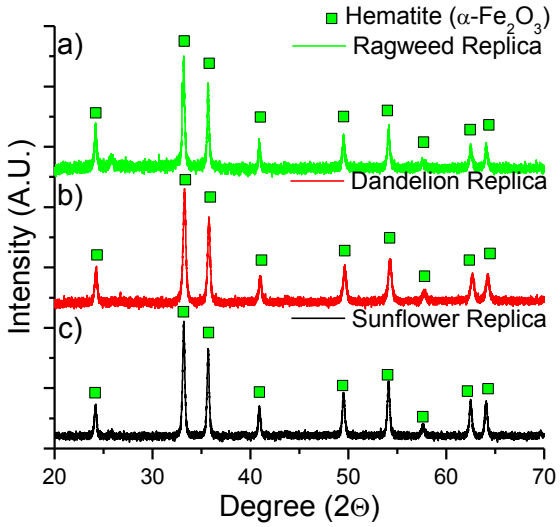

Figure 16: XRD analyses of iron oxide replicas of pollen grains generated by exposing the pollen particles to 30 SSG LbL deposition cycles and then firing at a peak temperature of 600°C for 4 h in air of a) ragweed pollen, b) dandelion pollen, and c) sunflower pollen.

2.4.3. Sunflower Pollen Shape Preservation and Magnetic Conversion

Sunflower replicas were converted to magnetite (Fe_3O_4) using the process described in section 2.3.4.. Secondary electron (SE) images of a starting, cleaned pollen grain are shown in Figure 17. The sunflower pollen grains were roughly spherical in shape and possessed echini (spines) of relatively high aspect ratio (height: width-at-midheight ratio of ~5:1). A SE image and energy-dispersive X-ray (EDX) analysis of a sunflower pollen particle after exposure to 30 SSG deposition cycles are shown Figure 18

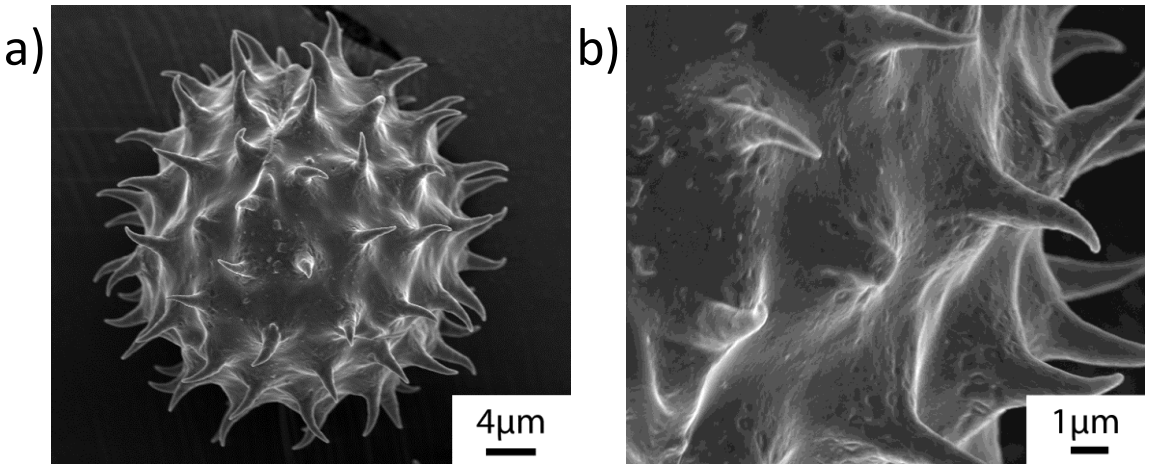

Figure 17: Low magnification a) and high magnification b) secondary electron (SE) micrograph of an individual sunflower pollen.

a, b and Figure 19 b, respectively. Comparison of the EDX analyses in Figure 19 a and b confirmed that the SSG-coated particle was enriched in iron and oxygen. The highly-conformal nature of the SSG Fe-O-bearing coating was evident from the preservation of the echini and the fine pores at the base of the echini (as indicated by the arrows in Figure 18 a, b).

The coated pollen particles were then heated in air at 600^{o}C for 4 h to allow for pyrolysis of the pollen template, and crystallization of the oxide coating. Complete pyrolysis of the sporopollenin during this treatment was confirmed by thermogravimetric analysis (Figure 20). TG analyses, of coated sunflower pollen particles that had been exposed to 10, 20, or 30 surface sol-gel deposition cycles (Figure 21) revealed that the amount of oxide retained after complete pyrolysis increased linearly with an increase in the number of SSG deposition cycles. The percentage of weight retained upon such complete organic pyrolysis was found to be 9.8, 13.8, and 17.7% of the starting weight of the pollen coated with 10, 20, and 30 surface sol-gel cycles, respectively. The increase in retained weight of these fired samples upon increasing the number of deposition cycles from 10 to 20 (13.8% - 9.8% = 4.0%) was similar to the increase in retained weight upon increasing the number of deposition cycles from 20 to 30 (17.7% - 13.8% = 3.9%). This linear increase in retained weight (i.e., an increase in the relative amount of hematite

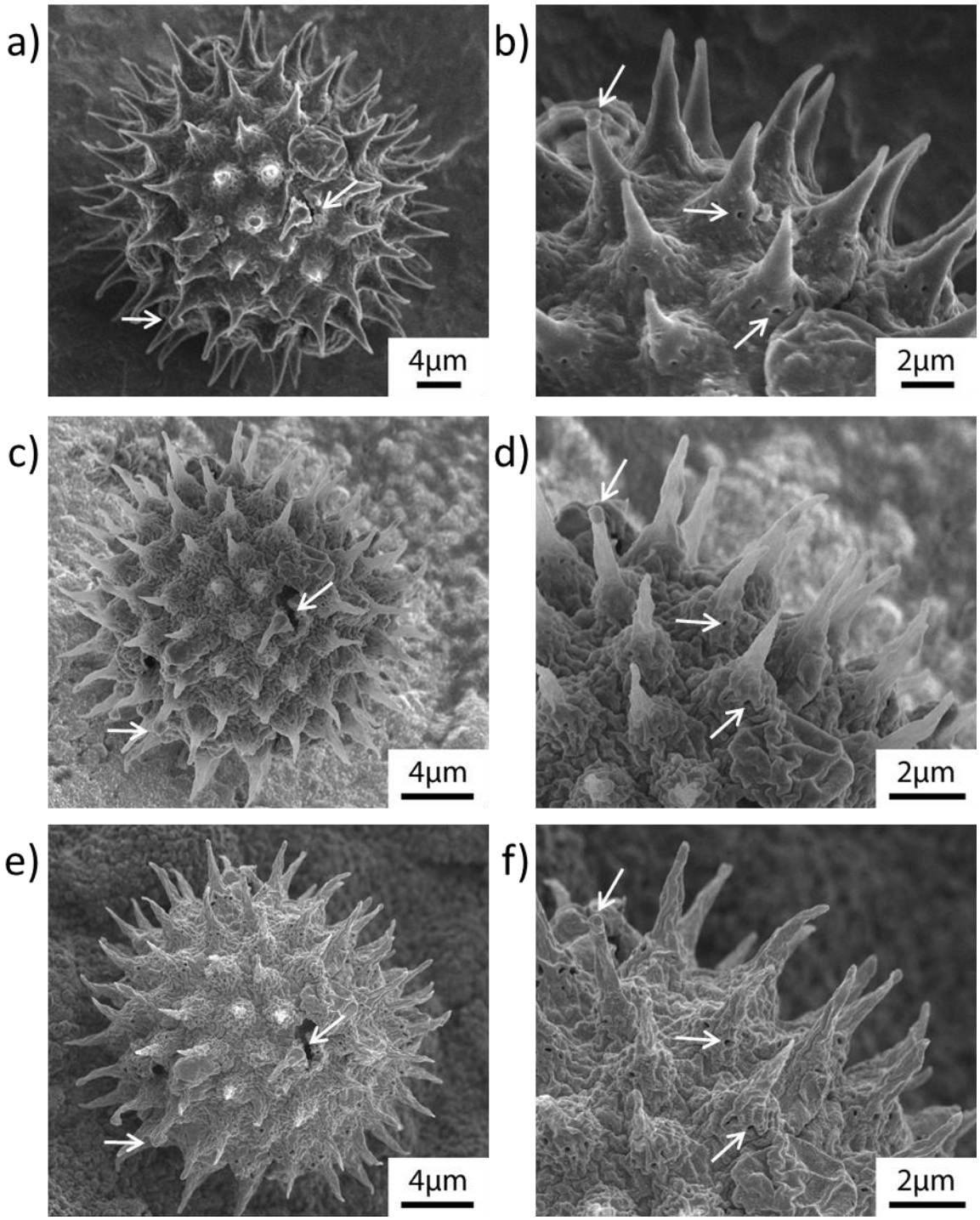

Figure 18: SE images of sunflower pollen particles at various stages of conversion into Fe_3O_4: a, b) an Fe-O-coated grain after 30 SSG deposition cycles, c, d) an α-Fe_2O_3 replica of the same grain in a, b) after pyrolysis at 600°C for 4 h in air, e ,f) a Fe_3O_4 replica of the same α-Fe_2O_3 grain in c, d) generated by partial reduction using a Rhines pack (Fe/Fe_3O_4) at 550°C for 2 h. Arrow point to select features that are preserved through the reaction process.

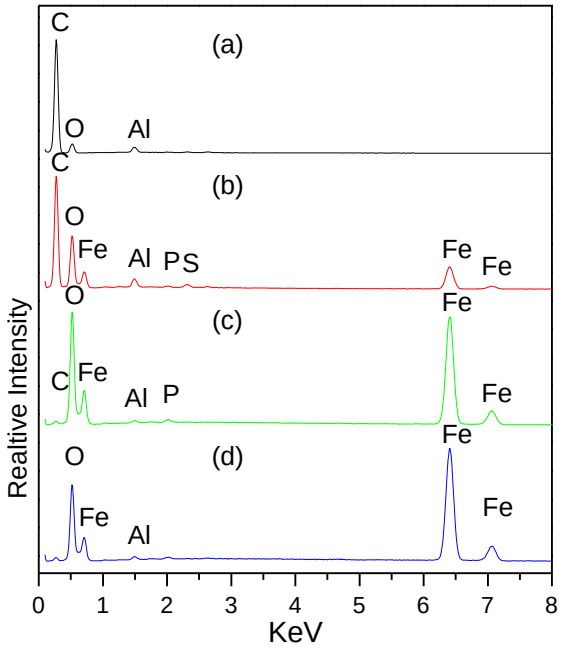

Figure 19: EDX analyses of: (a) the exine of a natural sunflower pollen grain, (b) an Fe-O-coated sunflower grain after 30 SSG deposition cycles, (c) an α-Fe_2O_3 replica of a sunflower grain generated by pyrolysis at 600°C for 4 h in air, and (d) a Fe_3O_4 replica of a α-Fe_2O_3 grain generated by partial reduction using a Rhines pack (Fe/Fe_3O_4 powder mixture) at 550°C for 2 h. (Note: the Al peak was obtained from the underlying aluminum stub used to support the particles during EDX analyses.)

present in the fired replicas) with the number of deposition cycles was consistent with a progressive linear buildup in the amount of Fe-O deposited on the pollen grains with an increase in the number of SSG cycles.

EDX analyses (Figure 19) also revealed the loss of carbon, and retention of iron and oxygen, after such pyrolysis. X-ray diffraction (XRD) analysis (Figure 25) indicated that these fired particles were comprised of phase-pure, nanocrystalline hematite (ICDD# 01-079-0007, α-Fe_2O_3). Scherrer analyses of the XRD peaks yielded an average hematite crystallite size of 35 nm. Although smaller than the starting, as-coated pollen particles (by about 40% Table 2), these hematite particles retained the 3-D shapes and surface features of the starting pollen grains (Figure 18 c, d). Indeed, the high-fidelity nature of

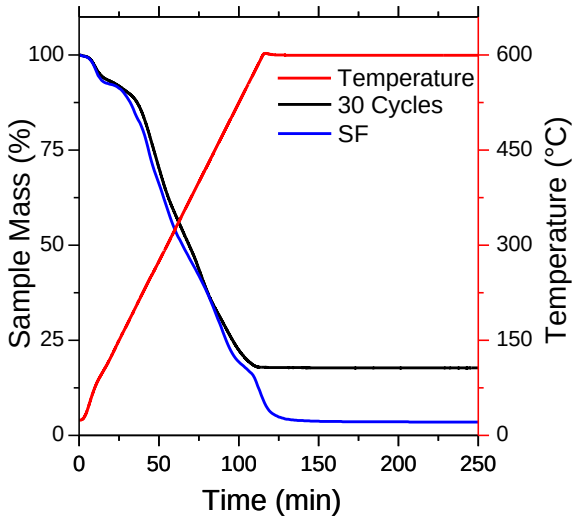

Figure 20: TG analysis of Sunflower pollen grains (blue) and Fe-O-coated sunflower pollen (30 SSG deposition cycles, black) during pyrolysis by heating in air at 5°Cmin^{-1} to 600°C.

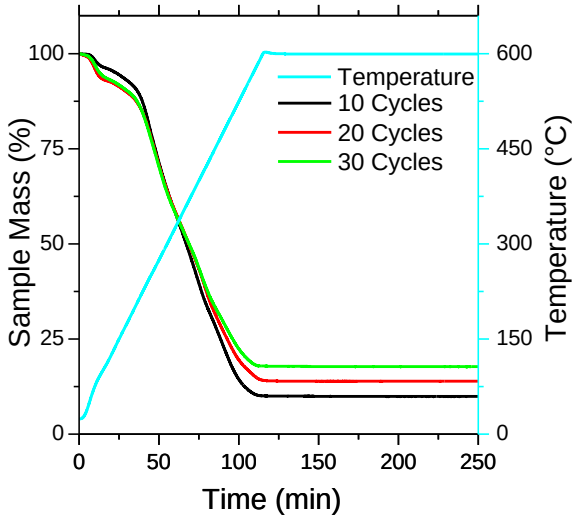

Figure 21: Thermogravimetric analyses of Fe-O-coated sunflower pollen (10, 20, and 30 SSG deposition cycles) during pyrolysis upon heating in air at 5°Cmin-1to 600°C. The percentage of weight retained upon complete organic pyrolysis was found to be 9, 8, 13.8, and 17.7% of the starting weight of the pollen coated with 10, 20, and 30 surface sol-gel deposition cycles, respectively. The increase in retained weight of these fired samples upon increasing the number of deposition cycles from 10 to 20 (13.8 - 9.8 = 4.0%) was similar to the increase in retained weight upon increasing the number of deposition cycles from 20 to 30 (17.7 - 13.8 = 3.9%).

such replication was revealed by SE images of *the same particle* before (Figure 18 a, b) and after (Figure 18 c, d) the 600°C/4 h treatment (note: the arrows in Figure 18 a/c and b/d reveal the same spine and fine pore present before and after this thermal treatment). At least 3 measurements of the diameter (spine tip to opposite spine tip) of a given grain

at a given stage of conversion were used to obtain the average values shown in Table 2 below. Thermal conversion of the as-coated grains into hematite resulted in a diameter reduction of 34-42%.

SE images of focus ion beam (FIB) milled samples (Figure 22) and fracture cross-sections of hematite pollen grain replicas (such as shown Figure 23) revealed that the walls of such replicas were porous and were comprised of interconnected oxide filaments. The FIB milled samples of native sunflower pollen and pollen grains coated with 30 layer of SSG both contain a solid inner core while the fired sample has a hollow interior. The interconnected coating SSG coating can be seen in the as coated FIB milled samples (Figure 22 c, d) and again on the fired FIB milled samples (Figure 22 e, f) and fractured cross section (Figure 23 a, b). The interconnected nature of the oxide filaments running through the wall thickness, and the absence of a distinct hollow core within the replica wall, indicated that the sporopollenin wall of the native pollen grains had been infiltrated by the iron isopropoxide precursor during surface sol-gel deposition. The average thickness of the porous wall of the hematite replicas was 540 nm. TEM cross-section images of hematite pollen grain replicas (Figure 24)

Table 2 Average values of the diameter (spine tip to spine tip) of the same pollen grain from the as-coated state (after 30 SSG deposition cycles) to the Fe_2O_3 state (after pyrolysis at 600°C for 4 h in air) to the Fe_3O_4 state (after Rhines pack treatment at 550°C for 2 h).

	Pollen Grain Average Diameter (Diameter Change)		
Specimen Number	As-Coated Grain	Fe_2O_3 Replica	Fe_3O_4 Replica
1	42.9 μm	26.5 μm (-38.2%)	26.4 μm (-0.4%)
2	30.5 μm	20.1 μm (-34.1%)	---
3	35.9 μm	21.8 μm (-39.3%)	---
4	31.4 μm	18.3 μm (-41.7%)	---

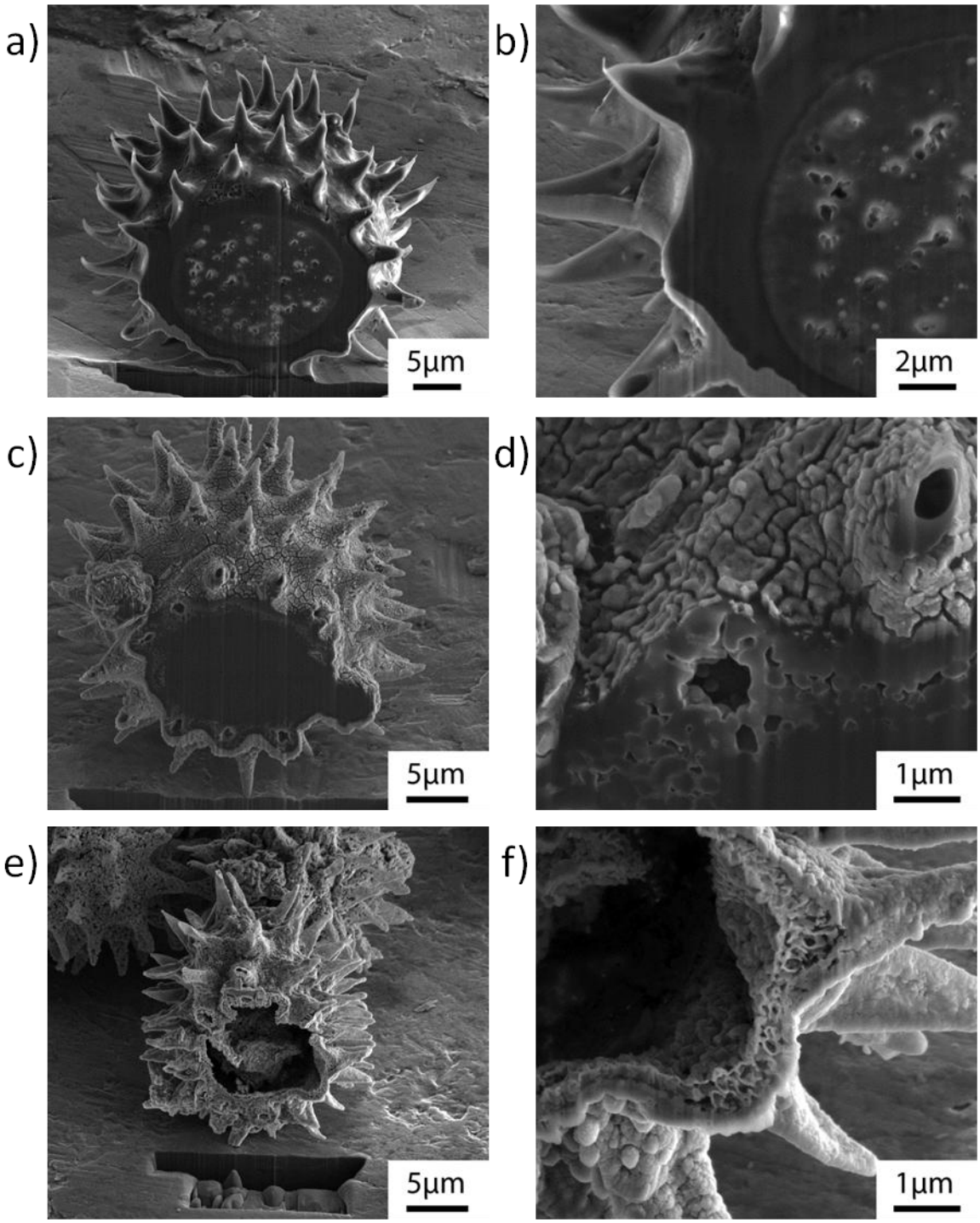

Figure 22: SE images of a FIB milled sunflower pollen particles at various stages of conversion into Fe_2O_3: a, b) a native pollen grain, c, d) an Fe-O-coated grain after 30 SSG deposition cycles, e, f) an α-Fe_2O_3 replica.

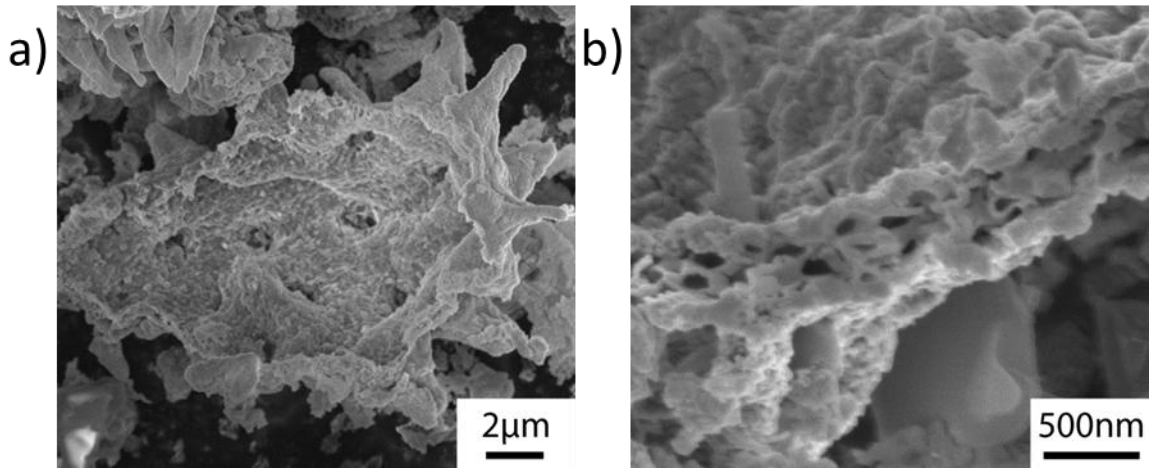

Figure 23: SE image of a fractured cross-section of the porous wall of an α-Fe_2O_3 replica sunflower pollen grain generated with 30 SSG deposition cycles and pyrolysis in air at 600°C for 4 h.

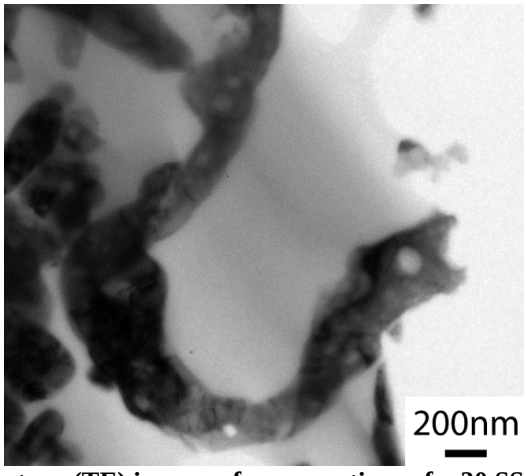

Figure 24: Transmission electron (TE) images of cross-sections of a 30 SSG deposition cycles α-Fe_2O_3 replicas of sunflower pollen grains (obtained by fracturing the grains).

Conversion of the hematite replicas into magnetite was conducted via use of a thermal treatment with a Rhines pack.[81] An excess powder mixture of iron and magnetite was sealed along with hematite pollen replicas within a mild steel ampoule. The ampoule was then heated to 550°C and held at this temperature for 2 h. The oxygen partial pressure established within the ampoule by the Fe/Fe_3O_4 equilibrium at 550°C (note: wüstite, $Fe_{1-x}O$, is thermodynamically unstable below 570°C[84]) allowed for complete conversion of the replica particles into phase-pure nanocrystalline magnetite (ICDD# 01-072-2303), as confirmed by XRD analysis (Figure 25 b). Scherrer analyses

yielded an average magnetite crystallite size of 34 nm. SE images (Figure 18 e, f) indicated that the 3-D morphology and sharp echini of the sunflower pollen were retained by the magnetite replicas (note: the arrows in Figure 18 c/d and e/f show the same spine and fine pore before and after this Rhines pack thermal treatment). No detectable change in replica particle size was detected upon conversion of the hematite into magnetite (note: increased handling of the specimens on the nickel foil substrates, due to loading into and removal from the steel ampoule used to seal the specimen with the Rhines pack, resulted in loss of 3 of the 4 specimens tracked to the Fe_3O_4 conversion stage in Table 2), which was consistent with the similarity in the volumes of these oxides on a per mole of iron basis (15.2 cm^3 Fe_2O_3/mole Fe; 14.9 cm^3 Fe_3O_4/mole Fe[85]).

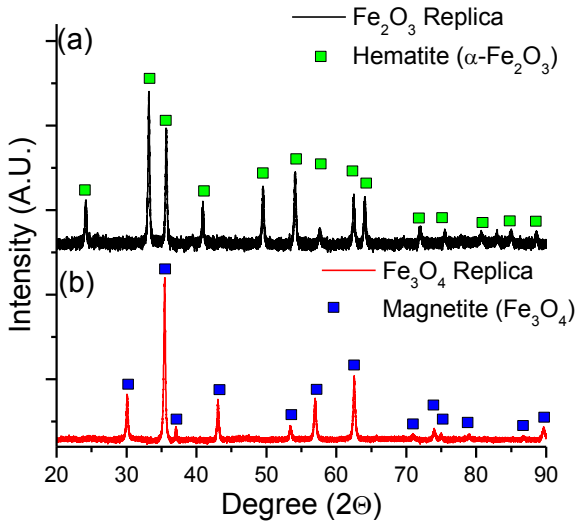

Figure 25: XRD analyses of iron oxide replicas of sunflower pollen generated by exposing the pollen particles to 30 SSG LbL deposition cycles and then: (a) firing at a peak temperature of 600°C for 4 h in air, followed by (b) sealing the resulting α-Fe_2O_3 samples, along with an excess powder mixture of Fe and Fe_3O_4 (a Rhines pack), within a mild steel ampoule and heating to a peak temperature of 550°C for 2 h.

2.4.4. SSG Cycles Effect on Pollen Replicas

The LbL SSG deposition Fe-O-bearing layers was used to control the amount of iron oxide deposited and study the effect cycle layer on shape and size retention upon subsequent thermal treatment and conversion into freestanding iron oxide replicas. The

previous section has shown that such a LbL SSG process can be used to deposit highly-conformal coatings onto complex 3-D templates, provided that the substrate possesses (or has been functionalized so as to possess) a high density of surface hydroxyl groups.[77-80, 86] While the sporopollenin comprising the exine (outer layer) of pollen particles has been reported to contain significant amounts of dicarboxylic and/or fatty acids[75], direct measurements of the density and spatial distribution of such OH-bearing molecules across the exine surface have not been reported. Because the chemisorption of iron alkoxide molecules to the pollen surface requires reaction with surface hydroxyl groups[61], the SSG process provides an indirect means of evaluating the surface -OH density/distribution. Secondary electron (SE) images of sunflower pollen particles after exposure to 10, 20, 30, 40 or 50 SSG deposition cycles are shown in Figure 26 a-e, respectively, with higher magnification images of the surfaces of a cleaned pollen particle and a coated particle presented in Figure 27 a, b. The roughly spherical shape and the sharp high aspect ratio (height: width-at-midheight ratio of ~5:1).echini (spines) and other surface features (e.g., pores present at the base of the echini) in the uncoated pollen particles were retained in the 10 - 50 SSG cycle samples, and significant gaps in the Fe-O-bearing coating were not detected. Such conformal coatings were consistent with the presence of a high and uniform concentration of hydroxyl groups on the sunflower pollen grain surface.

Conversion of Fe-O-coated pollen particles into freestanding (sporopollenin-free) polycrystalline Fe_2O_3 was accomplished via organic pyrolysis and oxide crystallization upon heating to 600°C in air. Dynamic TG analyses (Figure 28) indicated that such

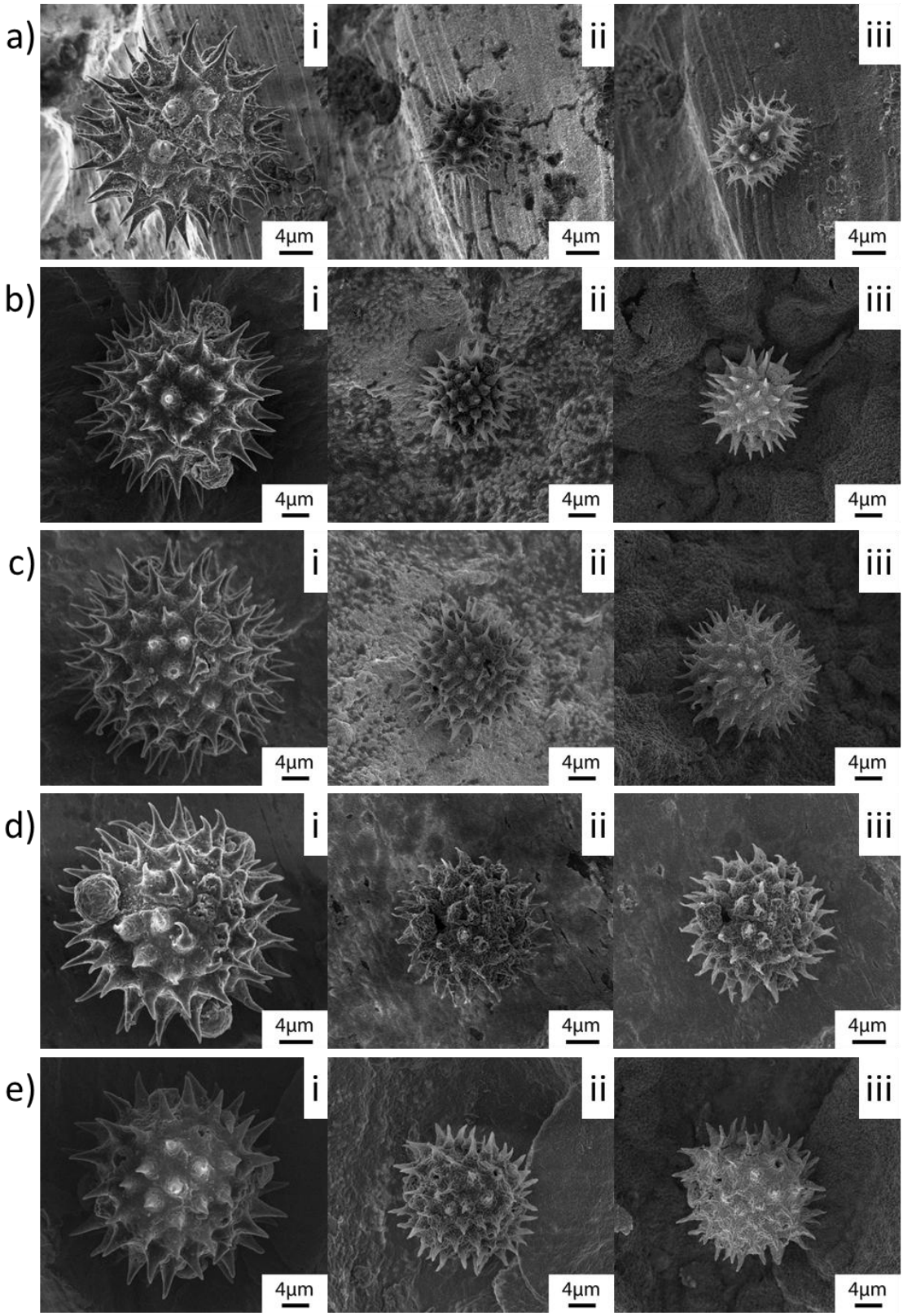

Figure 26: SE images of sunflower pollen particles with different number of LbL SSG coating cycles a) 10, b) 20, c) 30, d) 40, and e) 50 layers of Fe-O at various stages of conversion into Fe_3O_4: i) as coated pollen, ii) conversion into α-Fe_2O_3 replica, and iii)conversion into Fe_3O_4 replica.

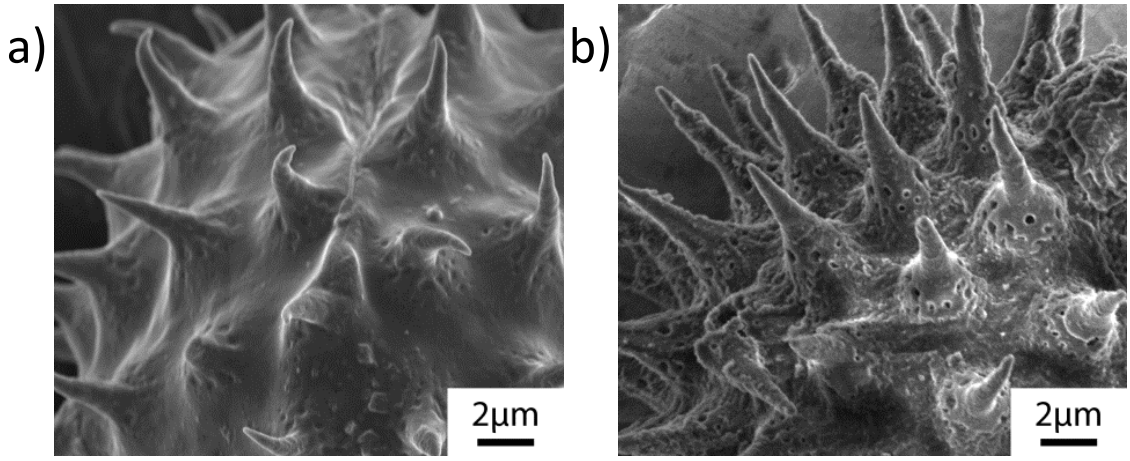

Figure 27: SE images of a) a cleaned sunflower pollen particle and b) a sunflower pollen particle exposed to 10 SSG deposition cycles.

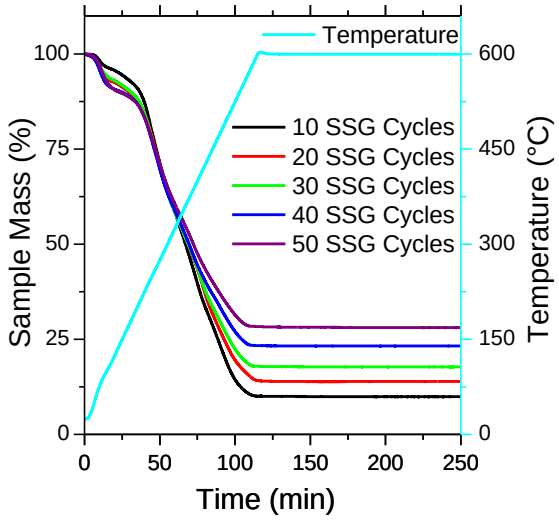

Figure 28:Thermogravimetric analyses of Fe-O-coated sunflower pollen (10, 20, 30, 40, and 50 SSG deposition cycles) during pyrolysis upon heating in air at 5°Cmin-1to 600°C. The percentage of weight retained upon complete organic pyrolysis was found to be 9, 8, 13.8, 17.7, 23.2, and 28.1% of the starting weight of the pollen coated with 10, 20, 30, 40 and 50 surface sol-gel deposition cycles, respectively.

pyrolysis was completed within a few minutes after reaching the peak temperature of 600°C.The percentage of weight retained upon such complete organic pyrolysis was found to be 9.8, 13.8, 17.7, 23.2, and 28.1% of the starting weight of the pollen coated with 10, 20, 30, 40, and 50 surface sol-gel cycles, respectively. The increase in retained weight of these fired samples upon increasing the number of deposition cycles from 10 to 20 (13.8% - 9.8% = 4.0%) was similar to the increase in retained weight upon increasing

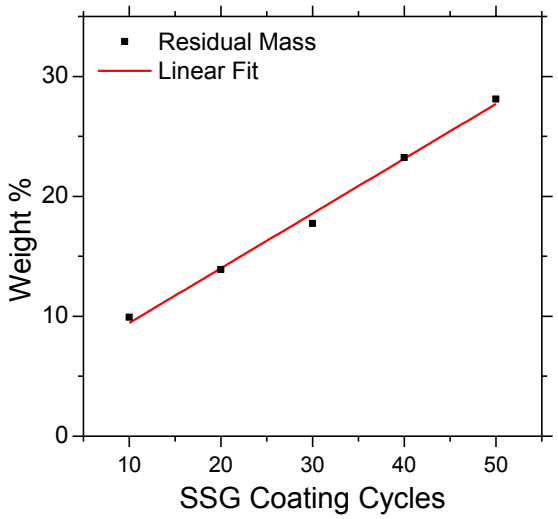

Figure 29: Remaining weight % after pyrolysis for TG analyses of Fe-O coated sunflower pollen particles (10-50 SSG deposition cycles) after pyrolysis to 600°C in flowing synthetic (20% O_2/80% N_2) air. Red line represents a linear fit of the data

the number of deposition cycles from 20 to 30 (17.7% - 13.8% = 3.9%), 30 to 40 (23.2% - 17.7% = 5.5%), and 40 to 50 (28.1% - 23.2% = 4.9%). The monotonic increase of the relative amount of oxide present after complete organic pyrolysis gave a linear fit with an R^2 value 0.997 for the number of alkoxide/water deposition cycles applied to the pollen grains (Figure 29). This linear increase in retained weight (i.e., an increase in the relative amount of hematite present in the fired replicas) with the number of deposition cycles was consistent with a gradual in the amount of iron oxide deposited on the pollen during the LbL SSG process.

XRD analyses (Figure 30 a) confirmed the presence of phase-pure hematite (α-Fe_2O_3) in the pollen replicas after the 600°C/4 h treatment in air, with Scherrer analyses yielding an average crystallite size of 35-39 nm (Figure 30). SE images (Figure 26 a ii, b ii, c ii, d ii, and e ii) revealed that the 3-D morphology of the sunflower pollen grains was retained by these Fe_2O_3-converted specimens. Such shape preservation in the freestanding Fe_2O_3 replicas provided confirmation of the conformity and continuity of

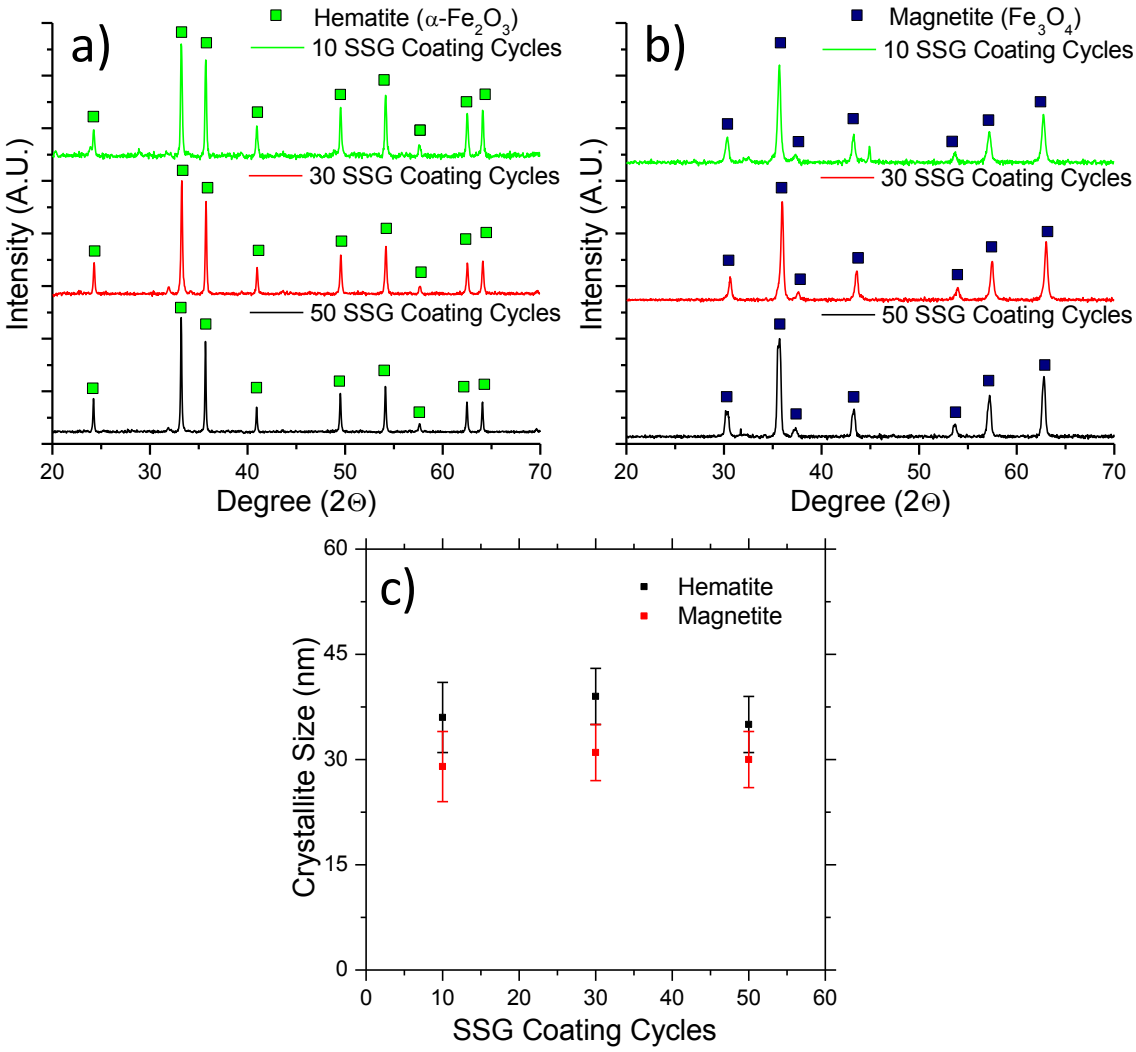

Figure 30: XRD analyses of iron oxide replicas of pollen grains generated by exposing sunflower pollen particles to 10, 30, and 50 SSG LbL deposition cycles and a) then firing at a peak temperature of 600°C for 4 h in air for conversion into α-Fe_2O_3 replicas, b) after conversion into Fe_3O_4 via exposure to a Fe/Fe_3O_4 Rhines pack treatment at 550°C for 2 h, and c) average crystallite size for each sample as determined from Scherrer analyses.

the SSG deposited Fe-O layers. In fact, Samples coated with just two deposition cycles were able to maintain the general pollen morphology after pyrolysis, as shown in Figure 31. While the Fe_2O_3 replicas were noticeably smaller than the starting pollen grains (Figure 26), the extent of shrinkage upon firing was found to decrease monotonically with an increase in the number of deposited Fe-O layers (Figure 32). The increase in the number of Fe-O deposition cycles from 10 to 50 resulted in an increase in the retention of

the as-coated pollen particle diameter from 48% to 70% upon pyrolysis at 600°C in air (Figure 32).

To further evaluate such thermally-induced shrinkage and oxide crystallization, uncoated pollen grains and pollen grains coated with 50 SSG layers were heated in air at a constant rate of 0.5°C/min to a peak temperature in the range of 200°C to 600°C, and then held at this peak temperature for 4 h. The change in average diameter of an uncoated

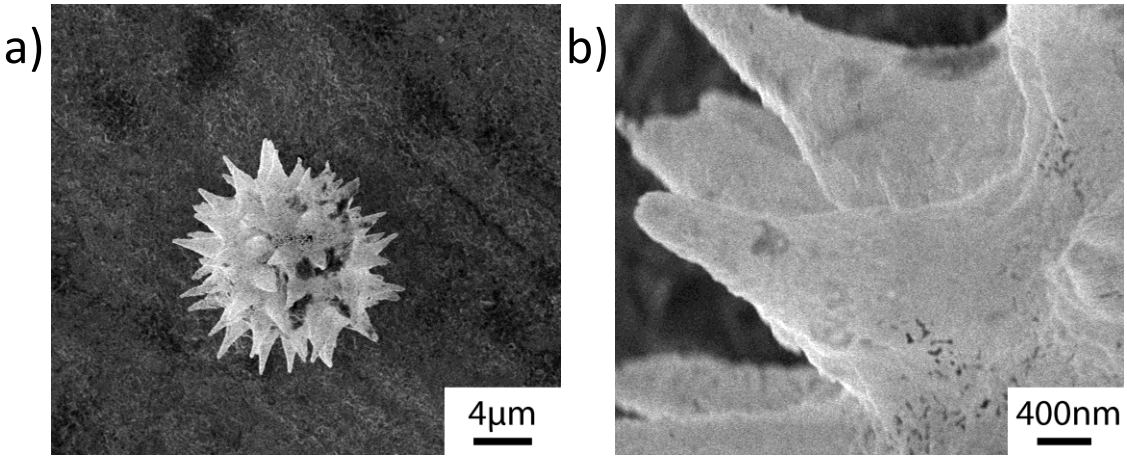

Figure 31: SE images of a Fe_2O_3 sunflower pollen replica after exposed to 2 SSG deposition cycles and pyrolysis at 600°C for 4 h in air..

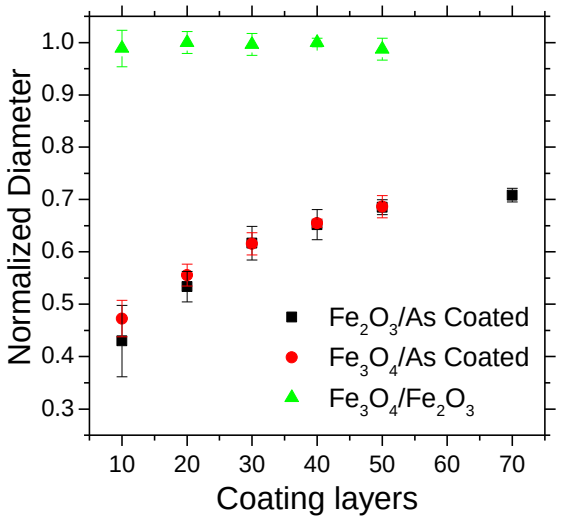

Figure 32: Plot of the average relative diameters of Fe-O-coated sunflower pollen particles as a function of the number of surface sol-gel deposition cycles (10-70) after various stages of thermal treatment: Black squares: pollen particle diameters after conversion into α-Fe_2O_3 replicas at 600°C for 4 h in air (relative as-coated particles); Red circles: pollen particle diameters after conversion into Fe_3O_4 via exposure to a Fe/Fe_3O_4 Rhines pack treatment at 550°C for 2 h (relative to the as coated pollen grains and green triangles relative to the α-Fe_2O_3 pollen replicas).

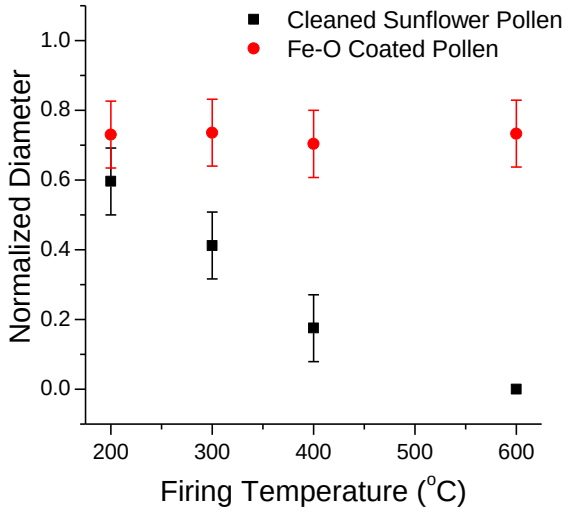

Figure 33: Shrinkage of a cleaned sunflower pollen grain and a Fe-O-coated (50 SSG cycles) pollen grain as a function of thermal treatment in air for 4 h at the indicated temperature.

or coated pollen grain was then determined from SE images of the same particle before and after such a thermal treatment. As shown in Figure 33 and Figure 34 a-h, the grains exhibited a monotonic decrease in size with increasing temperature, with complete pyrolysis occurring within 4 h at 600°C (as expected from TG analyses). However, the change in diameter of the pollen grains coated with 50 SSG layers was the same after all of the thermal treatments examined (Figure 33 and Figure 35 a-h). In other words, the shrinkage of the pollen grains coated with 50 SSG layers was completed even after the 200°C/4 h treatment, which was well before the underlying organic template had been completely burned away. Interestingly, XRD analyses of the pollen grains with 50 SSG layers (Figure 36) revealed little crystallization after the 200°C/4 h treatment, whereas extensive hematite crystallization was detected after the 300°C/4 h and higher temperature treatments. Apparently, the 50 layer Fe-O-bearing coating became sufficiently rigid during the 200°C/4 h, without the need for extensive hematite crystallization, as to avoid further shrinkage.

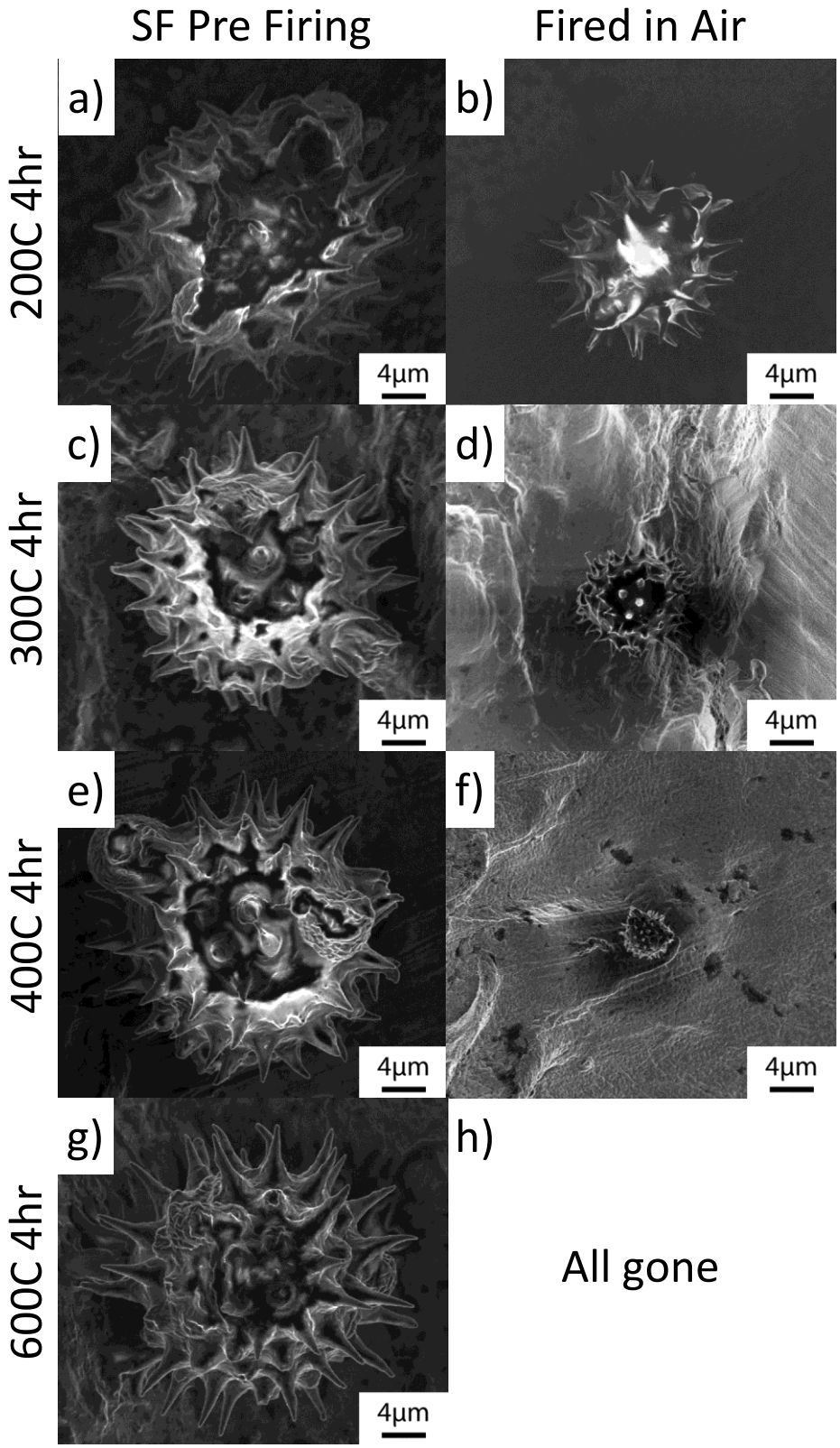

Figure 34: Secondary electron (SE) images of: (left column) native (defatted) sunflower pollen grains before (a), c), e), j)) and (column right) the same grains after pyrolysis in air for 4 h at 200°C (b)), 300°C (d)), 400°C (e)), or 600°C (f)).

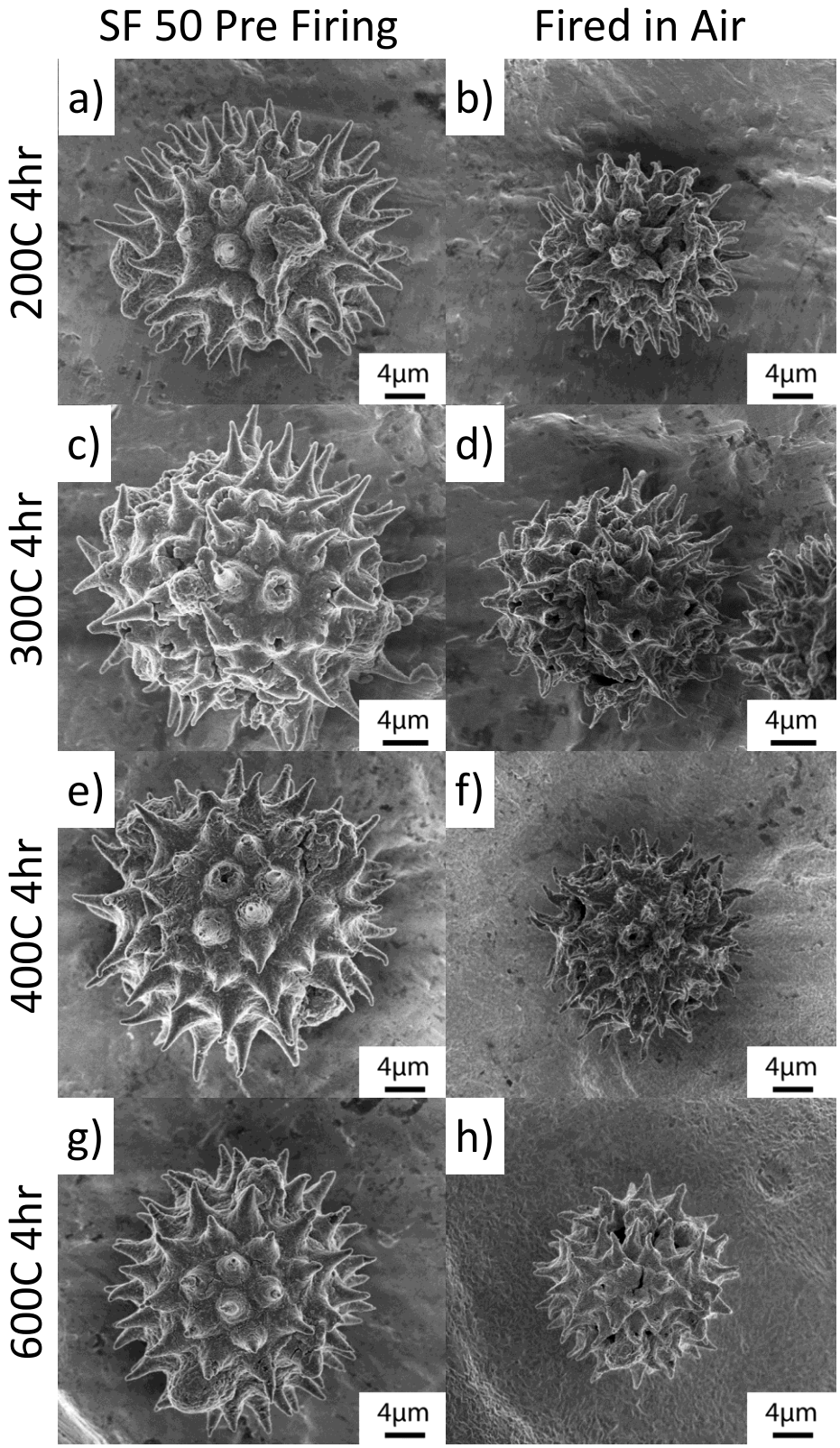

Figure 35:SE images (left column) Fe-O-coated pollen grains exposed to 50 surface sol-gel deposition cycles before (a), c), e), g)) and (right column) the same grains after pyrolysis in air for 4 h at 200°C (b)), 300°C (d)), 400°C (f)), or 600°C (g)).

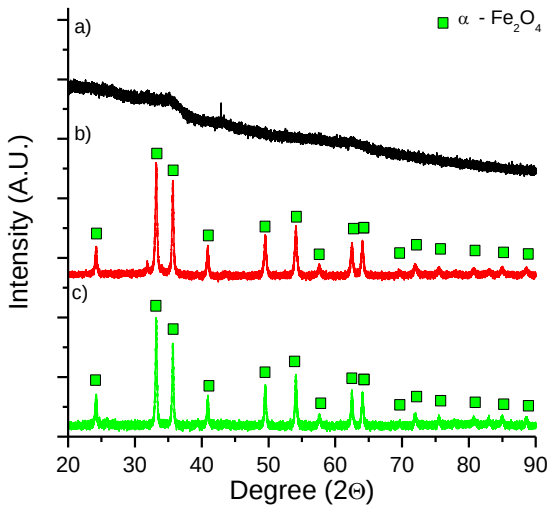

Figure 36: XRD analyses of Fe-O-coated sunflower pollen grains, exposed to 50 surface sol-gel deposition cycles, after pyrolysis for 4 h in air at: a) 200°C, b) 300°C, or c) 600°C.

If the overall rate of oxidative pyrolysis of pollen is controlled by a chemical reaction step that involves oxygen, then the rate of such pyrolysis should be reduced as the oxygen partial pressure is reduced. To investigate this possibility, pyrolysis experiments were conducted at appreciably lower oxygen partial pressures, so as to slow the rate of organic pyrolysis due to oxidation at 200-600°C. High purity argon, possessing a nominal oxygen partial pressure (pO_2) of 10^{-5}atm, was passed over a heated titanium getter, to further lower the pO_2 of this gas to $<10^{-18}$atm (as determined with an oxygen sensor).Native and Fe-O-coated (50 surface sol-gel exposure cycles) sunflower pollen grains were then heated in this oxygen-gettered argon atmosphere at 0.5°C/min to a peak temperature of 200°C, 300°C, 400°C, or 600°C and held at this peak temperature for 4 h. As shown in below, and plotted in Figure 37, the extent of shrinkage of the native pollen grains (Figure 38) and of the Fe-O-coated grains (Figure 39) after pyrolysis in this low pO_2 atmosphere were appreciably lower than for pyrolysis at the same peak temperature/time in air (compare Figure 34 Figure 35). After such low pO_2 pyrolysis at 200°C, 300°C, 400°C, or 600°C Fe-O-coated pollen grains exhibited diameter reductions

of only 9-17% (vs. 26-30% for Fe-O coated pollen grains pyrolyzed in air). The low pO_2 pyrolysis also experienced a more dramatic response to pyrolysis temperature with greater shrinkage at higher temperatures while the Fe-O coated samples pyrolyzed in air did not exhibit a similar trend. After the low-pO_2 pyrolysis at 300°C/4 h, XRD analysis (Figure 40) revealed diffraction peaks consistent with nanocrystalline magnetite, Fe_3O_4. At temperature above 300°C the oxide coatings start to be reduced and at 600°C the pollen replicas are almost single phase iron.

Given such extensive crystallization of hematite (a relatively stiff, non-plastic material) at only 300°C for 4 h, further experiments were conducted to evaluate the effect of the heating rate during pyrolysis in air. If the temperature dependence of the pyrolysis/shrinkage rate is appreciably different than the rigidification/crystallization rate, then a change in the heating rate to such modest temperatures during such simultaneous pyrolysis and crystallization could alter the extent of shrinkage. Little difference was detected, however, in the extent of shrinkage of the oxide pollen particle replicas generated with these different heating rates (Figure 41). While the choice of pyrolysis

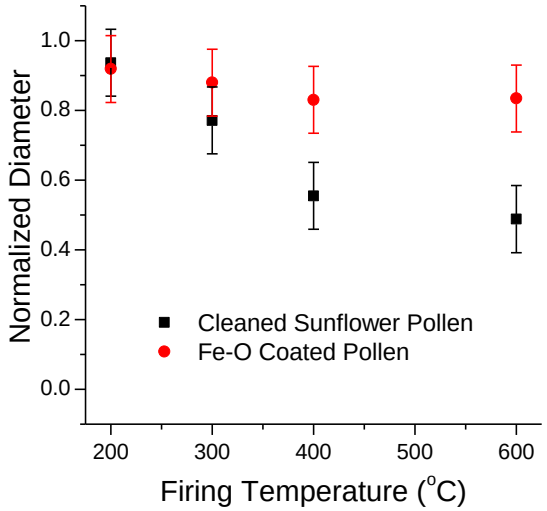

Figure 37: Shrinkage of a cleaned sunflower pollen grain and a Fe-O-coated (50 SSG cycles) pollen grain as a function of thermal treatment in O_2-gettered Ar for 4 h at the indicated temperature.

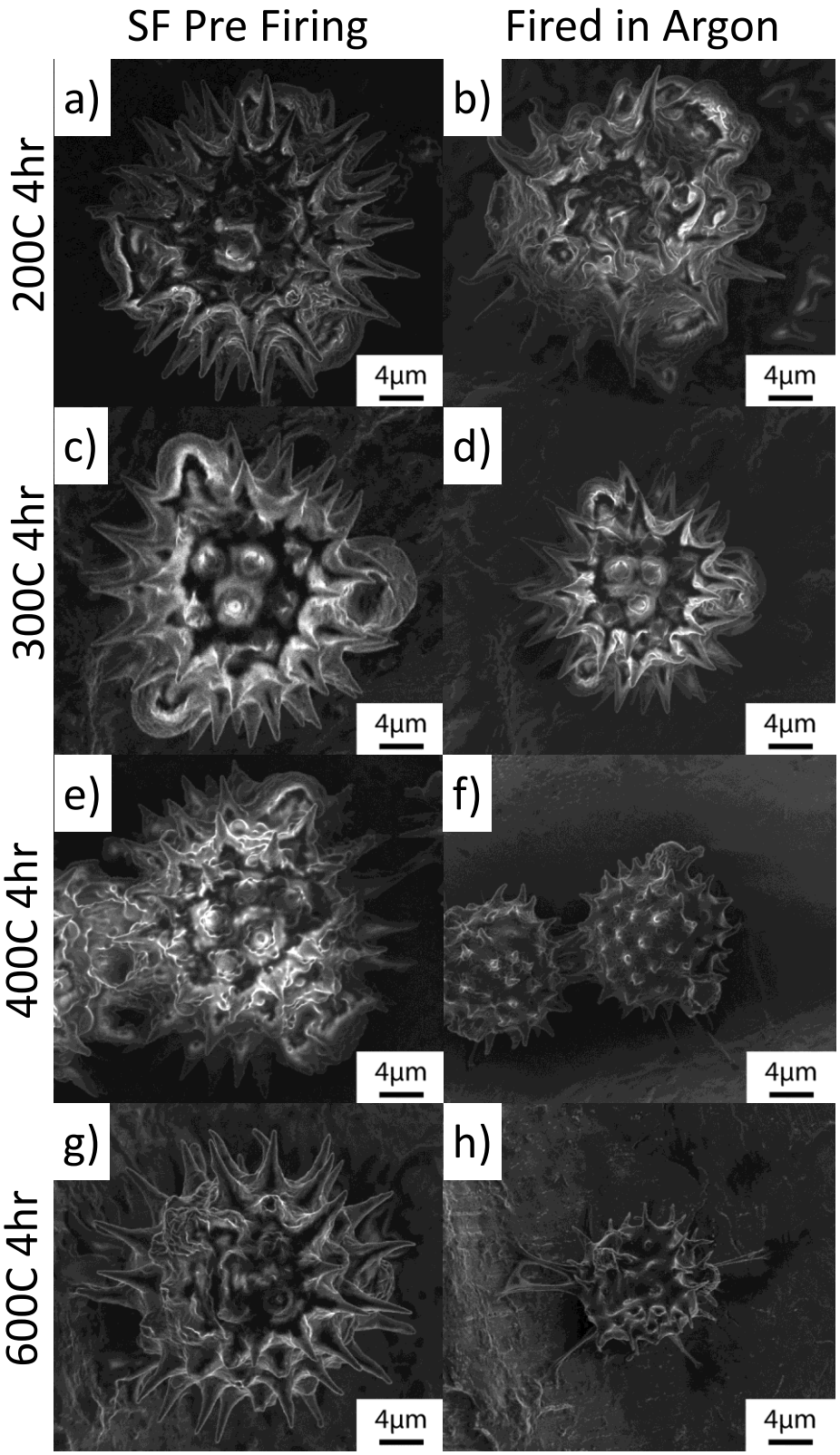

Figure 38: SE images of: (left column) native (defatted) sunflower pollen grains before (a), c), e), g)) and (right column) the same grains after pyrolysis in O_2-gettered Ar ($pO_2<10^{-18}$atm) for 4 h at 200°C (b)), 300°C (d)), 400°C (f)), or 600°C (g)).

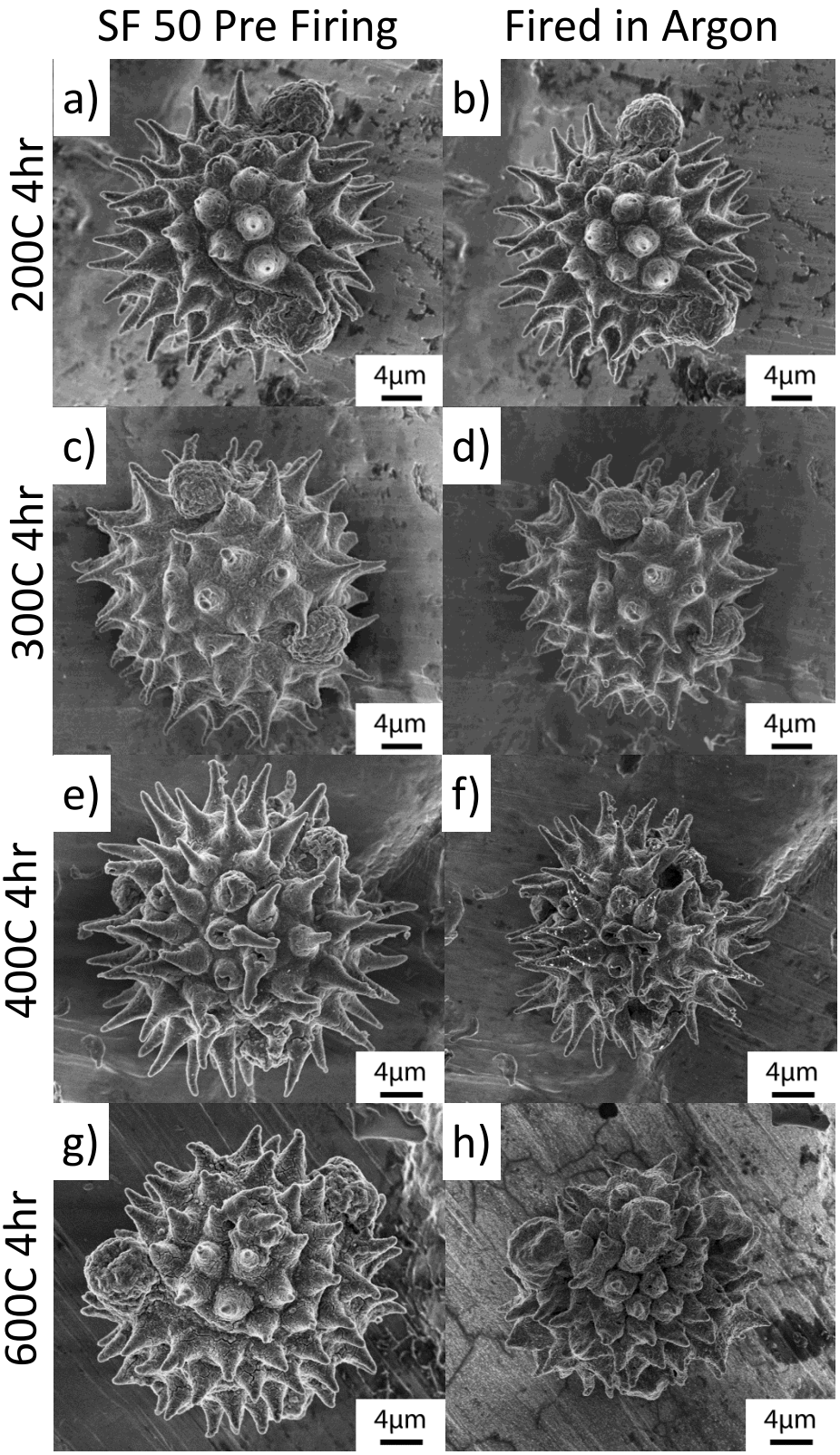

Figure 39: SE images of: (left column) Fe-O-coated sunflower pollen grains exposed to 50 surface sol-gel deposition cycles before (a), c), e), g)) and (right column) the same grains after pyrolysis in O_2-gettered Ar ($pO_2<10^{-18}$atm) for 4 h at 200°C (b)), 300°C (d)), 400°C (f)), or 600°C (g))

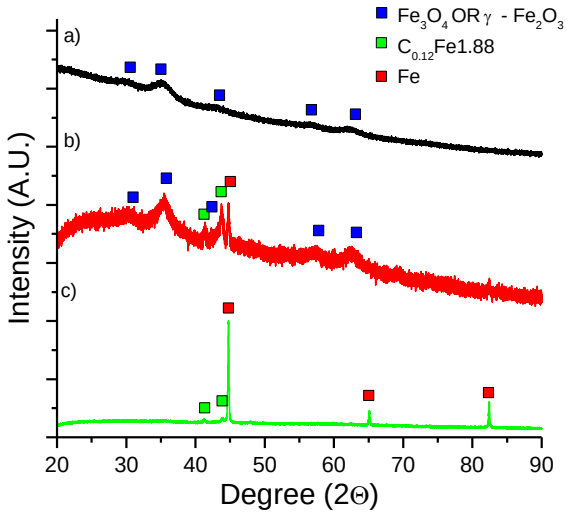

Figure 40: XRD analyses of Fe-O-coated sunflower pollen grains, exposed to 50 surface sol-gel deposition cycles, after pyrolysis in O2-gettered (pO_2<10^{-18}atm) for 4 h at: a)300°C, b)400°C, or c)600°C.

temperature, over the range of 200°C to 600°C, and heating rate to such temperatures (from to 0.5°C/min to 5.0°C/min) made little difference on the extent of shrinkage of Fe-O-coated pollen particles upon pyrolysis for 4 h in air (red data points in Figure 33), the pyrolysis-induced shrinkage was found to depend on the number of Fe-O layers applied to the pollen particles by the surface sol-gel process.

The conversion of hematite pollen replicas into phase-pure magnetite replicas was conducted via use of a controlled oxygen partial pressure heat treatment using a Rhines pack[81] mixture of Fe and Fe_3O_4; that is, the hematite pollen replicas were sealed, along with an excess mixture of iron and magnetite powder, inside a mild steel ampoule. At temperatures below 570°C, wüstite ($Fe_{1-x}O$) is thermodynamically unstable at ambient pressure[84], so that iron and magnetite can coexist at equilibrium at $\leq$ 550°C. Upon heating to 550°C, the oxygen partial pressure established by the excess Fe/Fe_3O_4 mixture can result in the reduction of Fe_2O_3 into Fe_3O_4 (i.e., via oxidation of some of the Fe into Fe_3O_4). Complete conversion of the hematite pollen replicas into magnetite was accomplished within 4 h at 550°C, as confirmed by XRD

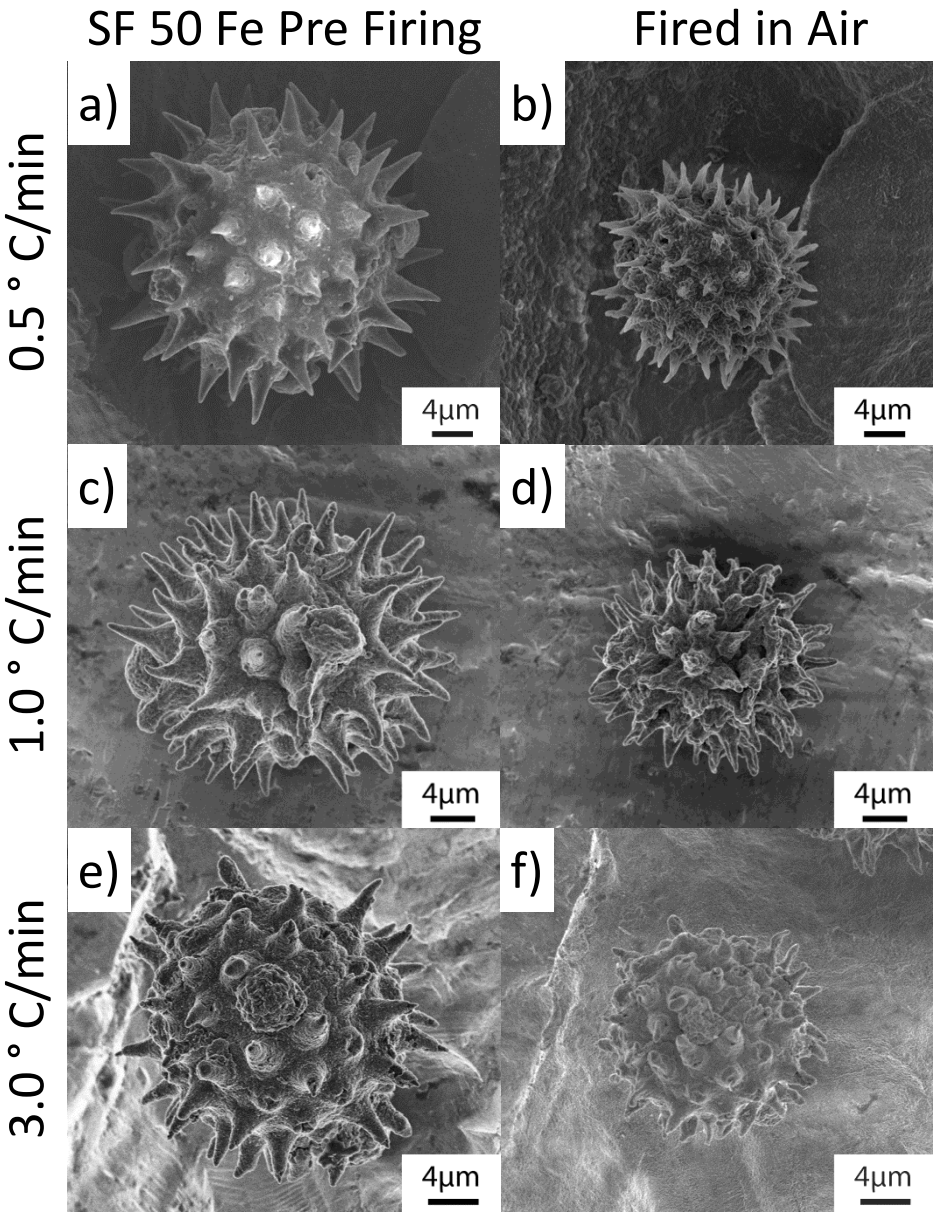

Figure 41: SE images of the Fe-O-coated (50 layers) Sunflower pollen grains before (left column: a), c), e)) and after (right column) pyrolysis in air via heating at 0.5°C/min (b)), 1.0°C/min (d)), or 5.0°C/min (f)) to a peak temperature of 600°C, and then holding at this temperature for 4 h.

analysis (Figure 30 b). The average crystallite size of the magnetite-converted pollen grains (Figure 30 c) was in the range of 29-31 nm. SE images of the magnetite-converted grains (Figure 26 a iii, b iii, c iii, d iii, and e iii) indicated that these specimens retained the 3-D morphologies and surface features of the starting pollen and hematite pollen replicas. The calculated change in solid volume associated with the conversion of dense

hematite into dense magnetite is small (-2.0%[85]). Indeed, for specimens coated with 30 or more SSG deposition cycles, measurements of the diameters of the magnetite replica grains revealed no detectable change relative to the same grains (as hematite) prior to the partial reduction thermal treatment (Figure 32). However, as the number of SSG coating cycles decreased to 20 and 10, a small decrease in the value of the average diameter was detected, which may have been a result of the susceptibility of such thinly-coated specimens to some additional particle shrinkage during the second 550^{o}C/4 h (Rhines pack) thermal treatment. Table 3 details the diameters of Fe-O-coated-sunflower, α-Fe_2O_3, and Fe_3O_4 replicas during the conversion process

Pollen particles exposed to 70 deposition cycles exhibited a similar shrinkage upon pyrolysis as for particles exposed to 50 cycles (Figure 42). Conversion of the resulting α-Fe_2O_3 pollen particle replicas into magnetite, Fe_3O_4, via treatment at 550°C for 2 h in an oxygen partial pressure pinned by a Fe/Fe_3O_4 (Rhines pack) mixture, resulted in little further change in average pollen particle diameter (Figure 32). (Note the volume of magnetite per mole of iron, 14.9 cm^3 Fe_3O_4/mole Fe, is similar to the volume of hematite per mole of iron, 15.2 cm^3 α-Fe_2O_3/mole Fe[85]). Since an increase in the Fe-

Table 3 Measured diameters of coated sunflower, α-Fe_2O_3 replicas, and Fe_3O_4 replicas of varying SSG deposition cycles (10-50 layers).

Coatings	Fe-O (D, μm)	α-Fe_2O_3 (D, μm)	Fe_3O_4 (D, μm)	$D_{\alpha\text{-}Fe2O3}/D_{Fe\text{-}O}$	$D_{Fe3O4}/D_{Fe\text{-}O}$	$D_{Fe3O4}/D_{\alpha\text{-}Fe2O3}$
10	27.9	13.3	13.2	0.48	0.47	0.99
20	31.5	17.5	17.5	0.56	0.56	1.00
30	42.9	26.5	26.4	0.62	0.62	1.00
40	30.5	20.0	20.0	0.66	0.66	1.00
50	33.8	23.5	23.2	0.70	0.69	0.99

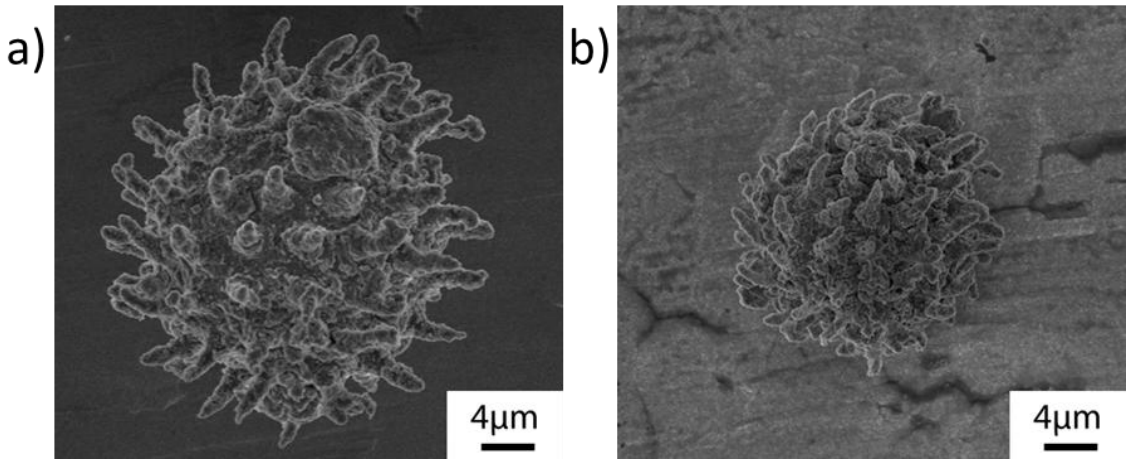

Figure 42: SE images of sunflower pollen particles with a) 70 LbL SSG coating cycles of Fe-O and b) the same pollen grain after conversion into conversion into a α-Fe_2O_3 replica

O coating thickness beyond that achieved with 50 deposition cycles did not result in a further reduction in pyrolysis-induced shrinkage, samples with a greater number SSG deposition cycles were not further investigated.

The magnetic hysteresis behavior of Fe_3O_4 replicas generated with the use of 10 and 50 SSG deposition cycles was examined with a SQUID magnetometer at 300 K. As shown in Figure 43, distinct magnetic hysteresis loops, consistent with ferrimagnetic materials, were obtained for both samples. The values of coercive field (H_c) for the 10 and 50 SSG cycle samples were 0.0191 T and 0.0172 T, respectively, which were similar to values reported by several authors for thin, polycrystalline magnetite films with average crystal sizes of 40-50 nm.[87-90] The difference in magnetic values between the 10 and 50 layered sample were less than 10% for the coercively and less the 5% percent for the saturation magnetization (M_s) (58 Am^2/Kg and 60 Am^2/Kg for the 10 and 50 SSG cycle samples respectively) and an average value was assumed to describe the magnetite properties for the 10, 20, 30, 40 and 50 SSG cycles samples for modeling purposes. Such modest values of H_c allowed for ready alignment of magnetic domains in these specimens upon exposure to the magnetic field present near the edge of the Ni-Nd substrate. Indeed,

the average magnetization values achieved with these Fe_3O_4 pollen replicas for the magnetic field strength encountered near the edge of the Ni-Nd magnetic substrate (about 0.38 T) were not far from the saturation magnetization values shown in Figure 43 and found to be 52 Am^2/Kg. The internal magnetization value of 52 Am^2/Kg allowed for magnetic related differences to be detected with adhesion measurements as shown section 2.4.5. and 2.4.6. However, the remanent magnetization and magnetic saturation are both measured on a per gram basis and only take into account the average magnetic properties a group of replicas, not individual pollen grains. On an individual pollen grain basis the 50 layered samples are expected to have a stronger magnetic attraction then the 10 layered samples due to a higher amount of material deposited on average. It should also be noted that size difference for the starting pollen grains (Table 3) may affect the mass of the pollen replicas with larger particles have higher mass then smaller particles. Note: the results described in Section 2.4.4. was developed and performed in collaboration with Dan Sabo (Georgia Institute of Technology, Atlanta, GA, USA).

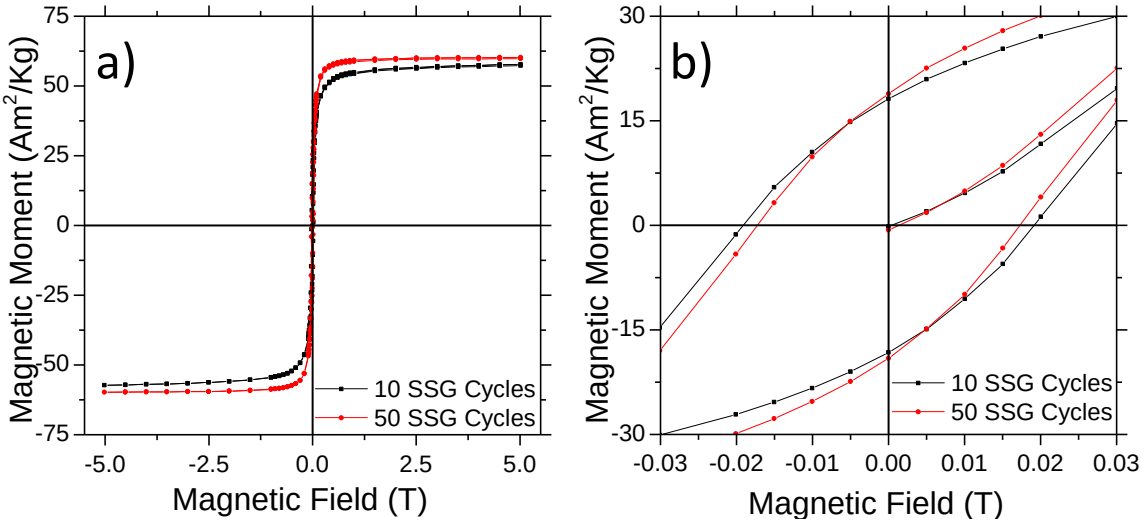

Figure 43: SQUID hysteresis plots conducted at 300K on Fe_3O_4 sunflower pollen replicas synthesized with 10 and 50 SSG layers of Fe-O.

2.4.5. AFM Adhesion Measurements

To allow for quantitative evaluation of the adhesion of the sunflower pollen and oxide pollen replicas to various substrate surfaces, the pollen and replica particles were attached to AFM cantilevers (Figure 44) using a procedure described previously.[60] Six substrates were chosen to analyze the effects of substrate surface chemistry and magnetic properties on particle attraction. Poly(vinyl alcohol) (PVA) and poly(vinyl acetate) (PVAc) were selected as model proton-donor and proton-acceptor substrates, respectively. Polystyrene (PS) was chosen as a model apolar hydrocarbon substrate. Piranha-etched silicon (Si), which possessed a thin (~2–10 nm) hydroxylated oxide layer,

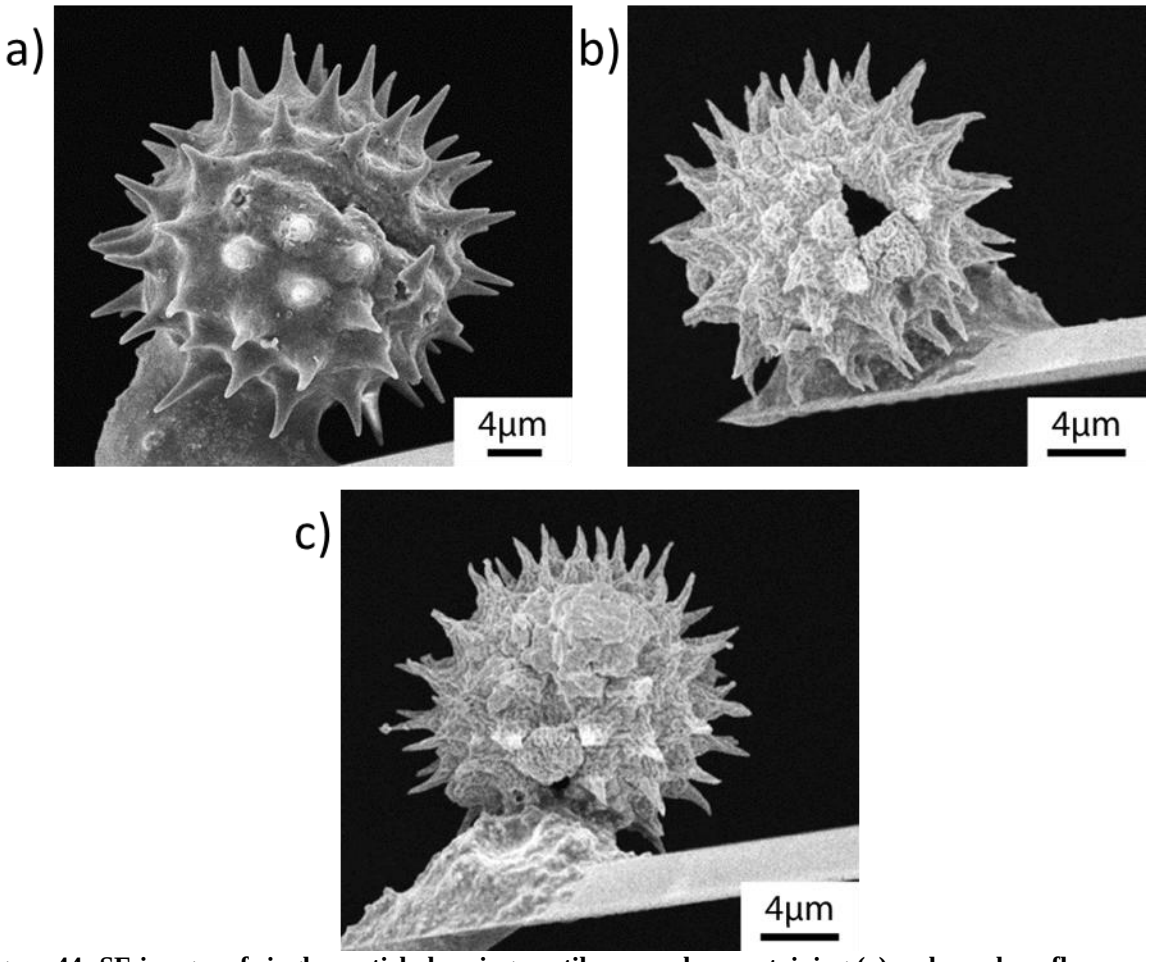

Figure 44: SE images of single-particle-bearing cantilever probes containing (a) a cleaned sunflower pollen grain, (b) an α-Fe_2O_3 sunflower pollen replica generated with 30 SSG cycles, and (c) a Fe_3O_4 sunflower pollen replica, generated with 30 SSG cycles, used in the AFM adhesion study.

acted as a hydrophilic substrate.[91] Unpoled, polished nickel (Ni) foil served as a weakly ferromagnetic substrate. An axially poled, neodymium–iron–boron alloy was used as a strongly magnetized ferromagnetic substrate (residual induction = 12,300 G). The polished nickel foil was attached to this permanent magnet to provide a substrate (Ni–Nd) with the same roughness as the Ni substrate. The measured average surface roughness values of the six substrates fell within a range of 0.2–2.8 nm (Table 4).

Contact mode AFM measurements were used to evaluate the short-range (VDW-based) adhesion of the sunflower pollen and the hematite and magnetite replica particles to the Si, PVA, PVAc, PS, Ni, and Ni–Nd substrates. Average values of the VDW-based adhesion for the different particle and substrate combinations are shown in Figure 45. (Note that each average value was obtained from 60 measurements consisting of 20 analyses for each of three similar particle/cantilever probes.) While the pollen tip radii were considerably larger than the variation in the average surface roughness of the substrates (0.2 nm to 2.8 nm), such variation in the substrate roughness could alter the contact area, and thereby alter the adhesion force. However, as revealed in Figure 45, similar adhesion forces were measured for native pollen and oxide replicas (within the range of experimental error bars) on the PVA and PS surfaces. The PVA and PS surfaces, which possess similar Hamaker constants, possessed different average roughness values (1.3 nm vs. 0.3 nm, respectively). Upon Examination of other values in Table 4 and Figure 45, no consistent trend could be detected between roughness (for Ra values between 0.2 nm and 2.8 nm) and adhesion force. Furthermore, no appreciable difference in contact mode adhesion force was detected for each type of particle on the different substrates. Combining the data from all of the substrates for a given type of particle

yielded average VDW adhesion force values of 55 ± 9, 36 ± 7, and 34 ± 7 nN for the cleaned sunflower pollen, α-Fe_2O_3 replicas, and Fe_3O_4 replicas, respectively.

First-order analyses of these values of VDW-based adhesion force were conducted using the following Hamaker equation:

$$F_{vdw} = \frac{A_{132}R}{6D^2} \tag{2.2}$$

where A_{132} is the nonretarded Hamaker constant of material 1 and 2 interacting across a medium 3 (air), R is the contact radius, and D is the cutoff separation distance for the VDW interaction (≈0.165 nm).[92]

By inserting the measured average values of adhesion force into equation 2.2 along with the calculated A_{132} constants, values of contact radii for the cleaned sunflower pollen, α-Fe_2O_3 replicas, and Fe_3O_4 replicas with the various substrates were calculated (Table 5) to be 93 ± 16, 27 ± 10, and 25 ± 11 nm, respectively. For the native sunflower

Table 4: Average Surface Roughness (Ra, in nm) of the Substrates

Si	PVA	PVAc	PS	Ni	Ni-Nd
0.2 ± 0.06	1.3 ± 0.03	0.3 ± 0.06	0.3 ± 0.02	2.7 ± 0.7	2.8 ± 0.4

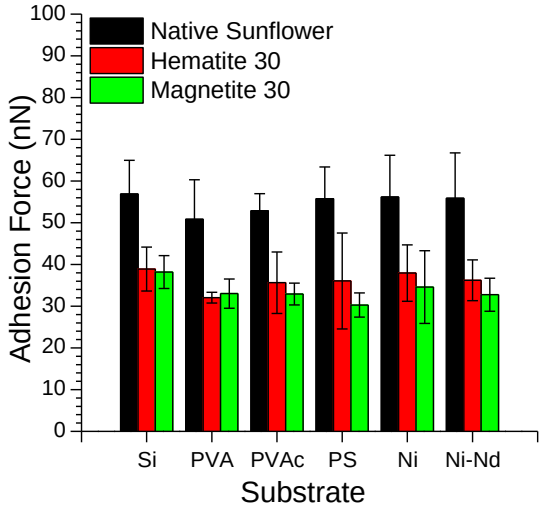

Figure 45: AFM measurements of short-range VDW-based adhesion forces for cleaned sunflower pollen probes, α-Fe_2O_3 sunflower replica probes, and Fe_3O_4 sunflower replica probes on various substrates. The error bars indicate a range of ±1 SD.

pollen, the calculated contact radius (93 ± 16 nm) was similar to the average spine-tip radius (120 ± 12 nm) measured by SEM analysis; that is, the VDW-based adhesion force for this native pollen particle was consistent with the contact of a single spine tip to a given substrate. However, the calculated contact radii for the hematite (27 ± 10 nm) and magnetite (25 ± 11 nm) replica particles were significantly smaller than the average spine tip radii of these replicas (i.e., 94 ± 14 and 100 ± 14 nm for hematite and magnetite, respectively) obtained from SEM analyses. Instead, the calculated contact radii for these oxide replicas were not far from the average crystallite radii (17 to 18 nm) of these particles obtained from XRD analyses; that is, the VDW-based adhesion forces of the oxide pollen replicas were consistent with the contact of one or two nanocrystals, located at the spine tips, to the substrates.

The longer-range magnetic forces acting between particle/cantilever probes and the axially magnetized permanent magnet Ni–Nd substrate were evaluated by scanning the probes across the diameter of this disk-shaped substrate at a fixed height of 140 μm above the substrate surface. As revealed in Figure 46, a noticeable attractive force was detected between the ferrimagnetic Fe_3O_4 sunflower pollen replica and the disk-shaped Ni–Nd substrate at locations near the outer perimeter of this substrate, which is where the magnetic field intensity associated with this magnetized Ni–Nd substrate was the highest.[93] No appreciable magnetic attraction was detected between the weakly ferromagnetic α-Fe_2O_3 replicas or the nonmagnetic native sunflower pollen at any location across the Ni–Nd substrate (at a distance of 140 μm from the surface of this substrate). The enhanced magnetic behavior of the magnetite replicas relative to the hematite replicas was also apparent from visual observations of the relative attraction of

magnetite and hematite replica particles, dispersed in water, to a permanent magnet (Figure 47).

The total adhesion force acting between a given type of particle and the Si or Ni–Nd substrate is plotted against probe distance from the substrate surface in Figure 46 a. (Note that for the Ni–Nd substrate, measurements were obtained either at the disk center or at a distance of ~300 μm from the disk edge.) Only short-range (~10 nm) attractive forces were detected between the native sunflower pollen or α-Fe_2O_3 sunflower replicas and these substrates (Figure 46 b, c). However, both magnetic and VDW attractive forces were detected (Figure 46 d) between the Fe_3O_4 sunflower pollen replicas and the magnetized Ni–Nd near the outer edge of this substrate. For the Fe_3O_4 particle/Ni–Nd-

Table 5: Average Measured Values of Adhesion Force (*F*, in nN), Calculated Hamaker Constants (A_{132} x10^{19}, in J), and Calculated Contact Radii (*R*, in nm).

	Si	PVA	PVAc	PS	Ni	Ni-Nd
Cleaned Sunflower						
A_{132}	0.85	0.84	0.98	0.84	1.2	1.2
F	57± 8	51 ± 9	53 ± 4	56 ± 8	56 ± 10	56 ± 11
R	109	98	88	109	78	77
Hematite						
A_{132}	1.7	2.0	1.8	2.1	3.4	3.4
F	39 ± 1	32 ± 1	36 ± 7	36 ± 11	38 ± 7	36 ± 5
R	37	27	32	28	18	17
Magnetite						
A_{132}	1.7	2.0	1.8	2.1	3.4	3.4
F	38 ± 4	33 ± 3	33 ± 3	30 ± 3	35 ± 9	33 ± 4
R	36	27	30	24	17	16

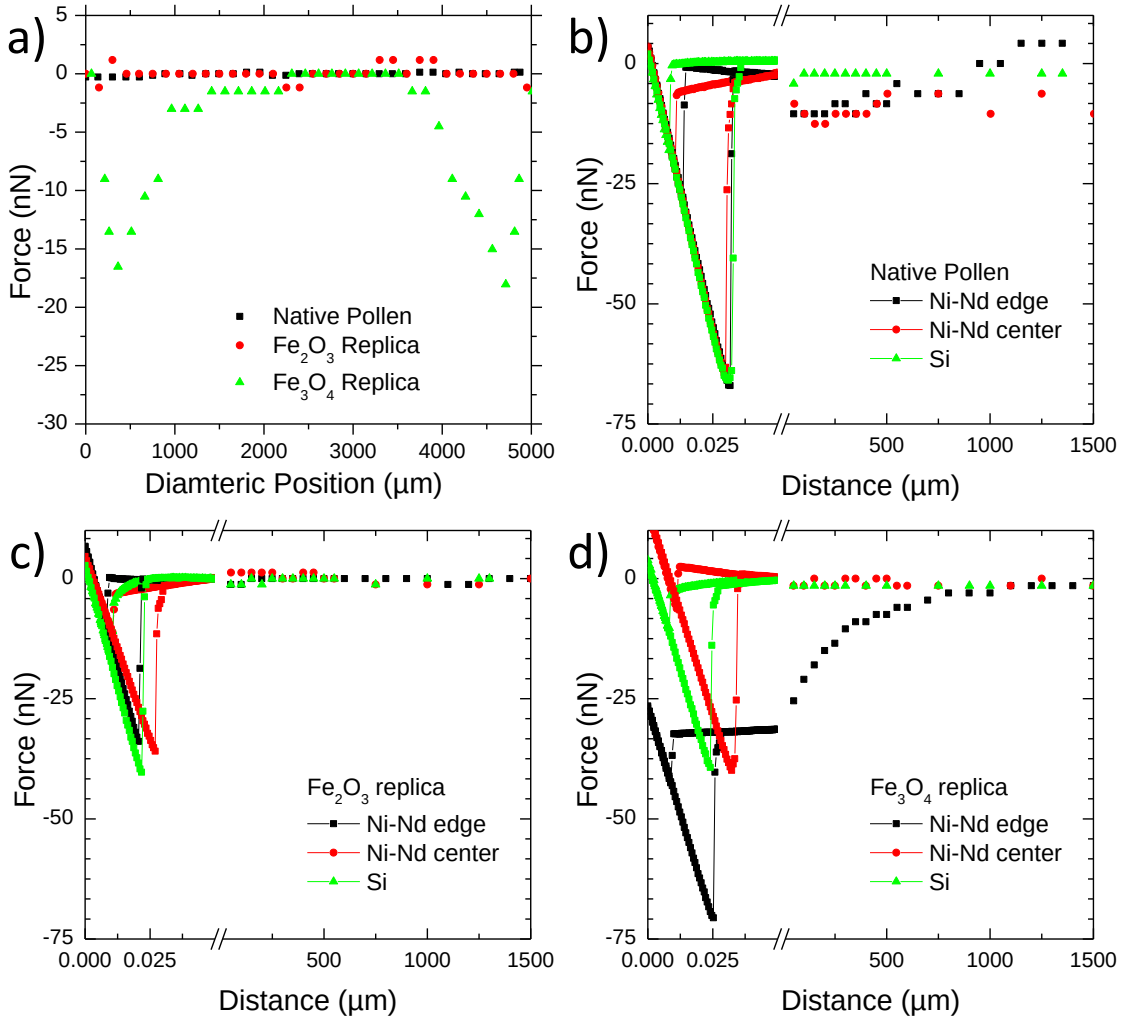

Figure 46: a) Analyses of the magnetic force acting on cleaned sunflower pollen, α-Fe_2O_3 sunflower pollen replicas, and Fe_3O_4 sunflower pollen replicas upon scanning across the diameter of the permanent magnet Ni–Nd substrate at a fixed height of 140 µm above the substrate surface. AFM measurements of the total (VDW + magnetic) adhesion force vs. distance for b) a cleaned sunflower pollen probe, c) an α-Fe_2O_3 sunflower replica probe, and d) an Fe_3O_4 sunflower pollen replica probe with the Si substrate and the Ni–Nd substrate (Ni–Nd center and Ni–Nd edge refer to analyses obtained at the center and at ~300 µm from the edge, respectively, of the disk-shaped Ni–Nd substrate).

edge substrate pairing, the total adhesion force (~70 nN) acting over a short distance (~ 10nm) consisted of the sum of the VDW force (~40 nN) and the magnetic force (~30 nN). At distances just beyond the range of VDW-based adhesion, a steady magnetic force (~30 nN) was detected. The magnetic interaction between the Fe_3O_4 sunflower pollen replicas and the magnetized edge of the Ni–Nd substrate persisted out to a separation

distance of ~1 mm. Figure 48 shows the total adhesive forces (long range, magnetic, and short range, van der Waals) of the native pollen and pollen replicas on different substrates. When the magnetic force is taken in account the Fe_3O_4 pollen replicas have a stronger attraction, due to multimodal adhesion, then the native sunflower grains on the Nd magnetic. (Note: the results described in section 2.4.5 were developed and performed in collaboration with Ismael Gomez, Georgia Institute of Technology, Atlanta, GA, USA).

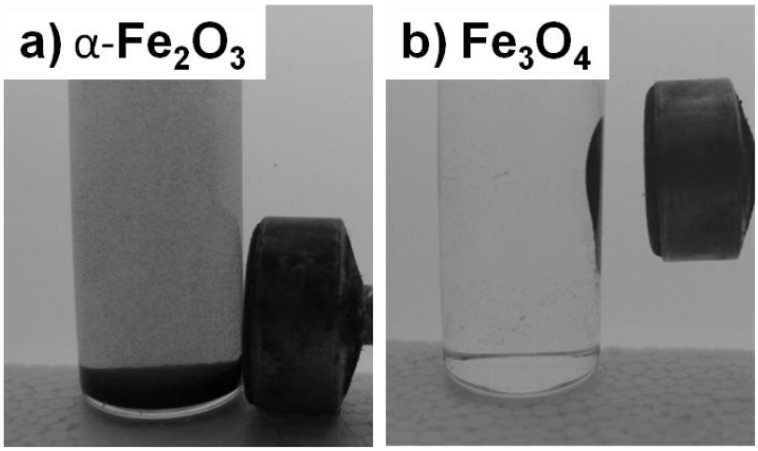

Figure 47: Optical images of sunflower replicas placed in water adjacent to a permanent magnet: a) α-Fe_2O_3 sunflower pollen replica, b) Fe_3O_4 sunflower pollen replica

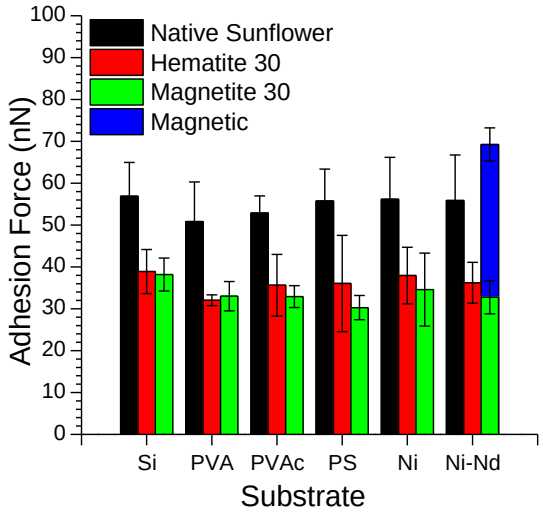

Figure 48: AFM measurements of short-range VDW-based adhesion forces and long range magnetic adhesion forces for cleaned sunflower pollen probes, α-Fe_2O_3 sunflower replica probes, generated with 30 SSG cycles, and Fe_3O_4 sunflower replica probes, generated with 30 SSG cycles, on various substrates. The error bars indicate a range of ±1 SD.

2.4.6. SSG Layer Effect on van der Waals Adhesion

The adhesion strength of cleaned sunflower pollen and oxide pollen replicas (Fe_2O_3 and Fe_3O_4 replicas generated with the use of 10-50 SSG deposition cycles) to various substrate surfaces was evaluated by attaching pollen and replica particles to AFM cantilevers (Figure 49) as described in section 2.3.7.. Flat substrates (AFM- determined values of average roughness, $R_a \leq 2.8$ nm, as shown in Table 4, section 2.4.5.) with a range of characteristics were selected. Polyvinyl alcohol (PVA), polyvinyl acetate (PVAc) were chosen as proton-donor and proton-accepter substrates, respectively, whereas polystyrene (PS), was selected as an apolar hydrocarbon substrate. Piranha solution treatment of a polished Si wafer was used to generate a thin hydroxylated silica layer to act as a hydrophilic surface.[91] Polished polycrystalline nickel foil was used as a conductive substrate, whereas the nickel-foil-coated, axially-poled neodymium iron boron magnet (Ni-Nd substrate) was used as a strongly-magnetized substrate.

Contact mode AFM measurements were used to evaluate the short-range (VDW-based) adhesion of α-Fe_2O_3 and Fe_3O_4 particles of various coating layers (10-50), to the Si, PVA, PVAc, PS, Ni, and Ni-Nd substrates. Average values of the VDW-based adhesion for the different particle and substrate combinations are shown in Figure 50 (note: each average value was obtained from 60 measurements consisting of 20 analyses for each of three similar particle/cantilever probes). Given the observed range in measured values, no appreciable difference in contact mode adhesion force was detected for each type of particle on different substrates. The similarity in short-range adhesion force values for a given type of particle with the electrically-conductive substrates (Ni, Ni-Nd) and the semi- conductive/non-conductive substrates (Si, PVA, PVAc, PS)

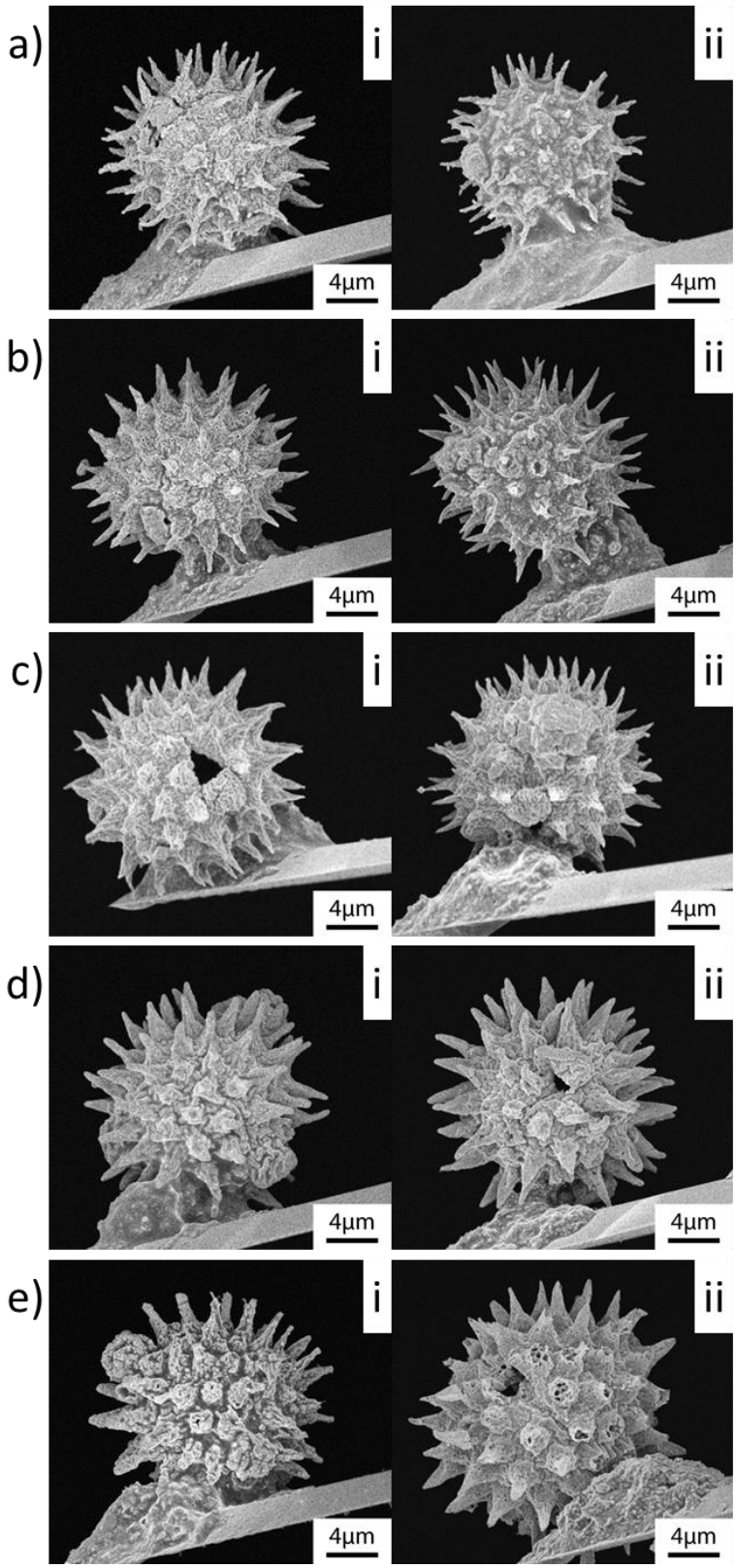

Figure 49: SE images of single-particle-bearing cantilever probes of i) α-Fe_2O_3 sunflower replicas and i) Fe_3O_4 sunflower replicas used in the AFM adhesion study. Label a, b, c, d, and e indicates 10, 20, 30, 40 and 50 coating layers, respectively

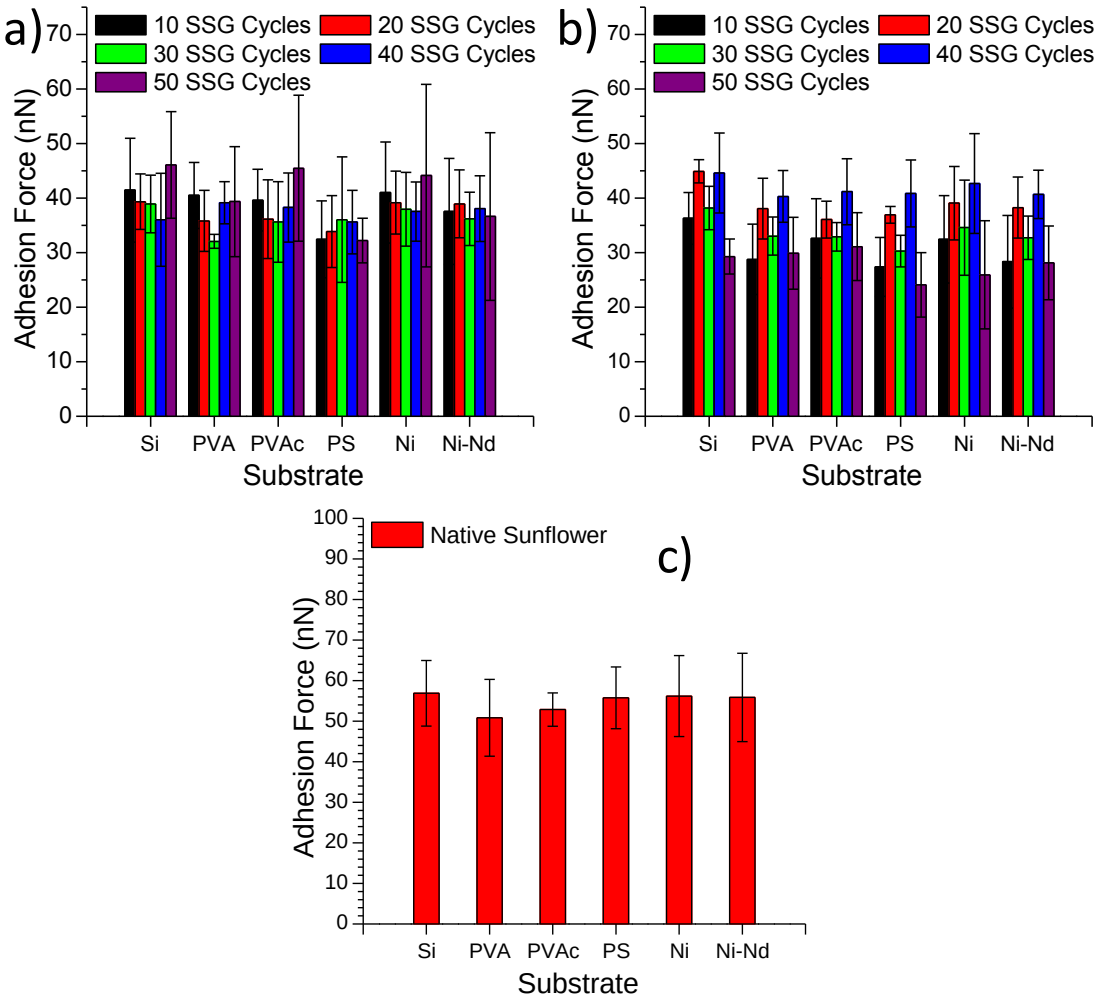

Figure 50: AFM adhesion measurements of short-ranged VDW-based adhesion forces for a) α-Fe_2O_3 sunflower replicas (10-50 layers), b) Fe_3O_4 sunflower replicas (10-50 layers), and c) cleaned sunflower pollen with various substrates. Error bars indicate ± one standard deviation.

suggests that such adhesion was not strongly influenced by sustained electrostatic attraction. The similarity in short-range adhesion force values for a given type of particle with the proton-donating and proton-accepting polymeric substrates (PVA, PVAc), the hydroxylated substrate (Si), and the metallic substrates (Ni, Ni-Nd) suggests that such adhesion was also not strongly influenced by hydrogen bonding. The contact-mode adhesion force data for all of the substrates for each type of particle was then combined to obtain the overall average values shown in Table 6. The average contact-mode adhesion force values of oxide pollen replicas (28-41 nN) were significantly smaller from the

average value for the cleaned sunflower pollen (55 nN). However, no significant differences were detected in the contact-mode adhesion force values with the number of SSG deposition cycles for the hematite and magnetite replicas.

The short-range, contact-mode adhesion of sunflower pollen and oxide pollen replicas was evaluated with the use of a simple Hamaker model of the van der Waals (VDW) force between a sphere and a flat plane[94]:

$$F_{vdw} = \frac{A_{132}R}{6D^2} \tag{2.2}$$

where A_{132} is the non-retarded Hamaker constant of material 1 and 2 interacting across a medium 3 (air in the present case), R is the contact radius, and D is the cutoff separation distance for the VDW interaction (≈0.165 nm).[92] Equation (2.2) was used by approximating the curvatures of the contacting surfaces of the cleaned sunflower pollen and pollen replicas as being spherical.

Owing to the dielectric nature of hematite and magnetite, Lifshitz theory was used to calculate the values of A_{132} for these materials[92]:

$$A_{132} \approx \frac{3}{4}kT\left(\frac{\varepsilon_1-\varepsilon_3}{\varepsilon_1+\varepsilon_3}\right)\left(\frac{\varepsilon_2-\varepsilon_3}{\varepsilon_2+\varepsilon_3}\right) + \frac{3h\nu_e}{8\sqrt{2}}\frac{(n_1^2-n_3^2)(n_2^2-n_3^2)}{(n_1^2+n_3^2)^{1/2}(n_2^2+n_3^2)^{1/2}\left\{(n_1^2+n_3^2)^{1/2}+(n_2^2+n_3^2)^{1/2}\right\}} \tag{2.3}$$

where k is Boltzmann's constant, T is temperature, h is Planck's constant, ν_e is the media absorption frequency in air, ε_1 and ε_2 are dielectric constants, and n_1 and n_2 are refractive

Table 6: Average adhesion forces for cleaned sunflower, α-Fe_2O_3 sunflower replicas, and Fe_3O_4 sunflower replicas of various coating layers for all substrates investigated. Error indicates ± one standard deviation.

Coatings	0	10	20	30	40	50
Cleaned	55 ± 9	--	--	--	--	--
α-Fe_2O_3	--	39 ± 9	37 ± 6	36 ± 7	38 ± 6	41 ± 13
Fe_3O_4	--	31 ± 8	39 ± 5	34 ± 7	42 ± 7	28 ± 7

indices. A_{132} values for various coating layers of hematite or magnetite replicas on all substrates were calculated from equation (2.3) by using appropriate ε_1, ε_2, n_1, and n_2 values[95-101], with the assumption that the absorption frequencies of all media are the same. By inserting the AFM- measured values of adhesion force(average values on the various substrates) into equation (2.2) along with the calculated A_{132} constants, values of contact radii for the α-Fe_2O_3 replicas, and Fe_3O_4 replicas could be obtained (Figure 51 a). The value obtained for a given pollen grain or pollen grain replica could then be compared with direct measurement (via electron microscopy) of the average radius of curvature of those spine tips positioned closest to the location where the particle made contact to the substrate. For cleaned sunflower pollen grains, the average values of adhesion-derived contact radii (93 $\pm$ 16 nm) and microscopy-derived spine tip radii (120 $\pm$ 12 nm) were in reasonable agreement. However, the calculated contact radii for all hematite and magnetite pollen replicas (28 $\pm$ 8 nm and 26 $\pm$ 8 nm, respectively) were much smaller than the average spine tip radii of these replicas (105 $\pm$ 8 nm and 97 $\pm$ 8

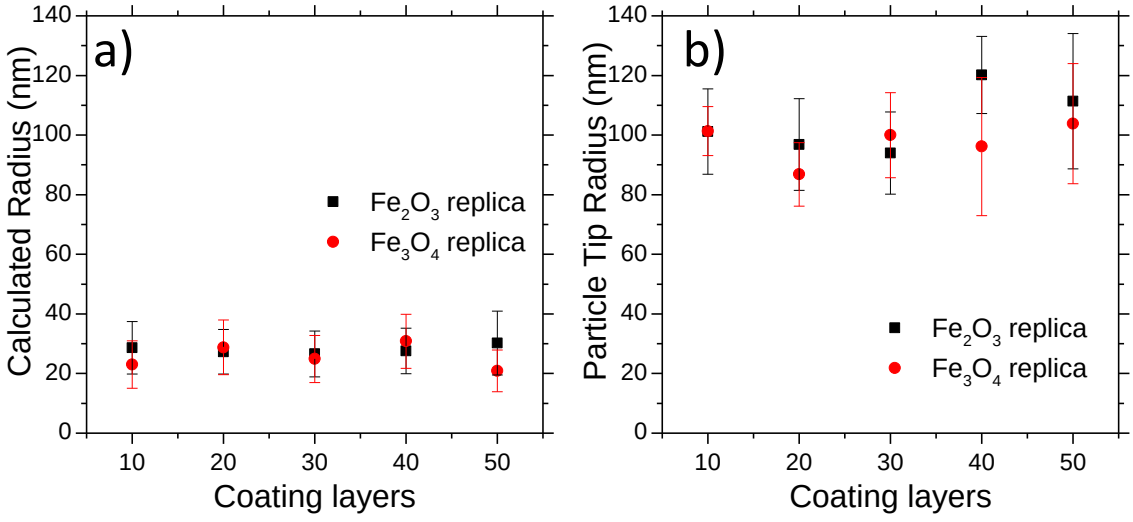

Figure 51: Average α-Fe_2O_3 and Fe_3O_4 sunflower replica (10-50 layers) a) calculated contact radii from the Hamaker model and b) measured contact radii from SEM images. Error bars indicate ± one standard deviation.

nm, respectively) obtained from SEM analyses as shown in Figure 51. The adhesion-derived contact radii were, instead, not far from the average values of the hematite and magnetite crystal radii (19 $\pm$ 2 nm and 15 $\pm$ 2 nm, respectively) obtained from Scherrer XRD analyses (Figure 30); that is, the VDW-based adhesion forces of the oxide pollen replicas were consistent with the contact of one or a few oxide nanocrystals located at the spine tips to the substrates, instead of by the curvature of the entire spine tip.

2.4.7. SSG Cycles Number Effect on Magnetic Adhesion

The additional, significant (magnetic) force of attraction that was detected for the 30 SSG cycle Fe_3O_4 sunflower pollen replicas (section 2.4.5) and the Ni-Nd substrate, particularly near the perimeter of this disk-shaped substrate where the magnetic field gradient was greatest, was observed for samples coated with 10-50 SSG deposition cycles. This force persisted out to a Fe_3O_4 particle/Ni-Nd substrate separation distance as far as ~1.5 mm. Such a force of attraction was not detected between the Ni-Nd substrate and the cleaned sunflower pollen or hematite pollen replicas generated with 10-50 SSG deposition cycles. The total (short + long range) adhesion force acting between a given Fe_3O_4 replica particle and the Ni-Nd substrate is plotted against the distance from this substrate in Figure 52 (note: such force-distance measurements were conducted ~300 μm from the outer edge of the disk-shaped Ni-Nd substrate, where the magnetic field strength was measured to be at a maximum). For each Fe_3O_4 particle/Ni-Nd-edge substrate pairing, the total attractive force (~50-90 nN) was comprised of a short-range (contact mode) contribution (35$\pm$14 nN) and a longer-range magnetic contribution. The magnitude of this magnetic force increased monotonically with the number of SSG deposition cycles used to generate these replicas, as shown in Figure 53. The linear fit to the data gave an

R^2 value of 0.997.

Control over the volume of magnetic material deposited during the LbL SSG process, therefore, provides a means for tuning the magnetic and, hence, total attraction of such Fe_3O_4 pollen replicas to magnetic substrates. As shown in Figure 54, the total force of adhesion of the Fe_3O_4 replicas to the Ni-Nd substrate could be increased by a factor of ~1.9 by increasing the number of SSG deposition cycles from 10 to 50. Indeed, while the magnitude of the short-range, contact-mode adhesion of the magnetite pollen

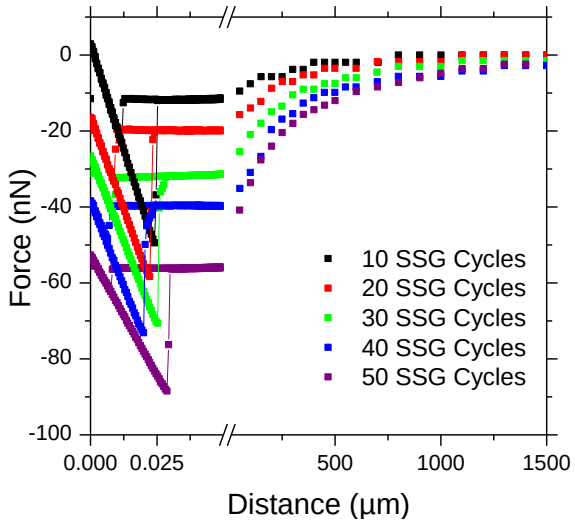

Figure 52 Total adhesion force as a function of distance between Fe_3O_4 sunflower pollen replicas (prepared with 10-50 SSG deposition cycles) and the Ni-Nd substrate (near the perimeter of this disk-shaped magnetic substrate).

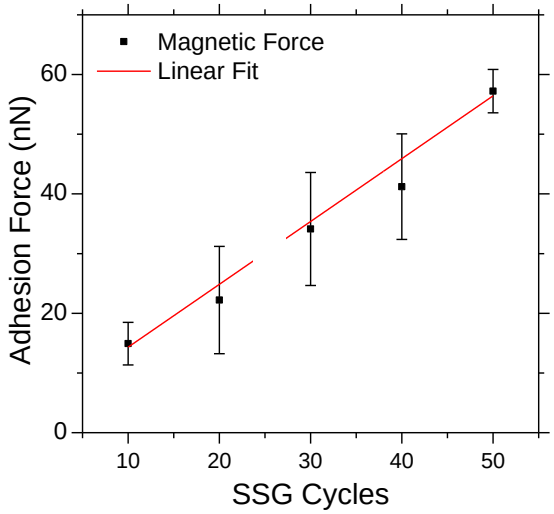

Figure 53: Magnetic force measurements of Fe_3O_4 sunflower replicas as a function of the number of SSG deposition cycles used to prepare the replicas.

replicas in the absence of an applied magnetic field (i.e., for adhesion to the non-magnetic PVA, PVAc, PS, Si, and Ni substrates) was smaller than for the cleaned sunflower pollen particles (Figure 50), the total (short + long range) force of attraction of the Fe_3O_4 replicas to the Ni-Nd substrate could be tailored (by adjusting the number of SSG deposition cycles) to exceed that for the cleaned sunflower pollen particles (e.g., by a factor of ~1.6 for 50 SSG cycles, as shown in Figure 54).

Using the mathematical model described in section 1.2.4, the space around the Ni-Nd permanent magnet substrate was discretized and Φ and H were simulated using the equation (1.10 1.11) and corresponding boundary conditions[102]. The simulated variations in the magnetostatic potential, Φ, and magnetic field strength, H, around the magnetic Ni-Nd substrate are presented in Figure 55 a and b. The gradient in magnetic field strength, $\partial H/\partial z$, was then determined as a function of position. The calculated magnetic field (Figure 55 b) matches the measured filed intensity obtained by scanning the pollen probe over the surface of the magnet as show in section 2.4.5, Figure 46 a. At highest gradient (300 μm from the magnets edge), the magnetic force is

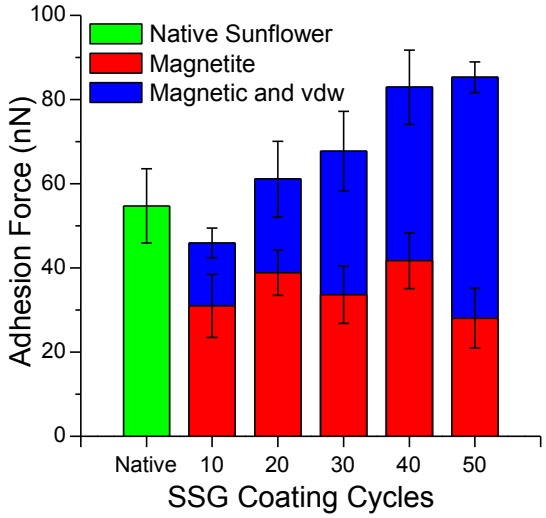

Figure 54: Total (short + long range) force of attraction of cleaned sunflower pollen and Fe_3O_4 sunflower pollen replicas as a function of the number of SSG deposition cycles used to prepare the latter replicas

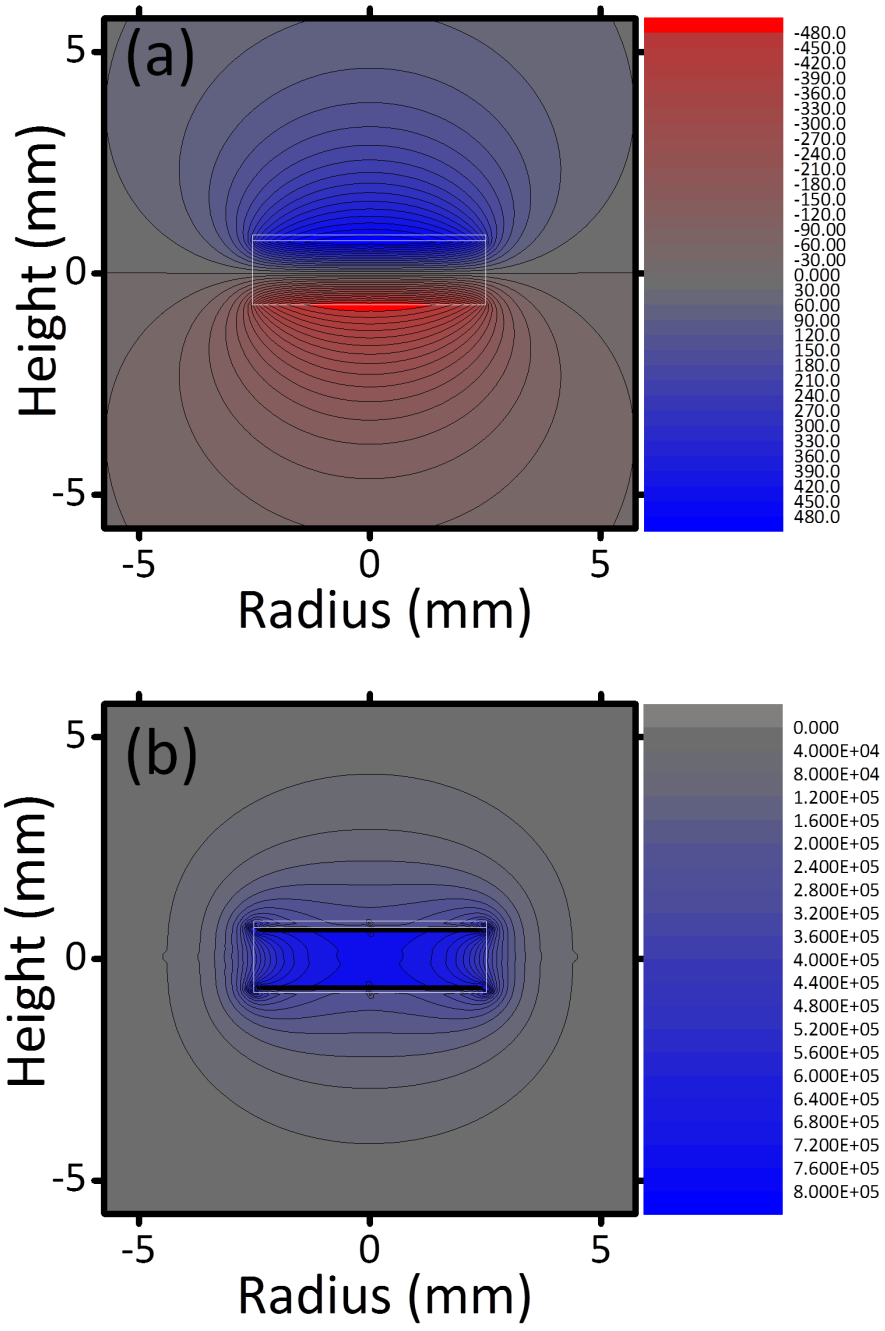

Figure 55: Simulations of a) the magnetostatic potential (Φ, A) and b) magnetic field (H, A m^{-1}) around a cross-section of the Ni-Nd permanent disk magnet. The dimensions of the Nd magnet and polished Ni foil are highlighted in white.

experimentally measured using colloidal AFM and fitted using equation 1.9. The validity of the magnetic force model developed in equation 1.9 between a magnetic particle and an axially magnetized disk magnet was assessed by probing the magnetic attractions of a CrO_2-PS microsphere standard with the Ni-Nd disk magnet. An excellent agreement was

obtained between the measured and simulated magnetic force-distance curves, additional information can be found in the dissertation of Ismael Gomez, Georgia Tech 2013.

With the results of the simulation model for the position dependence of $\partial H/\partial z$, along with knowledge of the magnetization, M (from the data in Figure 43), the AFM measured magnetic force-distance values were fitted to equation (1.9) and was used to calculate the volume of magnetite, V_m, present within a single magnetic replica. The average magnetization (M) of the magnetite replicas over the distances probed (average magnetic field = 3.0x105 A m-1) was found to be 52 Am^2/Kg. Figure 56 compares experimental force-distance curves with fitted with theoretical force-distance curves used to determine the volume of magnetite, V_m, present for Fe_3O_4 replicas with 10-50 coating layers. Each force measurement obtained at a given distance from the Ni-Nd substrate for a particular Fe_3O_4 pollen replica was used to obtain a V_m value. The V_m values obtained over a range of distances for a given Fe_3O_4 pollen replica were then used to obtain an average V_m value for that replica. The average magnetic volumes determined in this manner for the Fe_3O_4 replicas are shown in the inset of Figure 57. A monotonic, linear increase in the calculated volume of magnetite with the number of SSG deposition cycles was observed with and R^2 value of 0.997. This trend was consistent with the layer-by-layer nature of the SSG process, as had been independently confirmed by TG analyses (Figure 29). These average V_m values were re-inserted into equation (1.9) to obtain the F_m vs. distance curves shown along with the data in Figure 57. Error associated with comparing theoretical with experimental magnetic forces ranged from 5-13%. Interestingly, the magnetic force model does not account for structural effects and treats the magnetic volume as a shapeless mass of material. Therefore, agreement between

experimental and theoretical magnetic forces indicates the complex pollen replica shape is only affected by the internal magnetization, and can be independently measured for each sample, and does not affect the modeling of magnetic attraction, thus proving its potential for tailoring pollen replica magnetic attraction.

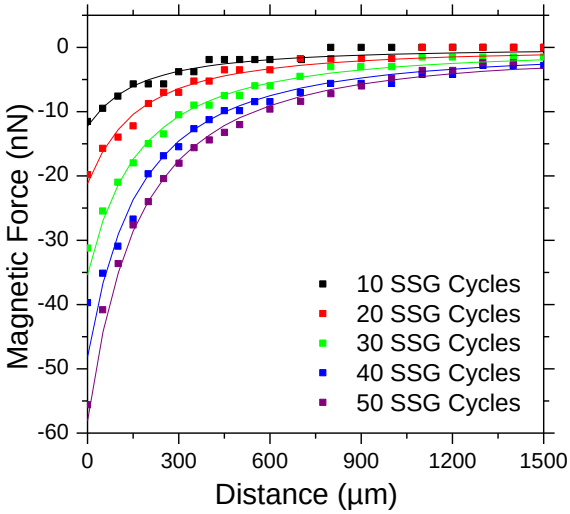

Figure 56: Magnetic force of attraction, f_m, of Fe_3O_4 sunflower replicas (generated with 10-50 SSG deposition cycles) as a function of distance from a magnetic Ni-Nd substrate fitted to equation 1.9.

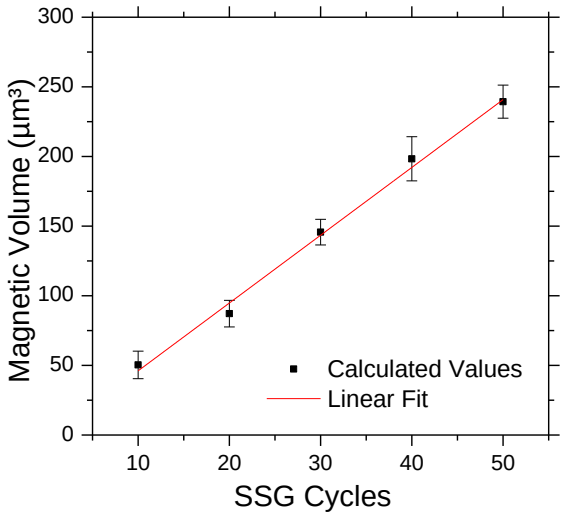

Figure 57: Calculated volume of magnetite, V_m, in a given particle obtained from the magnetic force measurements, simulation of δH/δz vs. distance, magnetization data in Figure 43, and use of equation 1.9.

2.4.8. Surface Area

BET and BJH analyses were conducted to obtain the values of specific surface area (SSA), specific mesopore (2-50 nm diameter) volume (SMeV), and specific micropore (< 2 nm diameter) volume (SMiV) of as-coated sunflower pollen particles (30 SSG cycles), of Fe_2O_3 sunflower pollen replicas (after treatment at 600°C for 4 h in air), and of Fe_3O_4 sunflower pollen replicas (after further Rhines pack treatment at 550°C for 2 h). The values of SSA, SMiV, and SMeV for these specimens are shown in Table 7 below. The reduction in the specific values of surface area, micropore volume, and mesopore volume upon firing of the coated pollen particles was presumably due to some collapse of the micro- and meso-pore volume upon firing. The slight increase in specific micro- and mesopore volumes upon conversion of the hematite replicas to magnetite replicas may have been due to the slightly lower molar volume of magnetite (14.9 cm^3 Fe_3O_4/mole Fe) relative to hematite (15.2 $cm^3Fe_2O_3$/mole Fe). Do the harmomegathy nature of the native pollen grains (ability to shrink and expand considerably to adjust to their shape according to moister and environmental conditions),[67, 103, 104] BET and BJH measurements were difficult to measure and values were obtained were much lower than the as coated and fired replicas (0.23 SSA m^2/g). While pollen replicas of *Brassica* genera have been reported to has SSA of up to 817 m^2g^{-1},[43] sunflower pollen grains are

Table 7: Specific surface area (SSA), specific micropore volume (SMiV), and specific mesopore volume (SMeV) for dried native sunflower pollen, coated sunflower pollen (30 SSG cycles), Fe_2O_3 sunflower pollen replicas, and Fe_3O_4 sunflower pollen replicas.

Specimen	SSA (m^2/g)	SMiV (cm^3/g)	SMeV(cm^3/g)
Coated pollen	16	$6.7 X10^{-2}$	$7.4 X10^{-2}$
Fe_2O_3 replicas	6.3	$1.1 X10^{-3}$	$6.6 X10^{-3}$
Fe_3O_4 replicas	6.5	$2.2 X10^{-3}$	$7.3 X10^{-3}$

not an ideal template for high surface area replicas and are better suited for adhesion studies.

2.4.9. Iron Pollen Replicas

Fe_3O_4 pollen replicas were further reduced into iron metal by reducing individual grains with a 2% H_2/ 98% Ar gas mixture. Initial test were conducted to determine the optimal firing conditions needed to fully convert the Fe_3O_4 replicas in to iron replicas. Samples were heated to 450°C, 500°C, 550°C, and 600°C in a sealed furnace tube as described in section 2.3.4.. Figure 58 show the XRD patterns of the samples fired at various temperatures after cooling down to room temperature. It was discovered that at temperatures at or above 550°C the samples were completely reduced into iron (ICDD# 04-003-3884). EDS of the 550°C 2 h thermal treatment also showed that the samples were converted into iron as no oxygen peak was detected (Figure 59). The 550°C 2 h thermal conditions were chosen for future work.

SE images comparing the *same individual* sunflower pollen grains after: i) coating with 10, 20, 30, 40, and 50 Fe-O layers, ii) conversion into Fe_3O_4 pollen replicas and iii) converted into Fe can be seen in Figure 60. For the iron reduced sample, the diameter change from Fe_3O_4 was more pronounced compared to the size change between Fe_2O_3 and Fe_3O_4 mentioned in section 2.4.3.. The molar volume of BCC iron is less than half the molar volume of magnetite, on a per mole of Fe basis (7.1 cm^3 Fe/mole Fe; 14.9 cm^3 Fe_3O_4/mole Fe). The average reduction in diameter, as seen in Figure 61, from Fe_3O_4 replicas to Fe replica (80.8%) correlates well to the diameter change of a spherical particle that undergoes a near 50% volume reduction indicating that the shrinkage may be solely do to the change in volume on a per mol of Fe basis between the phases. While the

Iron replicas did maintain the general shape and morphology as the as coated pollen grains (with a 30-50% diameter size reduction) they were not robust enough for adhesion measurements and would collapse during attempts to attach the iron replicas to an AFM cantilever tip.

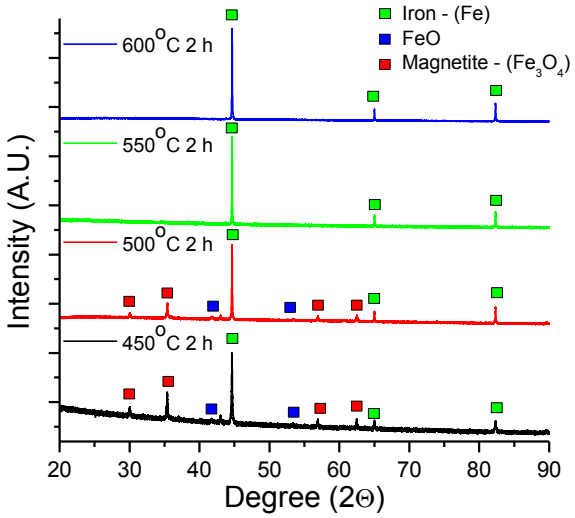

Figure 58: XRD analysis of Fe reduction in 2% H_2 / Ar gas mixture at various temperatures

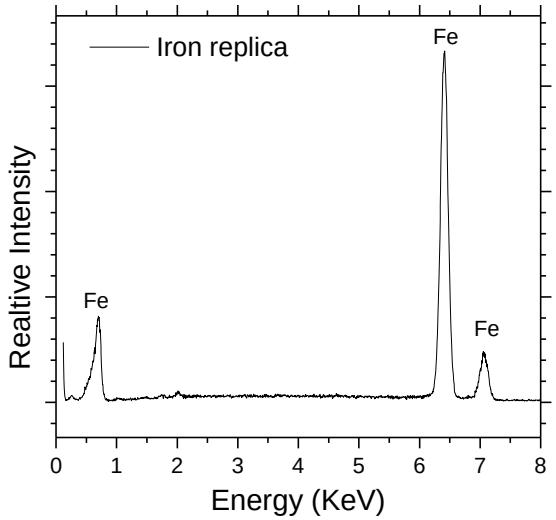

Figure 59: EDX analyses of a Fe sunflower replica of a Fe_3O_4 grain generated by reduction using a 2% H_2 / Ar gas mixture at 550°C for 2 h.

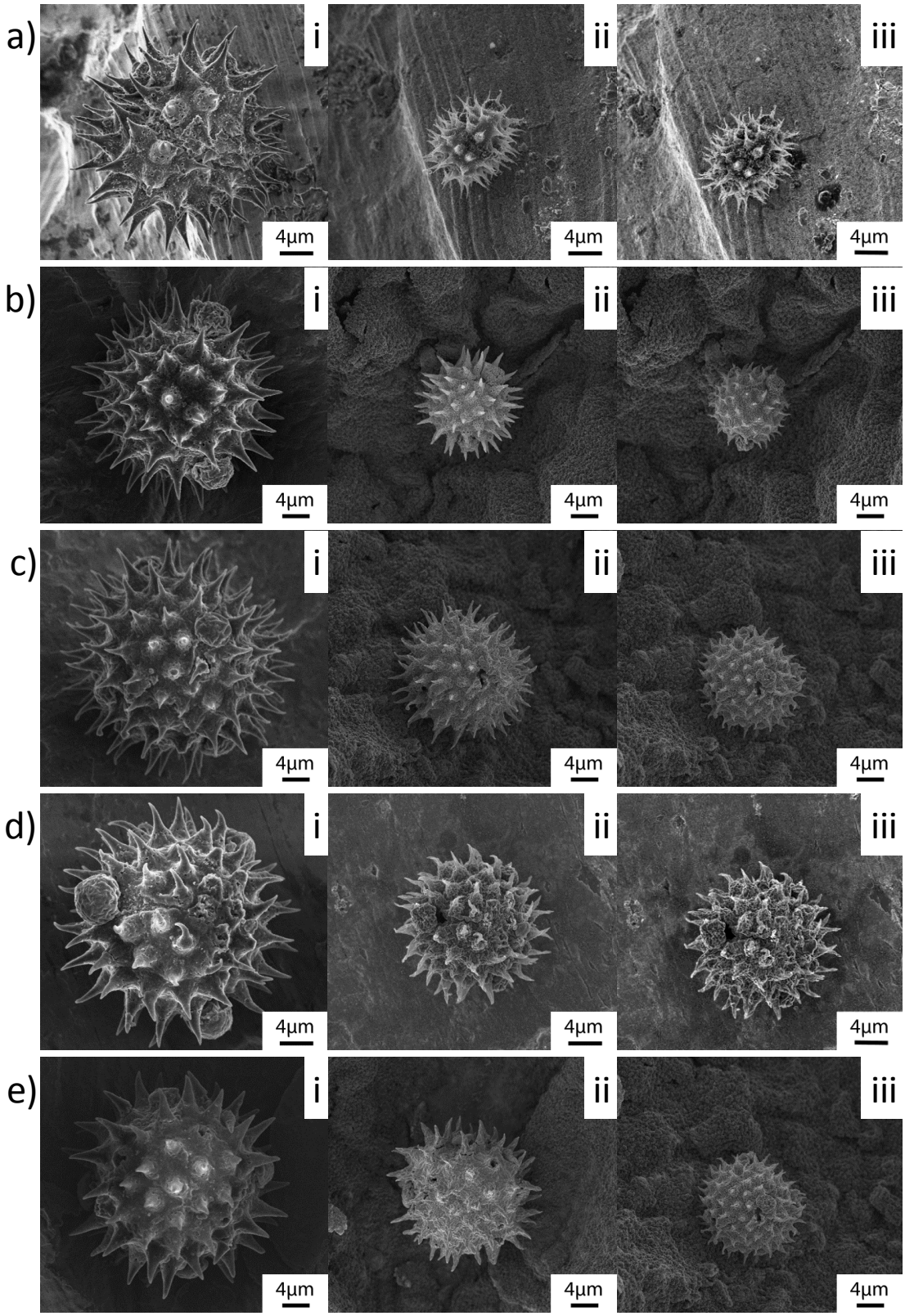

Figure 60: SE images of sunflower pollen particles with different number of LbL SSG coating cycles a) 10, b) 20, c) 30, d) 40, and e) 50 layers of Fe-O at various stages of conversion into Fe: i) as coated pollen, ii) conversion into Fe_3O_4 replica, and iii)conversion into Fe replica.

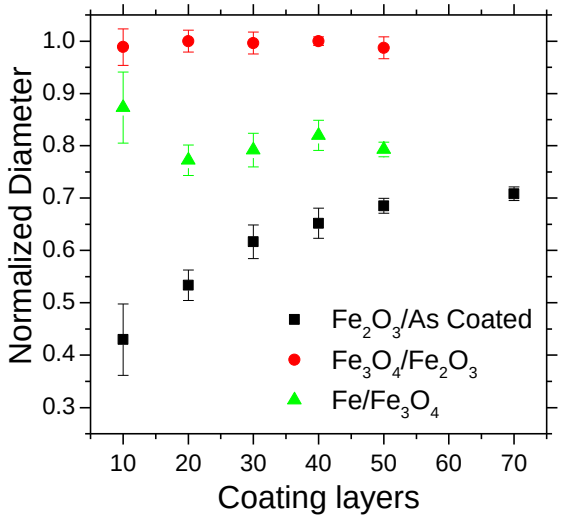

Figure 61: Plot of the average relative diameters of Fe-O-coated sunflower pollen particles as a function of the number of surface sol-gel deposition cycles (10-70) after various stages of thermal treatment: Black squares: pollen particle diameters after conversion into α-Fe_2O_3 replicas at 600°C for 4 h in air (relative as-coated particles); Red circles: pollen particle diameters after conversion into Fe_3O_4via exposure to a Fe/Fe_3O_4 Rhines pack treatment at 550°C for 2 h (relative to the α-Fe_2O_3 pollen replicas). Green triangles: pollen particle diameters after conversion into Fe via reduction in 2%H_2 / Ar gas treatment at 550°C for 2 h (relative to the Fe_3O_4 pollen replicas).

2.5. *Concluding Remarks*

This work demonstrates that: i) hematite (α-Fe_2O_3), magnetite (Fe_3O_4), and iron replicas of 3-D sustainable, biologically-formed organic microtemplates (ragweed, dandelion, and sunflower pollen particles) with tailorable oxide contents can be generated using a scalable, highly-conformal wet chemical coating process, ii) simple expressions may be used to model and predict the short-range VDW adhesion of such Fe_2O_3 and Fe_3O_4 replicas (to a variety of surfaces) and the longer-range magnetic attraction of Fe_3O_4 replicas (to magnetic surfaces), and iii) the attraction of 3-D Fe_3O_4 replicas to magnetic surfaces can be tailored via proper control of this coating/thermal treatment process.

The generation of inorganic replicas of 3-D sunflower pollen microparticles comprised of controlled amounts of hematite, magnetite, or iron has been accomplished via a surface sol-gel (SSG) deposition process followed by thermal treatment(s) at controlled oxygen partial pressure(s). Alternating exposure of the pollen microparticles to

an isopropanol solution of iron (III) isopropoxide and then to water was conducted 2-70 times with a computer-automated pumping system. The layer-by-layer (LbL) nature of the deposition process was confirmed by thermogravimetric analyses, which revealed a monotonic increase in the iron oxide content of the pollen particles with an increasing number of alkoxide/water cycles. After complete organic pyrolysis upon heating to 600^{o}C in air, particles comprised of nanocrystalline hematite were produced that retained the 3-D shapes of, but smaller sizes than, the starting pollen grains. The extent of shrinkage upon firing could be controlled, however, by adjusting the thickness of the deposited coating; that is, the pyrolysis-induced reduction in diameter of the Fe_2O_3 replicas decreased as the number of deposited SSG layers increased. The Fe_2O_3 replicas were fully converted into phase-pure Fe_3O_4 replicas of similar size by partial reduction at 550^{o}C at an oxygen partial pressure established by the Fe_3O_4/Fe equilibrium (via use of a Fe_3O_4/Fe Rhines pack).

Values of the short-range van der Waals (VDW) adhesion force obtained for the hematite and magnetite pollen replicas on a variety of flat organic and inorganic substrates (with nonretarded Hamaker constants ranging from 1.7-3.4) were smaller than for larger cleaned sunflower pollen particles. However, such a reduction in VDW adhesion could not be attributed to a reduction in the spine (echini) tip radii upon organic pyrolysis. Indeed, the hematite and magnetite replicas containing different amounts of iron oxide, and exhibiting different degrees of firing shrinkage, exhibited similar VDW adhesion force values. Application of a simple Hamaker model indicated that the VDW adhesion of these oxide replicas was governed by the contact of fine oxide nanocrystals

located on the spine tips (and not the curvature of the overall spine tip itself) with underlying surfaces.

The Fe_3O_4 pollen replicas exhibited significant longer-range attraction (out to ~1 mm) to a magnetic substrate, with the magnetic force increasing monotonically with an increase in the oxide content of the replica microparticles. Indeed, the total force (VDW + magnetic) of attraction to the magnetic substrate was 56% greater for the Fe_3O_4 pollen replicas prepared with 50 SSG cycles than for the native cleaned sunflower pollen. A simple model was developed that, with knowledge of the magnetization of the Fe_3O_4 pollen replica, the Fe_3O_4 content of the replica, and the simulated field gradient of the magnetic substrate, provided a good description of the magnetic force of attraction as a function of distance from the magnetic substrate.

Although the conformal coating-based replication process, coupled with the models for VDW and magnetic attraction, developed in this work has focused primarily on generating oxide replicas of sunflower pollen, it may be applied to a variety of hydroxyl-bearing micro-particles of biogenic or synthetic origin templates. Indeed, the wide variety of 3-D particle shapes and surface topographies available in nature generated by different plants and the ability of this LbL SSG-based process to produce high-fidelity nanocrystalline replicas with controlled amounts of magnetic oxide (by adjusting the number of deposition cycles) allows for the syntheses of biogenic or synthetic-derived microparticles with highly tailorable multimodal adhesion.

2.6. ***References***

[1] M. L. Ott and H. A. Mizes, "Atomic force microscopy adhesion measurements of surface-modified toners for xerographic applications," *Colloids and Surfaces A: Physicochemical and Engineering Aspects,* vol. 87, pp. 245-256, 8/16/ 1994.

[2] W. Richard Bowen and T. A. Doneva, "Atomic Force Microscopy Studies of Membranes: Effect of Surface Roughness on Double-Layer Interactions and Particle Adhesion," *Journal of Colloid and Interface Science,* vol. 229, pp. 544-549, 9/15/ 2000.

[3] K. Cooper, A. Gupta, and S. Beaudoin, "Simulation of the Adhesion of Particles to Surfaces," *Journal of Colloid and Interface Science,* vol. 234, pp. 284-292, 2/15/ 2001.

[4] M. A. Meitl, Z. T. Zhu, V. Kumar, K. J. Lee, X. Feng, Y. Y. Huang, *et al.*, "Transfer printing by kinetic control of adhesion to an elastomeric stamp," *Nat. Mater.,* vol. 5, p. 33, 2006.

[5] S. Mitragotri and J. Lahann, "Physical approaches to biomaterial design," *Nat. Mater.,* vol. 8, p. 15, 2009.

[6] Y. Huang, M. Liu, J. Wang, J. Zhou, L. Wang, Y. Song, *et al.*, "Controllable Underwater Oil-Adhesion-Interface Films Assembled from Nonspherical Particles," *Advanced Functional Materials,* vol. 21, pp. 4436-4441, 2011.

[7] K. E. Fischer, G. Nagaraj, R. H. Daniels, E. Li, V. E. Cowles, J. L. Miller, *et al.*, "Hierarchical nanoengineered surfaces for enhanced cytoadhesion and drug delivery," *Biomaterials,* vol. 32, p. 3499, 2011.

[8] L. Zhang, J. Shi, Z. Jiang, Y. Jiang, R. Meng, Y. Zhu, *et al.*, "Facile Preparation of Robust Microcapsules by Manipulating Metal-Coordination Interaction between Biomineral Layer and Bioadhesive Layer," *ACS Appl. Mater. Interfaces,* vol. 3, p. 597, 2011.

[9] S. Stassi and G. Canavese, "Spiky nanostructured metal particles as filler of polymeric composites showing tunable electrical conductivity," *J. Polym. Sci., Part B,* vol. 50, p. 984, 2012.

[10] I. Lee, "Molecular Self-Assembly: Smart Design of Surface and Interface via Secondary Molecular Interactions," *Langmuir,* vol. 29, p. 2476, 2013.

[11] J. d. Vicente, D. J. Klingenberg, and R. Hidalgo-Alvarez, "Magnetorheological fluids: a review," *Soft Matter,* vol. 7, p. 3701, 2011.

[12] K. Nandy, S. Chaudhuri, R. Ganguly, and I. K. Puri, "Analytical model for the magnetophoretic capture of magnetic microspheres in microfluidic devices," *J. Magn. Magn. Mater.,* vol. 320, p. 1398, 2008.

[13] S. Rudge, C. Peterson, C. Vessely, J. Koda, S. Stevens, and L. Catterall, "Adsorption and desorption of chemotherapeutic drugs from a magnetically targeted carrier (MTC)," *J. Controlled Release,* vol. 74, 2001.

[14] A. S. Wadajkar, S. Santimano, L. Tang, and K. T. Nguyen, "Magnetic-based multi-layer microparticles for endothelial progenitor cell isolation, enrichment, and detachment," *Biomater.,* vol. 35, p. 654, 2014.

[15] C. Gosse and V. Croquette, "Magnetic Tweezers: Micromanipulation and Force Measurement at the Molecular Level," *Biophys. J,* vol. 82, p. 3314, 2002.

[16] A. Rida and M. A. M. Gijs, "Manipulation of Self-Assembled Structures of Magnetic Beads for Microfluidic Mixing and Assaying," *Anal. Chem.,* vol. 76, p. 6239, 2004.

[17] J. C. Love, A. R. Urbach, M. G. Prentiss, and G. M. Whitesides, "Three-dimensional self-assembly of metallic rods with submicron diameters using magnetic interactions," *J. Am. Chem. Soc,* p. 12696, 2003.

[18] W. Wen, N. Wang, D. W. Zheng, C. Chen, and K. N. Tu, "Two- and three-dimensional arrays of magnetic microspheres," *J. Mater. Res.,* vol. 14, p. 1186, 1999.

[19] R. M. Erb, R. Libanori, N. Rothfuchs, and A. R. Studart, "Composites Reinforced in Three Dimensions by Using Low Magnetic Fields," *Science,* vol. 335, p. 199, 2012.

[20] K. L. Johnson, K. Kendall, and A. D. Roberts, "Surface Energy and the Contact of Elastic Solids," *Proc. R. Soc. London, Ser. A,* vol. 324, p. 301, 1971.

[21] B. V. Derjaguin, V. M. Muller, and Y. P. Toporov, "Effect of contact deformations on the adhesion of particles," *J. Colloid Interface Sci.,* vol. 53, p. 314, 1975.

[22] D. Tabor, *J. Colloid Interface Sci.,* vol. 58, p. 2, 1977.

[23] V. M. Muller, V. S. Yushchenko, and B. V. Derjaguin, *J. Colloid Interface Sci.,* vol. 77, p. 91, 1980.

[24] D. Maugis and H. M. Pollock, "Surface forces, deformation and adherence at metal microcontacts," *Acta Metall.,* vol. 32, p. 1323, 1984.

[25] W. A. Ducker, T. J. Senden, and R. M. Pashley, "Direct measurement of colloidal forces using an atomic force microscope," *Nature,* vol. 353, p. 239, 1991.

[26] D. Maugis, "Adhesion of spheres: The JKR-DMT transition using a dugdale model," *J. Colloid Interface Sci.,* vol. 150, p. 243, 1992.

[27] G. O. W. Kremp, *Morphologic Encyclopedia of Palynology,* 1968.

[28] J. W. Walker and J. A. Doyle, *Ann. Mo. Bot. Gard.,* vol. 62, p. 664, 1975.

[29] G. Erdtman, *Pollen Morphology and Plant Taxonomy*, 1986.

[30] A. Ressayre, B. Godelle, C. Raquin, and P. H. Gouyon, "Aperture Pattern Ontogeny in Angiosperms," *J. Exp. Zool.,* vol. 294, p. 122, 2002.

[31] P. J. Beggs, "Impacts of climate change on aeroallergens: past and future," *Clin. Exp. Allergy,* vol. 34, p. 1507, 2004.

[32] L. Ziska, K. Knowlton, C. Rogers, D. Dalan, N. Tierney, M. A. Elder, *et al.*, "Recent warming by latitude associated with increased length of ragweed pollen season in central North America," *Proc. Natl. Acad. Sci. U.S.A.,* vol. 108, p. 4248, 2011.

[33] W. Songnuan, "Wind-pollination and the roles of pollen allergenic proteins," *Asian Pac. J. Allergy Immunol,* vol. 31, p. 261, 2013.

[34] F. E. Round, R. M. Crawford, and D. G. Mann, *The Diatoms: Biology and Morphology of the Genera*. NewYork: Cambridge University Press, 1990.

[35] D. M. Nelson, P. Treguer, M. A. Brzezinski, and A. Leynaert, "Production and dissolution of biogenic silica in the ocean: Revised global estimates, comparison with regional data and relationship to biogenic sedimentation," *Global Biogeochem. Cycles,* vol. 9, p. 359, 1995.

[36] D. G. Mann and S. J. M. Droop, "Biogeography of freshwater algae," *Hydrobiologia,* vol. 336, p. 19, 1996.

[37] M. Hildebrand, "Diatoms, Biomineralization Processes, and Genomics," *Chem. Rev.,* vol. 108, 2008.

[38] N. Kroger and N. Poulsen, "Diatoms-from cell wall biogenesis to nanotechnology.," *Ann. Rev. Gen.,* vol. 42, p. 83, 2008.

[39] R. Wetherbee, J. L. Lind, J. Burke, and R. S. Quatrano, "Minireview—The First Kiss: Establishment and Control of Initial Adhesion by Raphid Diatoms," *J. Phycol.,* vol. 34, p. 9, 1998.

[40] K. S. Kopanska, B. Tesson, H. Lin, J. C. Meredith, M. Hildebrand, and A. Davis, "Morphological factors involved in adhesion of acid-cleaned diatom silica," *Silicon,* vol. 6, p. 95, 2014.

[41] A. F. Edlund, R. Sqanson, and D. Preuss, "Pollen and Stigma Structure and Function: The Role of Diversity in Pollination," *The Plant Cell,* vol. 16, p. S84, 2004.

[42] K. H. Sandhage, M. B. Dickerson, P. M. Huseman, M. A. Caranna, J. D. Clifton, T. A. Bull, *et al.*, "Novel, Bioclastic Route to Self-Assembled, 3D, Chemically

Tailored Meso/Nanostructures: Shape-Preserving Reactive Conversion of Biosilica (Diatom) Microshells," *Adv. Mater.*, vol. 14, p. 429, 2002.

[43] S. R. Hall, H. Bolger, and S. Mann, "Morphosynthesis of complex inorganic forms using pollen grain templates," *ChemComm*, pp. 2784-2785, 2003.

[44] C. S. Gaddis and K. H. Sandhage, "Freestanding Microscale 3-D Polymeric Structures with Biologically-derived Shapes and Nanoscale Features," *J. Mater. Res.*, vol. 19, p. 2541, 2004.

[45] J. Zhao, C. S. Gaddis, Y. Cai, and K. H. Sandhage, "Free-standing Microscale Structures of Zirconia Nanocrystals with Biologically Replicable 3-D Shapes,," *J. Mater. Res.*, vol. 20, p. 282, 2005.

[46] Y. Wang, Z. Liu, B. Han, Z. Sun, J. Du, J. Zhang, *et al.*, "Replication of biological organizations through a supercritical fluid route," *ChemComm*, pp. 2948-2950, Jun 21 2005.

[47] Y. Cai, S. M. Allan, F. M. Zalar, and K. H. Sandhage, "Three-dimensional Magnesia-based Nanocrystal Assemblies via Low-Temperature Magnesiothermic Reaction of Diatom Microshells," *J. Am. Ceram. Soc.*, p. 2005, 2005.

[48] S. R. Hall, V. M. Swinerd, F. N. Newby, A. M. Collins, and S. Mann, "Fabrication of Porous Titania (Brookite) Microparticles with Complex Morphology by Sol-Gel Replication of Pollen Grains," *Chem. Mater.*, vol. 18, pp. 598-600, 2006.

[49] U. Kusari, Z. Bao, Y. Cai, G. Ahmad, K. H. Sandhage, and L. G. Sneddon, "Formation of Nanostructured, Nanocrystalline Boron Nitride Microparticles with Diatom-Derived 3-D Shapes," *Chem. Commun.*, vol. 11, p. 1177, 2007.

[50] Y. Fang, V. W. Chen, Y. Cai, J. D. Berrigan, S. R. Marder, J. W. Perry, *et al.*, "Syntheses of nanostructured Cu-and Ni-based micro-assemblies with selectable 3-D hierarchical biogenic morphologies," *Adv. Funct. Mater.*, vol. 22, p. 2550, 2012.

[51] Y. Xia, W. Zhang, Z. Xiao, H. Huang, H. Zeng, X. Chen, *et al.*, "Biotemplated fabrication of hierarchically porous NiO/C composite from lotus pollen grains for lithium-ion batteries," *Journal of Materials Chemistry*, vol. 22, p. 9209, 2012.

[52] S. Blackmore and S. H. Barnes, *Pollen and Spores: Patterns of Diversification*, 1991.

[53] M. Hesse, H. Halbritter, R. Zetter, M. Weber, R. Buchner, A. Frosch-Radivo, *et al.*, *Pollen Terminology: An Illustrated Handbook*, 2009.

[54] E. Horn, *Trans. Kans. Acad. Sci.*, vol. 36, p. 91, 1933.

[55] W. Grater and T. Stemen, "The plant, the pollen and the patient," *Rev. Paleobot. Palynol.*, vol. 4, p. 187, 1967.

[56] L. H. Ziska, D. E. Gebhard, D. A. Frenz, S. Faulkner, B. D. Singer, and J. G. Straka, "Cities as harbingers of climate change: Common ragweed, urbanization, and public health," *J. Allergy Clin. Immunol.*, vol. 111, p. 290, 2003.

[57] C. A. Rogers, P. M. Wayne, E. A. Macklin, M. L. Mullenberg, C. J. Wagner, P. R. Epstein, *et al.*, "Interaction of the Onset of Spring and Elevated Atmospheric CO_2 on Ragweed Pollen Production," *Environ. Health Perspect.*, vol. 114, p. 865, 2006.

[58] B. Fumanal, B. Chauvel, and F. Bretagnolle, "Estimation of pollen and seed production of common ragweed in France," *Ann. Agric. Environ. Med.*, vol. 14, p. 233, 2007.

[59] M. D. Bajin, C. Cingi, F. Oghan, and M. K. Gurbuz, "Global warming and allergy in Asia Minor," *Arch. Oto-Rhino-Laryngol.*, vol. 270, p. 27, 2013.

[60] H. Lin, I. Gomez, and J. C. Meredith, "Pollenkitt wetting mechanism enables species-specific tunable pollen adhesion," *Langmuir*, vol. 29, pp. 3012-3023, Mar 5 2013.

[61] I. Ichinose, H. Senzu, and T. Kunitake, "Stepwise Adsorption of Metal Alkoxides on Hydrolyzed Surfaces: A Surface Sol-Gel Process," *Chem. Lett.*, vol. 10, p. 831, 1996.

[62] I. Ichinose, H. Senzu, and T. Kunitake, "A Surface Sol-Gel Process of TiO_2 and Other Metal Oxide Films with Molecular Precision," *Chem. Mater.*, vol. 9, pp. 1296-1298, 1997.

[63] W. Brandon Goodwin, I. J. Gomez, Y. Fang, J. C. Meredith, and K. H. Sandhage, "Conversion of Pollen Particles into Three-Dimensional Ceramic Replicas Tailored for Multimodal Adhesion," *Chemistry of Materials*, vol. 25, pp. 4529-4536, 2013.

[64] P. Li, C. F. Zeng, L. X. Zhang, and N. P. Xu, *J. Inorg. Mater.*, vol. 23, p. 49, 2008.

[65] F. Cao and D. X. Li, "Morphology-controlled synthesis of SiO_2 hollow microspheres using pollen grain as a biotemplate," *Biomed Mater*, vol. 4, pp. 1-6, Apr 2009.

[66] X. Yang, X. Song, Y. Wei, W. Wei, L. Hou, and X. Fan, "Synthesis of spinous ZrO_2 core–shell microspheres with good hydrogen storage properties by the pollen bio-template route," *Scripta Materialia*, vol. 64, pp. 1075-1078, 2011.

[67] B. J. Thio, K. K. Clark, and A. A. Keller, "Magnetic pollen grains as sorbents for facile removal of organic pollutants in aqueous media," *J Hazard Mater,* vol. 194, pp. 53-61, Oct 30 2011.

[68] M. W. Anderson, S. M. Holmes, N. Hanif, and C. S. Cundy, "Hierarchical Pore Structures through Diatom Zeolitization " *Angew. Chem., Int. Ed.,* vol. 39, p. 2707, 2000.

[69] N. L. Rosi, C. S. Thaxton, and C. A. Mirkin, "Control of nanoparticle assembly by using DNA-modified diatom templates," *Angew. Chem., Int. Ed.,* vol. 43, p. 5500, 2004.

[70] E. K. Payne, N. L. Rosi, C. Xue, and C. A. Mirkin, "Sacrificial biological templates for the formation of nanostructured metallic microshells," *Angew. Chem., Int. Ed.,* vol. 44, p. 5064, 2005.

[71] M. R. Weatherspoon, M. S. Haluska, Y. Cai, J. S. King, C. J. Summers, R. L. Snyder, *et al.*, "Phosphor Microparticles of Controlled 3-D Shape from Phytoplankton," *J. Electrochem. Soc.,* vol. 153, p. H34, 2006.

[72] D. Losic, J. G. Mitchell, R. Lai, and N. H. Voelcker, "Rapid Fabrication of Micro- and Nanoscale Patterns by Replica Molding from Diatom Biosilica," *Adv. Funct. Mater.,* vol. 17, p. 2439, 2007.

[73] Z. Bao, E. M. Ernst, S. Yoo, and K. H. Sandhage, "Syntheses of Porous Self-Supporting Metal Nanoparticle Assemblies with 3-D Morphologies Inherited from Biosilica Templates (Diatom Frustules)," *Adv. Mater.,* vol. 21, p. 474, 2009.

[74] Y. Fang, Q. Wu, M. B. Dickerson, Y. Cai, S. Shian, J. D. Berrigan, *et al.*, "Protein-Mediated Layer-by-Layer Syntheses of Freestanding Microscale Titania Structures with Biologically Assembled 3-D Morphologies," *Chemistry of Materials,* vol. 21, pp. 5704-5710, 2009.

[75] E. Domínguez, J. A. Mercado, M. A. Quesada, and A. Heredia, "Pollen sporopollenin: degradation and structural elucidation," *Sex Plant Reprod,* vol. 12, pp. 171-178, 1999.

[76] H. E. M. Dobson, " Survey of pollen and pollenkitt lipids - chemical cues to flower visitors," *Am. J. Bot.,* vol. 75, p. 170, 1988.

[77] M. R. Weatherspoon, M. B. Dickerson, G. Wang, Y. Cai, S. Shian, S. C. Jones, *et al.*, "Thin, conformal, and continuous SnO_2 coatings on three-dimensional biosilica templates through hydroxy-group amplification and layer-by-layer alkoxide deposition," *Angew Chem Int Ed Engl,* vol. 46, pp. 5724-5727, 2007.

[78] M. R. Weatherspoon, Y. Cai, M. Crne, M. Srinivasarao, and K. H. Sandhage, "3D rutile titania-based structures with morpho butterfly wing scale morphologies," *Angew Chem Int Ed Engl,* vol. 47, pp. 7921-7923, 2008.

[79] G. Wang, Y. Fang, P. Kim, A. Hayek, M. R. Weatherspoon, J. W. Perry, *et al.*, "Layer-By-Layer Dendritic Growth of Hyperbranched Thin Films for Surface Sol-Gel Syntheses of Conformal, Functional, Nanocrystalline Oxide Coatings on Complex 3D (Bio)silica Templates," *Advanced Functional Materials,* vol. 19, pp. 2768-2776, 2009.

[80] J. P. Vernon, N. Hobbs, Y. Cai, A. Lethbridge, P. Vukusic, D. D. Deheyn, *et al.*, "3D photoluminescent lanthanide-doped barium titanate structures synthesized by coating and shape-preserving reaction of complex-shaped bioorganic templates," *Journal of Materials Chemistry,* vol. 22, pp. 10365-10940, 2012.

[81] F. H. Rhines, W. A. Johnson, and W. A. Anderson, *Trans. AIME,* vol. 147, p. 205, 1942.

[82] B. D. Cullity and S. R. Stock, *Elements of X-Ray Diffraction, 3rd ed*: Prentice-Hall, Inc,, 2001.

[83] A. Percot, C. Viton, and A. Domard, "Optimization of Chitin Extraction from Shrimp Shells," *Biomacromolecules,* vol. 4, pp. 12-18, 2003.

[84] H. A. Wriedt, "Iron-Oxygen Binary Alloy Phase Diagram " *J. Phase Equilib.*, vol. 12, p. 170, 1991.

[85] Card No. 33-0664 for γ-Fe_2O_3, Card No. 19-0629 for Fe_3O_4; International Center for Diffraction Data: Newtown Square, PA USA, 2007.

[86] J. P. Vernon, Y. Fang, Y. Cai, and K. H. Sandhage, "Morphology-preserving conversion of a 3D bioorganic template into a nanocrystalline multicomponent oxide compound," *Angew Chem Int Ed Engl,* vol. 49, pp. 7765-7768, Oct 11 2010.

[87] K. Tanaka, T. Yoko, M. Atarashi, and K. Kamiya, "Preparation of Fe_3O_4 thin film by the sol-gel method and its magnetic properties," *J. Mater. Sci. Lett.*, vol. 8, p. 83, 1989.

[88] J. Tang, K.-Y. Wang, and W. Zhou, "Granular Growth of Fe_3O_4 Thin Films and Its Antiphase Boundaries Prepared by Pulsed Laser Deposition," *J. Appl. Phys,* vol. 89, p. 7690, 2001.

[89] S. Chatman, A. J. G. Noel, and K. M. Poduska, "Tuning magnetic hysteresis of electrodeposited Fe_3O_4," *J. Appl. Phys.,* vol. 98, p. 113902, 2005.

[90] M. Sanz, M. Oujja, E. Rebollar, J. F. Marco, J. d. l. Figuera, M. Monti, *et al.*, "Nanosecond laser-induced periodic surface structures on wide band-gap semiconductors," *Appl. Surf. Sci.,* vol. 282, p. 642, 2013.

[91] J. C. Meredith, A. P. Smith, A. Karim, and E. J. Amis, "Combinatorial Materials Science for Polymer Thin-Film Dewetting," *Macromolecules,* vol. 33, pp. 9747-9756, 2000.

[92] J. Israelachvili, *Intermolecular and Surface Forces*, 1992.

[93] N. Leventis and X. Gao, "Magnetohydrodynamic electrochemistry in the field of Nd-Fe-B magnets. Theory, experiment, and application in self-powered flow delivery systems," *Anal. Chem.,* vol. 73, p. 3981, 2001.

[94] H. C. Hamaker, "The London—van der Waals attraction between spherical particles," *Physica,* vol. 4, pp. 1058-1072., 1937.

[95] J. L. Rosenholtz and D. T. Smith, *Am. Mineral.,* vol. 21, p. 115, 1936.

[96] H. Daoust and M. Rinfret, "On ionic copolymerization," *J. Colloid Sci.,* vol. 7, p. 11, 1952.

[97] M. H. Chiu, J. Y. Lee, and D. C. Su, "Complex refractive-index measurement based on Fresnel's equations and the uses of heterodyne interferometry," *Appl. Opt.,* vol. 38, p. 4047, 1999.

[98] C. U. Devi, A. K. Sharma, and V. V. R. N. Rao, "Electrical and optical properties of pure and silver nitrate-doped polyvinyl alcohol films," *Mater. Lett.,* vol. 56, p. 167, 2002.

[99] R. J. Nussbaumer, W. R. Caseri, P. Smith, and T. Tervoort, "Polymer-TiO_2 Nanocomposites: A Route Towards Visually Transparent Broadband UV Filters and High Refractive Index Materials," *Macromol. Mater. Eng.,* vol. 288, p. 44, 2003.

[100] D. R. Lide, *CRC Handbook of Chemistry and Physics*, 2005.

[101] S. L. Atkin, S. Barrier, Z. Cui, P. D. I. Fletcher, G. Mackenzie, V. Panel, *et al.*, "UV and visible light screening by individual sporopollenin exines derived from Lycopodium clavatum (club moss) and Ambrosia trifida (giant ragweed)," *J. Photochem. Photobiol. B, Biol.,* vol. 102, p. 209, 2011.

[102] N. Leventis and X. Gao, "Magnetohydrodynamic electrochemistry in the field of Nd-Fe-B magnets. Theory, experiment, and application in self-powered flow delivery systems," *Analytical Chemistry,* vol. 73, pp. 3981-3992, 2001.

[103] E. Katifori, S. Alben, E. Cerda, D. R. Nelson, and J. Dumais, "Foldable structures and the natural design of pollen grains," *Proceedings of the National Academy of Sciences,* vol. 107, pp. 7635-7639, April 27, 2010 2010.

[104] R. P. Wodehouse, "Pollen Grains," *Hafner Publishing Co. Ltd.,* 1935.

CHAPTER 3 : Tunable Multimodal Adhesion of $CoFe_2O_4$ Ceramic Pollen Replicas Achieved via Grain Size Control

3.1. *Summary*

Three-dimensional (3-D) multicomponent $CoFe_2O_4$ replicas of pollen microparticles have been synthesized with tunable multimodal (VDW and magnetic) adhesion properties through the use of surface sol–gel (SSG) processing. High-fidelity replication allowed the pollen-shaped oxide microparticles to be utilized for adhesion via tailorable short-range (~10 nm) van der Waals (VDW) attraction, with the magnitude of such VDW-based adhesion influenced by the crystallite size on the surface features retained by the replicas. Conversion of the pollen into ferrimagnetic ($CoFe_2O_4$) microparticle replicas allowed the use of magnetic attraction at short and long ranges (up to ~1 mm). The combination of both controlled VDW and magnetic based adhesion allowed for pollen 3-D nanocrystalline microparticles replicas, generated by a SSG-enabled conversion process, with tunable short- and short to long-range attractive force.

3.2. *Introduction*

The tunability of magnetic and van der Waals attractive forces by or on microparticles is a key component of a wide range of developing and mature technologies, including targeted drug delivery, catalysis, water/chemical purification, sensing, anti-fouling coatings and membranes, semiconductor device processing, composite processing, paints, and the self-assembly of hierarchical structures.[1-11] The predominant models for understanding adhesion are based on smooth, spherical particles and many, if not most, experimental studies utilize smooth spherical models [12-18] as

opposed to microparticles with rough surfaces and non-spherical shapes. Numerous commercial particle processes and materials utilize irregularly-shaped particles with roughened surfaces. Development of a model to understand how adhesion is affected by non-spherical shaped particles is desired for a number of such technologies.[6, 9, 19] However, the study of adhesion properties of micro-particles with well-controlled surface asperities, in a variety of three-dimensional (3-D) morphologies, and with tunable chemistries is hindered due to scalable fabrication and remains a difficult synthetic challenge.

Pollen is a rich sustainable source of 3-D microparticles, with complex morphologies affecting dispersion and adhesion in nature. Pollen particles are produced in large and abundant quantities worldwide by plants each year [20-27] and come in a wide variety of species-dependent, 3-D shapes, and surface topographies.[28-33] Atomic force microscopy (AFM) based adhesion measurements have recently shown that, for 3-D replicas comprised of ferromagnetic hematite (α-Fe_2O_3)[34], or ferrimagnetic magnetite (Fe_3O_4)[34] VDW adhesion forces between pollen replicas and a planar surface may be based on crystallite size as opposed to the spine tip radius for native pollen.[35]

The purpose of this work is to learn how the crystallite size of ceramic replicas can be used to tailor the attraction forces of 3-D biogenic microparticles though synthetic chemical processing. Thermal processing can be used to control the average crystallite size (ACS) of the ceramic replicas to allow for the investigation of mechanisms affecting adhesion. Native pollen particles have been converted into a 3-D multicomponent oxide ($CoFe_2O_4$), via use of a highly-conformal surface sol-gel (SSG) coating process [36, 37].

The average nanoscale crystal size of the pollen replicas was controlled via thermal treatment. The prepared replicas were attached to AFM cantilevers, and short- and long-range attraction forces between the replicas and substrates (Ni, Cu, Au, and Ni-Nd) were evaluated with the scanning probe microscope. A Multi-Sphere Hamaker model and a Sphere-Plan magnetic force model were used to simulate the short- and long-range interactions, respectively. A reproducible non-monotonic relationship was observed between the average crystal size of the oxide replicas and the short-range VDW interaction.

The nanoscale surface topography, and the magnetic oxide content, of high-fidelity 3-D replicas can provide for multimodal attraction to surfaces via both short-range VDW and short-to-long-range magnetic forces. Although other authors have used coating or infiltration methods to chemically modify/transform pollen [38-45] and other biological microparticles [46-55] for desired (bio)chemical, optical, electrical, structural, or fluidynamic properties, the conversion of sustainable biogenic particles (like pollen) into all-inorganic 3-D replicas comprised of a spinel ferrite for the purpose of achieving controlled multimodal adhesion based on grain size has not been reported.

3.3. *Experimental Procedures*

3.3.1. Template

Owing to its adherent nature and its biological replicability (i.e., sustainability), ready availability, abundance, and low cost, pollen was considered to be a desirable type of microparticle template for conversion into magnetic replicas (to enable a new modality of tailorable adhesion). Sunflower pollen (Figure 1 d, Chapter 1) has been chosen based

on the overall size, shape, and wide range of features in both the micro- and nanometer ranges. The exine (outer layer) of pollen grains is composed of sporopollenin, a complex polymer consisting of carboxylic acids cross-linked with aliphatic chains (e.g. HOOC-$(CH_2)_n$-COOH).[56] The carboxylic acids provide an abundant amount of functional groups needed for the reaction with the isopropoxide precursors used in the SSG process. These surface groups can eliminate the need for surface modification in order to obtain conformal coatings.

3.3.2. Demineralization of Pollen Grains

Pollen grains obtained from Greer Laboratories, Lenoir, NC USA were cleaned, to remove pollenkitt, by immersion in a mixture of chloroform and methanol (3:1)[57] for 24 h, followed by deposition onto filter paper (P5, Fisher Scientific, Pittsburgh, PA USA) and drying under vacuum at 60°C for 12 h. A second immersion was conducted in 1 M hydrochloric acid (VWR, Suwanee, GA USA) for 1 h to remove residual inorganic material, followed by rinsing three times with de-ionized water and drying by vacuum aspiration at room temperature for 5 min.

3.3.3. SSG Coating of Pollen Grains

Fe-O-bearing and Co-O-bearing coatings were applied to cleaned, acid washed pollen grains via a computer-automated, layer-by-layer (LbL) SSG deposition process by:[58-61] i) immersing pollen grains for 10 min, with stirring, in a solution of either 0.0125 M Fe(III) isopropoxide (Alfa Aesar, Ward Hill, MA USA) in anhydrous 2-propanol (>99.8% purity, Acros Organics, Geel, Belgium) for the Fe-O-bearing layers or 0.0125 M Co(II) isopropoxide (Alfa Aesar, Ward Hill, MA USA) in anhydrous 2-

propanol (>99.8% purity, Acros Organics, Geel, Belgium) for the Co-O-bearing layers, to allow for the chemisorption of a Fe-O-bearing or Co-O-bearing layer, ii) rinsing three times with anhydrous 2-propanol followed by vacuum filtration, iii) immersion in de-ionized water (DIW) with stirring, for 5 min, to allow for hydrolysis of the chemisorbed alkoxide layer, iv) rinsing three times with anhydrous 2-propanol followed by vacuum filtration, and v) and drying by vacuum aspiration for 5 min. This process (alkoxide exposure, alcohol rinsing, water exposure, alcohol rinsing, drying) was repeated 50 times (for a total of 51 cycles) to build up a continuous and conformal coating. The pollen particles were coated with alternating Fe-O and Co-O layers, in a Fe-O:Co-O ratio of 2:1, so as to achieve the desired stoichiometry for the $CoFe_2O_4$ spinel. The alternating exposure of cobalt and iron alkoxides is illustrated in Figure 62. (Note: the SSG coating process was conducted at room temperature in a N_2 atmosphere glove box with a relative humidity maintained between 0-2%. The relative humidity was monitored using an Omega RH32 sensor from OMEGA Engineering, Inc., Stamford, Connecticut.)

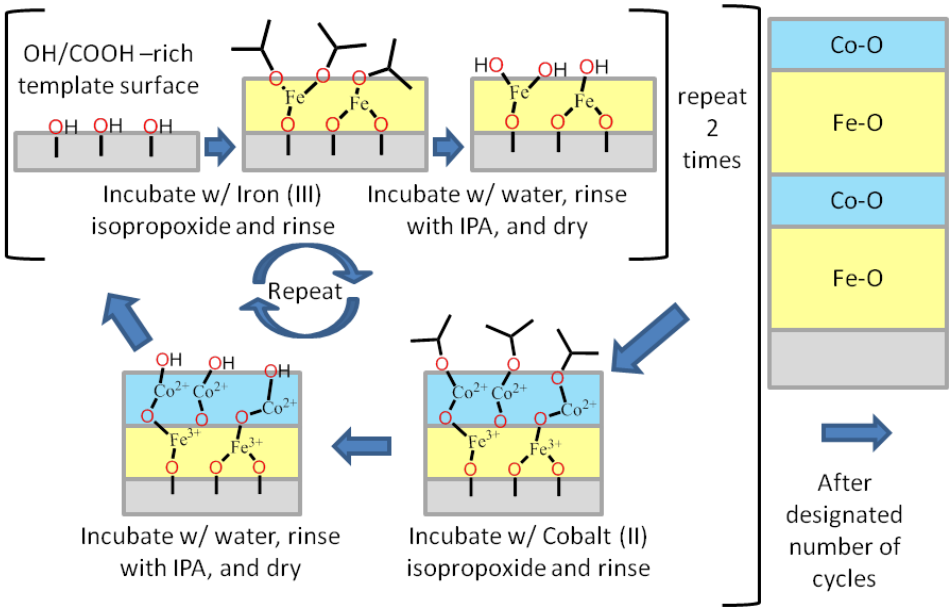

Figure 62: A schematic representation of the alternating LbL surface sol-gel process utilizing iron (III) isopropoxide and Co (II) isopropoxide as metal alkoxides.

3.3.4. Organic Pyrolysis and Conversion to Oxide and Metal Replicas

The SSG-coated pollen particles were prepared for pyrolysis in the following manner: i) SSG-coated pollen particles were suspended in IPA and then dispersed onto nickel foil (25.4 μm thick, McMaster-Carr, Cleveland, OH, USA) using a pipette, ii) SSG-coated pollen particles were suspended in IPA and then dispersed onto silicon wafers (Wafernet, Inc., San Jose, CA, USA) using a pipette, and iii) SSG-coated pollen particles were also placed in a MgO crucible (96.6% MgO, 2% Y_2O_3, 1.4% CaO, SiO_2, Al_2O_3, Fe_2O_3, and B_2O_3Ozark Technical Ceramics, Inc, Webb City, MO) with a coated pollen powder depth between 1-5 mm. Samples were fired in stagnant ambient air using a tube furnace (Lindberg / Blue M, NC, USA,) with a ramp rate of 3°C min^{-1} to a peak temperature of 600°C, 700°C, 800°C, or 900°C and held at this temperature for 2 h to allow for organic pyrolysis and oxide crystallization. The pyrolysis process was also studied using thermogravimetric analysis (TGA) (Netzsch STA 449C, Wolverhampton, UK). The TGA measurements were performed with the as received pollen and as coated pollen grains at a heating rate of 5 ºC min^{-1} up to 600 ºC in a flowing (flow rate of 50 cm^3min^{-1}) synthetic air gas mixture.

For conversion into $CoFe_2$, the $CoFe_2O_4$ pollen replicas, in a MgO crucible, were placed in a sealed steel tube furnace in which the atmosphere was: i) evacuated, and replaced with a 2%H_2/98%Ar gas mixture 3 times and ii) exposed to a flowing (flow rate of 30 cm^3min^{-1}) 2%H_2/98%Ar gas mixture for the duration of the thermal treatment.. The samples were then heated at 3°C min^{-1} to 550°C and held at this temperature for 2 h to reduce the magnetite replicas into iron replicas.

3.3.5. Shape, Size, and Morphology Analyses

For individual native pollen grains, SSG-coated grains, the pyrolyzed grains, and iron-cobalt-bearing replicas, the morphologies and spine tip dimensions were evaluated with a field emission scanning electron microscope (1530 FEG SEM, LEO / Carl Zeiss SMT, Ltd., Thorn-wood, NY USA).

To determine pollen replica size and morphology preservation between pre and post-thermal treatment, the same individual pollen grain was imaged before and after each thermal treatment. The procedure used has been previously reported [34] and further information on the measurements can be found in Section 2.3.5.

The average size of the nano-particles on the spine surfaces of oxide replicas of sunflower pollen particles were obtained from secondary electron (SE) images of particles attached to cantilever probes (described below in section 3.3.8). For each particle-bearing probe, 7-8 nanoparticles were counted on 3 spine tips located closest to the position where the particle made contact to the substrates (for a total of ~22 grains analyzed for all 3 similar types of particle-bearing probes). Note: for samples fired at 600°C, individual grains were not visible and could not be measured with SE micrographs.

3.3.6. Phase and Grain Size Determination

The phase identification for the fired pollen replicas were evaluated at room temperature using X-ray diffraction (XRD) analyses. XRD analyses were conducted on a diffractometer (X'Pert Pro Alpha-1, PANalytical B.V., ALMELO, Netherlands) with $Cu_{K\alpha 1}$(1.5405980 Å) radiation emanating from a 1.8 kW ceramic X-ray tube with a copper anode (45 kV, 40 mA) through an incident beam Johansson monochromator

(PANalytical) and detected by an X'Celerator detector. The incident beam optics were outfitted with 0.04 rad soller slits, a 2° fixed anti-scatter slit, a programmable divergence slit set to 5.5 mm irradiated length, and a 10 mm mask. The diffracted beam optics were outfitted with a 5.5 mm anti-scatter slit and 0.04 rad soller slits placed before the X'Celerator detector. Each pattern was produced with a summation of 40 identical 30 minute scans conducted with Bragg-Brentano geometry and a step size of 0.017° 2θ ranging from 20° to 90° 2θ. The minimum setting on the Pulse Height Discrimination (PHD) for the X'Celerator detector was increased to from 36 to 42 to help discriminate between the diffracted signals and fluorescence photons from the Fe and Co atoms.[62] Diffraction specimens were dispersed on quartz cut (6° from (0001)) low background specimen support (GEM dugout, PA, USA) via pipetting an aliquot of IPA/powder slurry onto the specimen support and allowing the IPA to evaporate.

Phase identification and average crystallite size (ACS) were determined using the HighScore Plus software (PANalytical B.V, Almelo, The Netherlands) using a profile fit function. A Pseudo-Voigt profile fit function was used in conjunction with a Williamson Hall plot to determine the average grain size of the pollen replicas. The profile fit function allows for each single peak to be characterized by position and height, width and shape along with being described by functions of 2θ. The Pseudo-Voigt function is shown below:[63]

$$G_{jk} = \gamma \frac{C_0^{1/2}}{H_k \pi} \left[1 + C_0 1 X_{jk}^2\right]^{-1} + (1-\gamma) \frac{C_1^{1/2}}{H_k \pi^{1/2}} exp\left[-C_1 X_{jk}^2\right] \qquad (3.1)$$

where: $C_0 = 4$; $C_1 = 4\ln 2$; X_{ij} is related to the peak position, 2θ angle and H_k (the full-width at half-maximum (FWHM) of the k^{th} Bragg reflection) by equation 3.2; and γ is a

refinable "mixing" parameter of Gaussian and Lorentzian peak shapes given by equation 3.3:

$$X_{ij} = \frac{(2\theta_j 2\theta_k)}{H_k} \tag{3.2}$$

$$\gamma = \gamma_1 + \gamma_2 2\theta + \gamma_3 (2\theta)^2 \tag{3.3}$$

The H_k values are then fitted to the Caglioti equation in a FWHM plot.

$$H_k = (Utan^2\theta + Vtan\theta + W)^{1/2} \tag{3.4}$$

where U, V, and W are fitting parameters related to grain size and microstrain. A Si NIST line standard (640c) was used to determine the instrument broadening of the diffracted peaks. Figure 63 show the profile fit of the Si standard. A Caglioiti fit was made for both the Gaussian and Lorentzian components of the peaks profiles (Figure 64).

The Caglioti fits were then converted to Line Profile (LP) Analysis Standard and used in calculating the structural breadth (Struct B) of $CoFe_2O_4$ ferrite replicas with the following formula:

$$\text{Struct B= Obs B – Inst B} \tag{3.5}$$

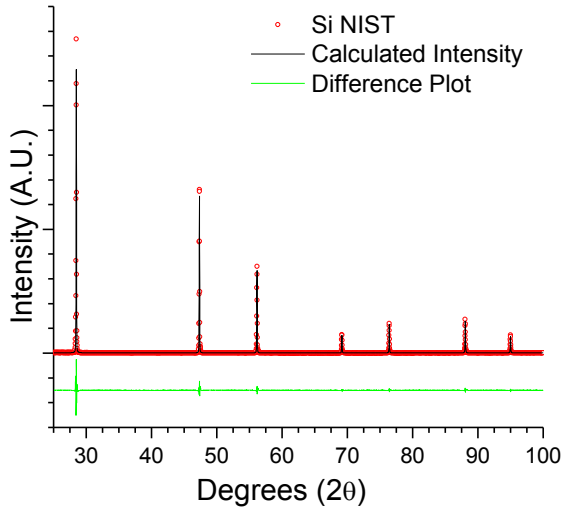

Figure 63: Pseudo-Voigt profile fit of Si NIST standard used for a Line Profile Analysis standard

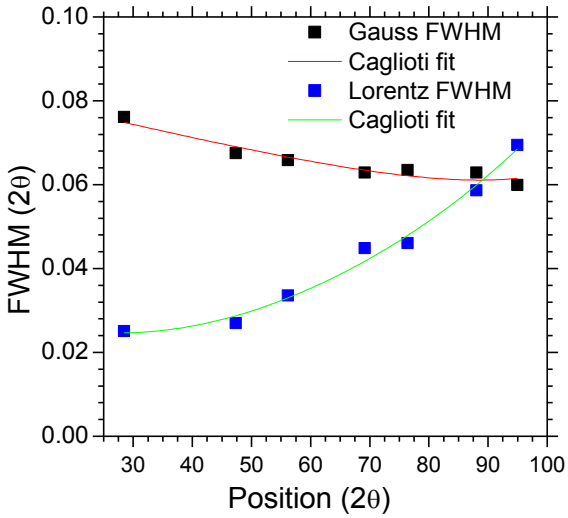

Figure 64: Gaussian and Lorentzian components of the SI NIST standard fitted to Caglioti equations

Obs B is the breadth of the experimental diffraction peak for the sample being analyzed and Inst B is the breadth calculated from the LP Analysis Standard created when the calibration data was used to analyze the instrument profile. In order to construct the Williamson-Hall plot, both net Gaussian and Lorentzian broadenings were combined using the empirical convolution shown below:

$$B_{Stuct.} = B_{G\,net}/\left[-0.5K * \sqrt{\pi} + 0.5C - 0.234K * \exp(-2.716K)\right] \quad (3.6)$$

with $$K = B_{L\,net}/\left[\sqrt{\pi} * B_{L\,net}\right] \quad (3.7)$$

and $$C = \sqrt{\pi * K^2 + 4} \quad (3.8)$$

where $B_{G\ net}$ and $B_{L\ net}$ are the net Gaussian and Lorentzian broadening terms. The Struct B values were then plotted in a linear Williamson-Hall plot. A straight line was fitted to all peaks of the same phase using the following equation

$$B * cos(\theta)/_{\lambda} = 1/_{D} + 4\varepsilon sin\theta/_{\lambda} \quad (3.9)$$

where B is the broadening term in radians, λ is the wavelength of the X-rays, θ is the angle of diffraction, ε is the microstrain, and D is the crystallite size. The slope of the

fitted line rendered the microstrain, while the offset was used to calculate the crystallite size.

3.3.7. Chemical Analysis

Elemental analysis were obtained by ICP-MS (Inductively coupled plasma mass spectroscopy: PerkinElmer ICP-MS model-ELAN 9000) by Gene Weeks at the Laboratory of Environmental Analysis, and with the use of an energy dispersive X-ray spectrometer (EDS) (INCA Model 7426, Oxford Instruments, Bucks, UK) attached to a scanning electron microscope (1530 FEG SEM, LEO / Carl Zeiss SMT, Ltd., Thornwood, NY USA). ICP-MS and EDS analyses were both conducted on three different samples in order to obtain the average Fe/Co ratio.

3.3.8. Substrate Preparation and Adhesion Measurements

To study the short-range (VDW) and long range (magnetic) adhesion, four types of substrates were utilized: copper (Cu), gold (Au), nickel (Ni), and a nickel-coated neodymium (Ni-Nd) alloy. The three different metal substrates (Ni, Au and Cu) were chosen to analyze intermolecular forces between these metal surfaces and the replicas. To minimize the effect of the surface roughness, 100 nm of nickel, copper, or gold were deposited on a silicon wafer (Silicon, Inc., Boise, ID) by CHA Ex e-beam evaporator (CHA Industries, Fremont, CA, USA) at a rate of 2 Å/sec and a background pressure of 10^{-6} torr. Nickel foil (0.150 mm thickness, grade 200, 99.5% purity, Shop-aid, Inc., Woburn, MA) with an area of 38.5 mm^2 was prepared by electro polishing using 1.3 A of current for 120 sec with a 8.9 mol L^{-1} solution of sulfuric acid as an electrolyte and a platinum rod as cathode. Both types of metal substrates were washed with acetone

(99.5% purity, BDH Chemicals Ltd., Radnor, PA USA) in an ultrasonic cleaner (FS20, Fisher Scientific, Pittsburgh, PA) for 10 min at room temperature before use.

For each type of substrate, the surface roughness of each substrate was evaluated by conducting 3 randomly-located scans (10 μm x 10 μm) with a scanning probe microscope (Dimension 3100 SPM equipped with a Nanoscope V Controller, Veeco Instruments, Inc., Plainview, NY USA) operated in tapping mode at 200-400 Hz using a pyramidal tip silicon cantilever (Applied NanoStructures, Inc., Santa Clara, CA USA). For each scan, 4 sectors (1 μm x 1 μm) were randomly selected to measure roughness values and the average roughness value for a given substrate was obtained from analysis of these 12 sectors.

To perform a given adhesion measurement, a single particle (a native sunflower pollen particle or oxide replica particle) was attached to an atomic force microscope (AFM) cantilever. A small amount of epoxy resin (Epoxy Marine, Loctite, Westlake, OH USA) was used to attach a given particle (see Figure 73) to a tipless silicon AFM cantilever (FORT-TL, Applied NanoStructures, Inc.). For each type of pollen-shaped particle (cleaned sunflower pollen or $CoFe_2O_4$ replica) and firing condition used (600°C, 700°C, 800°C, and 900°C), 3 single-particle-bearing cantilever probes were prepared (for a total of 15 particle/cantilever probes). The spring constants, as determined with the scanning probe microscope, of the sunflower-pollen-bearing, $CoFe_2O_4$-replica-bearing (fired at a peak temperature of 600°C, 700°C, 800°C, or 900°C) cantilever probes fell in the ranges of 1.87-2.98 N/m, 0.87-1.97 N/m, 0.90-1.85 N/m, 1.04-2.21 N/m, and 1.02-2.29 N/m, respectively. For an individual sunflower pollen particle, or oxide replica particle, the adhesion force between a particular substrate was evaluated with the

scanning probe microscope operated in contact mode. For each particular particle/cantilever probe and particular substrate, 10 separate force-distance scans were obtained at random locations, and the depth of adhesion wells upon retraction were averaged. The load force applied during the contact adhesion measurements was 2.5 nN. The ambient relative humidity in the laboratory during the adhesion measurements ranged from 30 to 35%. Note: the procedure described in section 3.3.8 was developed and performed with Donglee Shin (Georgia Institute of Technology, Atlanta, GA, USA).

3.3.9. Magnetic Property Measurements

Magnetic properties of $CoFe_2O_4$ spinel ferrite sunflower replicas were studied using a superconducting quantum interference device (SQUID) magnetometer (Quantum Design MPMS-5S, San Diego, CA USA) with a magnetic field up to 5 T. Measurements were conducted at 300 K. Further information on the measurements conditions can be found in section 2.3.8.

3.4. *Results & Discussion*

3.4.1. Pollen Shape Preservation

Sunflower pollen grains were converted into cobalt ferrite ($CoFe_2O_4$) replicas using the processes described in sections 3.3.3 and 3.3.4. SE images of the sunflower pollen particle after exposure to 51 SSG deposition cycles (17 Co-O cycles and 34 Fe-O cycles) and after firing at a peak temperature of 600^{o}C, 700^{o}C, 800^{o}C or 900^{o}C for 2 h are shown Figure 65 a/b, c/d, e/f, and g/h, respectively. White arrows mark individual features that were preserved from the as-coated samples by the pyrolyzed samples. The 3-D morphology and sharp echini of the sunflower pollen were retained by the $CoFe_2O_4$

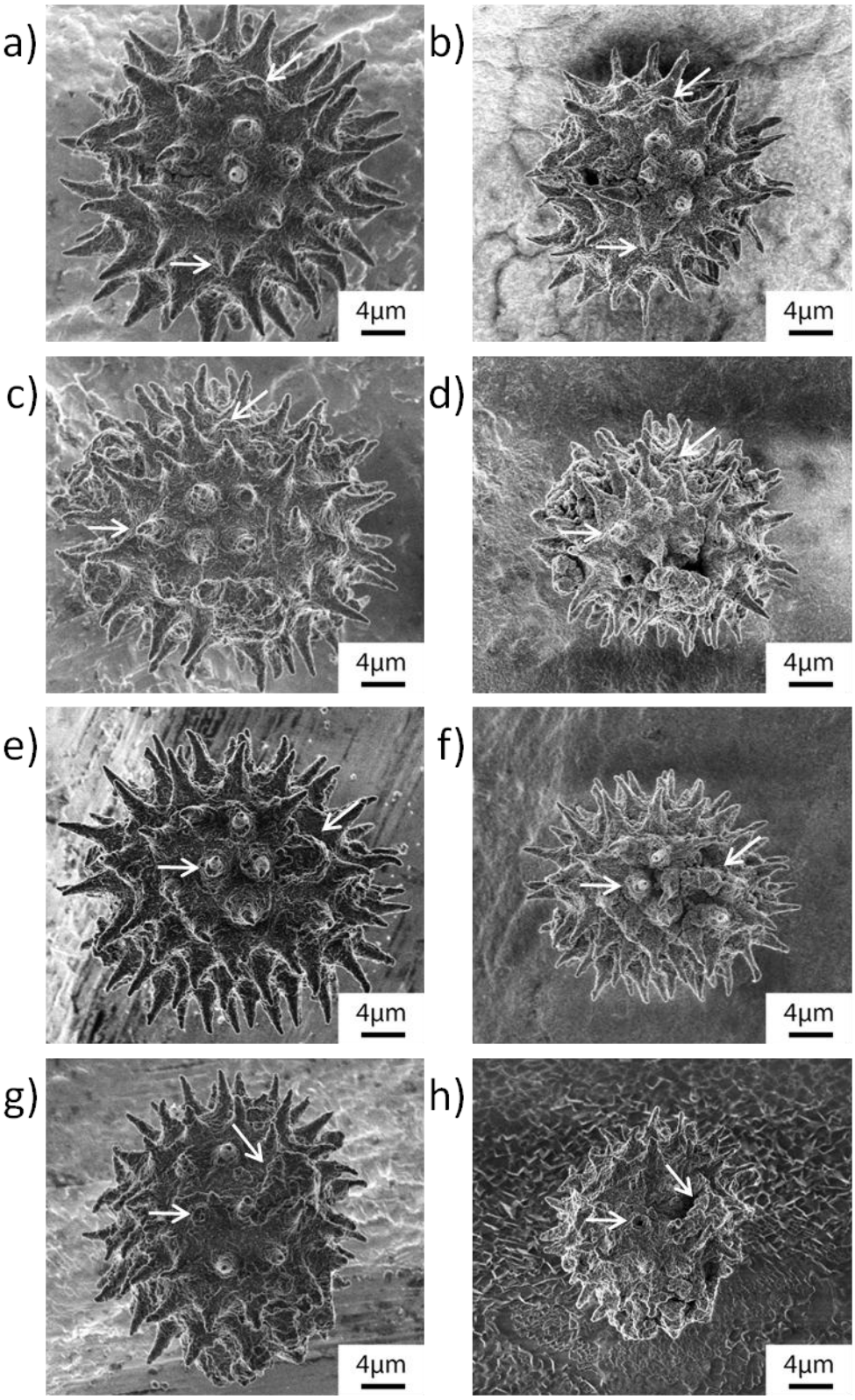

Figure 65: SE images of a), c), e), and g) Co-Fe-O-coated sunflower pollen particles exposed to 51 cycles of the surface sol-gel deposition process; and the same coated particles after pyrolysis for 2 h in air at a peak temperature of a/b) 600°C, c/d) 700°C, e/f) 800°C, or g/h) 900°C. Arrows point to select features that were preserved after thermal treatment.

ferrite replicas, even after firing to a peak temperature of 900°C in air for 2 h. TG analyses confirmed that these replicas were freestanding oxides with complete pyrolysis of the sporopollen achieved within 100 min at 600°C (Figure 66).

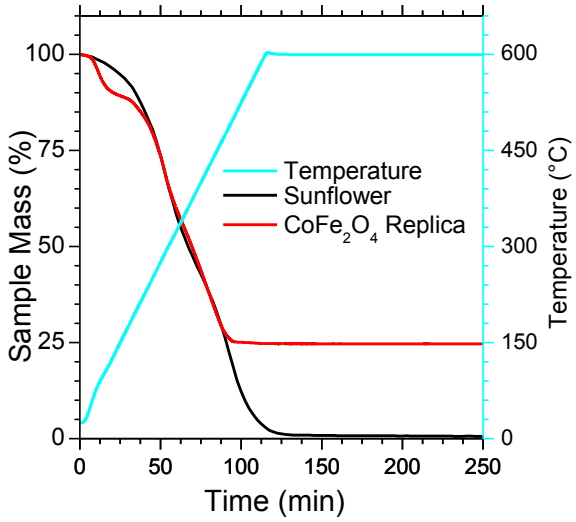

Figure 66: TG analysis of Sunflower pollen grains (black) and Co-Fe-O-coated sunflower pollen (51 SSG deposition cycles, red) during pyrolysis by heating in flowing (50 cm^3/min) synthetic air (20% O_2, 80%N_2) at 5°Cmin^{-1} to 600°C.

3.4.2. Replica Composition and Grain Size

Inductively-coupled plasma mass spectrometry (ICP-MS) analyses (by Mr. Gene Weeks in University of Georgia with ICP-MS, Wellesley, MA) of the $CoFe_2O_4$ pollen replicas fired at a peak temperature of 600°C for 2 h, were conducted by digesting the samples with aqua regia and heating in a sealed Teflon container in a microwave operated at 400W for 25 min. The ICP-MS analyses were repeated three times and yielded a Fe/Co atomic ratio of 1.96, 1.91, and 1.86. EDS analyses (Figure 67) of the $CoFe_2O_4$ pollen replicas yielded an average Fe/Co ratio of 1.98 ± 0.05. The phosphorus and sulfur peaks present in Figure 67 originated from the native pollen grains. The average measured values give a formula composition of $Co_{1.03}Fe_{1.97}O_4$ and of $Co_{1.01}Fe_{2.00}O_4$ for ICP-MS and EDS results, respectively. Both chemical analysis techniques indicated a composition close to the target composition of $CoFe_2O_4$ (2:1 Fresco ratio) which indicated that the

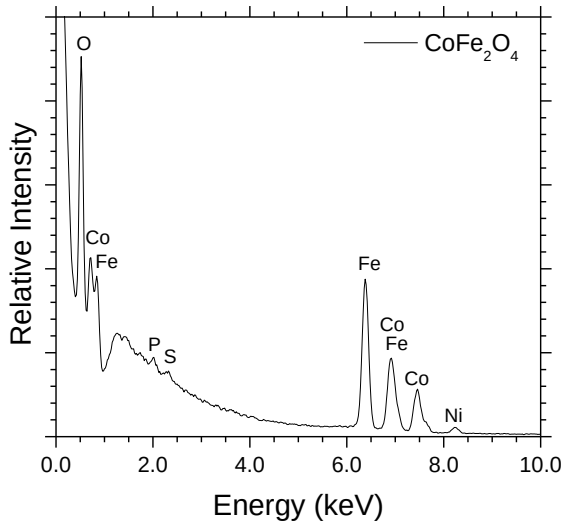

Figure 67: Representative EDS analysis of $CoFe_2O_4$ ferrite sunflower replicas after firing in air to a peak temperature of 600°C for 2 h.

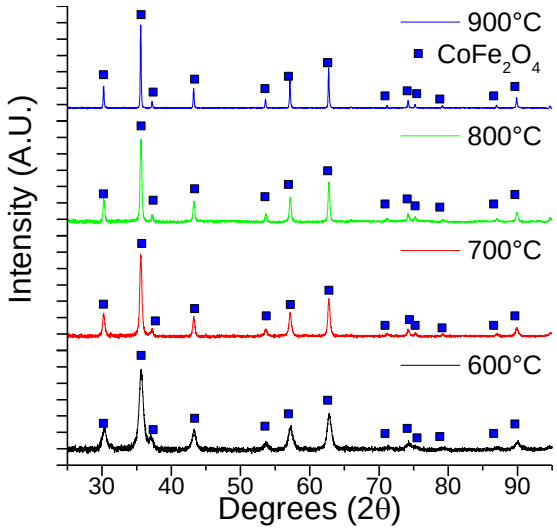

Figure 68: XRD patterns obtained from $CoFe_2O_4$ pollen replicas with the background removed

LbL SSG process can be used to control the chemistry of a multicomponent coating by depositing alternating coating layers of the desired chemistries.

XRD analyses were then used to evaluate the phase content of the $CoFe_2O_4$ ferrite replicas, and to determine the grain size resulting from each firing temperature. Figure 68 shows the XRD patterns obtained from $CoFe_2O_4$ pollen replicas for each firing temperature. Each sample was comprised of single phase $CoFe_2O_4$. The peak width became narrower at higher firing temperatures which was consistent with an increase in

average crystal size with an increase in firing temperature. Comparison of the experimental (311) diffraction peaks for the different peak firing temperatures can be seen in Figure 69. Full pattern profile fitting was conducted on these XRD patterns for crystallite size analyses. The difference plots, between the measured and calculated plots, are provided in Figure 70 a, b, c, and d for the samples fired at peak temperatures of 600^{o}C, 700^{o}C, 800^{o}C or 900^{o}C, respectively for 2 h. The FWHM values of each diffraction peak were fitted to the Caglioti equation[64] (as shown in Figure 71 a, b, c, and d for the samples fired at 600^{o}C, 700^{o}C, 800^{o}C or 900^{o}C, respectively and with the fitted data shown in Table 8) and linear Williamson-Hall plots [65] were then used to determine the ACS and microstrain resulting from each firing condition. A Si NIST profile standard (640c) was used to calibrate the peak broadening of the samples, to allow for quantitative crystallite size and microstrain analyses. Figure 72 reveals the Williamson-Hall plot for each of the four samples. The fitting data for the Williamson-Hall plot can be seen in Table 9. An average increase in crystallite size was observed with increasing peak firing temperature. Microstrain analyses indicated that all samples

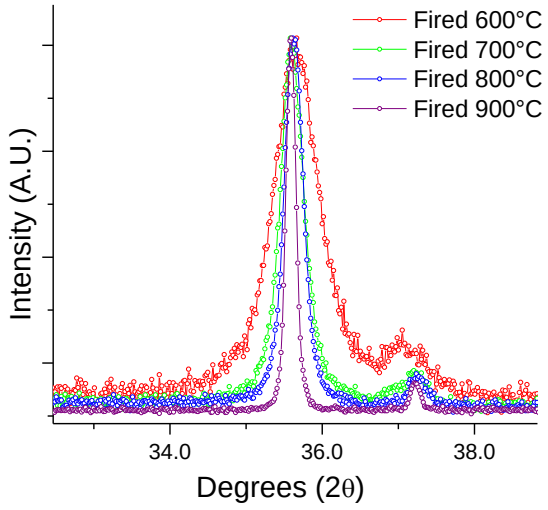

Figure 69: (311) diffraction peak of $CoFe_2O_4$ replicas showing a decrease in the FWHM of this peak as firing temperature (2 h) increased.

exhibited strain values under 0.1% indicating that the primary cause of peak broadening was a fine crystallite size. (The near horizontal linear fits on the Williamson-Hall plots indicated little microstrain in the material while the y intercepts were related to the ACS)

SEM images of individual pollen grains attached to the ends of AFM cantilever tips are shown in Figure 73. Higher magnification images were obtained of the individual spine tips (Figure 74) to enable measurement of the sizes of oxide nano-particles present on the spine surfaces. 20 particles were measured on 3 spine replica tips for each replica

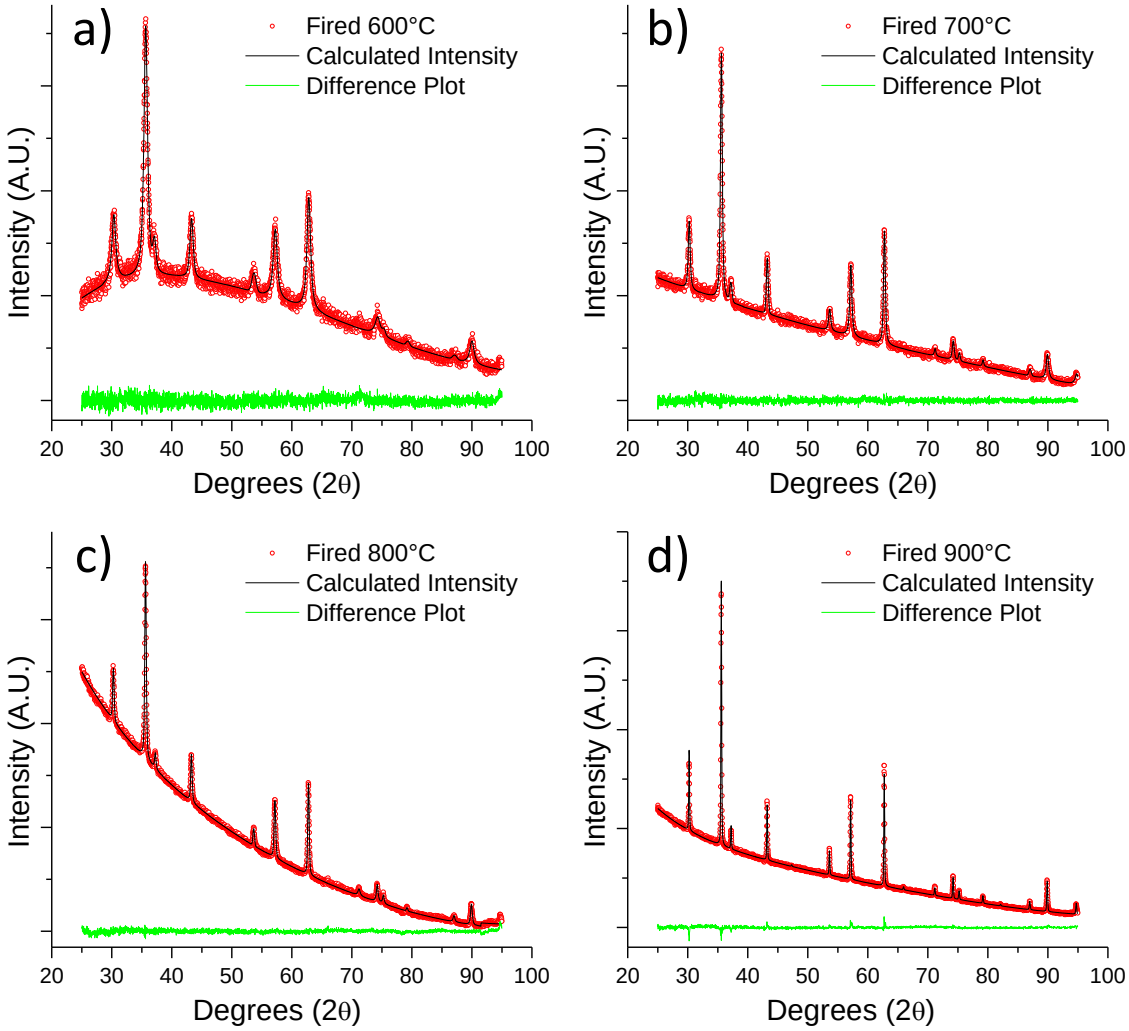

Figure 70: Pseudo-Voigt profile fit (black line) of the measured XRD diffraction patterns (red circles) with the differences between the two plots shown in green for the $CoFe_2O_4$ replicas fired at a peak temperature of: a) 600°C, b) 700°C, c) 800°C, or d) 900°C for 2 h.

sample. For the 600°C samples, individual nano-particles were too fine to allow for unambiguous nano-particle size determination. Figure 75 and Table 10 provides the average crystallite values measured by XRD analyses and the average particle size values measured by SEM analyses. While there are differences between the XRD and SEM results, possibly due to grain size differences on the spine tips vs. within the $CoFe_2O_4$ wall of the hollow replica particles and due to the partial exposure of the grains on the surface, both analytical methods indicated an increase in crystallite size with increasing peak firing temperature.

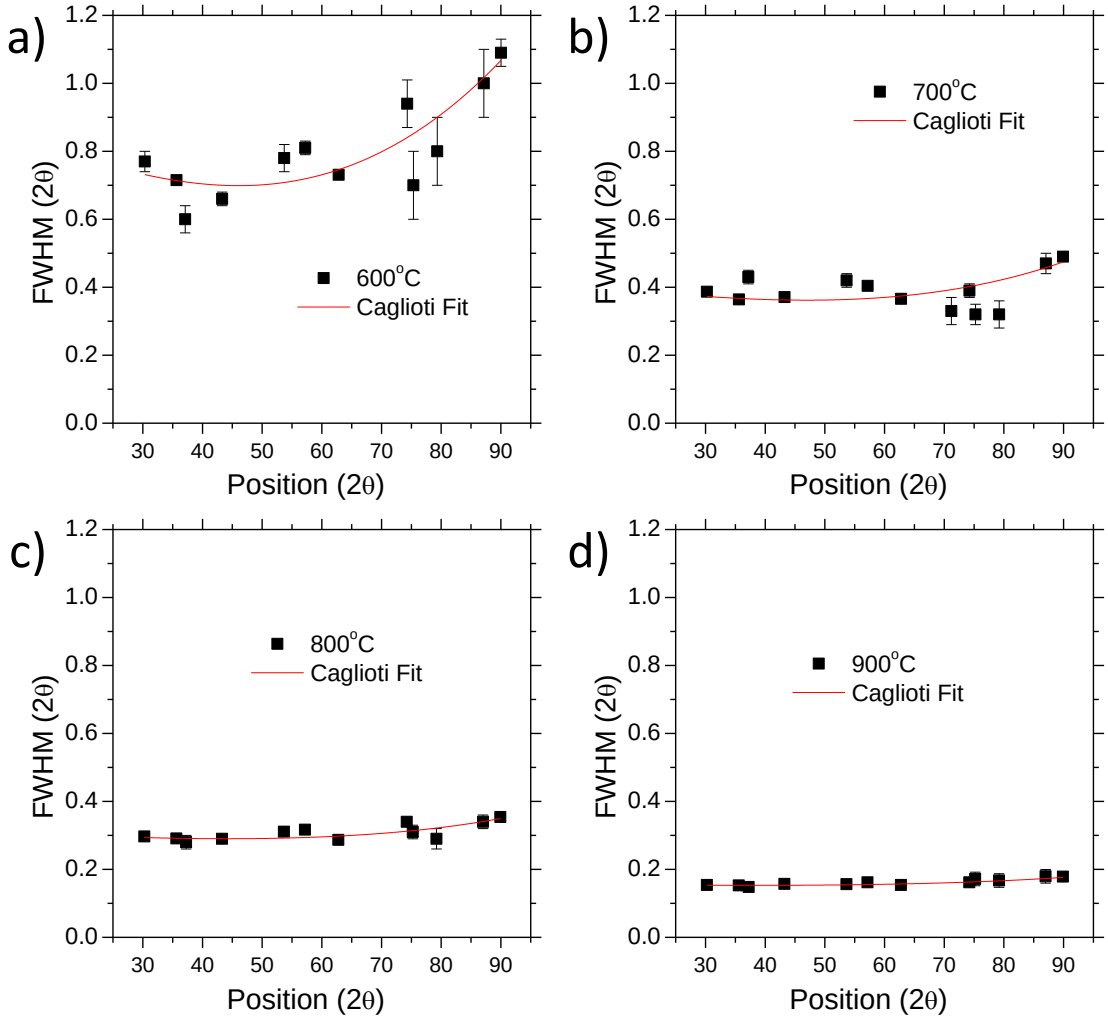

Figure 71: Caglioti fit to the FWHM values of each diffracted peak for specimens fired for 2 h at a peak temperature of: a) 600°C, b) 700°C, c) 800°C, or d) 900°C.

Table 8: Caglioti fit to the FWHM values of each diffracted peak for specimens fired for 2 h at a peak temperature of: a) 600ºC, b) 700ºC, c) 800ºC, or d) 900ºC.

Sample Firing Temperature	Fitted line	Chi^2 value
600ºC	$0.8(3) - 1(1)*\tan(\theta) + 2(1)*\tan(\theta)^2$	0.152
700ºC	$0.29(7) - 0.6(2)*\tan(\theta) + 0.5(2)*\tan(\theta)^2$	0.0125
800ºC	$0.09(3) - 0.0(1)*\tan(\theta) + 0.07(8)*\tan(\theta)^2$	0.00124
900ºC	$0.025(3) - 0.009(8)*\tan(\theta) + 0.016(7)*\tan(\theta)^2$	0.0000106

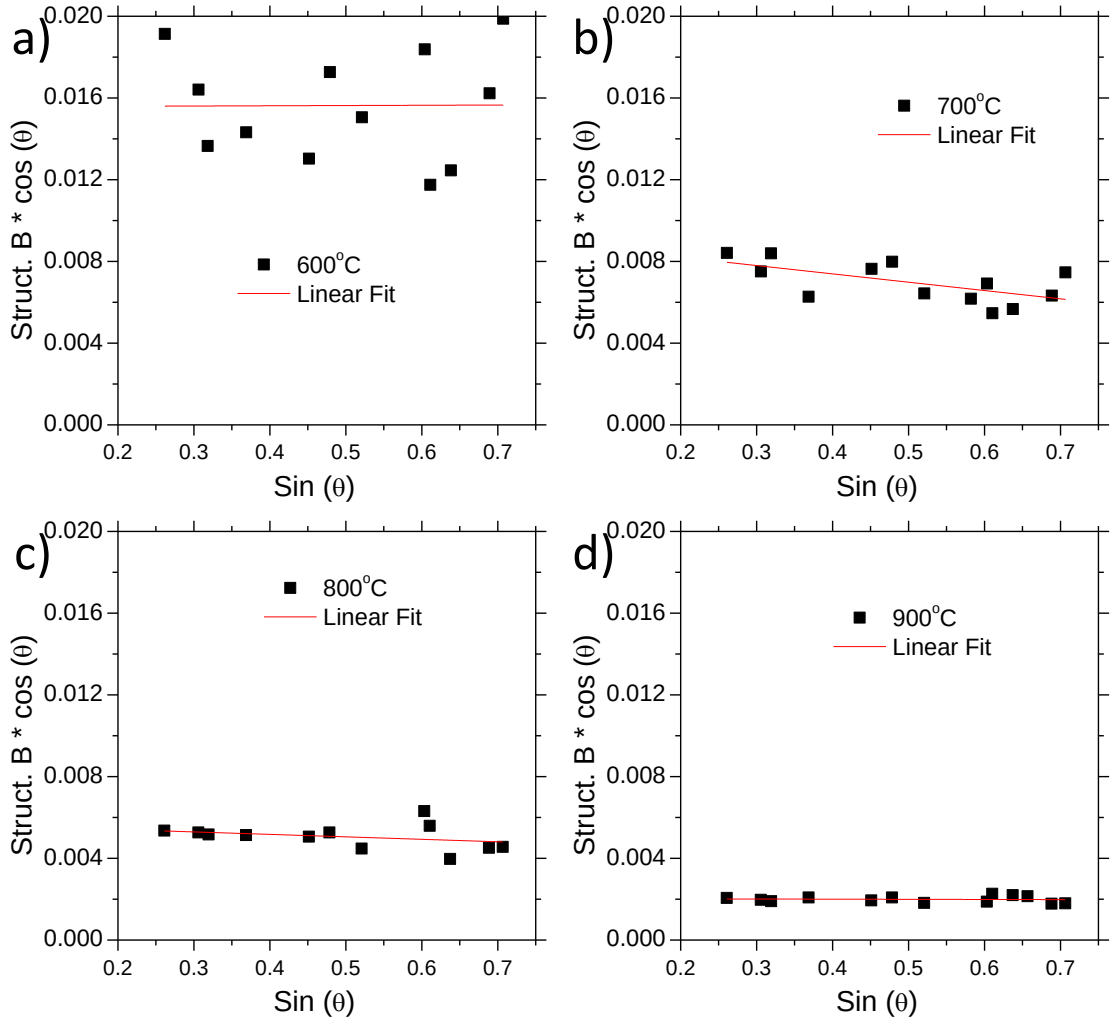

Figure 72: Williamson-Hall plots used to obtain the ACS for $CoFe_2O_4$ replicas exposed to different peak firing temperatures. The ACS values were found to be: a) 10 ± 2 nm for samples fired at a peak temperature of 600ºC for 2 h, b) 18 ± 2 nm for samples fired at 700ºC for 2 h, c) 27 ± 3 nm for samples fired at 800ºC for 2 h, and d) 75 ± 6 nm for samples fired at 900ºC for 2 h.

Table 9: Williamson-Hall plots fitting data used to obtain the crystallite size for $CoFe_2O_4$ replicas exposed to different peak firing temperatures.

Sample Firing Temperature	Fitted line	Chi^2 value
600ºC	0.016(3) + 0.00(5) sin(θ)	0.259
700ºC	0.0087 (9) - 0.0034(2) sin(θ)	0.0261
800ºC	0.0056(4) - 0.0012(2) sin(θ)	0.0121
900ºC	0.0021(2) + 0.000(9) sin(θ)	0.00098

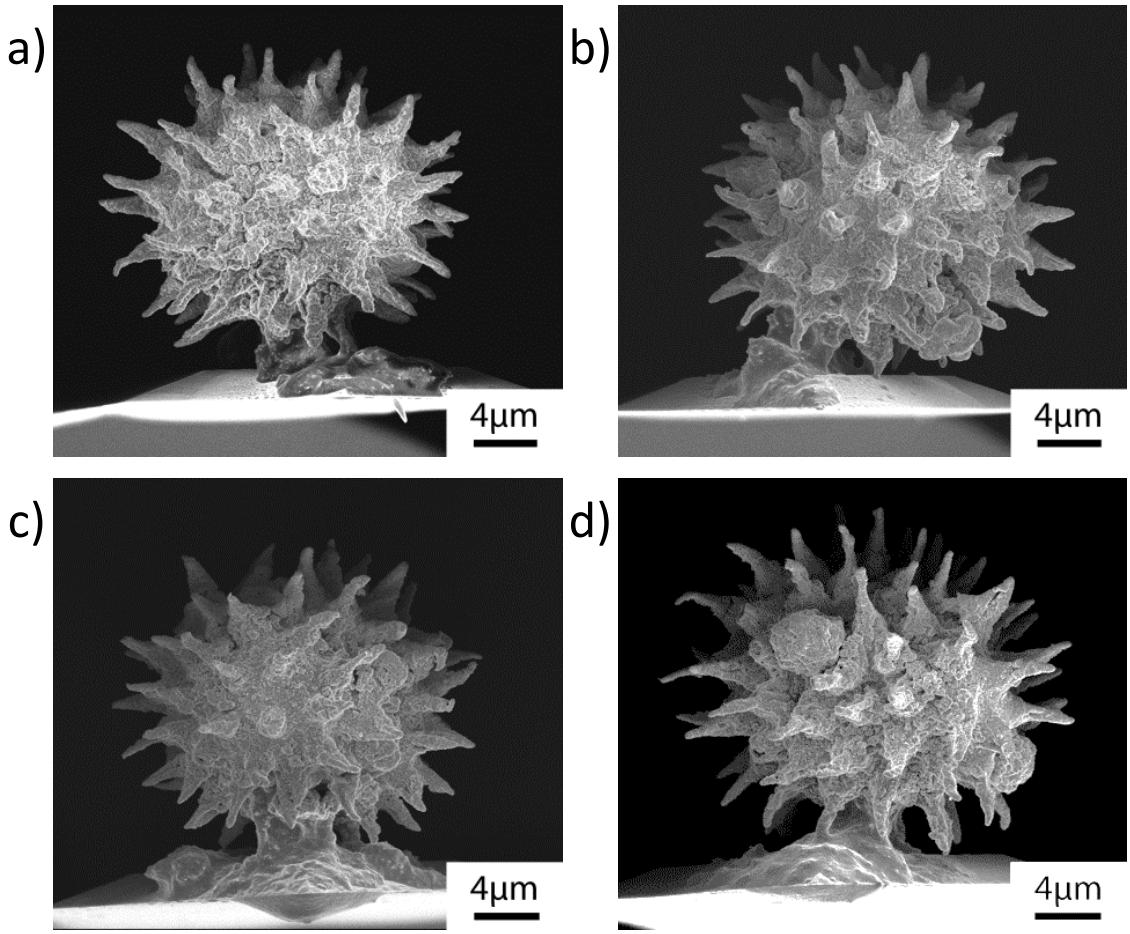

Figure 73: SE images of single-particle-bearing cantilever probes containing $CoFe_2O_4$ sunflower pollen replicas fired in air for 2 h at a peak temperature of a) 600°C, b) 700°C, c) 800°C, or d) 900°C.

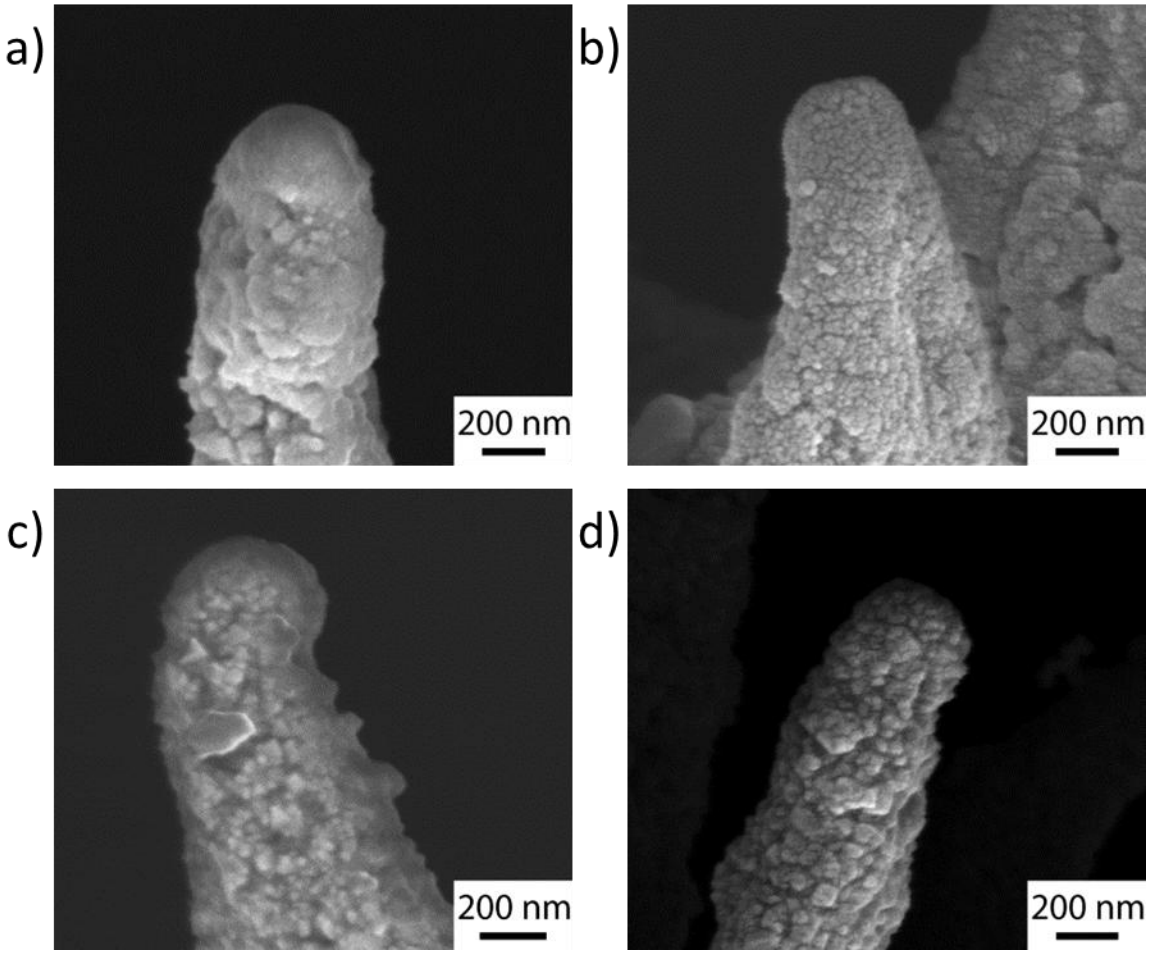

Figure 74: SE images of spike tips for single-particle-bearing cantilever probes containing $CoFe_2O_4$ sunflower pollen replicas fired in air for 2 h at a peak temperature of: a) 600°C, b) 700°C, c) 800°C, or d) 900°C.

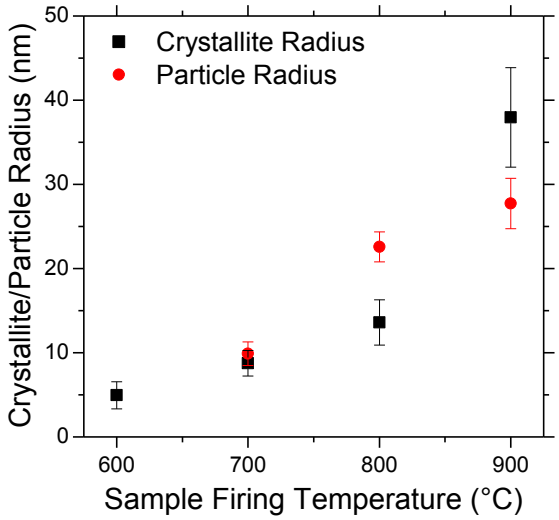

Figure 75: The crystallite/nano-particle radius as determined from XRD (black) and SEM (red) analyses for $CoFe_2O_4$ pollen replicas fired in air for 2 h at a peak temperature in the range of 600-900ºC.

Table 10: Radii of crystallites on/in $CoFe_2O_4$ sunflower replicas fired at various peak temperatures (2 h). XRD radii refer to average crystallite radii for the entire sample, and SEM radii reefer to the particle radii measured on the external surfaces of individual replica spines.

	Sample Firing Temperature			
	600ºC	700ºC	800ºC	900ºC
XRD Radius (nm)	5 ± 2	9 ± 2	14 ± 2	38 ± 6
SEM Radius (nm)	NA	10 ± 1	18 ± 2	21 ± 3

3.4.3. Magnetic Properties of $CoFe_2O_4$ Pollen Replicas

The magnetic hysteresis behavior of the $CoFe_2O_4$ replicas with varying grain size was examined with a SQUID magnetometer at room temperature (300 K) via active temperature control and at 5 K. As shown in Figure 76 and Figure 77, distinct magnetic hysteresis loops, consistent with ferrimagnetic materials, were obtained for all samples at 5 K and 300 K, respectively. The values of saturation magnetization (M_s) of the fired replicas at 5 K were 58 Am^2/Kg, 67 Am^2/Kg, 78 Am^2/Kg, and 85 Am^2/Kg and at 300 K were 53 Am^2/Kg, 60 Am^2/Kg, 72 Am^2/Kg, and 80 Am^2/Kg for samples fired at a peak temperature of 600°C, 700°C, 800°C, or 900°C, respectively. The values of remanent magnetization (M_r) (the magnetization values of the fired replicas retained after the applied field was removed) at 5 K were 38 Am^2/Kg, 46 Am^2/Kg, 52 Am^2/Kg, and 54 Am^2/Kg and at 300 K measurements were 9 Am^2/Kg, 20 Am^2/Kg, 27 Am^2/Kg, and 30 Am^2/Kg for samples fired at peak temperature of 600°C, 700°C, 800°C, or 900°C, respectively. The values of coercive field (H_c) (the minimum magnetic field required to switch the magnetic moment of the $CoFe_2O_4$ replicas to the direction of the applied field) at 5 K were 1.35 T, 1.22 T, 1.08 T, and 0.45 T, and at 300 K were 0.0490 T, 0.0885 T, 0.0940 T, and 0.0619 T, for samples fired at 600°C, 700°C, 800°C, or 900°C,

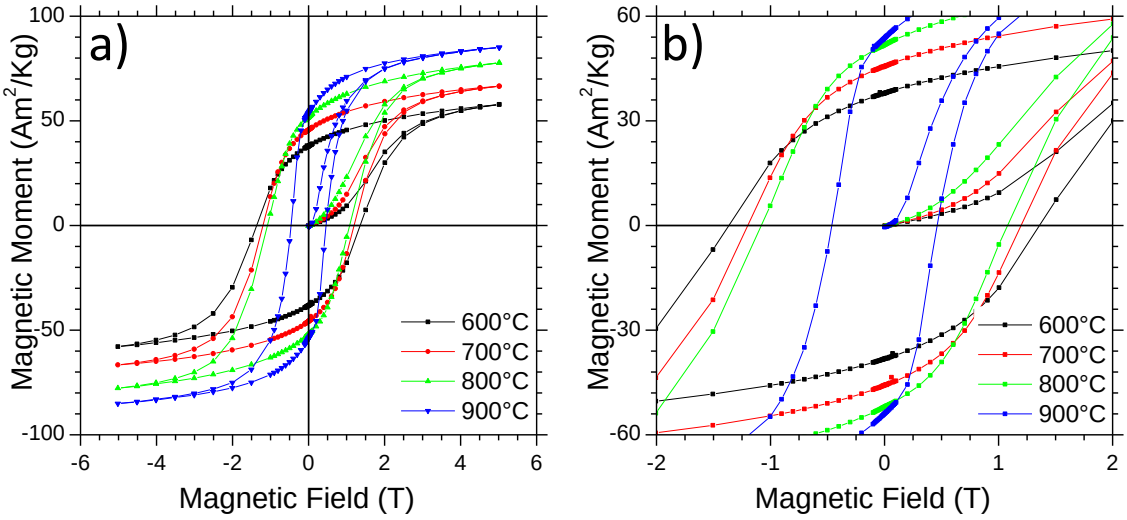

Figure 76: Superconducting Quantum Interference Device (SQUID) analyses conducted at 5 K for $CoFe_2O_4$ sunflower replicas synthesized at various peak reaction temperatures. a) Entire plots and b) magnified sections.

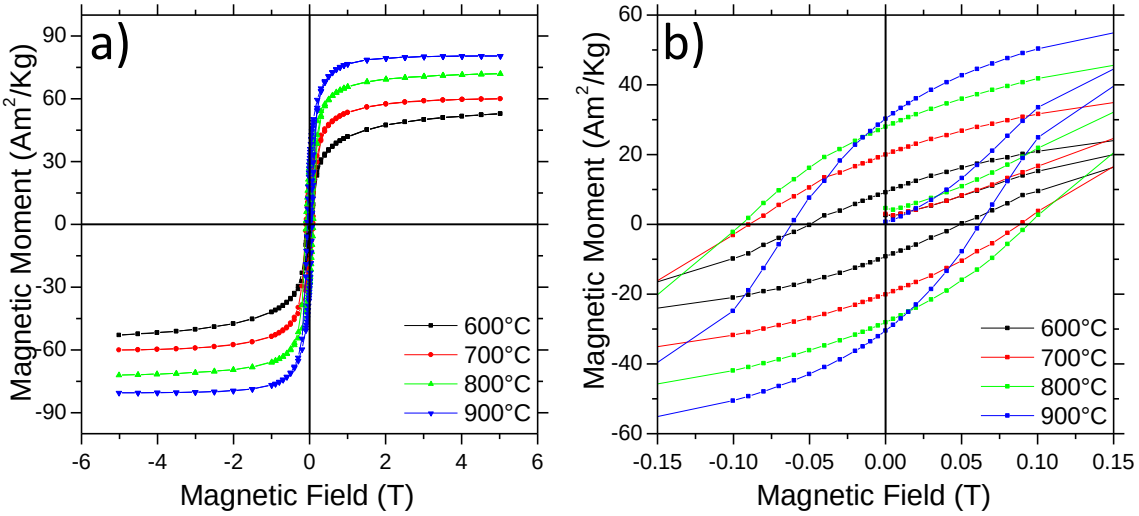

Figure 77: Superconducting Quantum Interference Device (SQUID) analyses conducted at 300 K for $CoFe_2O_4$ sunflower replicas synthesized at various peak reaction temperatures. a) Entire plots and b) magnified sections.

respectively. For both room temperature and 5 K measurements, the remanent magnetization (M_r) and magnetic saturation (M_s) values increased with increased peak firing temperature. The increase in saturation magnetization values for $CoFe_2O_4$, as a function of crystallite size (firing temperature) has been reported previously [66, 67] and a comparison between the values this work and reported values in the literature is provided in Figure 78. The referenced magnetic saturation values were obtained from

nanoparticles synthesized at room temperature by either a solution precipitation reaction or prepared by a redox process. (Note: the experiments and results described in section 3.4.3 were planned, performed, and analyzed in collaboration with Dr. Dan Sabo, Georgia Institute of Technology, Atlanta, GA, USA.)

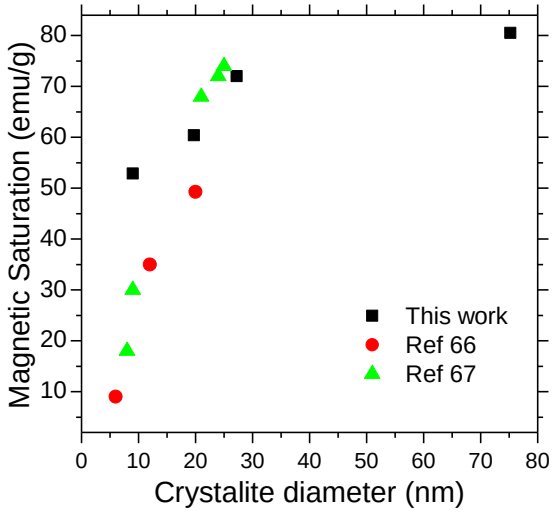

Figure 78: Magnetic saturation values as a function of crystallite diameter for this work (black), ref [66](red), and ref [67] (green).

3.4.4. Van der Waals Adhesion Measurements

In order to determine, and then model, the influence of the average crystal/particle size of $CoFe_2O_4$ pollen replicas on short-range van der Waals (VDW) attraction, contact mode AFM measurements were conducted to measure the force of adhesion of $CoFe_2O_4$ sunflower replica particles (attached to AFM cantilevers) to three different planar metallic substrates: Ni, Au, and Cu films on a silicon wafer. The measured roughness of all substrates fell within the range of 0.9-1.1 nm (Table 11). Plots of the measured average VDW adhesion force to such metallic substrates, as a function of surface nano-particle size (as measured from SEM analyses of the 700-900°C samples) and crystallite size (as measured from XRD for the 600-900°C samples) for the $CoFe_2O_4$ replicas are presented in Figure 79 a and b respectively.

Table 11: Average surface roughness (Ra, in nm) of metallic films on a silicon wafer (1µm x 1µm)

Au	Cu	Ni
1.1 ± 0.2	0.9 ± 0.2	0.9 ± 0.3

The values of average particle radii shown in Figure 79 a were obtained by SEM analyses of the nanoparticles at the surfaces of the spine tips of $CoFe_2O_4$ replicas annealed in air for 2 h at a peak temperature in the range of 700-900°C (note: the nano-particles present on the surfaces of replicas annealed at 600^oC were too fine to allow for unambiguous SEM analyses of particle size). Each SEM-derived value of average particle radius was obtained from measurements of >60 particles located at the spine tips of 3 similar replica particles. The values of average crystal radii shown in Figure 79 b were obtained by least-squares fitting of the Williamson-Hall plots for XRD peaks from $CoFe_2O_4$ replicas annealed for 2 h at a peak temperature in the range of 600-900°C. The plots in Figure 79 reveal a similar non-monotonic trend for all three metallic substrates; that is, the average adhesion force initially decreased with increasing crystal/nano-particle size, reached a minimum value at crystal/nano-particle radii of 14/18 nm (samples fired at a peak temperature of 800°C), and then increased with further increases in crystal/particle radii. Previous work has indicated that crystallite size played a role in the short range VDW adhesion of sunflower ceramic replicas (Fe_2O_3 and Fe_3O_4).[34] The reported adhesion values were consistent with the contact of one or two nanocrystals (average crystallite radii, 17~18 nm) located at the spine tips with the substrates as evaluated by a simple (sphere-on-plate) Hamaker equation.

The nonlinear behavior in the present case has been further evaluated with the use of the following simple Hamaker equation for the adhesion force between a sphere and a plate:[68]

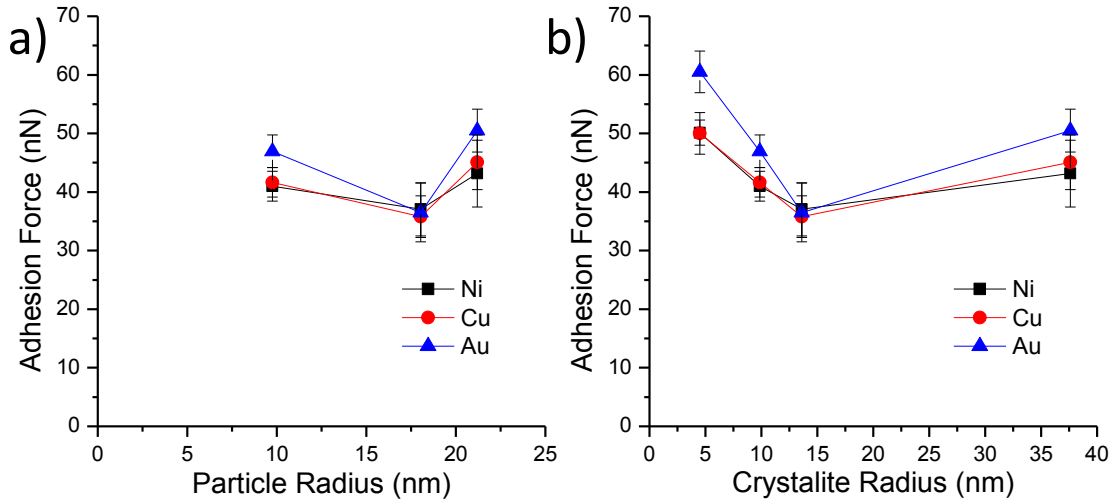

Figure 79: AFM measurements of the short-range VDW-based adhesion force for $CoFe_2O_4$ sunflower replicas of various: a) surface nanoparticle radii (from SEM analyses) and b) crystallite radii (from XRD analyses) on metallic substrates. The error bars indicate 95% confidence intervals.

$$F_{vdw} = -\frac{A_{132}}{24R}\left(\frac{2}{x} - \frac{1}{x^2} - \frac{2}{x+1} - \frac{1}{(x+1)^2}\right) \quad (3.10)$$

where A_{132} is the nonretarded Hamaker constant of material 1 (metal substrate) interacting with medium 2 ($CoFe_2O_4$) across a medium 3 (air); R is the contact radius of the sphere (or spherical nano-particle/crystal); x = D/2R; and *D* is the closest cutoff separation distance for the VDW interaction (≈0.165 nm).[69] An approximate value of A_{132} (≈ 3.29 X 10^{-19} J) for $CoFe_2O_4$ sunflower pollen replicas on the metal substrates was calculated by using the following equation [69]:

$$A_{132} \approx \left(\sqrt{A_{11}} - \sqrt{A_{33}}\right)\left(\sqrt{A_{22}} - \sqrt{A_{33}}\right) \quad (3.11)$$

with A_{11} (≈ 4 X 10^{-19} J)[69] and A_{22} (≈ 4 X 10^{-19} J)[70] values obtained from the literature, and with the assumption that A_{33} = 0. The value of F_{vdw} predicted by the Hamaker equation 3.10 should be linearly proportional to R for cases when D is much smaller than 2R (i.e., for these cases, the second term on the right side of this equation, $A_{132}R/6D^2$, becomes dominant). For contact radii in the range of values of the measured crystal/particle radii shown in Figure 79, the predicted values of the VDW adhesion force

associated with such a single crystal/nanoparticle contact are shown in Figure 80. The predicted monotonic increase in the adhesion force with single contact radius shown in this figure was not consistent with the non-monotonic change in the measured adhesion force with crystal/nano-particle radius (Figure 79).

The Hamaker equation (3.10) was then used to extract values of the effective contact radius (R_H) for each sample from measured adhesion force values. The ratio of the effective contact radius to the measured surface nano-particle radius (R_P) or crystal radius (R_C) is plotted against the measured nano-particle or crystal radius in Figure 81. An R_H/R_P or R_H/R_C ratio of unity would be consistent with adhesion via contact of a single nano-particle or crystal. As seen in Figure 81, the extracted value of R_H (15 nm) agrees reasonably well with the values of R_P = 18 nm and R_C = 14 nm (i.e., the measured force values of 35-38 nN for these nano-particle/crystal radii were close to the predicted force values of 27-36 nN). However, the extracted values of R_H were noticeably different from the measured values of R_P and R_C for samples with average crystal/nano-particle radii below and above 14/18 nm.

As illustrated in Figure 82 for a curved surface containing fine crystals/nano-particles (assumed simplistically to be spherical in shape with uniform radii of R_S), the number of crystals/nano-particles located within the VDW interaction region with the substrate will be depend on the size of the crystals/nano-particles. At a sufficiently large crystal/nano-particle size, the effect of multiple contact points becomes negligible and a curved surface with only a single contact point may be used to describe the short-range van der Waals attraction. As shown in Figure 80, such a single-contact model leads to a

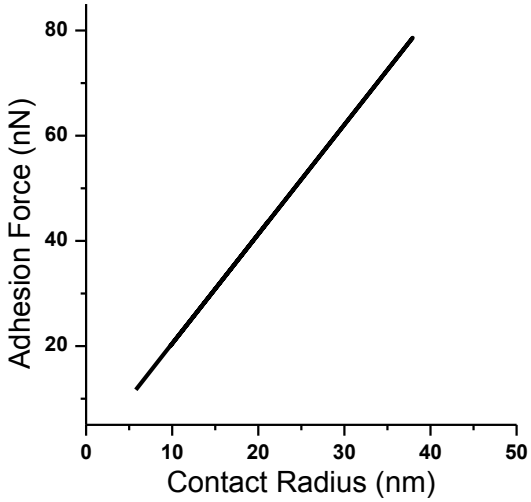

Figure 80 Estimated short-range VDW-based adhesion force as a function of contact radius for the case of a single particle contact.

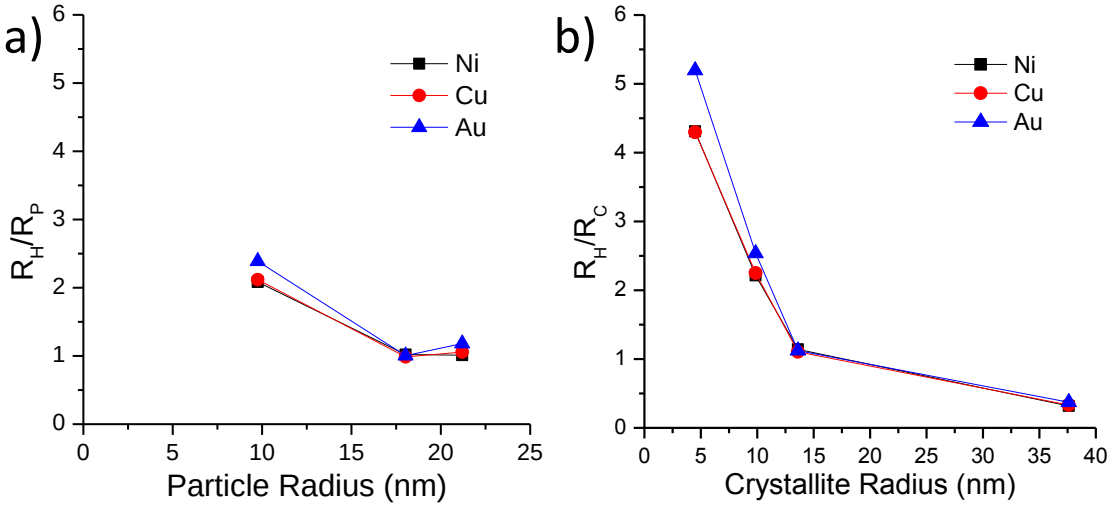

Figure 81: The ratio between the contact radius derived from the Hamaker constant (R_H) and measured a) nano-particle radius (R_P) and b) crystallite radius (R_C) vs. the nano-particle or crystal radius.

monotonic increase in the adhesion force with an increase in the crystal/nano-particle radius. However, for smaller R_S values, the adhesion force resulting from multiple contacts may be appreciable, so that an increase in VDW force may be observed with a decrease in the size of the crystals/nano-particles (and a corresponding increase in the number of effective contact points) on the curved surface. Hence, a VDW adhesion model that takes into account the number of contacts, and the radius of curvature of a

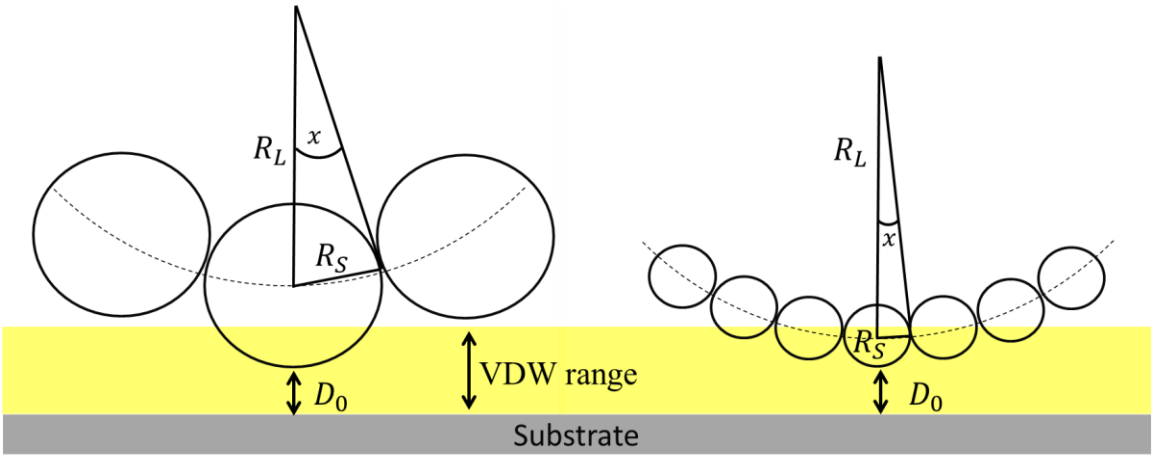

Figure 82: 2-D Diagram illustrating the multiple contact effect (an assembly of symmetrical small spheres comprising a larger hemisphere of radius R_L)

given contact, is needed.

A multi-contact model, utilizing the simple geometry illustrated in Figure 83, has been developed over the past year to describe the VDW adhesion of a nanocrystalline hemispherical shell (mimicking a $CoFe_2O_4$ pollen replica spine tip) interacting with a flat surface (a metal substrate). The shell was assumed to be comprised of multiple layers of symmetrically-arranged spherical particles with the total number of spheres comprising the n^{th} layer given by nx6. The radius of the hemisphere (R_L) was set at 200 nm, based on the measured (SEM) average spine (echini) radius of the $CoFe_2O_4$ replicas (198.8 ± 19.7 nm, Table 12). For a given layer of nano-particles, the separation distance of a given nano-particle from a planar substrate is given by:

$$D_m = D_0 + \sum_{m=1}^{i} 2R_S * \sin(x(2m-1)) \qquad (3.12)$$

where D_0 is the closest cut off distance for the VDW interaction (≈0.165 nm), R_S is the radius of each sphere, m is an integer labeling a given particle position relative to the particle of closest contact (for the latter particle, m = 0), and x refers to the angle shown in Figure 83 (calculated by $\arcsin[R_S/R_L]$). As R_S decreases, the number of spherical nano-particles in the VDW interaction zone (illustrated in yellow in Figure 83), increases

exponentially (Figure 84). By substituting D_m for x ($\approx D_m/2R$) in equation (3.12), the VDW force of attraction between the m^{th} sphere and the substrate can be calculated. The attraction force of multiple particles in the hemisphere can then be obtained by summing the forces for all of the spheres in the VDW interaction zone. This model yields a non-monotonic force of adhesion with increasing nano-particle size, as shown in Figure 85, which is qualitatively consistent with the experimental data in Figure 79. This model suggests that an initial decrease in the force of adhesion with particle radius was primarily due to a reduction in the number of nano-particles (contact points) within the VDW interaction zone. Above a certain particle radius (≈7 nm in Figure 85), however, the influence of the size of the individual nano-particles on the total adhesion force begins to dominate, so that the total adhesion force increases with nano-particle radius.

While this multi-contact model does explain the general behavior observed in Figure 79, it does not yet provide an accurate quantitative prediction of such experimental behavior. Likely sources of error include: i) the assumption of a perfect spherical nano-particle shape, ii) the assumption of a perfectly hemispherical spine tip, and iii) the

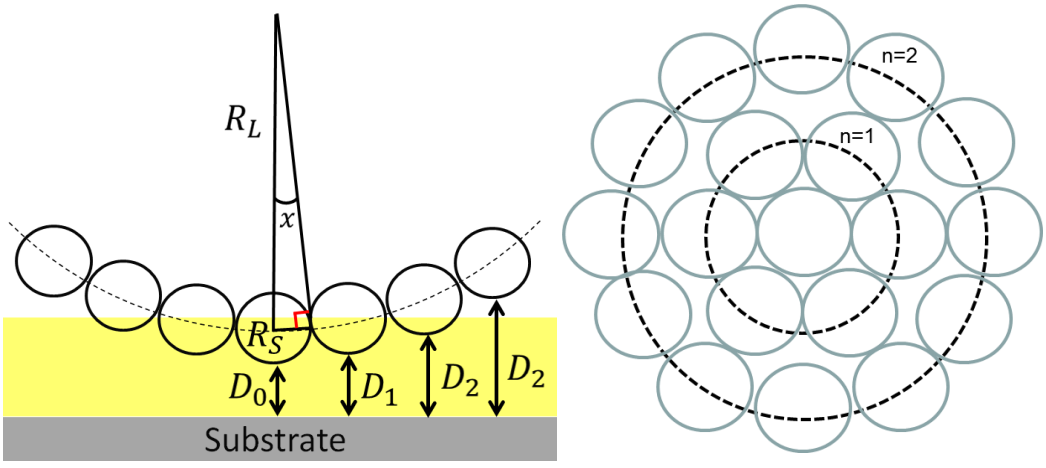

Figure 83: Diagrams illustrating the multiple contact effect (an assembly of symmetrical small spheres comprising a larger hemisphere)

assumption of a symmetrical arrangement of spherical nano-particles. The model does, however, provide initial insight as to the general relationship between the number and size of crystallites/nanoparticles and the short range VDW adhesion. While further work is needed to better understand the quantitative relationship between surface particle size and short-range VDW interactions, the data to date indicate that such short range adhesion may be tailored by controlling the oxide crystal/nanoparticle size. (Note: the experiments and results described in Section 3.4.4 were planned, performed, and analyzed in collaboration with Donglee Shin, Georgia Institute of Technology, Atlanta, GA, USA.)

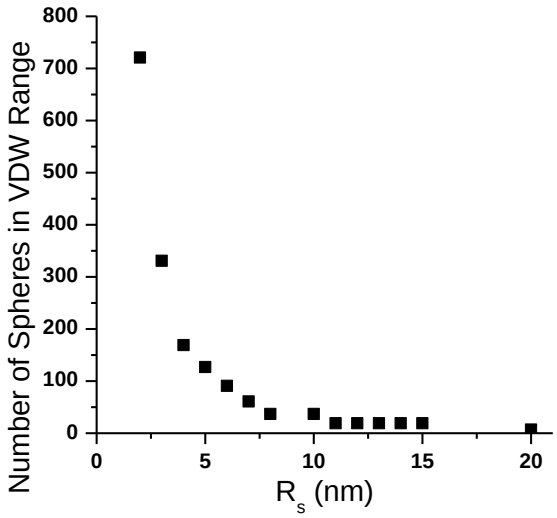

Figure 84: Number of small spheres within the VDW interaction zone for various radii of the small spheres (R_s).

Table 12: Replica spine tip radii obtained from SEM analyses of each sample, and the combined average of all samples. Error ranges refer to ± 95% confidence levels.

	600°C	700°C	800°C	900°C	Average
Radius (nm)	184.9 ± 9.7	191.1 ± 12.2	211.5 ± 7.4	201.5 ± 4.5	197.8 ± 19.7

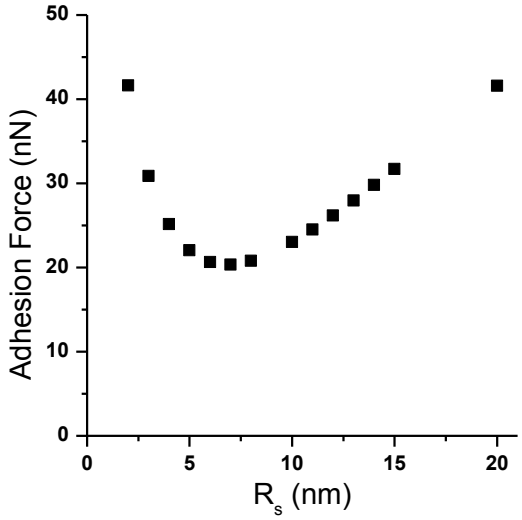

Figure 85: Summation of adhesion forces of multiple small spheres located within the VDW interaction zone.

3.4.5. Long Range Magnetic Attraction

To investigate the effect of crystallite size on the longer-range magnetic force, the attraction forces between various crystallite-sized $CoFe_2O_4$ sunflower replicas and a permanent magnet Ni-Nd substrate were measured by AFM. The force measurements were conducted at a lateral distance ~300 μm from the outer edge of the disk-shaped Ni-Nd magnet and measured at height intervals of 50 μm from the surface. The measured attraction forces for the 600°C, 700°C, 800°C, and 900°C samples are shown in Figure 86. This figure revealed a monotonic increase in the measured magnetite force of attraction with peak firing temperature which, in turn, was consistent with an increase in the ACS with peak firing temperature (Figure 75). Such an increase in magnetic force with average crystal size was consistent with the measured increase in the values of magnetization (at a given applied magnetic field) with crystal size of the $CoFe_2O_4$ replicas (Figure 77). The magnetic attractions forces were then fitted via use of the following equation:

$$F_m = \mu_0 V_m M \frac{\partial \mathrm{H}}{\partial \mathrm{Z}} \hat{Z} \tag{3.13}$$

where V_m (m^3/particle) is the solid volume of magnetic material within the replica particle, z is the unit vector parallel to the z (height) direction, μ_0 is permeability of free space (1.26 $\mu N/A^2$), M (Am^{-1}) is the magnetization, and H (Am^{-1}) is the magnetizing field. Using the validated simulation for the position dependence of $\partial H/\partial z$ (described in section 2.4.7.), measurements of the magnetic force-distance behavior of a given $CoFe_2O_4$ pollen replica was used, along with knowledge of the magnetization, *M* (from the data in Figure 77), to calculate the volume of $CoFe_2O_4$, V_m, present within the replica via equation (3.13). That is, each force measurement obtained at a given distance from the Ni-Nd substrate for a particular $CoFe_2O_4$ pollen replica was used to obtain a V_m value. The V_m values obtained over a range of distances for a given $CoFe_2O_4$ pollen replica were then used to obtain an average V_m value for that replica.

The average magnetic volumes determined in this manner for the $CoFe_2O_4$ replicas are shown in Table 13 (note: the calculated V_m values for each of the $CoFe_2O_4$ samples were all within 7% of the average volume for all of these samples, 424.0 μm^3). The calculated volumes were expected to be very similar to each other, as the same pollen species and coating process were used for each sample. However, the variance in pollen grain size (and surface area) can lead to non-uniform total mass deposition on each pollen grain, which could have led to the slight differences in calculated magnetic volumes for each sample. These average V_m values were re-inserted into equation (3.13) to obtain the F_m vs. distance curves shown along with the data in Figure 86. As can be seen in this figure, the fits of the calculated curves to the data were quite good, which indicated that such a model of magnetic adhesion was reasonable.

Control over the average crystal/nano-particle size of the nanocrystalline $CoFe_2O_4$ pollen replicas, through adjustment of the peak firing temperature, provided a means for controlling both the short-range (VDW) and long-range (magnetic) forces of attraction. To reveal the extent to which the total force of attraction (short-range + long-range) of the $CoFe_2O_4$ pollen replicas could be tailored relative to the native (cleaned) sunflower pollen, the total attraction of such pollen replicas and native pollen to the magnetic substrate is shown in Figure 87. The total force of adhesion of the $CoFe_2O_4$ replicas to the Ni-Nd substrate could be increased by a factor of ~3 (for a peak firing temperature of 900^{o}C) relative to the native pollen grains. (Note: the experiments and results described in section 3.4.5 were developed and conducted in collaboration with Donglee Shin, Georgia Institute of Technology, Atlanta, GA, USA.)

Table 13: Magnetization values used in the magnetic fitting model and the calculated volume for each sample.

Firing temperature	600°C	700°C	800°C	900°C
Magnetization (Am^2/Kg)	33.08	44.55	56.72	67.97
Calculated Volume (μm^3)	397.64	429.09	452.47	416.64

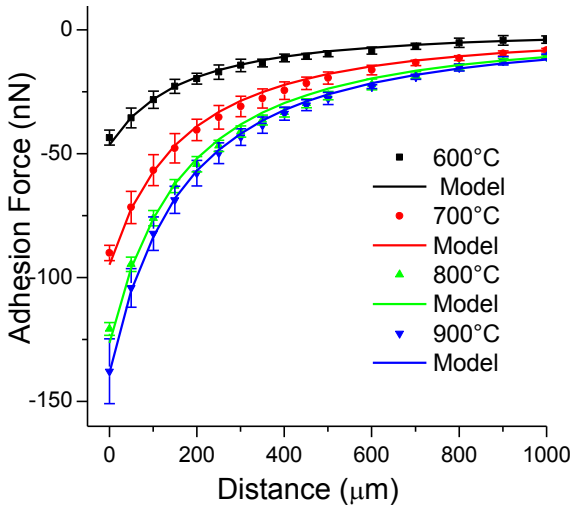

Figure 86: AFM measurement of the magnetic adhesion force vs. distance for $CoFe_2O_4$ sunflower replica probe on a Ni-Nd substrate (dots) fitted with a magnetic model (line). The force was obtained at ~300 μm from the edge of the disk-shaped Ni-Nd substrate.

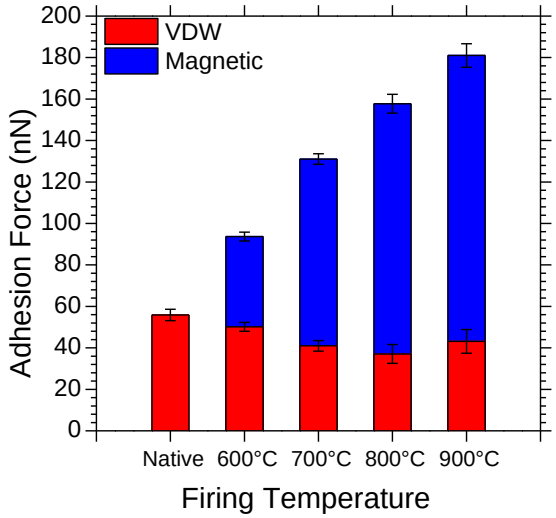

Figure 87: Combined short range (VDW) and short to long range (magnetic) adhesion for native sunflower pollen and sunflower pollen replicas.

3.4.6. Metallic Pollen Replicas

Fe-Co alloys exhibit significantly higher values of magnetic saturation (σ_s) at room temperature than most other known materials. Compositions near 30 wt% Co yield the highest values for σ_s (Figure 88**)**. The coercive field is similar to that of soft ferrites, such as magnetite, but the magnetic saturation can be about an order of magnitude larger. The conversion of Fe-Co oxide replicas into Fe-Co alloy replicas was examined. The Fe-Co inverse spinel replicas were exposed to a flowing (flow rate of 30 cm^3min^{-1}) 2% H_2/98% Ar gas mixture then heated at 1.5°C/min to 550°C and held at this temperature

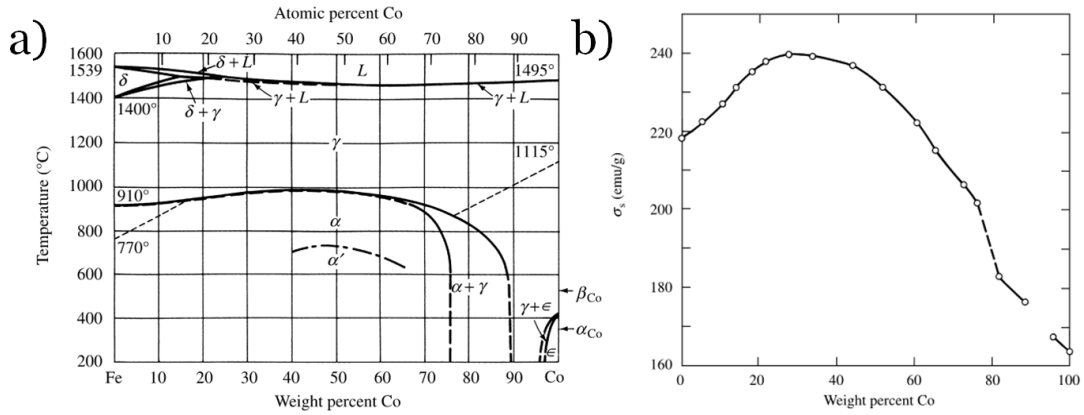

Figure 88: a) Phase diagram for Fe-Co alloys and b) plot of σ_s vs. weight % Co.[71]

for 2 h. This reducing thermal treatment resulted in complete conversion of the $CoFe_2O_4$ into $CoFe_2$, as confirmed by the XRD analysis in Figure 89. Scherrer analysis yielded an ACS of 42 ± 2 nm for the $CoFe_2$ replicas. SEM images (Figure 90) confirmed that the overall size and shape of the pollen grains were preserved with the reduction process. While the cobalt-iron replicas did maintain the general shape and morphology as the as-coated pollen grains, they were not mechanically robust enough for adhesion measurements (i.e., the $CoFe_2$ replicas shattered during attempts to attach the replicas to an AFM cantilever tip). Further investigation is required in order to synthesize more robust replicas for adhesion-based measurements.

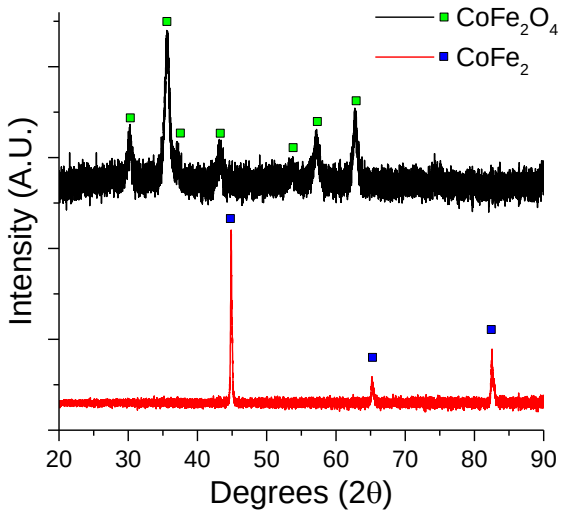

Figure 89: XRD analyses of: (black) $CoFe_2O_4$ pollen replicas after firing in air at a peak temperature of 600°C for 4 h and (red) $CoFe_2$ replicas after reduction of $CoFe_2O_4$ replicas vis exposure to flowing 2%H_2/ 98%Ar for 2 h at 550°C.

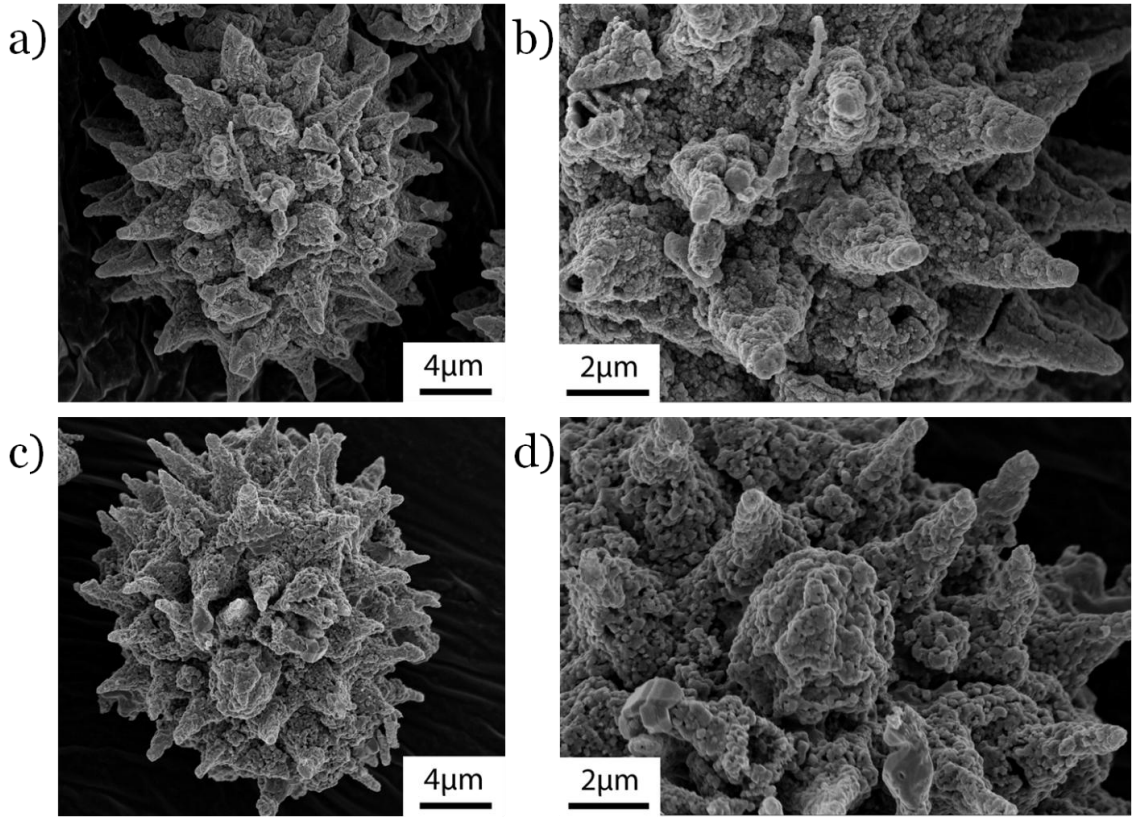

Figure 90: SE images of a, b) $CoFe_2O_4$ inorganic replicas of *H. Annuus* sunflower pollen particles prepared with Fe:Co SSG cycle ratios of 2:1 and with thermal treatments in air at a peak temperature of 600°C for 4 h. c, d) $CoFe_2$ replica after reduction in 2%H_2/ 98%Ar at 550°C for 2 h.

3.5. *Concluding Remarks*

This work demonstrates that a highly-conformal SSG-coating process can be used, along with controlled thermal treatments, to convert sunflower pollen particles into nanocrystalline ferrimagnetic ($CoFe_2O_4$) replicas exhibiting controlled multimodal adhesion via short-range (~10 nm) VDW-based attraction and short-to-long-range (up to ~1 mm) magnetic attraction. An increase in crystallite size, from higher temperature thermal treatments, resulted in increases in the values of both remanent and saturation magnetization. The improved magnetic properties led to a detectable increase in long range attraction to magnetic substrate. A reproducible non-monotonic relationship was also observed between average $CoFe_2O_4$ crystal size and short-range VDW adhesion. The

crystallite size / VDW adhesion correlation was attributed to the counteracting effects of crystal size on the VDW force of an individual crystal and on the number of crystals within the VDW interaction zone. This tendency was explained by the Multi-Sphere Hamaker model. The long-range magnetic force was also tailored by adjusting the average crystal size, because an increase in grain size resulted in an increase in the magnetization of the replicas. The measured long-range force behavior agreed well with the Sphere-Plane magnetic force model. By controlling the crystallite size of the ceramic pollen replicas, both the long range (magnetic) and short range (VDW) adhesion force could be tuned.

3.6. ***References***

[1] M. L. Ott and H. A. Mizes, "Atomic force microscopy adhesion measurements of surface-modified toners for xerographic applications," *Colloids and Surfaces A: Physicochemical and Engineering Aspects,* vol. 87, pp. 245-256, 8/16/ 1994.

[2] W. Richard Bowen and T. A. Doneva, "Atomic Force Microscopy Studies of Membranes: Effect of Surface Roughness on Double-Layer Interactions and Particle Adhesion," *Journal of Colloid and Interface Science,* vol. 229, pp. 544-549, 9/15/ 2000.

[3] K. Cooper, A. Gupta, and S. Beaudoin, "Simulation of the Adhesion of Particles to Surfaces," *Journal of Colloid and Interface Science,* vol. 234, pp. 284-292, 2/15/ 2001.

[4] M. A. Meitl, Z. T. Zhu, V. Kumar, K. J. Lee, X. Feng, Y. Y. Huang, *et al.*, "Transfer printing by kinetic control of adhesion to an elastomeric stamp," *Nat. Mater.,* vol. 5, p. 33, 2006.

[5] S. Mitragotri and J. Lahann, "Physical approaches to biomaterial design," *Nat. Mater.,* vol. 8, p. 15, 2009.

[6] Y. Huang, M. Liu, J. Wang, J. Zhou, L. Wang, Y. Song, *et al.*, "Controllable Underwater Oil-Adhesion-Interface Films Assembled from Nonspherical Particles," *Advanced Functional Materials,* vol. 21, pp. 4436-4441, 2011.

[7] K. E. Fischer, G. Nagaraj, R. H. Daniels, E. Li, V. E. Cowles, J. L. Miller, *et al.*, "Hierarchical nanoengineered surfaces for enhanced cytoadhesion and drug delivery," *Biomaterials,* vol. 32, p. 3499, 2011.

[8] L. Zhang, J. Shi, Z. Jiang, Y. Jiang, R. Meng, Y. Zhu, *et al.*, "Facile Preparation of Robust Microcapsules by Manipulating Metal-Coordination Interaction between Biomineral Layer and Bioadhesive Layer," *ACS Appl. Mater. Interfaces,* vol. 3, p. 597, 2011.

[9] S. Stassi and G. Canavese, "Spiky nanostructured metal particles as filler of polymeric composites showing tunable electrical conductivity," *J. Polym. Sci., Part B,* vol. 50, p. 984, 2012.

[10] I. Lee, "Molecular Self-Assembly: Smart Design of Surface and Interface via Secondary Molecular Interactions," *Langmuir,* vol. 29, p. 2476, 2013.

[11] W. Wen, N. Wang, D. W. Zheng, C. Chen, and K. N. Tu, "Two- and three-dimensional arrays of magnetic microspheres," *J. Mater. Res.,* vol. 14, p. 1186, 1999.

[12] K. L. Johnson, K. Kendall, and A. D. Roberts, "Surface Energy and the Contact of Elastic Solids," *Proc. R. Soc. London, Ser. A,* vol. 324, p. 301, 1971.

[13] B. V. Derjaguin, V. M. Muller, and Y. P. Toporov, "Effect of contact deformations on the adhesion of particles," *J. Colloid Interface Sci.,* vol. 53, p. 314, 1975.

[14] D. Tabor, *J. Colloid Interface Sci.,* vol. 58, p. 2, 1977.

[15] V. M. Muller, V. S. Yushchenko, and B. V. Derjaguin, *J. Colloid Interface Sci.,* vol. 77, p. 91, 1980.

[16] D. Maugis and H. M. Pollock, "Surface forces, deformation and adherence at metal microcontacts," *Acta Metall.,* vol. 32, p. 1323, 1984.

[17] W. A. Ducker, T. J. Senden, and R. M. Pashley, "Direct measurement of colloidal forces using an atomic force microscope," *Nature,* vol. 353, p. 239, 1991.

[18] D. Maugis, "Adhesion of spheres: The JKR-DMT transition using a dugdale model," *J. Colloid Interface Sci.,* vol. 150, p. 243, 1992.

[19] D. Rimai, M. Dejesus, and D. Weiss, "The Effect of Surface-Adhering Nanoclusters on the Adhesion and Cohesion of Micrometer-Size Particles," *J. Adhes. Sci. Technol.,* vol. 22, pp. 529-543, 2008.

[20] E. Horn, *Trans. Kans. Acad. Sci.,* vol. 36, p. 91, 1933.

[21] W. Grater and T. Stemen, "The plant, the pollen and the patient," *Rev. Paleobot. Palynol.*, vol. 4, p. 187, 1967.

[22] L. H. Ziska, D. E. Gebhard, D. A. Frenz, S. Faulkner, B. D. Singer, and J. G. Straka, "Cities as harbingers of climate change: Common ragweed, urbanization, and public health," *J. Allergy Clin. Immunol.*, vol. 111, p. 290, 2003.

[23] P. J. Beggs, "Impacts of climate change on aeroallergens: past and future," *Clin. Exp. Allergy*, vol. 34, p. 1507, 2004.

[24] C. A. Rogers, P. M. Wayne, E. A. Macklin, M. L. Mullenberg, C. J. Wagner, P. R. Epstein, *et al.*, "Interaction of the Onset of Spring and Elevated Atmospheric CO_2 on Ragweed Pollen Production," *Environ. Health Perspect.*, vol. 114, p. 865, 2006.

[25] B. Fumanal, B. Chauvel, and F. Bretagnolle, "Estimation of pollen and seed production of common ragweed in France," *Ann. Agric. Environ. Med.*, vol. 14, p. 233, 2007.

[26] L. Ziska, K. Knowlton, C. Rogers, D. Dalan, N. Tierney, M. A. Elder, *et al.*, "Recent warming by latitude associated with increased length of ragweed pollen season in central North America," *Proc. Natl. Acad. Sci. U.S.A.*, vol. 108, p. 4248, 2011.

[27] M. D. Bajin, C. Cingi, F. Oghan, and M. K. Gurbuz, "Global warming and allergy in Asia Minor," *Arch. Oto-Rhino-Laryngol.*, vol. 270, p. 27, 2013.

[28] G. O. W. Kremp, *Morphologic Encyclopedia of Palynology*, 1968.

[29] J. W. Walker and J. A. Doyle, *Ann. Mo. Bot. Gard.*, vol. 62, p. 664, 1975.

[30] G. Erdtman, *Pollen Morphology and Plant Taxonomy*, 1986.

[31] S. Blackmore and S. H. Barnes, *Pollen and Spores: Patterns of Diversification*, 1991.

[32] A. Ressayre, B. Godelle, C. Raquin, and P. H. Gouyon, "Aperture Pattern Ontogeny in Angiosperms," *J. Exp. Zool.*, vol. 294, p. 122, 2002.

[33] M. Hesse, H. Halbritter, R. Zetter, M. Weber, R. Buchner, A. Frosch-Radivo, *et al.*, *Pollen Terminology: An Illustrated Handbook*, 2009.

[34] W. Brandon Goodwin, I. J. Gomez, Y. Fang, J. C. Meredith, and K. H. Sandhage, "Conversion of Pollen Particles into Three-Dimensional Ceramic Replicas Tailored for Multimodal Adhesion," *Chemistry of Materials*, vol. 25, pp. 4529-4536, 2013.

[35] H. Lin, I. Gomez, and J. C. Meredith, "Pollenkitt wetting mechanism enables species-specific tunable pollen adhesion," *Langmuir,* vol. 29, pp. 3012-3023, Mar 5 2013.

[36] I. Ichinose, H. Senzu, and T. Kunitake, "Stepwise Adsorption of Metal Alkoxides on Hydrolyzed Surfaces: A Surface Sol-Gel Process," *Chem. Lett.,* vol. 10, p. 831, 1996.

[37] I. Ichinose, H. Senzu, and T. Kunitake, "A Surface Sol-Gel Process of TiO_2 and Other Metal Oxide Films with Molecular Precision," *Chem. Mater.,* vol. 9, pp. 1296-1298, 1997.

[38] S. R. Hall, H. Bolger, and S. Mann, "Morphosynthesis of complex inorganic forms using pollen grain templates," *ChemComm,* pp. 2784-2785, 2003.

[39] Y. Wang, Z. Liu, B. Han, Z. Sun, J. Du, J. Zhang, *et al.,* "Replication of biological organizations through a supercritical fluid route," *ChemComm,* pp. 2948-2950, Jun 21 2005.

[40] S. R. Hall, V. M. Swinerd, F. N. Newby, A. M. Collins, and S. Mann, "Fabrication of Porous Titania (Brookite) Microparticles with Complex Morphology by Sol-Gel Replication of Pollen Grains," *Chem. Mater.,* vol. 18, pp. 598-600, 2006.

[41] P. Li, C. F. Zeng, L. X. Zhang, and N. P. Xu, *J. Inorg. Mater.,* vol. 23, p. 49, 2008.

[42] F. Cao and D. X. Li, "Morphology-controlled synthesis of SiO_2 hollow microspheres using pollen grain as a biotemplate," *Biomed Mater,* vol. 4, pp. 1-6, Apr 2009.

[43] X. Yang, X. Song, Y. Wei, W. Wei, L. Hou, and X. Fan, "Synthesis of spinous ZrO_2 core–shell microspheres with good hydrogen storage properties by the pollen bio-template route," *Scripta Materialia,* vol. 64, pp. 1075-1078, 2011.

[44] B. J. Thio, K. K. Clark, and A. A. Keller, "Magnetic pollen grains as sorbents for facile removal of organic pollutants in aqueous media," *J Hazard Mater,* vol. 194, pp. 53-61, Oct 30 2011.

[45] Y. Xia, W. Zhang, Z. Xiao, H. Huang, H. Zeng, X. Chen, *et al.,* "Biotemplated fabrication of hierarchically porous NiO/C composite from lotus pollen grains for lithium-ion batteries," *Journal of Materials Chemistry,* vol. 22, p. 9209, 2012.

[46] M. W. Anderson, S. M. Holmes, N. Hanif, and C. S. Cundy, "Hierarchical Pore Structures through Diatom Zeolitization " *Angew. Chem., Int. Ed.,* vol. 39, p. 2707, 2000.

[47] N. L. Rosi, C. S. Thaxton, and C. A. Mirkin, "Control of nanoparticle assembly by using DNA-modified diatom templates," *Angew. Chem., Int. Ed.,* vol. 43, p. 5500, 2004.

[48] C. S. Gaddis and K. H. Sandhage, "Freestanding Microscale 3-D Polymeric Structures with Biologically-derived Shapes and Nanoscale Features," *J. Mater. Res.,* vol. 19, p. 2541, 2004.

[49] J. Zhao, C. S. Gaddis, Y. Cai, and K. H. Sandhage, "Free-standing Microscale Structures of Zirconia Nanocrystals with Biologically Replicable 3-D Shapes,," *J. Mater. Res.,* vol. 20, p. 282, 2005.

[50] E. K. Payne, N. L. Rosi, C. Xue, and C. A. Mirkin, "Sacrificial biological templates for the formation of nanostructured metallic microshells," *Angew. Chem., Int. Ed.,* vol. 44, p. 5064, 2005.

[51] M. R. Weatherspoon, M. S. Haluska, Y. Cai, J. S. King, C. J. Summers, R. L. Snyder, *et al.*, "Phosphor Microparticles of Controlled 3-D Shape from Phytoplankton," *J. Electrochem. Soc.,* vol. 153, p. H34, 2006.

[52] D. Losic, J. G. Mitchell, R. Lai, and N. H. Voelcker, "Rapid Fabrication of Micro- and Nanoscale Patterns by Replica Molding from Diatom Biosilica," *Adv. Funct. Mater.,* vol. 17, p. 2439, 2007.

[53] U. Kusari, Z. Bao, Y. Cai, G. Ahmad, K. H. Sandhage, and L. G. Sneddon, "Formation of Nanostructured, Nanocrystalline Boron Nitride Microparticles with Diatom-Derived 3-D Shapes," *Chem. Commun.,* vol. 11, p. 1177, 2007.

[54] Z. Bao, E. M. Ernst, S. Yoo, and K. H. Sandhage, "Syntheses of Porous Self-Supporting Metal Nanoparticle Assemblies with 3-D Morphologies Inherited from Biosilica Templates (Diatom Frustules)," *Adv. Mater.,* vol. 21, p. 474, 2009.

[55] Y. Fang, Q. Wu, M. B. Dickerson, Y. Cai, S. Shian, J. D. Berrigan, *et al.*, "Protein-Mediated Layer-by-Layer Syntheses of Freestanding Microscale Titania Structures with Biologically Assembled 3-D Morphologies," *Chemistry of Materials,* vol. 21, pp. 5704-5710, 2009.

[56] E. Domínguez, J. A. Mercado, M. A. Quesada, and A. Heredia, "Pollen sporopollenin: degradation and structural elucidation," *Sex Plant Reprod,* vol. 12, pp. 171-178, 1999.

[57] H. E. M. Dobson, " Survey of pollen and pollenkitt lipids - chemical cues to flower visitors," *Am. J. Bot.,* vol. 75, p. 170, 1988.

[58] M. R. Weatherspoon, M. B. Dickerson, G. Wang, Y. Cai, S. Shian, S. C. Jones, *et al.*, "Thin, conformal, and continuous SnO_2 coatings on three-dimensional biosilica templates through hydroxy-group amplification and layer-by-layer alkoxide deposition," *Angew Chem Int Ed Engl,* vol. 46, pp. 5724-5727, 2007.

[59] M. R. Weatherspoon, Y. Cai, M. Crne, M. Srinivasarao, and K. H. Sandhage, "3D rutile titania-based structures with morpho butterfly wing scale morphologies," *Angew Chem Int Ed Engl,* vol. 47, pp. 7921-7923, 2008.

[60] G. Wang, Y. Fang, P. Kim, A. Hayek, M. R. Weatherspoon, J. W. Perry, *et al.*, "Layer-By-Layer Dendritic Growth of Hyperbranched Thin Films for Surface Sol-Gel Syntheses of Conformal, Functional, Nanocrystalline Oxide Coatings on Complex 3D (Bio)silica Templates," *Advanced Functional Materials,* vol. 19, pp. 2768-2776, 2009.

[61] J. P. Vernon, N. Hobbs, Y. Cai, A. Lethbridge, P. Vukusic, D. D. Deheyn, *et al.*, "3D photoluminescent lanthanide-doped barium titanate structures synthesized by coating and shape-preserving reaction of complex-shaped bioorganic templates," *Journal of Materials Chemistry,* vol. 22, pp. 10365-10940, 2012.

[62] M. J. Fransen, "On The Influence of Generator and Detector Settings in X-ray Powder Diffractometry," *Adcancs in X-ray Analysis,* vol. 48, pp. 143-149, 2005.

[63] B. D. Cullity and S. R. Stock, *Elements of X-Ray Diffraction, 3rd ed*: Prentice-Hall, Inc,, 2001.

[64] G. Caglioti, A. Paoletti, and F. P. Ricci, "Choice of collimators for a crystal spectrometer for neutron diffraction," *Nucl. Inst.,* vol. 3, pp. 223 - 228, 1958.

[65] J.I. Langford, ed. E. Prince & J.K. Stalick, NIST Spec. Pub. No. 846 (Gaithersburg MA: Dept of Commerce) pp 110-126 (1992). .

[66] M. Rajendran, R. C. Pullar, A. K. Bhattacharya, D. Das, S. N. Chintalapudib, and C. K. Majumdarc, "Magnetic properties of nanocrystalline $CoFe_2O_4$ powders prepared at room temperature variation with crystallite size," *Journal of Magnetism and Magnetic Materials,* pp. 71-78, 2000.

[67] V. Kumar, A. Rana, M. S. Yadav, and R. P. Pant, "Size-induced effect on nano-crystalline $CoFe_2O_4$," *Journal of Magnetism and Magnetic Materials,* vol. 320, pp. 1729-1734, 2008.

[68] H. C. Hamaker, "The London—van der Waals attraction between spherical particles," *Physica,* vol. 4, pp. 1058-1072., 1937.

[69] J. Israelachvili, *Intermolecular and Surface Forces,* 1992.

[70] M. B. Fernández, P. M. Zélis, D. F. Coral, T. E. Torres, C. Marquina, G. F. Goya, *et al.*, "Self organization in oleic acid-coated $CoFe_2O_4$ colloids: a SAXS study," *J Nonopart Res,* vol. 14, pp. 1072-1082, 2012.

[71] B. D. Cullity and C. D. Graham, *Introduction to Magnetic Materials 2ed*: A. john Wiley & Sons, Inc., 2009.

CHAPTER 4 : Synthesis of Low Temperature Magnetic Pollen with Controlled Magnetic Properties

4.1. *Summary*

Three-dimensional (3-D) Fe_3O_4-coated pollen microparticles have been synthesized with tunable magnetic properties through the use of surface sol–gel (SSG) processing and allow low-temperature reduction process. Modifying the number of deposition cycles (10, 20, 30, and 40) provides a means for tuning the amount of iron oxide deposited and, in turn, the magnetic properties of the coated pollen particles. In addition, controlling the reaction temperature during the reduction of γ-Fe_2O_3 into Fe_3O_4 provides a means for controlling the grain size of the coatings which, in turn, allows for tailored magnetic properties and magnetic attraction at short and long ranges (up to ~1 mm). This work demonstrates that sustainable pollen microparticles, with particular surface features, can be conformally coated with γ-Fe_2O_3, and converted into shape-preserved Fe_3O_4-coated pollen grains (with retention of the pollen template) with predictable and tailorable magnetic properties and multimodal adhesion.

4.2. *Introduction*

Magnetite (Fe_3O_4) and maghemite (γ-Fe_2O_3) are common magnetic materials and used in applications ranging from, magnetorheological fluids (e.g., for vibration damping), magnetophoretic separations, biological cell isolation and manipulation, microfluidics, targeted drug delivery, magnetic self-assembly of hierarchical structures, the magnetic-field enabled tailoring of composite microstructures, and as hard drive materials.[1-14] The ability to synthesize micro-particles of either magnetite or

maghemite with tunable magnetic properties and in controlled 3-D shapes and sizes for a given application remains a non-trivial challenge.

Synthesizing magnetite from Fe_2O_3 can be achieved through several chemical and thermal processes. For example, a Rhines pack setup can be used to pin the oxygen partial pressure between that of iron and magnetite to a particular temperature to allow for the partial reduction of Fe_2O_3 into Fe_3O_4.[15] Fe_2O_3 can be reduced into Fe_3O_4 using a controlled (buffered) reducing atmosphere, such as a mixture of H_2 and H_2O.[16] Fe_3O_4 can also be synthesized from Fe_2O_3 through the use of wet chemical reducing agents, such as $NaBH_4$ or N_2H_4.[17, 18] The presented work utilizes a low-temperature aqueous reduction process, with hydrazine as the reducing agent, to convert γ-Fe_2O_3-coated pollen grains into Fe_3O_4-coated pollen grains.

The aims of this chapter are: i) to show how a low-temperature (70^{o}C) hydrazine-based reduction process can be used to generate nanocrystalline magnetite-coated pollen particles, ii) to investigate the effect of the number of SSG deposition cycles on the magnetic properties of the pollen specimens, iii) to examine the tailorability of the sizes of ultrafine crystals present in the oxide coating via a microwave hydrothermal (MWHT)/hydrazine reduction process using temperatures ranging from 100 to 250^{o}C, and iv) to investigate the effect of ultrafine crystals on the magnetic properties and adhesion properties for the coated pollen samples.

4.3. *Experimental Procedures*

4.3.1. Template

Pollen can be a desirable type of microparticle template due to its biological replicability (i.e., sustainability), ready global availability, abundance, low cost, and wide range of features at both the micro- and nanometer ranges. Pollen templates can be chosen from different plant species with a variety of overall sizes and shapes. The exine (outer layer) of pollen grains is composed of sporopollenin, a complex polymer consisting of carboxylic and fatty acids cross-linked with aliphatic chains (e.g. HOOC-$(CH_2)_n$-COOH).[19] The carboxylic and fatty acids provide an abundant concentration of hydroxyl groups needed for reaction with the isopropoxide precursors used in the SSG process (i.e., further surface modification is not required in order to obtain conformal coatings). The initial templates chosen in this work to demonstrate inorganic replication and nano-feature retention are Sunflower (*Helianthus annuus*) pollen grains, as shown in Figure 1 d (1.2.1).

4.3.2. Demineralization of Pollen Grains

Pollen grains obtained from Greer Laboratories (Lenoir, NC USA) were cleaned, to remove pollenkitt, by immersion in a mixture of chloroform and methanol (3:1 by volume [20]) for 24 h, followed by deposition onto filter paper (P5, Fisher Scientific, Pittsburgh, PA USA) and drying under vacuum at 60°C for 12 h. A second immersion was conducted in 1 M hydrochloric acid (VWR, Suwanee, GA USA) for 1 h to remove residual inorganic material, followed by rinsing three times with de-ionized water and drying by vacuum aspiration at room temperature for 5 min.

4.3.3. SSG Coating of Pollen Grains Process

Fe-O-bearing coatings were applied to cleaned, demineralized pollen grains via a computer-automated, layer-by-layer (LbL) SSG deposition process by:[21-24] i) immersing pollen grains for 10 min, with stirring, in a solution of 0.0125 M Fe(III) isopropoxide (Alfa Aesar, Ward Hill, MA USA) in anhydrous 2-propanol (>99.8% purity, Acros Organics, Geel, Belgium), to allow for the chemisorption of a Fe-O-bearing layer, ii) rinsing three times with anhydrous 2-propanol followed by vacuum filtration, iii) immersion in de-ionized water (DIW), with stirring, for 5 min, to allow for hydrolysis of the chemisorbed alkoxide layer, iv) rinsing three times with anhydrous 2-propanol followed by vacuum filtration, and v) and drying by vacuum aspiration for 5 min. This process (alkoxide exposure, 2-propanol rinsing, DIW exposure, 2-propanol rinsing, drying) was repeated for a total of 20, 30, or 40 cycles to build up a Fe-O-bearing coating. A schematic illustration of this SSG process is presented in Figure 91. (Note: the SSG coating process was conducted at room temperature in a N_2 atmosphere glove box with a relative humidity maintained between 0-2%. The relative humidity was monitored using an Omega RH32 sensor from OMEGA Engineering, Inc., Stamford, Connecticut.)

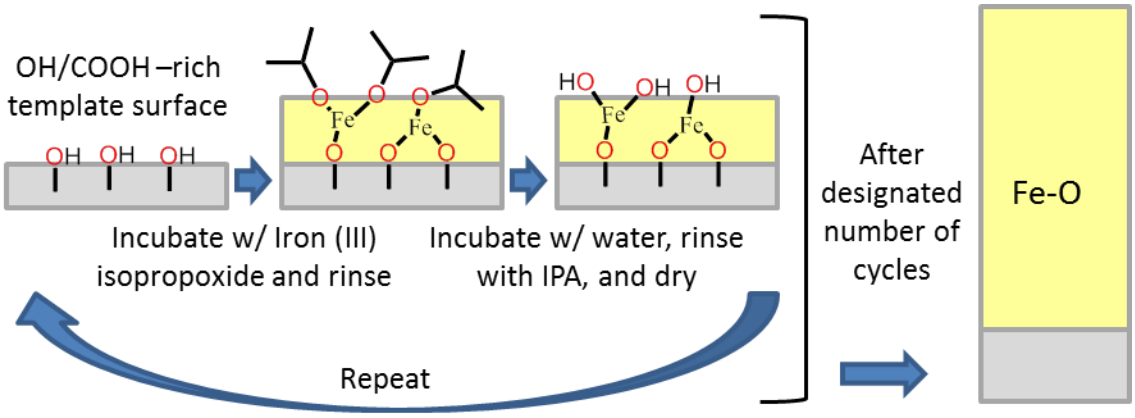

Figure 91: A schematic representation of the surface sol-gel process utilizing an iron (III) isopropoxide precursor.

4.3.4. Conversion to Magnetite Coated Pollens

The coated Fe-O-bearing specimens were partially reduced (to magnetite) via two different reaction methods. For the first method: specimens were sealed in 50 mL centrifuge tubes (Corning, MA, USA) containing a 20 mL solution of 0.07 wt% hydrazine (N_2H_4, 35 wt%, %, Sigma Aldrich, MO, USA) in DIW. Specimens were then placed in a drying oven at 70°C for 24 to allow for the iron oxide in the coatings to reduce into Fe_3O_4. Specimens were then rinsed twice with 20 mL of water, and then twice with 20 mL of IPA, followed by drying in air at 70°C for 1 hr. Each wash/rinse step was conducted out in a 50 mL centrifuge tube (Corning, MA, USA) using a neodymium-iron-boron alloy permanent magnet disk (ND022N-35, 10 mm diameter, 10 mm thick, Master Magnetics, Inc., Castle Rock, CO USA) to hold the specimen in place.

For the second method: the coated Fe-O bearing specimens were sealed within 100 mL Teflon^{TM} vessels (XP1500 Plus, CEM Corp., Matthews, NC, USA) containing a 20 mL solution of 0.07 wt% hydrazine (N_2H_4, 35 wt%, %, Sigma Aldrich, MO, USA) in DIW. The sealed specimens were then heated within 5 min to 100°C, 150°C, 200°C, or 250°C in a microwave reaction system (MARS 230/60, 2.45 GHz, CEM Corp., Matthews, NC, USA) using a maximum power setting of 1600W and held at this temperature for 90 min to allow for reduction into Fe_3O_4. Specimens were then rinsed twice with 20 mL of water, and then twice with 20 mL of IPA, followed by drying in air at 70°C for 1 hr. Each wash/rinse step was conducted in a 50 mL centrifuge tube (Corning, MA, USA) using a neodymium-iron-boron alloy permanent magnet disk to hold the specimen in place as discussed above.

4.3.5. Shape and Morphology Analyses

The morphologies of the native pollen grains, SSG-coated Fe-O-bearing grains, and partially reduced (Fe_3O_4 bearing) samples were evaluated with a field emission scanning electron microscope (1530 FEG SEM, LEO / Carl Zeiss SMT, Ltd., Thornwood, NY USA).

4.3.6. Phase and Grain Size Determination

Thermogravimetric (TG) analyses (Netzsch STA 449C, Wolverhampton, UK) were used to determine the oxidation state of hydrolyzed sol-gel-derived powders precursors before and after hydrazine reduction, as well as of commercially-purchased 325 mesh Fe_2O_3 powders (Alfa Aesar, 99% metal basis) and 325 mesh Fe_3O_4 powders (Alfa Aesar, 97% metals basis). Samples were fully reduced into elemental iron using a heating rate of 5°C min^{-1} up to 1000°C in a flowing (flow rate of 50 cm^3min^{-1}) gas mixture of 2% H_2 and 98% Ar. The change in mass from loss of oxygen was used to determine the initial Fe/O ratio. Thermogravimetric (TG) analysis measurements were also performed with the as coated pollen grains (20-40 layers) at a heating rate of 0.5°C min^{-1} up to a peak temperature of 1000°C flowing (flow rate of 50 cm^3min^{-1}) synthetic air (21% O_2, 79% N_2) gas mixture. The mass change was used to evaluate the amount of Fe-O applied (using 10-40 SSG cycles) to the native organic pollen. The sample mass was ~ 0.5 g for each TG analyses.

Phase identification was conducted at room temperature using X-ray diffraction (XRD) analyses. XRD analyses were conducted on a diffractometer (X'Pert Pro Alpha-1, PANalytical B.V., ALMELO, Netherlands) using $Cu_{K\alpha1}$(1.5405980 Å) radiation emanating from a 1.8 kW ceramic X-ray tube with a copper anode (45 kV, 40 mA)

through an incident beam Johansson monochromator (PANalytical) and with an X'Celerator detector. The incident beam optics were outfitted with 0.04 rad soller slits, a 2° fixed anti-scatter slit, a programmable divergence slit set to 5.5 mm irradiated length, and a 10 mm mask. The diffracted beam optics were outfitted with a 5.5 mm anti-scatter slit and 0.04 rad soller slits placed before the X'Celerator detector. Each pattern was produced with a summation of 40 identical 30 minute scans conducted using Bragg-Brentano geometry and a step size of 0.017° 2θ, ranging from 20° to 90° 2θ. The minimum Pulse Height Discrimination (PHD) setting, for the X'Celerator detector was increased to from 36 to 42 to help discriminate between the diffracted signals and fluorescent photons from the Fe atoms.[25] Diffraction specimens were dispersed on a quartz (cut 6° from a (0001) orientation) low background specimen support (GEM dugout, PA, USA) via pipetting an aliquot of IPA/powder slurry onto the specimen support and allowing the IPA to evaporate.

Values of average crystallite size (ACS) were determined with the HighScore Plus software (PANalytical B.V, Almelo, The Netherlands) using a Pseudo-Voigt profile fit function in conjunction with a Williamson Hall plot. The profile fit function allowed for each single peak to be characterized by position, height, width, and shape along with being described by functions of 2θ. A detailed explanation of the fitting process was provided in section 3.3.6.

4.3.7. Magnetic Property Measurements

The magnetic behavior of Fe_2O_3- and Fe_3O_4-coated sunflower pollen grains was studied using a superconducting quantum interference device (SQUID) magnetometer (Quantum Design MPMS-5S, San Diego, CA USA) with an applied magnetic field up to 5 T. Measurements were conducted in a temperature controlled chamber at 5 K and 300 K. Further information on these measurements was provided in Section 2.3.9.

4.3.8. Substrate Preparation and Adhesion Measurements

To evaluate the long range (magnetic) adhesion, a nickel-coated neodymium (Ni-Nd) alloy substrate was utilized. Substrate preparation and surface roughness measurements were provided in section 3.3.8. To perform long-range adhesion measurements, single grains of Fe_3O_4 coated pollen grains were attached to a tipless silicon AFM cantilever (FORT-TL, Applied NanoStructures, Inc.) with a small amount of epoxy resin (Epoxy Marine, Loctite, Westlake, OH USA) For each hydrazine reaction temperature (100°C, 150°C, 200°C, or 250°C), 1 single-particle-bearing cantilever probe was prepared (for a total of 4 particle/cantilever probes). The long-range adhesion force between an individual Fe_3O_4 coated pollen grain and a particular substrate was evaluated with the scanning probe microscope operated in a manner presented in sections 2.3.7 and 2.3.9 Note: the procedure described in section 4.3.8 was developed and performed with Donglee Shin (Georgia Institute of Technology, Atlanta, GA, USA).

4.4. *Results & Discussion*

4.4.1. Pollen Shape Preservation and Coating Quality

SE images of the sunflower (*Helianthus annuus*) pollen after exposure to 40 SSG Fe-O deposition cycles are shown in Figure 92. The coated pollen grains retained the shape and morphology of native sunflower pollen with the same general spherical shape and echini. The continuous and conformal coating covered the pollen grain with some cracks visible near the spine tips. A TEM cross-sectional image (Figure 93) confirmed that the external coating was continuous and conformal with some internal features also coated. HRTEM images (Figure 94) of the coatings revealed the presence of oxide nano grains on the order of 3 to 5 nm in size. The lattice spacing's associated with the crystallographic (311), (100), and (200) planes of maghemite (γ-Fe_2O_3) are shown in Figure 94.

SE images of a sunflower pollen grain after 40 SSG Fe-O deposition cycles followed by hydrazine reduction at 70°C for 24 h, are shown Figure 95. The coated, partially-reduced pollen grains retained the 3-D morphology, echini, and surface features

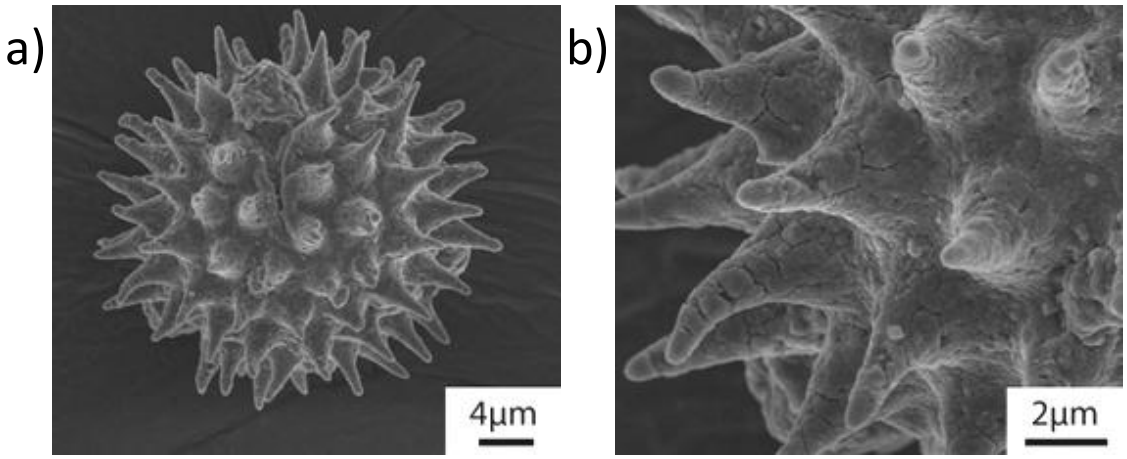

Figure 92: Secondary electron (SE) images of *H. Annuus* pollen grains coated with 40 SSG Fe-O deposition cycles: a) a low magnification SE image and b) a high magnification SE image.

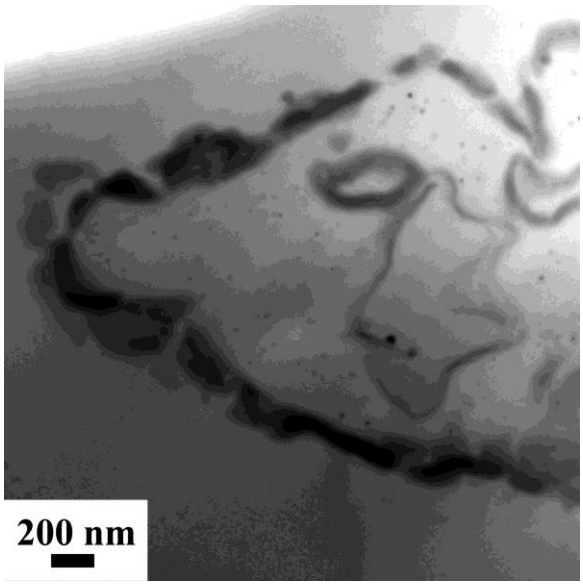

Figure 93: TEM cross-section of an individual sunflower pollen grain echini exposed to 40 Fe-O SSG deposition cycles.

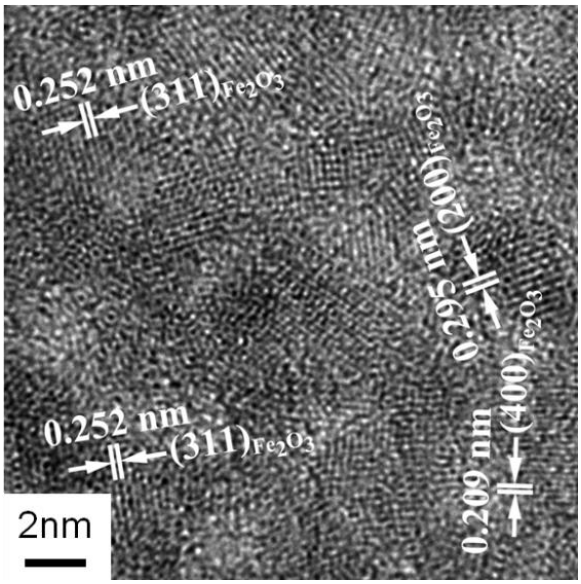

Figure 94: High resolution TEM image of the coating applied to a sunflower pollen grain via 40 Fe-O SSG deposition cycles.

of the native pollen and the as-coated pollen. A TEM cross-sectional image of single echini from a SSG coated/reduced specimen (Figure 96) indicated that the reacted coating covered the external surface of the echini, as well as internal features of the pollen grain. HRTEM analysis (Figure 97) revealed nano grains on the order of 3 to 5 nm within the coated/reduced oxide, with lattice fringes associated with the (311) crystallographic plane indicated.

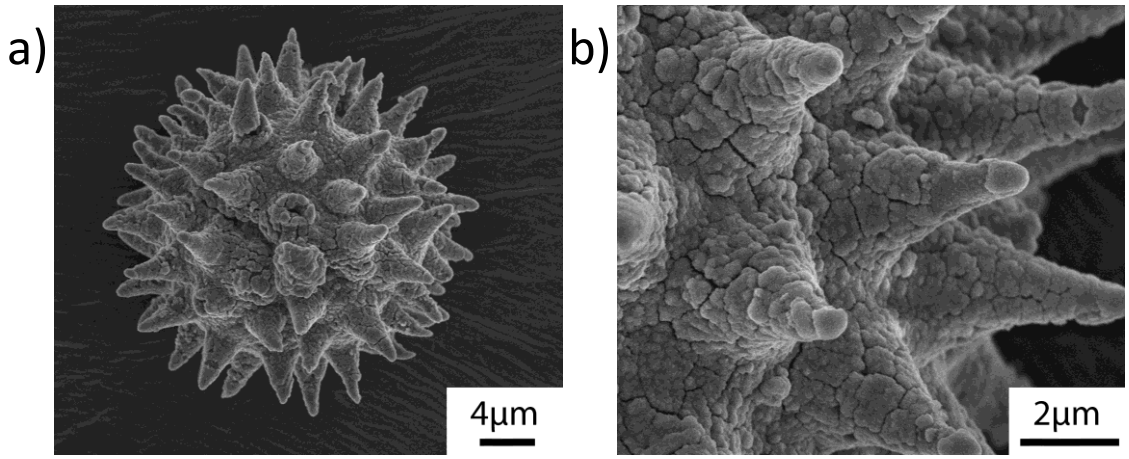

Figure 95: Secondary electron (SE) images of sunflower pollen grains coated with 40 Fe-O SSG deposition cycles followed by hydrazine induced partial reduction at 70°C for 24 h, into Fe_3O_4: a) a low magnification SE image and b) a high magnification SE image.

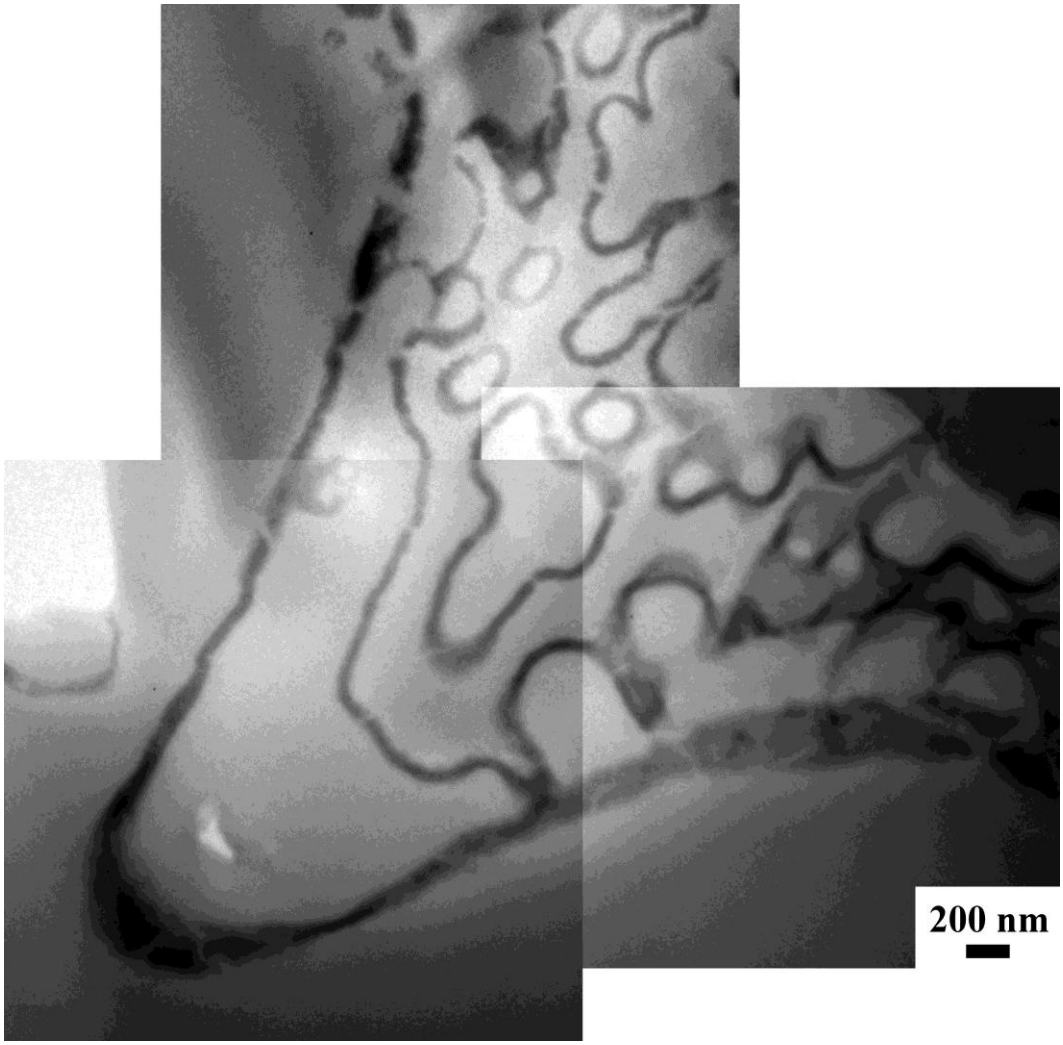

Figure 96: TEM cross-section of an individual sunflower pollen grain echini coated with 40 Fe-O SSG deposition cycles followed by hydrazine induced partial reduction at 70°C for 24 h into Fe_3O_4.

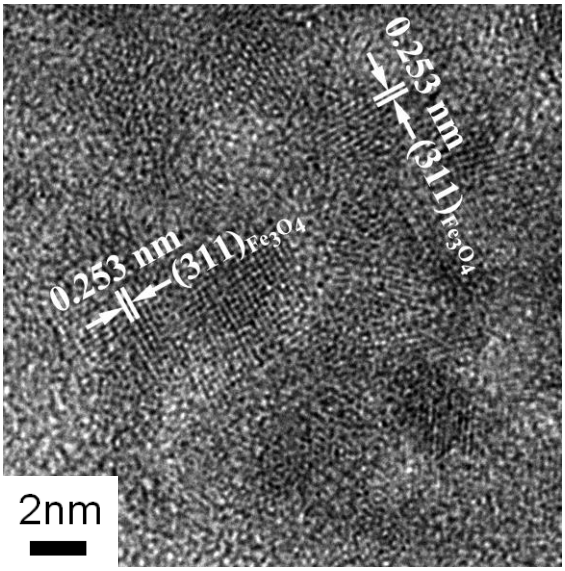

Figure 97: High resolution TEM image of the coating on a sunflower pollen grain obtained via 40 Fe-O SSG deposition cycles and then hydrazine-induced partial reduction at 70°C for 24 h into Fe_3O_4.

4.4.2. Coating Phase Analysis

A variety of characterization techniques were used to investigate the phase content of the iron oxide coatings on pollen grains before and after the hydrazine reduction process. XRD analyses were initially used to examine the phase content of the as-deposited coatings (Figure 98). However, the diffraction patterns of magnetite and maghemite are quite similar, with only a few more weak diffraction peaks, resulting from vacancy ordering, present in the case of maghemite. These weak diffraction peaks were not clearly evident in the diffraction patterns and may have been absent or difficult to detect due to the nanometer grain size of the samples.[26] Hence, the broadness of the XRD peaks from the 3 to 5 nm grains made it difficult to unambiguously assign a single phase to either sample (as-coated or coated/partially reduced). Both samples could be characterized as being comprised of γ-Fe_2O_3 and/or the partially-reduced phase of Fe_3O_4. The difference between the primary diffracted peaks of the two phases, maghemite (γ-Fe_2O_3, 0.25177 d(nm), PDF# 39-134) and magnetite (Fe_3O_4, 0.25320 d(nm), PDF# 19-

629) was such that it difficult to distinguish one from the other with a high degree of certainty via XRD analyses alone.[26] Electron diffraction analyses were performed on both the as-coated or coating/partially reduced pollen grains. These diffraction patterns also suggested that the as-coated sample contained the γ-Fe_2O_3 phase and the partially reduced samples contained Fe_3O_4 (magnetite) phase (Figure 99). However, similar to XRD analyses, the difference between the d spacing is small enough that the two phases cannot be clearly distinguished with a high degree of certainty. However, the coatings were deposited using only the iron (III) isopropoxide precursor and no reducing agent was used in the coating process, making maghemite the more-likely candidate phase for the as-deposited film. Prior work [27] has also indicated that hydrazine is capable of reducing maghemite into magnetite at or above room temperature.

Another technique used to identify maghemite vs. magnetite included monitoring the color change of the coated pollen particles before and after hydrazine treatment. Optical micrographs of the as-coated and chemically reduced samples are shown in Figure 100. The color change from dark brown to grayish black, upon hydrazine treatment, was consistent with the reported colors of maghemite and magnetite,

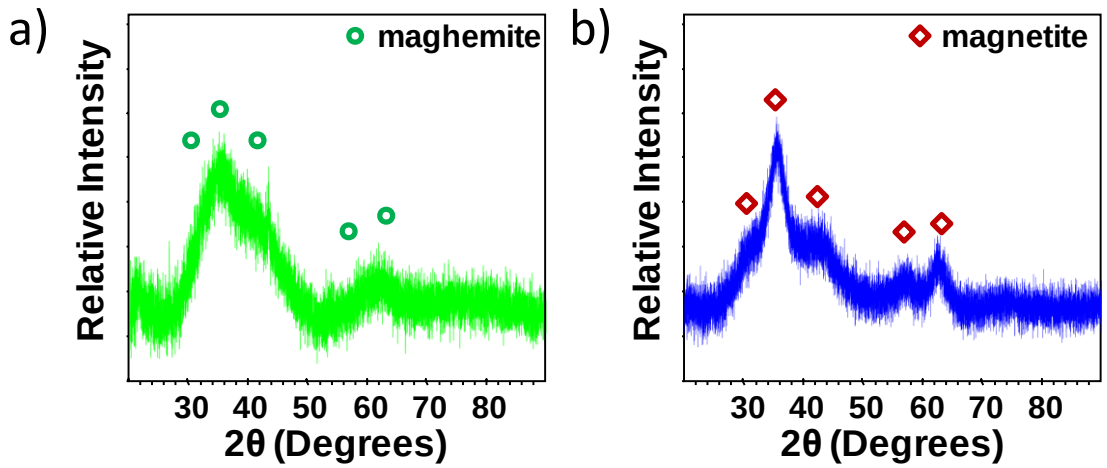

Figure 98: XRD analyses of pollen grains coated using 40 Fe-O SSG deposition cycles a) before and b) after the 70°C 24 h hydrazine treatment.

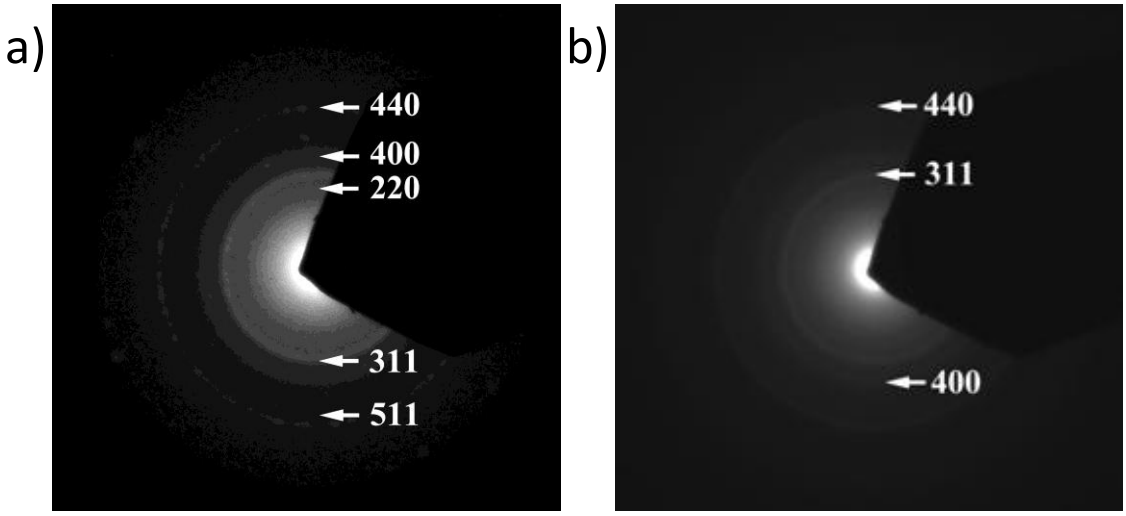

Figure 99: Electron diffraction analyses of sunflower pollen grains coated with 40 Fe-O SSG deposition cycles: a) indexed as γ-Fe_2O_3 (maghemite) and b) after the 70°C/24 h hydrazine treatment, indexed as Fe_3O_4 (magnetite).

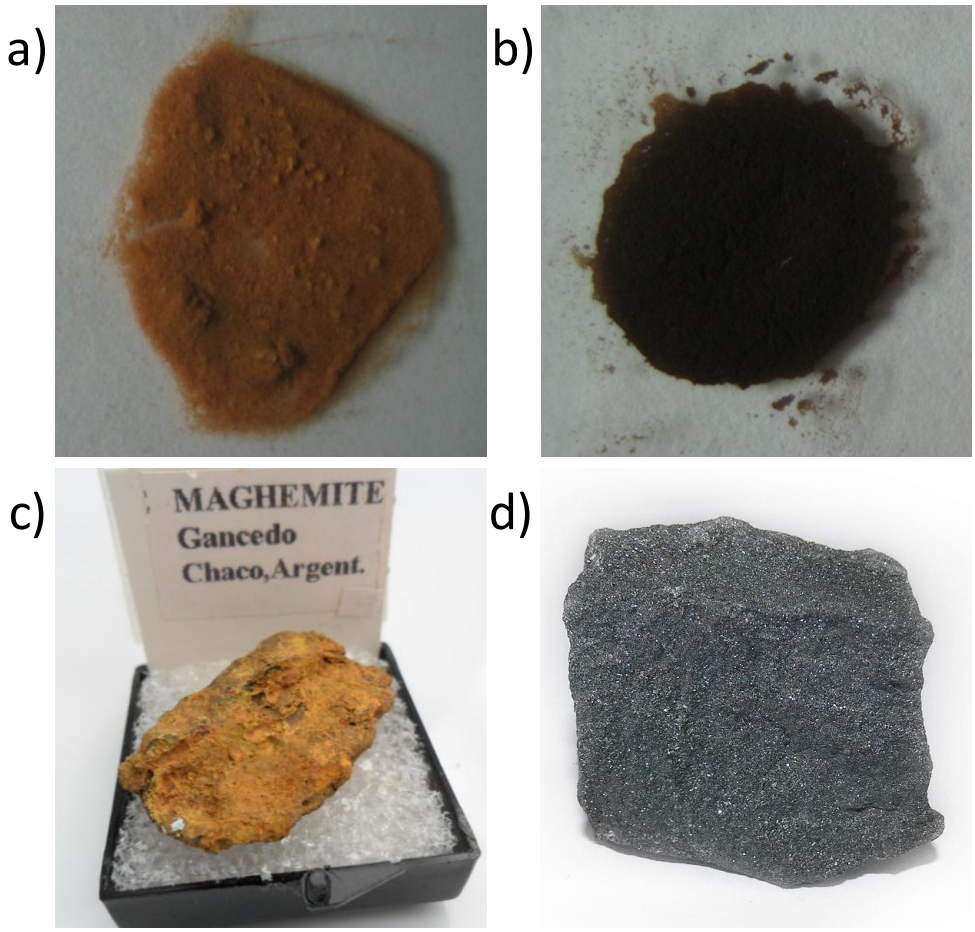

Figure 100: Optical images of sunflower pollen grains coated with 40 Fe-O SSG deposition cycle: a) as-coated pollen grains, b) after the 70°C/24 h hydrazine treatment, c) bulk maghemite, and d) bulk magnetite.[28]

respectively. Optical reflection analyses of the coated pollen grains before and after hydrazine exposure are shown Figure 101. When compared to the reflection spectra of the bulk powder samples, the associated coated pollen sample was more similar to bulk γ-Fe_2O_3 compared to bulk Fe_3O_4, while the hydrazine-treated sample was more similar to bulk Fe_3O_4 compared to bulk γ-Fe_2O_3. The differences in the coated and coated/hydrazine pollen reflection spectra could be attributed to differences in the crystallite sizes of the coatings vs. bulk powders, and/or the presence of the pollen template, or even due to a mixture of phases present in each coating. If a mixture of phases were present, it would be difficult to quantitatively determine the amount of each phase using such reflection spectra alone.

In order to determine the oxidation state of the iron in the coating before and after hydrazine reduction, TG analyses were used. With TG analyses, it was possible to measure the mass lost when iron oxide was fully reduced into elemental iron. For

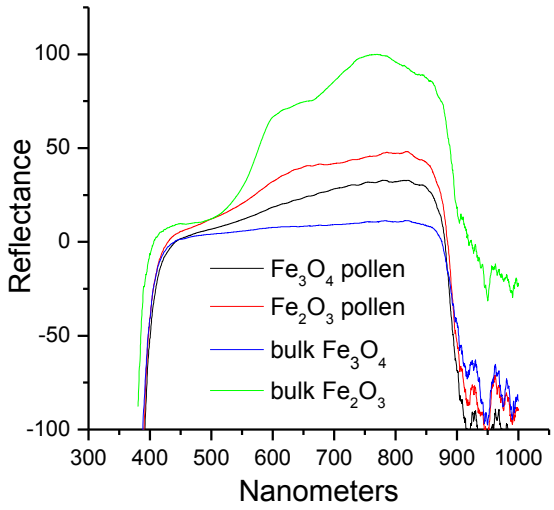

Figure 101: reflection spectra of pollen grained coated with 40 SSG cycles of Fe-O before and after reduction and of bulk γ-Fe_2O_3 and bulk Fe_3O_4

maghemite (γ-Fe_2O_3), the residual mass should be 69.6% of the starting mass when fully reduced to iron. For magnetite (Fe_3O_4), the residual mass of the resulting iron should be 72.0% of the starting mass. This difference of 2.4% is well within the sensitivity of TG analysis and can be used to distinguish γ-Fe_2O_3 from Fe_3O_4. However, the relative difference in percent change from a magnetite-coated pollen grain to iron compared to a maghemite coated-pollen grain to iron was less than 2.4%. The coatings made up a~10-20% of the total mass, meaning that that difference in mass change would be less than 0.3% and may be more difficult to accurately detect. In addition, with the coated-pollen grains, differences in the mass of the pollen particles per grain can introduce uncertainty in the measurements leading to some variation in residual mass percent after complete reduction. The pollen mass variation was avoided by performing TG analyses on γ-Fe_2O_3 powders generated by hydrolysis of the iron (III) isopropoxide precursors in solution, as opposed to SSG deposition of the iron (III) isopropoxide on the surfaces of pollen grains. The sol-gel-derived powder samples were then exposed to hydrazine under the same conditions as the Fe-O-coated pollen samples, for subsequent TG analyses. Control

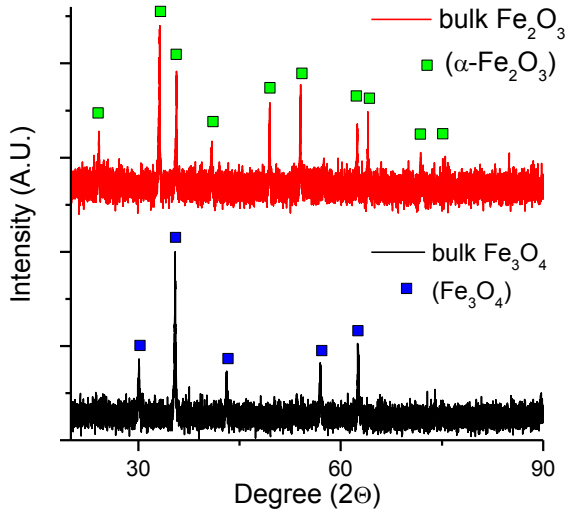

Figure 102: XRD analyses of commercially purchased (red) α-Fe_2O_3 and (black) Fe_3O.

samples of commercially purchased powders of both γ-Fe_2O_3 and Fe_3O_4 were then used to test the accuracy of the TG analyses. XRD analyses of showed that the commercially purchased samples were phase pure (Figure 102). The results of this experiment are discussed in section 5.5.2. The hydrazine-reduced samples were found to have a similar weight loss as that of commercially-purchased magnetite powder.

Other techniques, such as electron energy loss spectroscopy (EELS), X-ray photoelectron spectroscopy (XPS), time of flight (ToF) secondary ion mass spectrometry (SIMS), Rutherford backscattering spectrometry (RBS), Mössbauer spectroscopy, Raman spectroscopy, infrared spectroscopy, hardness tests, and chemical titration were also considered as techniques for distinguishing γ-Fe_2O_3 vs. Fe_3O_4. However, none of these other techniques proved useful due to the similarities between the compositions of both phases and due to the small grain sizes of both phases (~4 nm) in these samples.

4.4.3. Low Temperature Magnetic Properties

The magnetic hysteresis behavior of iron oxide coated pollen grains before and after the hydrazine reduction process with 20, 30, or 40 Fe-O SSG deposition cycle were examined with a SQUID magnetometer at room temperature (300 K), via active temperature control, and at 5 K to investigate the effects of coating thickness and the partial-reduction process on magnetic properties. For the as-coated samples (γ-Fe_2O_3), an increase in coercivity (H_c), remanent magnetization (M_r), and magnetic saturation (M_s) was observed with an increase in the layer thickness (Figure 103). The coercivity for the 20, 30, and 40 SSG cycle samples was found to be 0.0535 T, 0.0710 T, and 0.0752 T, respectively. The M_r values for the 20, 30, and 40 SSG cycle samples were found to be 0.140 Am^2/Kg, 0.214 Am^2/Kg, and 0.269 Am^2/Kg, respectively. The M_s values for the

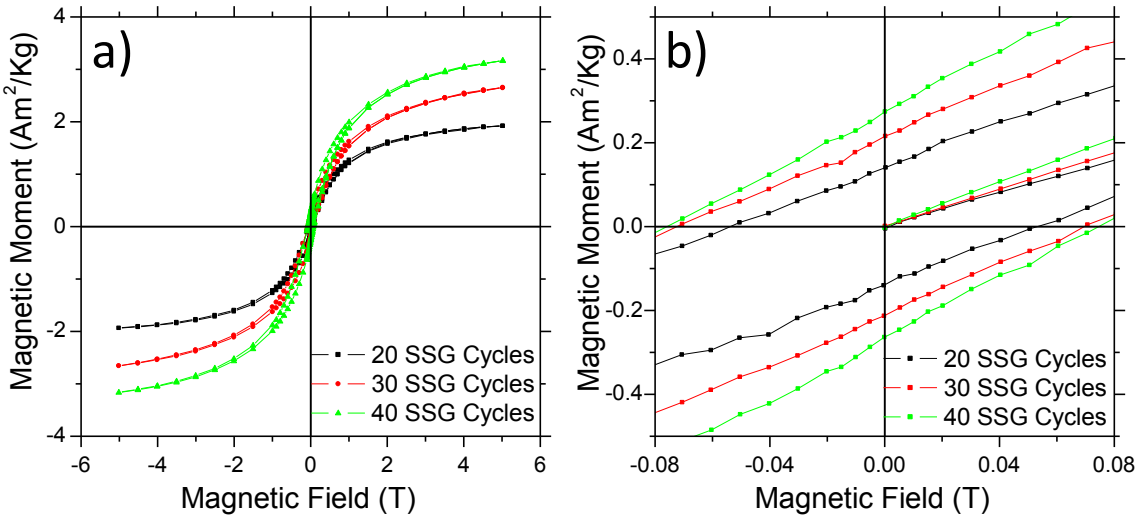

Figure 103: SQUID magnetometer data for Sunflower pollen samples with 20, 30, and 40 Fe-O SSG deposition cycle show an increase in a) remanent magnetization, b) coercivity, and magnetic saturation with an increase with in maghemite layer thickness.

20, 30 and 40 SSG cycle samples were found to be 1.92 Am^2/Kg, 2.65 Am^2/Kg, and 3.18 Am^2/Kg, respectively. The increase in the magnetic moment (M_r and M_s) was expected due to the increasing relative amount of magnetic material deposited with each coating layer. M_r and M_s values were affected by the mass of the pollen template and as the coating thickness (or number of coating layers) increased, the relative mass percent of the underlying pollen template decreased, so that the relative mass of the magnetic coating increased.

TG analyses of the sunflower pollen grains indicated that HCl-washed pollen grains contained ~.4% inorganic content, while the as-coated samples (γ-Fe_2O_3) contained 13.8%, 17.7% and 23.2% inorganic material for the 20, 30 and 40 Fe-O SSG deposition cycle samples, respectively (section 2.4.4 Figure 28). Using the TG analyses, it was possible to calculate the magnetic properties of the coating on a per gram of oxide basis. By dividing the measured M_r and M_s values by the percent of the inorganic content from TG analyses data, it was possible to obtain template-independent values. This led to M_r values of 1.02 Am^2/Kg, 1.20 Am^2/Kg, and 1.16 Am^2/Kg for the coating without the

extra mass from the pollen, or an average value of 1.13 ± 0.10 Am^2/Kg for all of the coatings, and M_s values of 13.9 Am^2/Kg, 14.9 Am^2/Kg, and 13.7 Am^2/Kg for the coating without the extra mass from the pollen, or an average value of 14.2 ± 0.68 Am^2/Kg for all of the coatings.

The 5 K measurements on the hydrazine-reduced samples revealed an increase in coercivity, remanent magnetization, and magnetic saturation with an increase in the layer thickness (Figure 104). The coercivity values for the 20, 30, and 40 Fe-O SSG deposition cycle samples were 0.0212 T, 0.0230 T, and 0.0323 T, respectively. The M_r values for the 20, 30, and 40 Fe-O SSG deposition cycle samples were found to be 0.576 Am^2/Kg, 0.820 Am^2/Kg, and 1.387 Am^2/Kg respectively. The M_s values for the 20, 30, and 40 Fe-O SSG deposition cycle samples were 3.70 Am^2/Kg, 5.10 Am^2/Kg, and 6.98 Am^2/Kg respectively. If the assumption is made that hydrazine reacted samples contained 3.4% less inorganic content compared to the as-coated samples, then new values of M_r can be obtained. This led to M_r values of 4.27 Am^2/Kg, 4.75 Am^2/Kg, and 6.13 Am^2/Kg and M_s values of 27.5 Am^2/Kg, 29.5 Am^2/Kg, and 30.8 Am^2/Kg, for the coating without the extra mass from the pollen. Compared to as-coated (γ-Fe_2O_3 bearing) samples, the hydrazine-reacted coatings (Fe_3O_4 bearing) had increased M_r values (1.02-1.20 Am^2/Kg vs.4.27-6.13 Am^2/Kg, respectively) and M_s values (13.7-14.9 Am^2/Kg vs. 27.5-30.8 Am^2/Kg, respectively), and decreased H_c values (0.0533-0.0752 T vs. 0.0212-0.0323 T, respectively).

Room temperature (300 K) and 5 K SQUID analyses were then conducted on the 40 SSG cycle/ hydrazine reacted sample (Figure 105). The 300 K experiment demonstrated an s curve shape, while the 5 K plot exhibited hysteresis typical of a

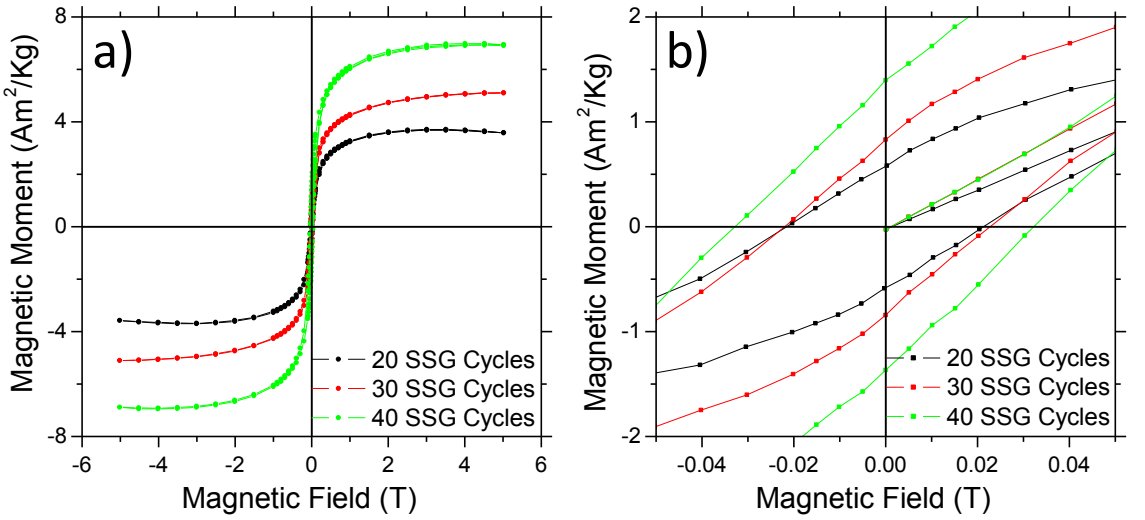

Figure 104: SQUID magnetometer data for Sunflower pollen samples with 20, 30, and 40 40 Fe-O SSG deposition cycle after reacting with hydrazine, show an increase in a) remanent magnetization, b) coercivity, and magnetic saturation with an increase with in magnetite layer thickness.

ferrimagnetic material. Due to the small grain size, the curie temperature was depressed and prevented the typical hysteresis characteristics from being exhibited at 300 K.[29] (Note: the experiments and results described in section 4.4.3 were developed and performed in collaboration with Dan Sabo ,Georgia Institute of Technology, Atlanta, GA, USA).

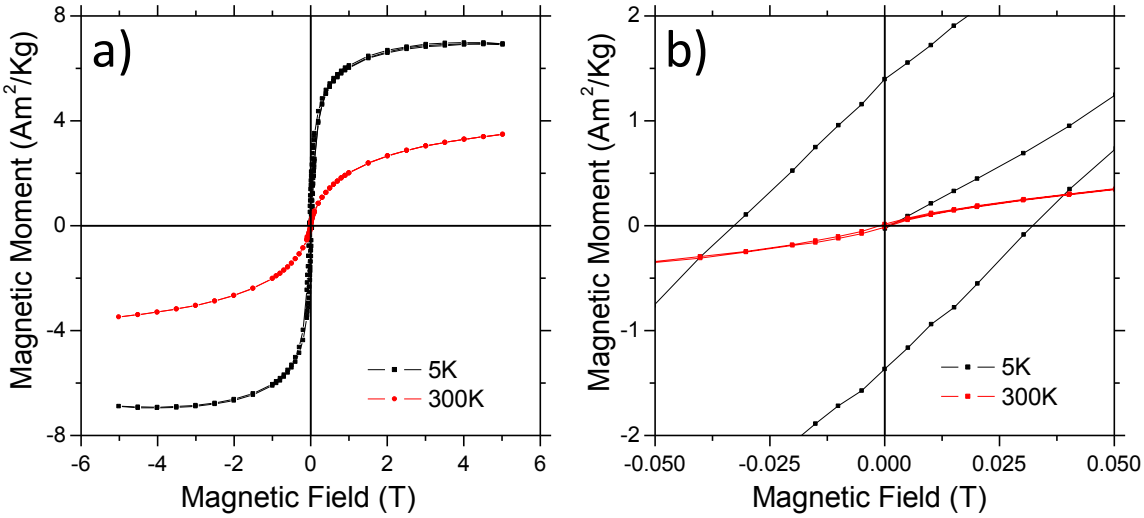

Figure 105: SQUID magnetometer data conducted at 5K and 300K for Sunflower pollen samples 40 layers coatings, after reacting with hydrazine a) full hysteresis curve b) zoomed in region

4.4.4. Microwave Hydrothermal Synthesized Magnetic Pollen Replicas with Tailorable, Ultrafine Crystal Size

SE images of sunflower (*Helianthus annuus*) pollen grains after 40 Fe-O SSG deposition cycles and hydrothermal reaction with hydrazine at 100°C, 150°C, 200°C, or 250°C are presented in Figure 106 and Figure 107. The pollen grains retained the 3-D shape and surface morphology of native sunflower pollen. At higher reaction temperatures, individual oxide nano-particles could more readily be detected on the surfaces of the pollen grains due to apparent grain coarsening. Figure 107 shows an echini tip of pollen grains with increasing number of nanocrystals visible at higher reaction temperatures.

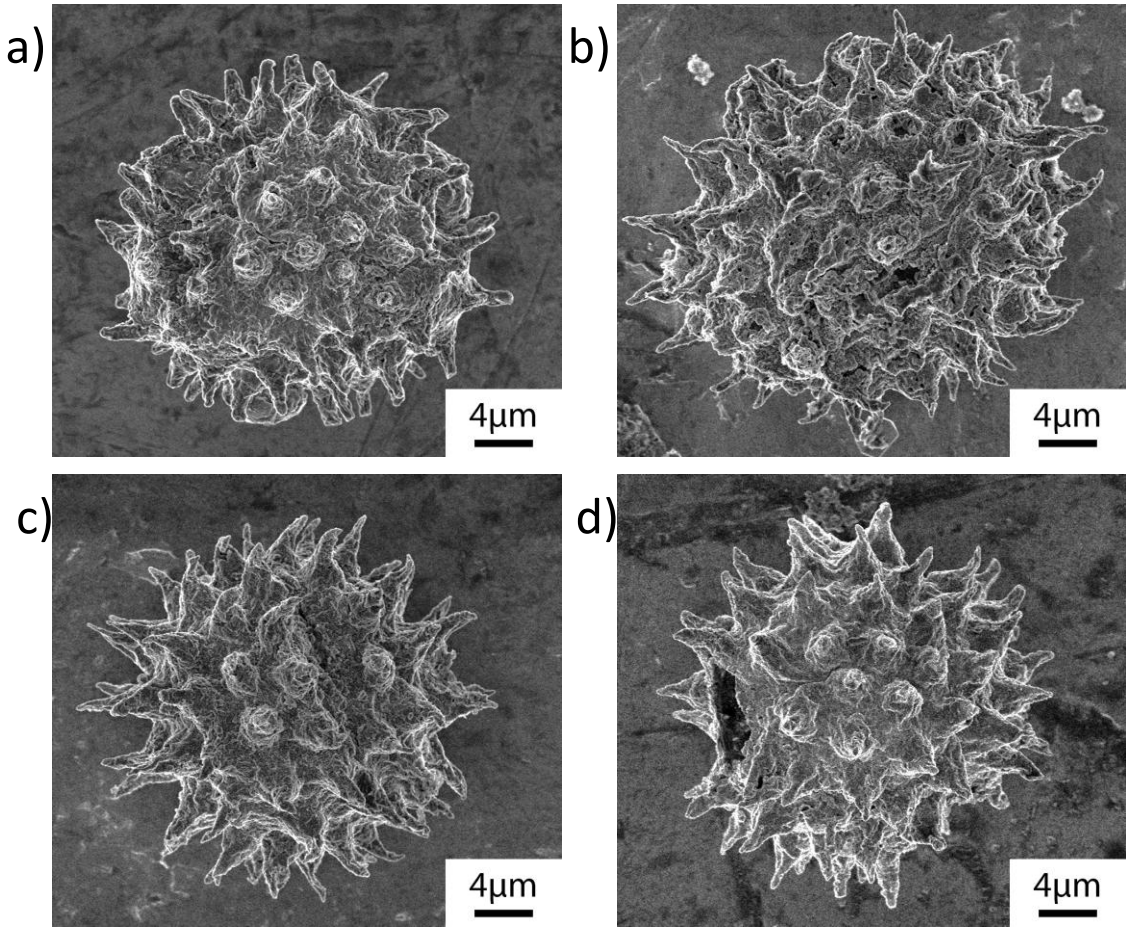

Figure 106: SE image of pollen grains coated with 40 Fe-O SSG deposition cycles and reacted with a 0.07 wt% hydrazine solution at: a) 100°C, b) 150°C, c) 200°C, or d) 250°C for 90 min in a MWHT apparatus.

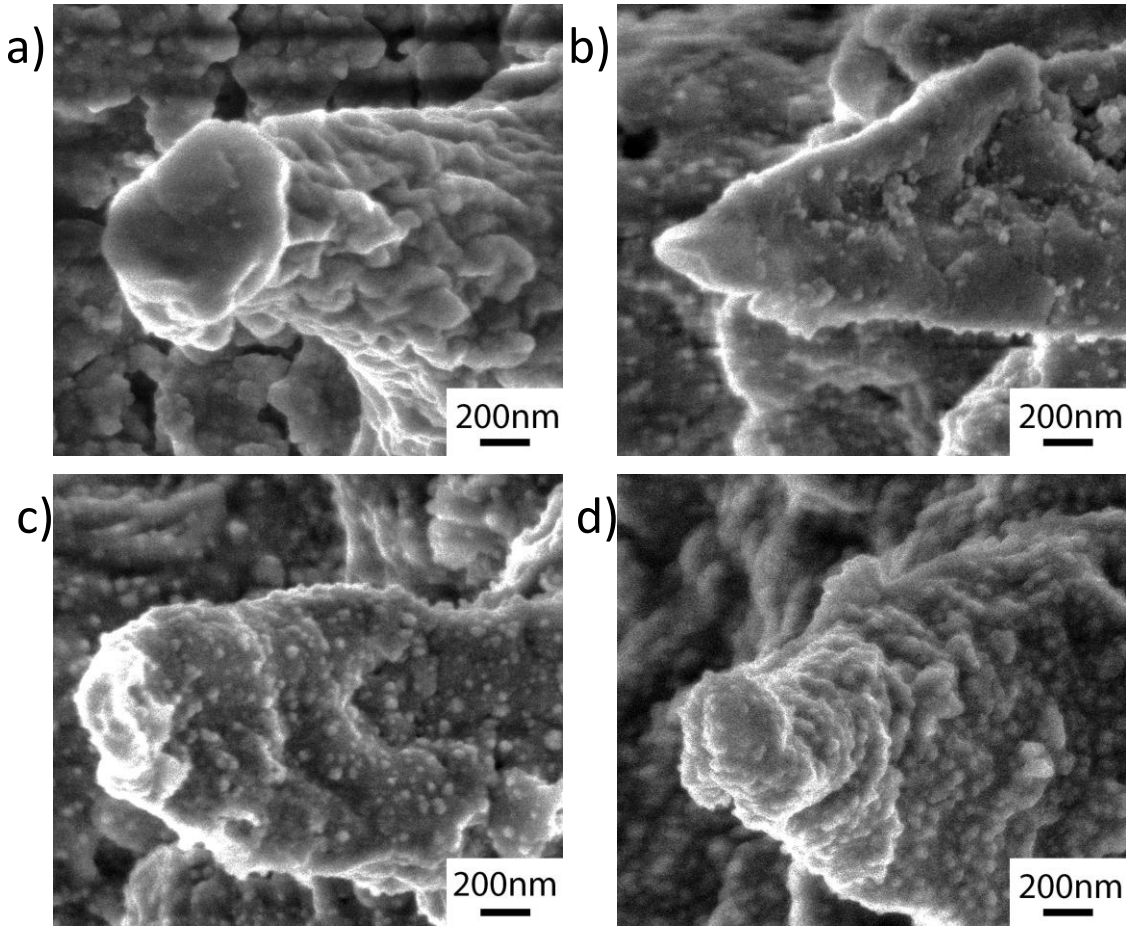

Figure 107: SE image of pollen grain echini coated with 40 Fe-O SSG deposition cycles and reacted with a 0.07 wt% hydrazine solution at a) 100°C, b) 150°C, c) 200°C, or d) 250°C for 90 min in a MWHT apparatus.

XRD analyses of these MWHT hydrazine-reduced samples (Figure 108) revealed distinct diffraction peaks consistent with only the magnetite (Fe_3O_4) phase. With increasing MWHT reduction temperature, appreciable narrowing in the widths of the diffraction peaks was observed, as shown specifically for the (311) diffraction peak in Figure 109. Full pattern profile fitting was then conducted on these XRD patterns to allow for evaluation of the average magnetite crystal size. Measured and calculated diffraction patterns, along with difference plots, are shown in Figure 110 a, b, c, and d for the samples reacted at 100^{o}C, 150^{o}C, 200^{o}C, and 250^{o}C, respectively.

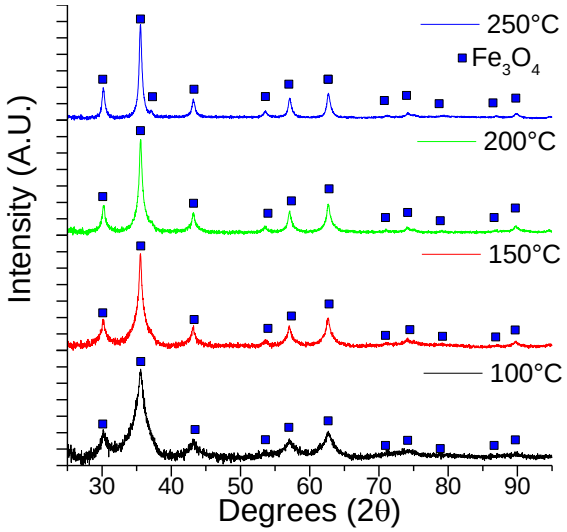

Figure 108: XRD analyses of Fe_3O_4-coated pollen grains exposed to a MWHT hydrazine reduction process for 90 min at the indicated temperature (Note: the background has been removed)

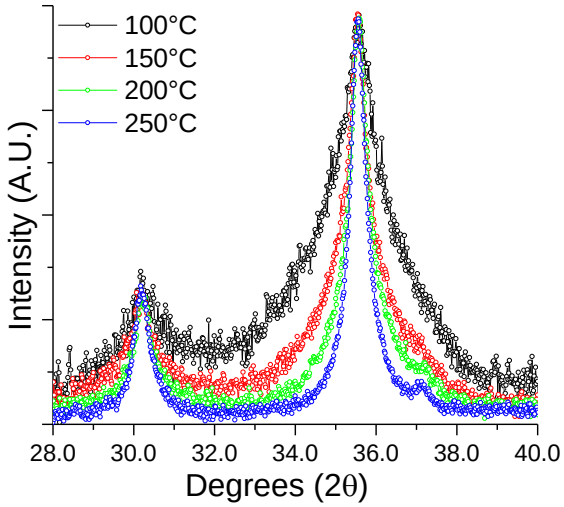

Figure 109: (311) X-ray diffraction peak of MWHT hydrazine-treated Fe_3O_4 replicas, showing a decrease in FWHM as reaction temperature increased

The full-width-at-half-maximum (β) values for each diffraction peak were then fitted to the Caglioti equation:

$$\beta = [U\tan^2\theta + V\tan\theta + W]^{1/2} \qquad (4.1)$$

as shown in Figure 111 a, b, c, and d for the samples reacted at 100°C, 150°C, 200°C, or 250°C, respectively with the fitted data listed in Table 14. The fitted values of U, V, and W were used to obtain β values for each diffraction peak. After correcting for the

instrumental contribution to peak broadening, the resulting β_{str} values were then plotted against sinθ (Figure 112) and the Williamson-Hall relation:

$$\beta_{str}(\cos\theta) = [\lambda/D] + 4\varepsilon_{str}\sin\theta \qquad (4.2)$$

was used to obtain the average values of crystallite size, D, and microstrain, ε_{str}, for each reaction condition (from the intercepts and slopes, respectively, of the fitted lines for Cu Kα radiation with λ= 0.15406 nm). A Si NIST profile standard (standard 640c) was used to calibrate the peak broadening of the samples to allow for quantitative crystallite size

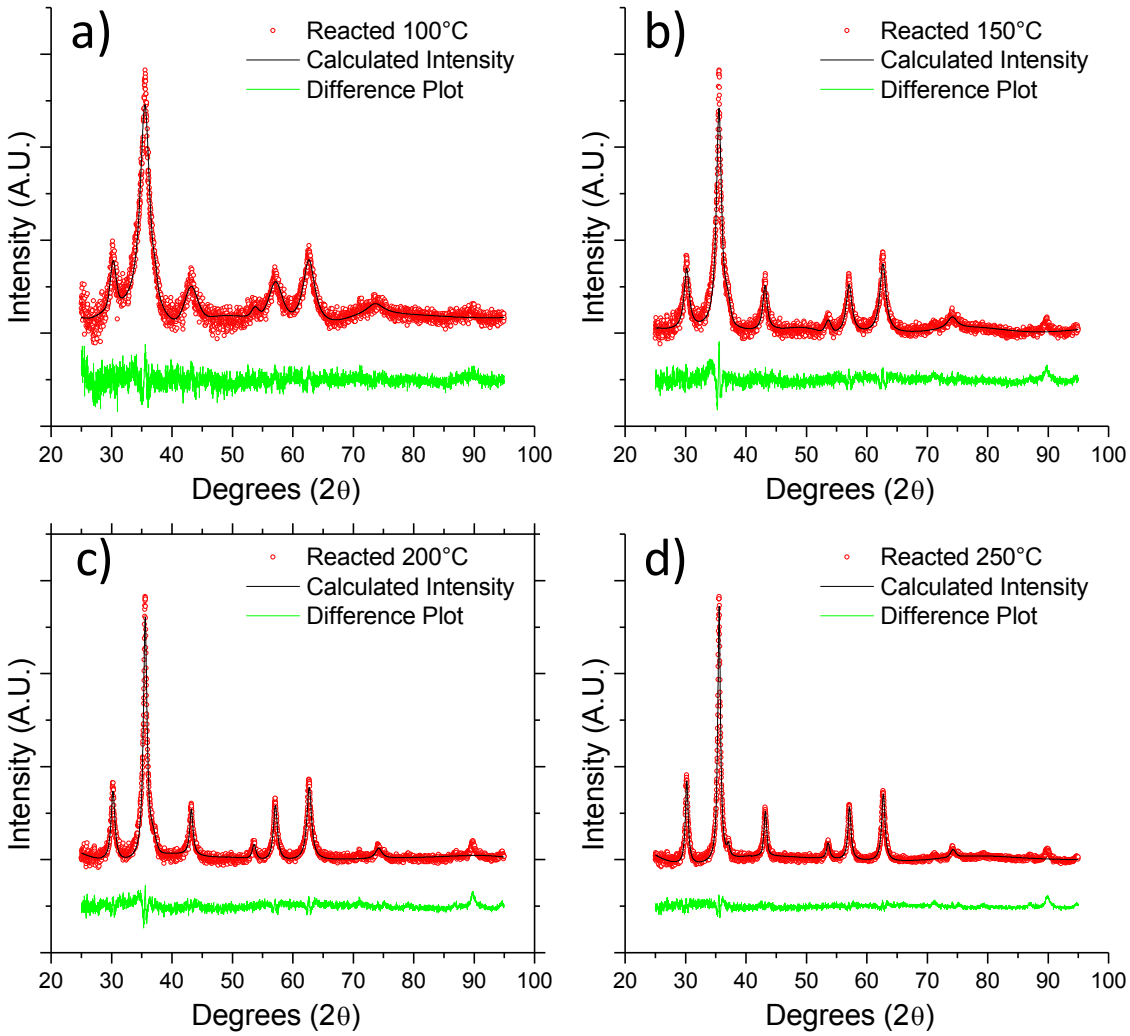

Figure 110: Pseudo-Voigt fitting (thin black line) of the measured XRD patterns (red circles), and associated difference plots (green curves) between the measured and fitted patterns, obtained from Fe-O-coated pollen grains prepared with 40 Fe-O SSG deposition cycles followed by MWHT hydrazine reduction for 90 min at: a) 100°C, b) 150°C, c) 200°C, or d) 250°C.

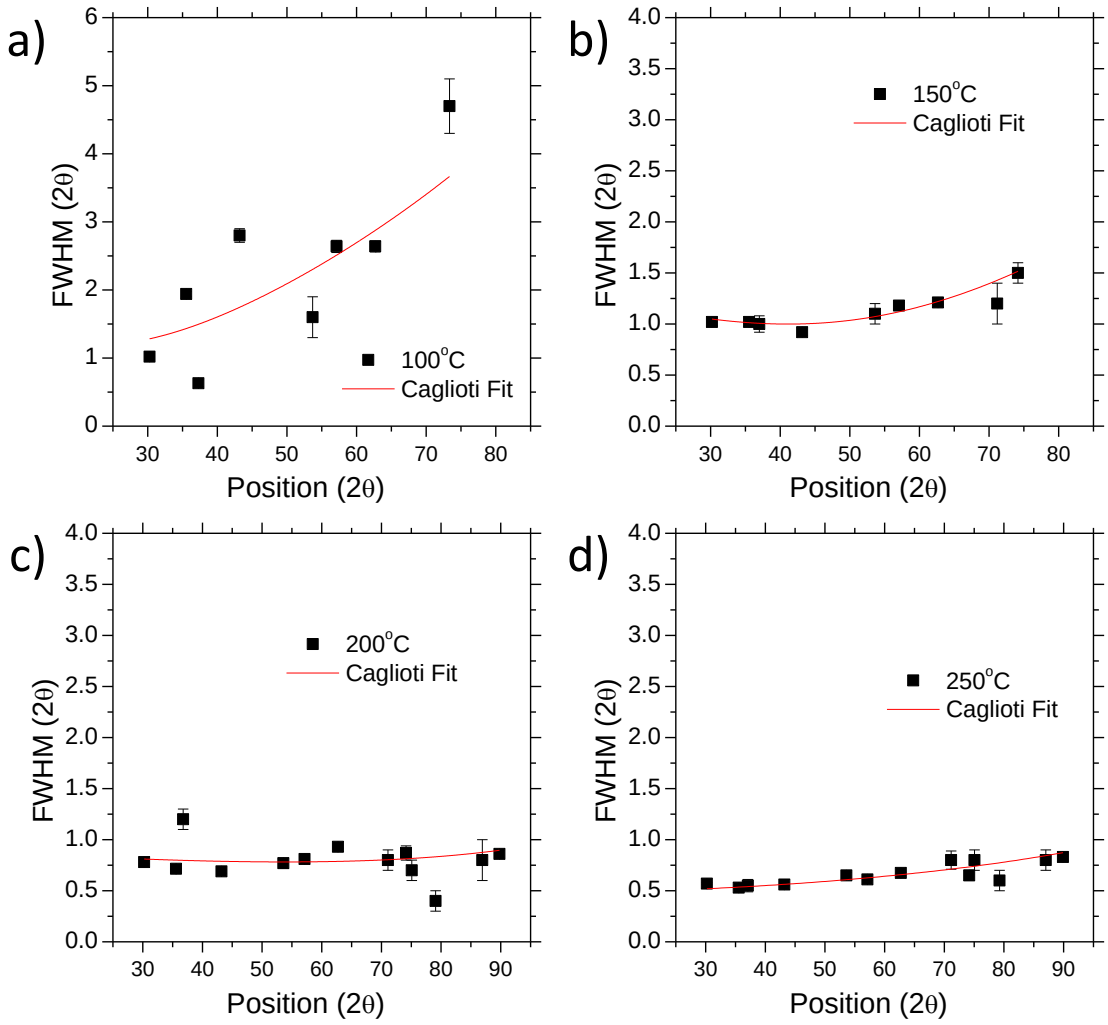

Figure 111: Fits of the full-width-at-half-maximum values of XRD peaks to the Caglioti equation for Fe-O-coated pollen grains prepared with 40 Fe-O SSG deposition cycles followed by MWHT hydrazine reduction for 90 min at: a) 100°C, b) 150°C, c) 200°C, or d) 250°C.

and microstrain analyses. Least-squares fitting of the Williamson-Hall plots (Figure 112) yielded lines that were nearly horizontal, which indicated that microstrain was not a major contributor to peak broadening (the microstrain values were less than 0.1%). The fitted data is available in Table 15. The resulting average values of magnetite crystallite size are shown in Figure 113 as a function of the MWHT reduction temperature.

Table 14: Caglioti fit to the FWHM values of each diffracted peak for specimens reacted in a microwave hydrothermal chamber at a peak temperature of: a) 100ºC, b) 150ºC, c) 200ºC, or d) 250ºC.

Sample Firing Temperature	Fitted line	Chi^2 value
100ºC	$4\ (11) - 15(49)*\tan(\theta) + 33(49)*\tan(\theta)^2$	34.9
150ºC	$5(1) - 20(4)*\tan(\theta) + 25(4)*\tan(\theta)^2$	0.228
200ºC	$3(2) - 9(7)*\tan(\theta) + 10(7)*\tan(\theta)^2$	0.736
250ºC	$0.9(2) - 3(1)*\tan(\theta) + 4(1)*\tan(\theta)^2$	0.00813

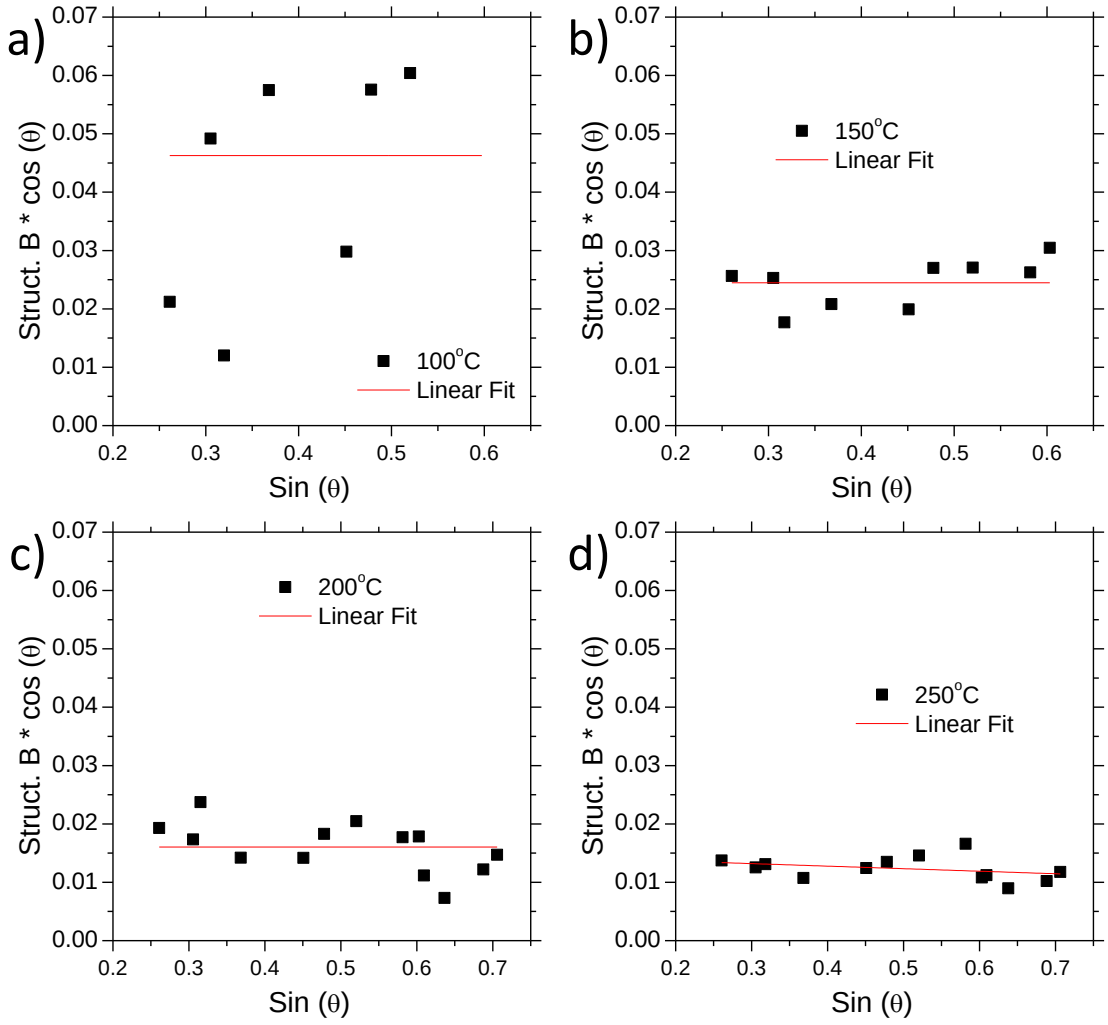

Figure 112: Williamson-Hall plots used to calculate the crystallite size for each reaction temperature. The crystallite diameters were found to be: a) 5 ± 1.0 nm for samples reacted at 100ºC, b) 9 ± 1.0 nm for samples reacted at 150ºC, c) 11 ± 1.0 nm for samples reacted at 200ºC, and d) 16 ± 1.0 nm for samples reacted at 250ºC. (Note: while errors from the fitted lines suggested grain size error ranges less than 1.0 nm, the resolution limits for crystallite size analyses is ± 1.0 nm and these error ranges were chosen instead.)

Table 15: Williamson-Hall plots fitting data used to obtain the crystallite size for hydrazine derived Fe_3O_4 coatings reacted in a microwave hydrothermal chamber at different peak temperatures.

Sample Firing Temperature	Fitted line	Chi^2 value
100ºC	0.016(4) + 0.00(5) sin(θ)	3.80
150ºC	0.0245(3) - 0.00(2) sin(θ)	0.377
200ºC	0.0160(9) - 0.00(2) sin(θ)	0.253
250ºC	0.0021(2) - 0.0043(9) sin(θ)	.0576

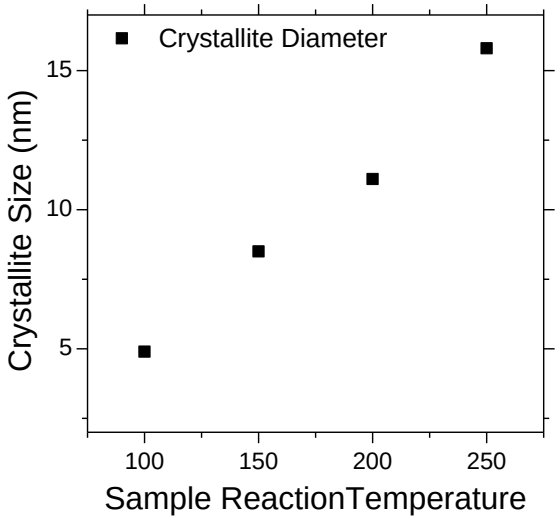

Figure 113: Average magnetite crystal diameter, obtained via Williamson-Hall analyses, for Fe-O-coated pollen grains prepared with 40 Fe-O SSG deposition cycles followed by MWHT hydrazine reduction for 90 min at a peak temperature of 100°C to 250°C.

4.4.5. Magnetic Properties and Adhesion Data

Magnetic properties of the Fe_3O_4 coated samples were evaluated at room temperature (300 K) to determine the effect of crystallite size on magnetic properties. Figure 114 reveals the SQUID hysteresis data for measurements made at 300 K respectively. The saturation magnetization (M_s) values of the hydrothermally reacted coatings were 4.442 Am^2/Kg, 15.044 Am^2/Kg, 18.630 Am^2/Kg, and 49.764 Am^2/Kg for samples reacted at 100°C, 150°C, 200°C, or 250°C, respectively. The magnetization value at an applied field of 5 T for the specimen reduced at 250°C was more than an

order of magnitude larger than for the specimen reduced at 100°C (49.76 vs. 4.44 Am^2/Kg). The remanent magnetization (M_r), values were 0.033 Am^2/Kg, 0.241 Am^2/Kg, 0.911 Am^2/Kg, and 3.750 Am^2/Kg for samples reacted at 100°C, 150°C, 200°C, or 250°C, respectively. The remanent magnetization of the specimen reduced at 250°C was more than 2 orders of magnitude greater than for the specimen reduced at 100°C (3.75 vs. 0.033 Am^2/Kg). The increase in remanent magnetization values, for ferrites, as a function of crystallite size (reaction temperature) have been reported previously.[30-32] The coercivity (H_c) values for the hydrothermally-reacted coatings were 0.000576 T, 0.000840 T, 0.00187 T, and 0.00286 T for samples reacted at 100°C, 150°C, 200°C, or 250°C, respectively. The coercive field (H_C) was also found to increase with an increase in the MWHT reduction temperature (i.e., from $5.76x10^{-4}$ T for 100°C reduction to $2.86x10^{-3}$ T for 250°C reduction).

TG analyses of the 40 Fe-O SSG deposition cycle coated pollen grains indicated that the as-coated samples (γ-Fe_2O_3) contained 23.2% Fe_2O_3 (section 2.4.4 Figure 28). Using such TG analyses and the known mass change between γ-Fe_2O_3 and Fe_3O_4 (2.4%),

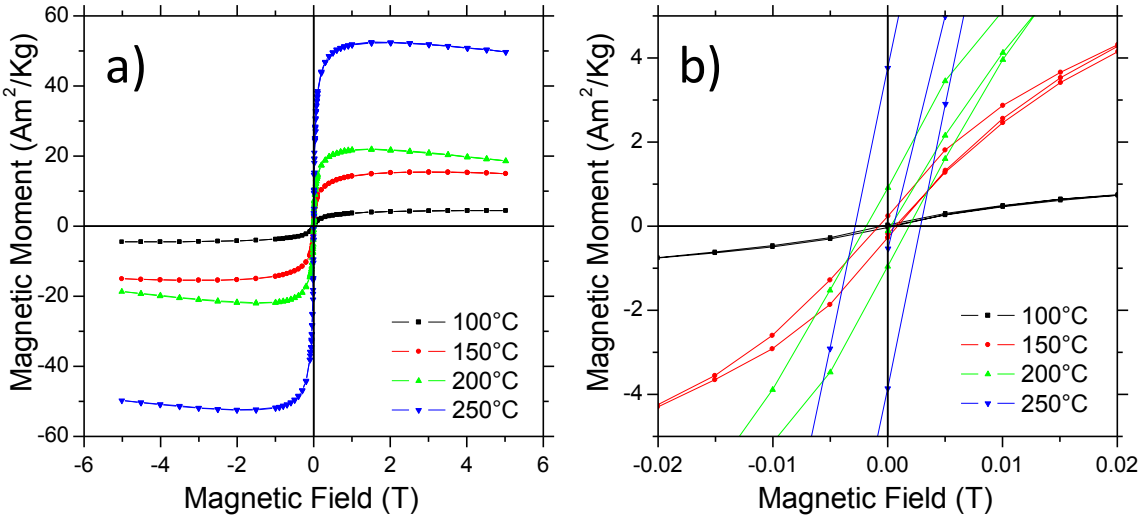

Figure 114: Superconducting Quantum Interference Device analysis conducted at 300 K for Fe_3O_4 coated sunflower particles synthesized at various MWHT hydrazine reaction temperatures: a) entire plots and b) zoomed in regions

it was possible to calculate the magnetic properties of the coating on a per gram of oxide basis. That is, by dividing the measured M_r and M_s values by the percent of the inorganic content from TG analyses data, it was possible to obtain template-independent values. This treatment led to M_s values of the hydrothermally-reacted coatings as 18.6 Am^2/Kg, 63.3 Am^2/Kg, 78.4 Am^2/Kg, and 209 Am^2/Kg for samples reacted at 100°C, 150°C, 200°C, or 250°C, respectively. The high M_s value calculated for Fe_3O_4 coating of the sample reacted at 250°C was much greater than the M_s value for bulk Fe_3O_4 (~90 Am^2/Kg [33]). The large value could indicate that some of the pollen mass was lost during the MWHT reaction, so that the percent mass of the coating, compared to the underlying pollen template may be different for the MWHT reacted samples and as coated samples. The remanent magnetization M_r values of the oxide coatings were 0.139 Am^2/Kg, 1.10 Am^2/Kg, 3.83 Am^2/Kg, and 15.8 Am^2/Kg for samples reacted at 100°C, 150°C, 200°C, or 250°C, respectively.

To investigate the effect of crystallite-size on the longer-range magnetic force, the attraction force between various crystallite sized Fe_3O_4-coated sunflower grains and a permanent magnet Ni-Nd substrate was evaluated by AFM. The force measurements were conducted at a lateral distance of ~300 μm from the edge of a disk-shaped Ni-Nd magnet and measured at height intervals of 50 μm from the magnet surface. The force of attraction of the magnetite-coated pollen particles was then measured as a function of vertical distance from the substrate surface (i.e., at intervals of every 50 μm). The force-distance curves for the 100°C, 150°C, 200°C, and 250°C specimens can be seen in Figure 115. The adhesion results followed the same trend as the SQUID data for the samples reacted at 100°C, 150°C, and 200°C, with increasing magnetic adhesion values observed

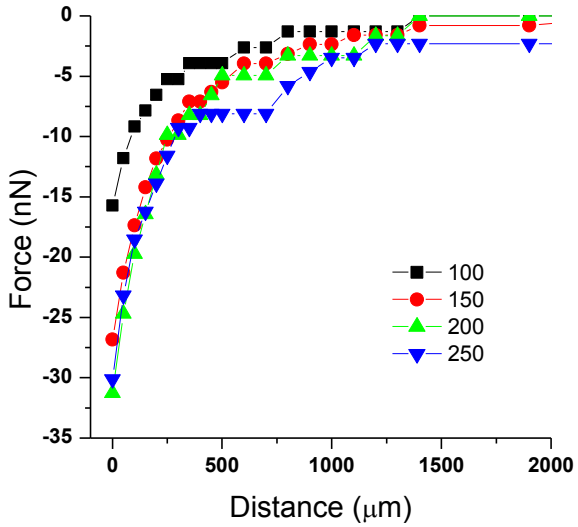

Figure 115: AFM measurement of the magnetic adhesion force vs. distance for Fe_3O_4 coated sunflower grains attached to a probe on a Ni-Nd substrate. The force was obtained at a lateral position ~300 μm from the edge of the disk-shaped Ni-Nd substrate.

for samples with enhanced magnetic (M_r, M_s, and H_c) properties. However, the force of attraction of specimens reduced at 200°C and 250°C were similar, which was somewhat surprising, given the differences in the M_R and M_S values observed in Figure 114. This discrepancy may be due to a damaged pollen grain with parts of the coating missing or other possible defects. By increasing the sample number tested from 1 pollen grain per MWHT condition to 3-5 pollen grains or greater per MWHT condition, improved statistical analyses may be obtained. Note: the results described in Section 4.4.4 were developed and performed in collaboration with Donglee Shin and Julianne Robbins, Georgia Institute of Technology, Atlanta, GA, USA).

4.5. *Concluding remarks*

A new low-temperature (70°C) process for generating nanocrystalline magnetite-bearing pollen particles has been developed. After surface sol-gel, layer-by-layer conformal deposition of Fe-O onto sunflower pollen grains (with the use of Fe(III)

isopropoxide), the grains were exposed to an aqueous hydrazine (N_2H_4) solution at 70°C to allow for partial reduction of the oxide coating and crystallization of magnetite, Fe_3O_4. XRD, SAED, HRTEM, SQUID, and optical analyses were consistent with the generation of nanocrystalline (~4 nm) Fe_3O_4-bearing coatings on the pollen grains. Varying the number of applied SSG coating cycles allowed for control of the magnetic properties of the coated pollen grains. In addition the low temperature and aqueous nature of the reaction process resulted in little or no shrinkage of the type associated with organic pyrolysis at $\geq 200^{o}C$.

Magnetite (Fe_3O_4)-coated pollen replicas, with tailored ultrafine crystal sizes, have been synthesized from maghemite (γ-Fe_2O_3) coated pollen (generated via LbL SSG deposition) via a microwave hydrothermal (MWHT)/hydrazine reduction process conducted for 90 min at a peak temperature in the range of only 100-250^{o}C. Use of such low-temperature treatments allowed the pollen template to be retained, which, in turn resulted in negligible change in the coated pollen morphology and size. Full pattern profile fitting of the XRD patterns was conducted to evaluate the full-width-at-half-maximum values for a number of magnetite diffraction peaks. Williamson-Hall plots were then used to determine the average magnetite crystal size for a given MWHT treatment. The average crystal diameter, in the range of 3 to 12 nm, was found to exhibit a monotonic (near linear) correlation with the MWHT treatment temperature.

The influence of thermal treatment/crystal size on the magnetic hysteresis and magnetic force of attraction of ultrafine-grained, magnetite-coated pollen particles has been examined. SQUID magnetometry has revealed that the induced magnetization, for the Fe_3O_4-coated particles, at an applied field of 5 T could be altered by more than an

order of magnitude with an increase in MWHT temperature from 100 to 250^{o}C (or with an increase in average magnetite crystal diameter from 3 to 12 nm). The remanent magnetization could be increased by more than 2 orders of magnitude over this temperature/crystal size range. Initial AFM measurements have indicated that the magnetic force of attraction of the ultrafine-grained Fe_3O_4-coated pollen grains increased with an increase in average crystal size, although less dramatically than expected by the magnetic hysteresis measurements.

4.6. ***References***

[1] C. M. Lee, H. J. Jeong, S. T. Lim, M. H. Sohn, and D. W. Kim, "Synthesis of Iron Oxide Nanoparticles with Control over Shape Using Imidazolium-Based Ionic Liquids," *ACS Appl. Mater. Interfaces,* vol. 2, p. 756, 2010.

[2] L. Motte, F. Benyettou, C. de Beaucorps, M. Lecouvey, I. Milosevic, and Y. Lalatonne, "Multimodal superparamagnetic nanoplatform for clinical applications: immunoassays, imaging & therapy," *Faraday Discuss,* vol. 149, p. 211, 2011.

[3] N. Tran and T. J. Webster, "Magnetic nanoparticles: biomedical applications and challenges," *J. Mater. Chem.,* vol. 20, p. 8760, 2010.

[4] R. Dronskowski, "The Little Maghemite Story A Classic Functional Material," *Adv. Funct. Mater.,* vol. 11, 2001.

[5] R. M. Cornell and U. Schwertmann, *The Iron Oxides*: Weinheim: VCH Verlagsgesellschaft, 1996.

[6] J. d. Vicente, D. J. Klingenberg, and R. Hidalgo-Alvarez, "Magnetorheological fluids: a review," *Soft Matter,* vol. 7, p. 3701, 2011.

[7] K. Nandy, S. Chaudhuri, R. Ganguly, and I. K. Puri, "Analytical model for the magnetophoretic capture of magnetic microspheres in microfluidic devices," *J. Magn. Magn. Mater.,* vol. 320, p. 1398, 2008.

[8] S. Rudge, C. Peterson, C. Vessely, J. Koda, S. Stevens, and L. Catterall, "Adsorption and desorption of chemotherapeutic drugs from a magnetically targeted carrier (MTC)," *J. Controlled Release,* vol. 74, 2001.

[9] A. S. Wadajkar, S. Santimano, L. Tang, and K. T. Nguyen, "Magnetic-based multi-layer microparticles for endothelial progenitor cell isolation, enrichment, and detachment," *Biomater.,* vol. 35, p. 654, 2014.

[10] C. Gosse and V. Croquette, "Magnetic Tweezers: Micromanipulation and Force Measurement at the Molecular Level," *Biophys. J,* vol. 82, p. 3314, 2002.

[11] A. Rida and M. A. M. Gijs, "Manipulation of Self-Assembled Structures of Magnetic Beads for Microfluidic Mixing and Assaying," *Anal. Chem.,* vol. 76, p. 6239, 2004.

[12] J. C. Love, A. R. Urbach, M. G. Prentiss, and G. M. Whitesides, "Three-dimensional self-assembly of metallic rods with submicron diameters using magnetic interactions," *J. Am. Chem. Soc,* p. 12696, 2003.

[13] W. Wen, N. Wang, D. W. Zheng, C. Chen, and K. N. Tu, "Two- and three-dimensional arrays of magnetic microspheres," *J. Mater. Res.,* vol. 14, p. 1186, 1999.

[14] R. M. Erb, R. Libanori, N. Rothfuchs, and A. R. Studart, "Composites Reinforced in Three Dimensions by Using Low Magnetic Fields," *Science,* vol. 335, p. 199, 2012.

[15] F. H. Rhines, W. A. Johnson, and W. A. Anderson, *Trans. AIME,* vol. 147, p. 205, 1942.

[16] S. K. El-Rahaiby and Y. K. Rao, "The Kinetics of Reduction of Iron Oxides at Moderate Temperatures," *Metallurgical Transactions B,* vol. 10B, 1979.

[17] X. Huang, X. Zhou, K. Qian, D. Zhao, Z. Liu, and C. Yu, "A magnetite nanocrystal/graphene composite as high performance anode for lithium-ion batteries," *Journal of Alloys and Compounds,* vol. 514, pp. 76-80, 2012.

[18] I. Milosevic, H. Jouni, C. David, F. Warmont, D. Bonnin, and L. Motte, "Facile Microwave Process in Water for the Fabrication of Magnetic Nanorods," *The Journal of Physical Chemistry C,* vol. 115, pp. 18999-19004, 2011.

[19] E. Domínguez, J. A. Mercado, M. A. Quesada, and A. Heredia, "Pollen sporopollenin: degradation and structural elucidation," *Sex Plant Reprod,* vol. 12, pp. 171-178, 1999.

[20] H. E. M. Dobson, " Survey of pollen and pollenkitt lipids - chemical cues to flower visitors," *Am. J. Bot.,* vol. 75, p. 170, 1988.

[21] M. R. Weatherspoon, M. B. Dickerson, G. Wang, Y. Cai, S. Shian, S. C. Jones, *et al.*, "Thin, conformal, and continuous SnO_2 coatings on three-dimensional biosilica templates through hydroxy-group amplification and layer-by-layer alkoxide deposition," *Angew Chem Int Ed Engl,* vol. 46, pp. 5724-5727, 2007.

[22] M. R. Weatherspoon, Y. Cai, M. Crne, M. Srinivasarao, and K. H. Sandhage, "3D rutile titania-based structures with morpho butterfly wing scale morphologies," *Angew Chem Int Ed Engl*, vol. 47, pp. 7921-7923, 2008.

[23] G. Wang, Y. Fang, P. Kim, A. Hayek, M. R. Weatherspoon, J. W. Perry, *et al.*, "Layer-By-Layer Dendritic Growth of Hyperbranched Thin Films for Surface Sol-Gel Syntheses of Conformal, Functional, Nanocrystalline Oxide Coatings on Complex 3D (Bio)silica Templates," *Advanced Functional Materials*, vol. 19, pp. 2768-2776, 2009.

[24] J. P. Vernon, N. Hobbs, Y. Cai, A. Lethbridge, P. Vukusic, D. D. Deheyn, *et al.*, "3D photoluminescent lanthanide-doped barium titanate structures synthesized by coating and shape-preserving reaction of complex-shaped bioorganic templates," *Journal of Materials Chemistry*, vol. 22, pp. 10365-10940, 2012.

[25] M. J. Fransen, "On The Influence of Generator and Detector Settings in X-ray Powder Diffractometry," *Adcancs in X-ray Analysis*, vol. 48, pp. 143-149, 2005.

[26] R. Grau-Crespo, A. Y. Al-Baitai, I. Saadoune, and N. H. D. Leeuw, "Vacancy ordering and electronic structure of γ-Fe_2O_3 (maghemite): a theoretical investigation," 2008.

[27] C.V. Gopal Reddy, K. K. Seela, and S. V. Manorama, "Preparation of γ-Fe_2O_3 by the hydrazine method Application as an alcohol sensor," *International Journal of Inorganic Materials*, vol. 2, pp. 301–307, 2000.

[28] (October 15). Available: https://en.wikipedia.org/wiki/Magnetite

[29] J. P. Chen, C. M. Sorensen, K. J. Klabunde, G. C. Hadjipanayis, E. Devlin, and A. Kostikas, "Size-dependent magnetic properties of fine particles synthesized by coprecipitation," *Physical Review B*, vol. 54, pp. 9288-9296, 10/01/ 1996.

[30] Q. Song and Z. J. Shang, "correlation between spin orbital coupling and the superparamagnetic praperties in magnetite and cobalt ferrite spinel nano crystals," *J. Phys. Chem. B*, pp. 11205-11209, 2006.

[31] V. Kumar, A. Rana, M. S. Yadav, and R. P. Pant, "Size-induced effect on nano-crystalline $CoFe_2O_4$," *Journal of Magnetism and Magnetic Materials*, vol. 320, pp. 1729-1734, 2008.

[32] D. V. Karpinsky, R. C. Pullar, Y. K. Fetisov, K. E. Kamentsev, and A. L. Kholkin, "Local probing of magnetoelectric coupling in multiferroic composites of $BaFe_{12}O_{19}$–$BaTiO_3$," *Journal of Applied Physics*, vol. 108, p. 042012, 2010.

[33] S. Chikazumi, *Physics of Ferromagnetism*. New York: Oxford Univiersity Press, 1997.

CHAPTER 5 : **Mechanism of Reduction of Maghemite to Magnetite**

5.1. ***Summary***

A detailed investigation of the kinetic mechanism governing the low temperature (<90°C) reduction of nanocrystalline maghemite thin films into magnetite is presented. In this work, a quartz crystal microbalance was used for in-situ monitoring of the aqueous reduction process. The oxidation rate was found to be governed by two different diffusion regimes: a grain boundary diffusion-dominated region and lattice diffusion-dominated region. The kinetic model yielded diffusion constants of 2.07 +/- 1.04*$10^{-12}$$cm^2$/sec for oxygen along grain boundaries and 1.49 +/- 0.41*$10^{-18}$$cm^2$/sec for iron through the lattice, which were consistent with previously reported values.

5.2. ***Introduction***

Maghemite (γ-Fe_2O_3) is metastable polymorph of iron oxide at temperatures below 300°C.[1, 2] Maghemite is a naturally-occurring mineral and found in soil as a weathering product of magnetite (Fe_3O_4).[3] Maghemite exhibits a spinel like crystal structure with an array of vacancies in order to maintain charge neutrality. The maghemite structure can be obtained by creating 8/3 vacancies out of the 16 octahedral sites Fe sites in a cubic spinel structure. The structure of maghemite can be approximated as a cubic unit cell with F*d3m* space group by the following equation:

$$(Fe^{3+})_8\left[Fe^{3+}_{5/6}\square_{1/6}\right]_{16}O^{2-}_{32} \qquad (5.1)$$

The partial reduction of maghemite leads to the full occupation of the octahedral sites and formation of the inverse spinel magnetite (Fe_3O_4). The maghemite to magnetite transformation also involves a transition from the octahedral crystal structure to that of a

cubic crystal structure. The crystal structures of maghemite and magnetite can be seen in Figure 116 demonstrating the tripled spinel structure and location of the ordered octahedral vacancies. The unit cell is shifted from the origin to match that of the spinel structure of magnetite, as it is not immediately apparent to see the spinel structure, with a unit cell generated from (000) with the P4_12_12 space group.[4]

The γ-Fe_2O_3 to Fe_3O_4 transition is well described using the spinel notation, as below:

$$(Fe_9^{+3})[Fe_{15}^{+3}\square_3]O_{36} + 2N_2H_{4(aq)} \leftrightarrow (Fe_8^{+3})[Fe_8^{+3}Fe_8^{+2}]O_{32} + 4H_2O + 2N_2(g) \quad (5.2)$$

where the brackets ( ) and [ ] designate tetrahedral and octahedral sites, respectively, corresponding to 8a and 16d Wyckoff positions in space group F$d3m$.[5] A schematic of

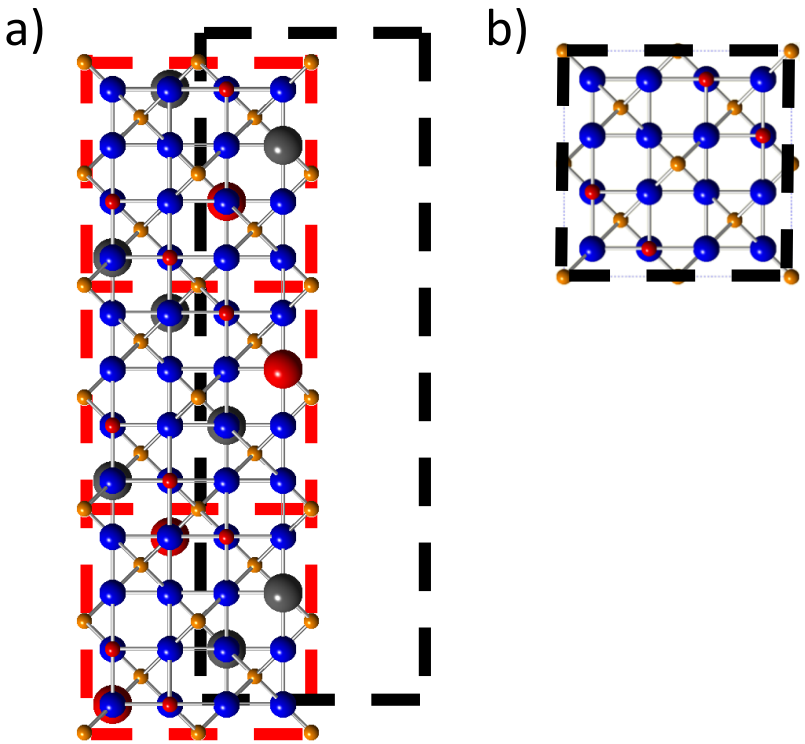

Figure 116: a) (100) orientation of a maghemite unit cell offset by ($a^1/_2$, $b^5/_{24}$, $-c^1/_{24}$) from the origin. The black box represents the initial unit cell dimensions for the P4_12_12 space group, red boxes represent unit cells for the FCC spinel structure with an F$d3m$ symmetry, b) (100) orientation of a magnetite unit cell. The blue spheres represent oxygen atoms, orange spheres are iron atoms at tetrahedral sites, small red spheres are iron atoms at octahedral sites, large red and grey spheres represent octahedral sites with ordered iron atoms and vacancies located at the Wyckoff 4b sites.

the general structure is shown in Figure 116.

While little work has been conducted on the transformation of maghemite into magnetite, the main mechanism for the reverse reaction has been previously studied and a number of experimental and theoretical studies have proposed that the oxidation process is controlled via cation diffusion through maghemite from the core towards the surface as the material is oxidized.[6-11] Cation diffusion was thought to dominate due to the difference in effective ionic radii between Fe^{2+} and Fe^{3+} and that for O^{2-} (0.077 nm, 0.065 nm, and 0.140 nm, respectively). Ion radius values were obtained using an effective ionic radii based on ($^{VI}O^{2-}$) = 0.14 nm).[12] In addition, during oxidation of magnetite, a maghemite film was found to grow on the surface that preserved the oxygen lattice.

5.3. ***Theory***

The net reduction of maghemite into magnetite can be described using one of the following reactions:

$$12\gamma - Fe_2O_3 + 2N_2H_{4(aq)} \leftrightarrow 8Fe_3O_4 + 4H_2O + 2N_2(g) \quad (5.3)$$

or

$$(Fe_9^{+3})[Fe_{15}^{+3}\square_3]O_{36} + 2N_2H_{4(aq)} \leftrightarrow (Fe_8^{+3})[Fe_8^{+3}Fe_8^{+2}]O_{32} + 4H_2O + 2N_2(g) \quad (5.4)$$

where γ-Fe_2O_3 and Fe_3O_4 are solid reactants and products, respectively, hydrazine is in solution, and H_2O and N_2 gas are the byproducts. This reaction is highly favorable for α-Fe_2O_3 with a $\Delta G°_{rxn}$ of -263.1 kJ mol^{-1} at 65°C and should be even higher for the metastable phase of γ-Fe_2O_3 (HSC 5.1 software). Two mass transport mechanisms can be envisioned to describe the reduction process. The first is where oxygen outward diffusion through the magnetite product layer is the rate-limiting step. This mechanism is shown in

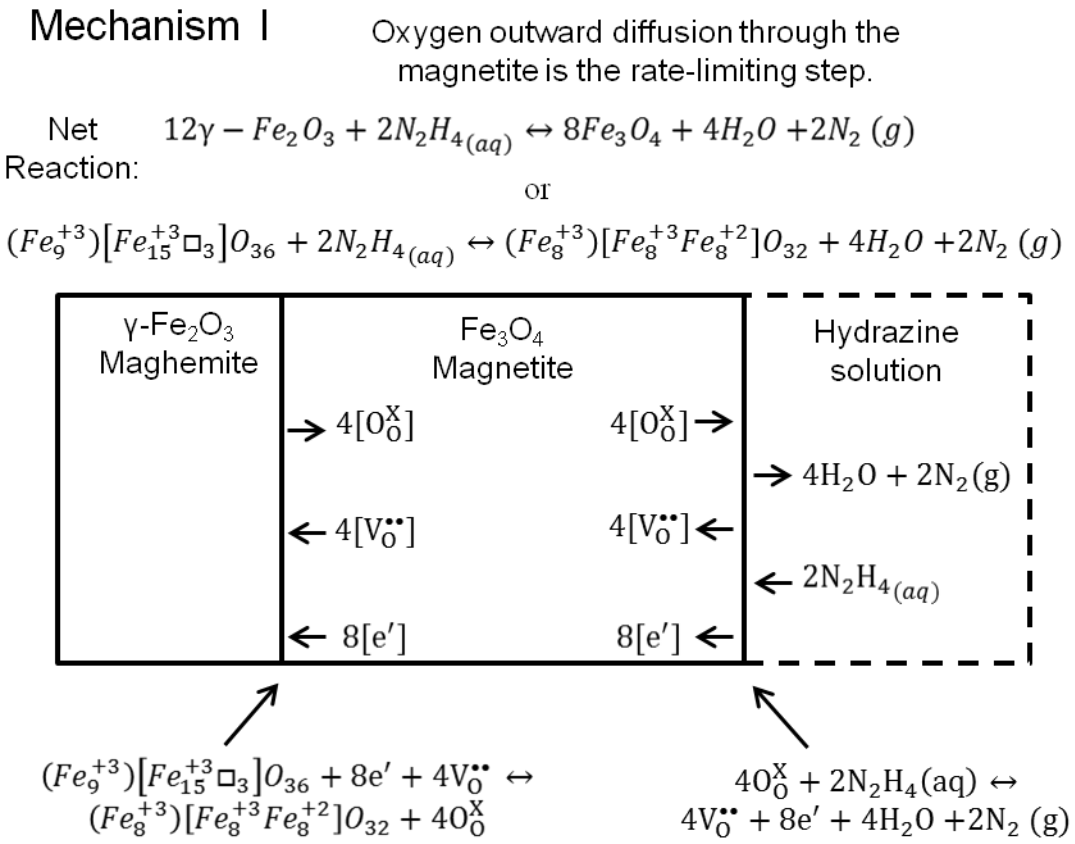

Figure 117: Schematic for reaction mechanism I where oxygen outward diffusion through the magnetite is the rate-limiting step.

Figure 117. For mechanism I, oxygen anions in magnetite are reacted with hydrazine at the solid- liquid interface to form water, nitrogen gas, free electrons and oxygen vacancies. The oxygen vacancies then diffuse toward the magnetite/maghemite solid-solid interface. At the solid-solid interface, electrons and the oxygen vacancies are consumed as maghemite transforms into magnetite. With mechanism I, 2 mols of hydrazine are consumed at the liquid-solid interface; while 12 mols of maghemite are consumed and 8 mols of magnetite are generated at the solid-solid interface.

An alternative path can also be envisioned with Fe^{+2} and Fe^{+3} cations diffusion inward through magnetite as the rate-limiting step. This mechanism is shown in Figure 118. For mechanism II, magnetite is reacted with hydrazine at the solid-liquid interface to

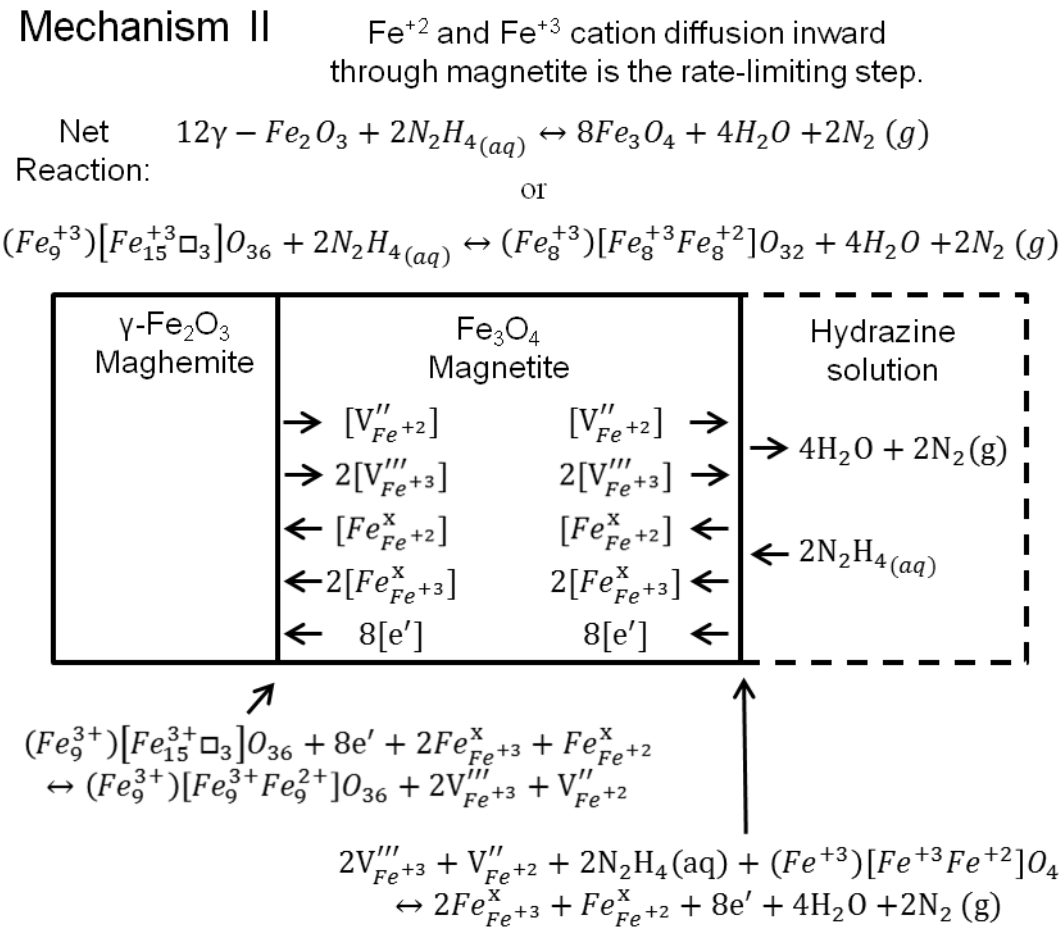

Figure 118: Schematic for reaction mechanism II where iron cation inward diffusion through magnetite is the rate limiting step.

form water, nitrogen gas, and free electrons. During the reaction process, iron cations exchange with vacancies and diffuse toward the magnetite/maghemite solid-sold interface. At the solid-solid interface, electrons and the diffusing iron cations are consumed as maghemite transforms into magnetite. With mechanism II, 1 mol of magnetite and 2 mols of hydrazine are consumed at the liquid-solid interface; while 12 mols of maghemite are consumed and 9 moles of magnetite are generated at the solid-solid interface.

Among the well-known kinetic models, the shrinking core model (SCM) may be used to describe the reduction process.[13] The SCM has been used to describe the

reduction of α-Fe_2O_3 into magnetite where the rate-limiting step was governed by a reaction controlled process.[14] The shrinking core model describes a diminishing solid reactant covered by a growing, continuous, coherent layer of product during reaction with a fluid or gas. The diminishing solid reactant for the system being investigated is the maghemite coating, the growing solid product is magnetite, and the reaction fluid contains hydrazine. The potential rate-limiting steps for the SCM can then be described as follows (Figure 119):

1. Liquid phase mass transfer of a reactant (e.g., prior to N_2H_4 reaction) or product species;
2. Diffusion through a solid product layer of a reactant or product species;
3. Chemical reaction control (e.g., at the magnetite/maghemite interface or at the hydrazine/magnetite interface).

These steps (as illustrated in Figure 119) are assumed to occur in series, with a single rate-limiting step among these being a very slow step.[13] Within each serial step, there are also parallel steps. For example, in the case of transport through magnetite, iron cation inward diffusion and oxygen anion outward diffusion may both be occurring in parallel. For parallel processes, a single rate-liming step refers to a step that is much faster than the others. The governing equations, for flat plate geometry, of each potential rate-limiting step can be used to evaluate the rate-limiting mechanism. Consider the following general reaction (equation 5.5) with a flat plate-shaped solid reactant, $B_{(s)}$:

$$A_{(aq)} + bB_{(s)} \rightarrow cC_{(s)} + dD_{(aq)} + eE_{(aq)} \quad (5.5)$$

where b, c, d, and e are the stoichiometric coefficients of the solid reactant B, the solid product C, and the aqueous products D and E, respectively. A represents N_2H_4(aq), B is

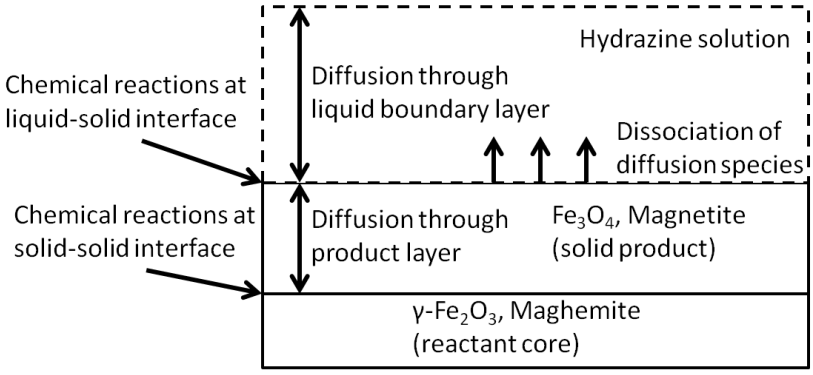

Figure 119: Schematic of possible rate-limiting steps during the hydrazine-induced reduction of maghemite into magnetite.

maghemite, C is magnetite, D is N_2(aq), and E is H_2O.

For a system with diffusion through a concentration boundary layer in the liquid as the rate-limiting step, the following equations can be used to describe the rate.[13]

$$\frac{t}{\tau_{film}} = X_b \tag{5.6}$$

$$\tau_{film} = \frac{\rho_B L}{b k_g C_{A(aq)}} \tag{5.7}$$

where t is time, τ_{film} is the time for complete conversion of the film, X_b is percent reacted, $C_{A(aq)}$ is the saturation concentration of the product species in solution at the liquid/solid interface, ρ_B is the density of the reactant oxide B, L is half the thickness of the plate, and k_g is the mass transfer coefficient of the aqueous species. The extent of reaction of the film is determined by measuring the ratio of unreacted zone thickness, ℓ, to the starting thickness, L, and then calculated using the definition $X_B = 1–(\ell/L)$. For diffusion through a concentration boundary layer of constant thickness with time, X_B should increase linearly with time, t.[13]

If diffusion through the solid product layer is rate-limiting (Figure 120 left), then the following equation is one possibility that may be used to describe the solid B consumption rate:

$$\frac{t}{\tau_{diffusion}} = X_B^2 \tag{5.8}$$

$$\tau_{diffusion} = \frac{\rho_B L^2}{2b\mathrm{D}_e C_{Aaq}} \tag{5.9}$$

where D_e is the solid-state diffusion coefficient of a particular species across the solid product layer (in this case, iron ions or oxygen anions through magnetite). This will lead to X_B increasing at a parabolic rate with respect to reaction time, t. For a spherical system, instead of planar system, equations 5.8 and 5.9 become the following (Figure 120 right):

$$\frac{t}{\tau_{diffusion}} = 1 - 3(1 - X_B)^{2/3} + 2(1 - X_B) \tag{5.10}$$

$$\tau_{diffusion} = \frac{\rho_B R^2}{2b\mathrm{D}_e C_{Aaq}} \tag{5.11}$$

where R is the radius of the sphere and the rest of parameters are the same for that of the planar case. For the final case, in which a chemical reaction at either the magnetite/maghemite or the maghemite/liquid interface is the rate limiting step, then the following equations can be used.[13]

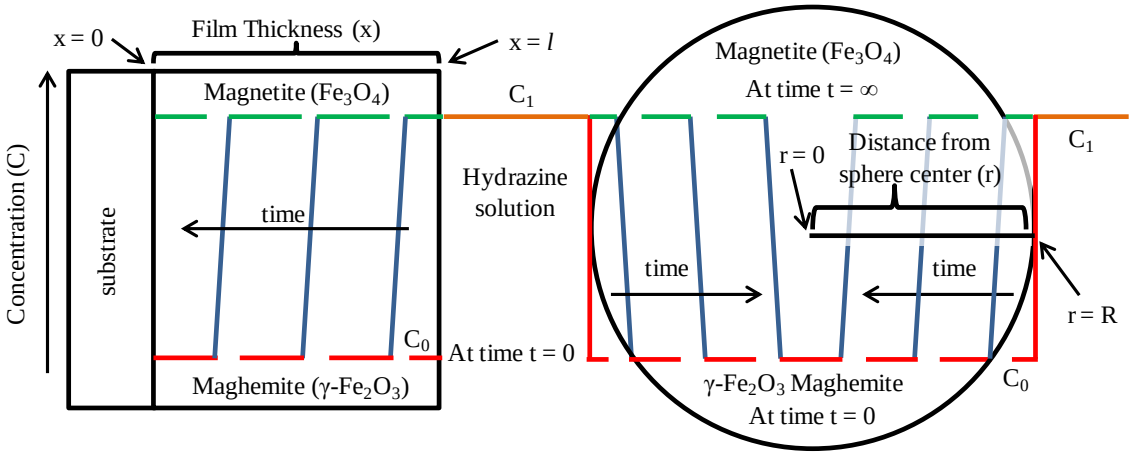

Figure 120: Schematic for the initial boundary conditions for steady state diffusion through based on a SCM: for (left) plane sheet or membrane geometry with thickness *l* and (right) sphere geometry with radius R, initial film concentration C_0, and surface concentration C_1. The red line represents concentration for maghemite, blue lines are intermediate concentration profiles at different times, green line represents concentration at t = ∞, when the sample is fully reacted into magnetite, orange represents the concentration at the surface.

$$\frac{t}{\tau_{reaction}} = X_B \tag{5.12}$$

$$\tau_{reaction} = \frac{\rho_B L}{bk'' C_i} \tag{5.13}$$

where k'' is a first-order rate constant with respect to a species i. If the SCM adequately explains the reduction process, then the reduction rate should be parabolic if solid-state lattice diffusion is the rate-limiting step, or linear if liquid-phase diffusion (through a concentration boundary layer of constant thickness with time) or a chemical reaction at the maghemite/magnetite or magnetite/liquid interface is the rate-limiting step.

The shrinking core model does have its limitations and may not match reality precisely. For example, reactions may occur along a diffuse front rather than along a sharp interface, thus giving behavior intermediate between the shrinking core and the continuous reaction models. The model also does not describe fast reactions in which a significant thermal gradient accrues within the solid reaction product or between reactant, product, and the bulk fluid. There are also other some exceptions, such as: "when [a] solid is converted by the action of heat, and without needing contact with gas [or liquid]. Baking bread, boiling missionaries, and roasting puppies are mouthwatering examples of such reactions."[13] If a linear relation is found for a planar geometry, then the reduction may be limited by a chemical reaction either at a solid-liquid or solid-solid interface. If a process does not have a linear relation with time, then diffusion of a reactant or product species may be the rate-limiting step and diffusion models will need to be investigated.

Previous studies on the oxidation of magnetite to maghemite have suggested that, in dry [5, 10] or aqueous [9] conditions, the rate-limiting step is a non-steady-state outward diffusion of iron cations. Prior results suggest that there is no sharp interface between magnetite and maghemite,[15] which is one of the assumptions needed for the

SCM.[13] Maghemite and magnetite form a complete series of solid solutions.[15] Natural magnetite can contain excess Fe_2O_3 and form solid solution crystals with a composition of Fe_3O_4-Fe_2O_3.[16] The solid solution between the two phases allowed the authors in references [10] and [5] to monitor the kinetics as samples were oxidized from magnetite to maghemite by comparing the change in relatively stress free lattice parameters vs. time. Assuming an analogous inward iron diffusion mechanism is responsible for the reduction of maghemite into magnetite, and that the size change after reduction is negligible, the non-steady state diffusion of non-interacting ions through a plane sheet can be considered. The following diffusion-related derivations were provided by references [17] and [18]. Linear flow in the x direction can be represented by the following, if $\frac{\partial c}{\partial y} = \frac{\partial c}{\partial z} = 0$.

$$\frac{\partial C}{\partial t} = D\left(\frac{\partial^2 C}{\partial^2 x}\right) \tag{5.14}$$

where D is the diffusion constant, which is independent of the concentration gradient, C is the concentration of the iron species, and x is the position along the thickness direction in the film. Fick's second law (equation 5.14) can be solved with the following equation.

$$C(x,t) = X(x)T(t) \tag{5.15}$$

where X(x) and T(t) separately express spatial and temporal functions of C, respectively, while C is a function of both x and t. In the case of linear flow, equations 5.14 and 5.15 yield:

$$\frac{1}{DT}\frac{\partial T}{\partial t} = \frac{1}{X}\frac{\partial^2 X}{\partial x^2} \tag{5.16}$$

With the separation of variables solution, both sides must be equal to the same function ($-\lambda^2$) as they are independent of each other.

$$\frac{1}{DT}\frac{\partial T}{\partial t} = \frac{1}{X}\frac{\partial^2 X}{\partial x^2} = -\lambda^2 \quad (5.17)$$

Two different ordinary linear differential equations can then be solved (one first order for T(t), and the other second order for X(x)). The solutions to these equations are well known and shown below.

$$T(t) = T_0 exp(-\lambda^2 Dt) \quad (5.18)$$

And

$$X(x) = a \sin \lambda x + b \cos \lambda x \quad (5.19)$$

where T_0, a, and b are constants. Inserting equations 5.18 and 5.19 into equation 5.15 yields a particular solution of the form:

$$C(x,t) = [A \sin \lambda x + \mathrm{B}\cos \lambda x] exp(-\lambda^2 Dt) \quad (5.20)$$

where A = aT_0 and B = bT_0 are constants of integration. Since equation 5.14 is a linear differential equation, its general solution may be obtained by summing solutions of the type of equation 5.20 yielding the following:

$$C(x,t) = \sum_{n=1}^{\infty} [A_n \sin \lambda_n x + \mathrm{B_n}\cos \lambda_n x] exp(-\lambda_n^2 Dt) \quad (5.21)$$

where A_n, B_n, and λ_n are determined by the initial boundary conditions of the particular problem.

For non-steady state diffusion through a plane sheet or membrane, the solution to a concentration gradient in the film can be solved by using the boundary conditions illustrated in Figure 121 and represented in the following equations:

$C = C_1$, $x = \pm l$, $t \geq 0$, (5.22)

$C = f(x) = C_0$ $-l < x < l$, $t = 0$, (5.23)

The boundary conditions demand that,

$A_n = 0$ and $\lambda_n = \frac{n\pi}{l}$, where n = 1, 2, 3, … (5.24)

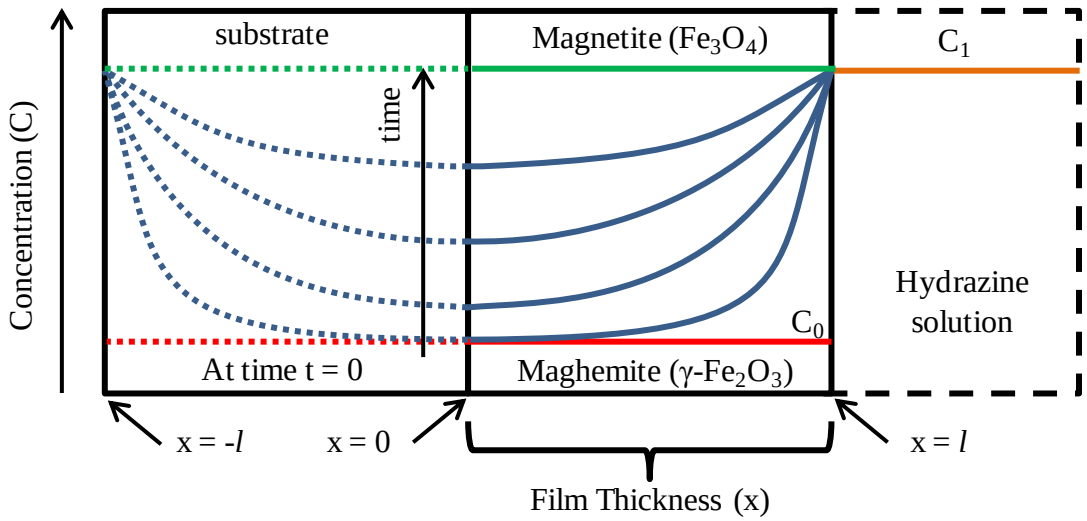

Figure 121: Schematic for the initial boundary conditions for non-steady state diffusion through a plane sheet or membrane of thickness *l*, initial film concentration C_0, and surface concentration C_1. The red line represents concentration for maghemite, blue lines are intermediate concentration profiles at different times, green line represents concentration at t = ∞, when the sample is fully reacted into magnetite, orange represents the concentration at the surface. The dotted lines represented a mirrored concentration profile over x = 0 and were to help solve the initial boundary conditions.

The numbers λ_n are the Eigen values of the plan-sheet problem. Inserting these values into equation 5.21 yields

$$C(x,t) = \sum_{n=1}^{\infty} B_n \cos\left[\frac{n\pi}{l}x\right] \exp\left(-\frac{n^2\pi^2}{l^2}Dt\right) \qquad (5.25)$$

where l is the film thickness, D is the diffusion coefficient, and t is time. The initial condition also requires that

$$f(x) = \sum_{n=1}^{\infty} B_n \cos\frac{n\pi}{l}x \qquad (5.26)$$

where f(x) is a diffusion function. If f(x) is considered equal to a constant C_0 then by multiplying both sides by $\cos\frac{p\pi x}{l}$ from 0 to l the following equation is obtained for n ≠ p..

$$\int_0^l \cos\frac{n\pi x}{l}\cos\frac{p\pi x}{l}dx = 0 \qquad (5.27)$$

The value of this integration is l/2 for $n = p$. Using these orthogonality relations, all terms vanish when n is even. Thus, the following is obtained.

$$B_n = \frac{4C_0}{n\pi}(-1)^{\mathrm{n}} \qquad ; \qquad \mathrm{n} = 1, 3, 5, \ldots \tag{5.28}$$

The final solution of the problem of diffusion into a plane sheet with constant surface concentrations becomes

$$\mathrm{C(x,t)} = \sum_{\mathrm{n}=1}^{\infty} \frac{4C_0(-1)^{\mathrm{n}}}{n\pi} \cos\frac{\mathrm{n}\pi}{l}\mathrm{x} \exp\left(-\frac{\mathrm{n}^2\pi^2}{l^2}\mathrm{Dt}\right) \tag{5.29}$$

The solution for non-steady state diffusion can be rewritten as follows:

$$\frac{\mathrm{C}-\mathrm{C}_0}{\mathrm{C}_1-\mathrm{C}_0} = 1 - \frac{4}{\pi}\sum_{\mathrm{n}=0}^{\infty}\frac{(-1)^{\mathrm{n}}}{2\mathrm{n}+1}\exp\left(\frac{-\mathrm{D}(2\mathrm{n}+1)^2\pi^2\mathrm{t}}{4l^2}\right)\cos\frac{(2\mathrm{n}+1)\pi\mathrm{x}}{2l} \tag{5.30}$$

where C_0 is a uniform initial concentration in the region $-l < x < l$ and the surface concentration is kept at C_1. Equation 5.30 can be validated by testing the initial boundary condition used in equations 5.22 - 5.23 and illustrated in Figure 121. When $x = \pm l$ and $C = C_1$, $\cos([2n+1]\pi x/2l)$ becomes 0 and both sides equal 1. If M_t denotes the total amount of diffusing substance which has entered the sheet at time t and M_∞ the corresponding quantity after infinite time, then:

$$\frac{\mathrm{M_t}}{\mathrm{M}_\infty} = -\int_0^{\mathrm{t}} \mathrm{D}\left(\frac{\partial \mathrm{C}}{\partial \mathrm{x}}\right)_{\mathrm{x}=l} \mathrm{dt} \Big/ -\int_0^{\infty} \mathrm{D}\left(\frac{\partial \mathrm{C}}{\partial \mathrm{x}}\right)_{\mathrm{x}=l} \mathrm{dt} \tag{5.31}$$

From equation 5.30, when $x = l$, the following is obtained:

$$\frac{\partial \mathrm{C}}{\partial \mathrm{x}} = -\frac{8}{\pi^2}\sum_{\mathrm{n}=0}^{\infty}\frac{1}{(2\mathrm{n}+1)^2}\exp\left(\frac{-\mathrm{D}(2\mathrm{n}+1)^2\pi^2\mathrm{t}}{4l^2}\right) \tag{5.32}$$

By inserting equation 5.32 into equation 5.31 and integrating,

$$\frac{\mathrm{M_t}}{\mathrm{M}_\infty} = 1 - \sum_{\mathrm{n}=0}^{\infty}\frac{8}{(2\mathrm{n}+1)^2\pi^2}\exp\left(\frac{-\mathrm{D}(2\mathrm{n}+1)^2\pi^2\mathrm{t}}{4l^2}\right) \tag{5.33}$$

The corresponding solution can then be rewritten as:

$$\frac{\mathrm{M_t}}{\mathrm{M}_\infty} = 2\left(\frac{\mathrm{Dt}}{l^2}\right)^{\frac{1}{2}}\left\{\pi^{-\frac{1}{2}} + 2\sum_{\mathrm{n}=1}^{\infty}(-1)^{\mathrm{n}}\mathrm{ierfc}\left(\frac{\mathrm{n}l}{\sqrt{(\mathrm{Dt})}}\right)\right\} \tag{5.34}$$

where ierfc denotes the inverse of the complementary error function.

With the assumption that diffusion of cations or anions, electrons or holes, vacancies or other species is the rate-limiting step of for the conversion of maghemite into magnetite, the fractional conversion can be found, An approximation for the diffusion with plane sheet geometry is described by:

$$\frac{M_t}{M_\infty} = 2\pi^{-\frac{1}{2}}\left(\frac{Dt}{l^2}\right)^{\frac{1}{2}} \quad (5.35)$$

where M_t is the quantity of the rate-limiting diffusion species that has diffused inward/outward after time t; M_∞ is the corresponding quantity after infinite time; D = diffusion constant; *l* is the thickness of the plate. Therefore, a plot of (M_t/ M_∞) versus $t^{1/2}$ should have a linear dependence and can be fitted to a straight line. The diffusion constant is obtained from the slope if the film thickness is known.

However, the previously-derived equations are only relevant for a single type of rate-limiting diffusion mechanism. With nanometer sized grains, it is expected that grain boundary diffusion mechanism maybe vital in describing the reduction of a polycrystalline thin film. For many oxide materials, such as NiO, the metal cations migrate through the bulk oxide lattice as well as diffuse through an array of low-resistance paths associated with crystallite boundaries.[19] Diffusion in the grain boundaries can be orders or magnitude higher than that within the bulk crystalline lattice.[5] In addition, certain species may diffuse preferentially in either the grain boundaries or bulk crystalline lattice. For polycrystalline materials, the different diffusion rates through the grain boundaries and lattice may increase as the temperature decreases. However, temperature is not the only parameter that affects grain boundary diffusion; that is the grain boundary width can also affect the diffusion rate.[5]

For materials for which grain boundary diffusion cannot be neglected, equation 5.35 needs to be adjusted to include both lattice diffusion and grain boundary diffusion. By replacing the generic diffusion term, D, with an effective diffusion term, D_{eff}, that contains lattice and grain boundary diffusion, the following equation is obtained:

$$\frac{M_t}{M_\infty} = 2\pi^{-\frac{1}{2}}\left(\frac{D_{eff}t}{l^2}\right)^{\frac{1}{2}} \tag{5.36}$$

where the effective diffusion coefficient D_{eff} represents a weighted average of the crystal or lattice diffusivity, D, and grain boundary diffusivity, D_{GB}, after taking into account the grain boundary width and is given by the following equation:

$$D_{eff} = fD_{gb} + (1 - f)D \tag{5.37}$$

where f is the cross-sectional area fraction of available sites lying within the low resistance paths or grain boundaries in the material. For conditions in which the lattice diffusion can be ignored and only grain boundary diffusion is dominant, equation 5.37 simplifies to:

$$D_{eff} = fD_{gb} \tag{5.38}$$

In order to express the area fraction of sites located on the grain boundaries or on short-circuit paths at any time, a first order approximation may be used where the crystallites are considered as small, space-filling cubes with a side of length G. When the grain boundary width, δ, is known or approximated, the area fraction for the grain boundaries can be calculated as follows:

$$f = \frac{Area_{GB}}{Area_{tot}} \tag{5.39}$$

$$f = \frac{G^2 - (G - \delta)^2}{G^2} \tag{5.40}$$

The grain boundary width, δ, has been considered to have values on the order of 0.5 nm to 1.0 nm.[18, 19] For previous work on Co_3O_4 , which has a spinel structure similar to that of Fe_3O_4, the grain boundary has been assumed to equal 0.5 nm.[20] In cases where G >> δ, the area fraction of grain boundaries can be approximated as:

$$f \sim \frac{2\delta}{G} \tag{5.41}$$

The error between the approximation, equation 5.40, and equation 5.41 is less than 5% for grain sizes above 5 nm. A plot comparing the two equation can be seen in Figure 122 a. For hexagonal shaped grains, where the grain size, G, is twice the length of an edge of the hexagon, the volume fraction approximation can be seen below in equation 5.41. The comparison of the grain size dependence for cubic and hexagonal approximations (equation 5.41 and equation 5.42) can be seen in Figure 122 b:[20]

$$f \sim \frac{2.3\delta}{G} \tag{5.42}$$

The area faction models presented so far are for grain boundaries with columnar

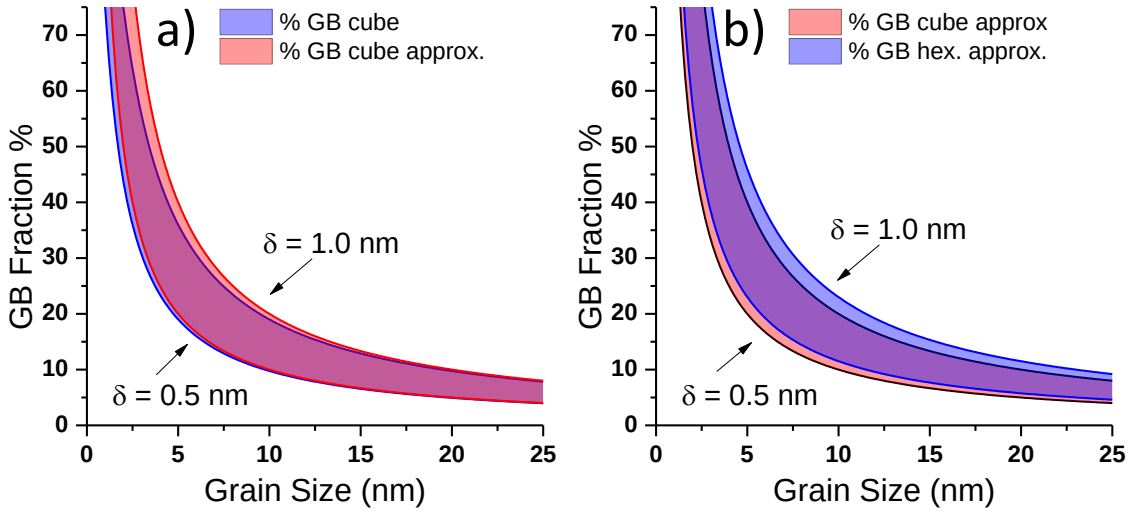

Figure 122: a) Grain boundary fractional cross-sectional area percent for cubic grains for the actual value (blue) and the approximation (red) with a grain boundary width varying from 0.5 nm to 1.0 nm (shaded region) b) Grain boundary fractional cross-sectional area percent for a cubic grain approximation (red) and hexagonal grain approximation (blue) with a grain boundary width varying from 0.5 nm to 1.0 nm (shaded region)

structures which are parallel to the diffusion direction and may not be valid for randomly oriented nano grain material. An average diffusion angle may be used to compensate for the extra distance needed to travel through the film for randomly oriented grains compared to the ideal case of oriented columnar crystals.

For samples with 4 nm sized grains and a grain boundary width of 0.5 nm, 4 extreme cases can be envisioned in 2-D (Figure 123). For grains in the configuration depicted in Figure 123 a, when the edges of square grains are parallel to the diffusion direction and the grains are stacked directly on top of each other with no lateral off-set, the average angle for the deviation length will be 0 and the grain boundary diffusion length will remain the same as the film thickness. Figure 123 b shows square grains whose edges are parallel to the diffusion direction with the grains stacked in a brick-like (off-set) configuration. For grains in this arrangement, the grain boundary diffusion length will be longer than the film thickness and a multiplication factor is needed. The average diffusion deviation angle and increase in diffusion distance for Figure 123 b is ~25° and ~10%, respectively. The grain boundary pathways shown in Figure 123 c and d are similar to that of those shown in Figure 123 a and b, but have been rotated 45° so the grain edges are no longer parallel to diffusion direction. For Figure 123 c, the average grain boundary diffusion deviation angle is ~26° and the grain boundary diffusion distance is 12% longer then the film thickness. For Figure 123 d, the grain boundary diffusion distance increases by 8% and an average diffusion deviation angle of ~22° was found. Depending on the grain orientations and stacking arrangements shown in Figure 123, the effective grain boundary diffusion length may be 12% greater than the film thickness. The average increase in grain boundary diffusion length for Figures 123 a and

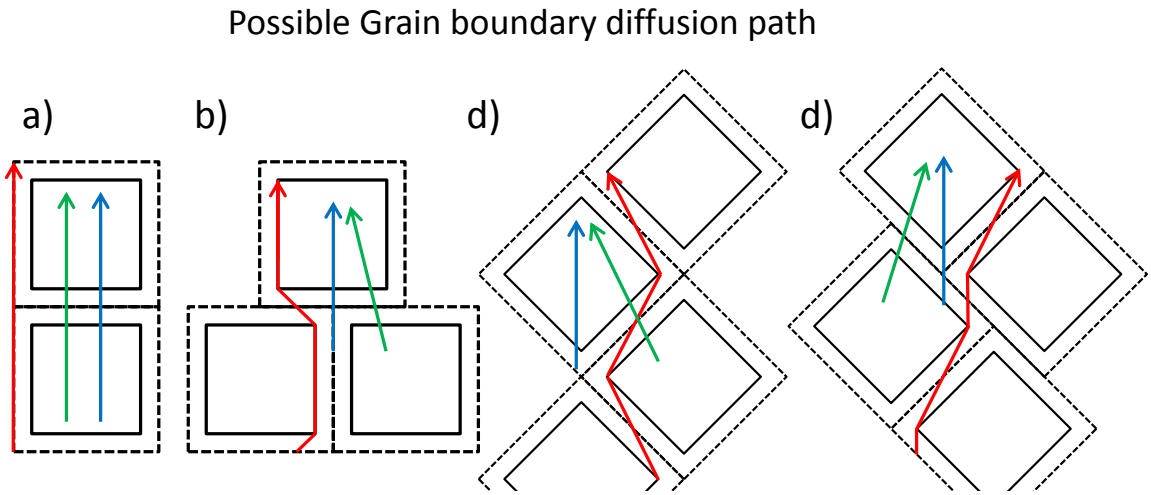

Figure 123: Possible grain boundary diffusion paths for 4 nm cubic grains with a grain boundary width of 0.5 nm. a) grains parallel to diffusion direction with no staggered stacking arraignment, b) grains are parallel to the diffusion direction with a maximum horizontal staggered stacking pattern, c) grains are at a 45° angle compared to diffusion direction with no vertical staggered stacking arraignment, b) grains are at a 45° angle compared to the diffusion direction with a maximum horizontal staggered stacking pattern. The red arrows represent shortest diffusion pathways, green arrows are effective diffusion direction, and blue arrows represent the shortest diffusion length possible.

b is ~5% and for Figures 123 c and d is ~10%. These numbers only serve as rough estimates. Irregular grain sizes and packing arrangements may also affect the average diffusion deviation angle and are beyond the consideration of this work. For this work, an average value for the increased grain boundary diffusion distance of 8% for the four extreme cases was used. That is, an effective film thickness length was set at 108% of the actual film thickness in order to account for the increase in grain boundary diffusion length compared to the film thickness.

While diffusion modeled as a plane front can be describe some cases it cannot describe every case. When lateral leakage from the grain boundaries is limited to distances smaller than the average grain size, diffusion can be described by using a spherical diffusion model, similar to the oxidation of individual/spherical metal particles (Figure 124). The solution for diffusion in a sphere can be obtained in a manner similar to that of a thin film. Diffusion with a radial flux can be described by the following

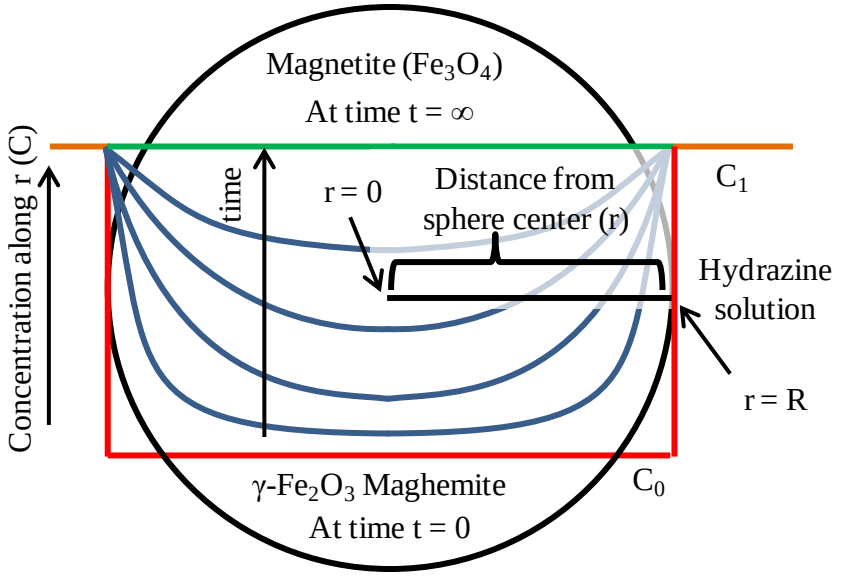

Figure 124: Schematic for the initial boundary conditions for non-steady state diffusion in a sphere with a radius of R, initial internal concentration C_0, and external concentration C_1. The red line represents concentration for maghemite, blue lines are intermediate concentration profiles at different times, green line represents concentration at t = ∞, when the sample is fully reacted into magnetite, orange represents the concentration at the surface.

equation:[17, 18]

$$\frac{\partial C}{\partial t} = \mathrm{D}\left(\frac{\partial^2 C}{\partial r^2} + \frac{2}{\mathrm{r}}\frac{\partial C}{\partial r}\right) \tag{5.43}$$

where C is the concentration, D is the diffusion constant and r is the radial distance from the center of a sphere. By substituting by $u(r,t) = C(r,t)r$ equation 5.41 becomes:

$$\frac{\partial u}{\partial t} = \mathrm{D}\frac{\partial^2 u}{\partial r^2} \tag{5.44}$$

The solution to this equation is analogous to that of linear flow in one dimension which was described earlier. Using the boundary conditions that the sphere (with radius R) has an initial uniform concentration of C_1 (for 0 < r < R, where r is the distance from the center of the sphere) and a surface concentration of C_0 (for r = R, t ≥ 0) the solution for non-steady state diffusion in a sphere becomes:

$$\frac{\mathrm{C}-\mathrm{C}_1}{\mathrm{C}_0-\mathrm{C}_1} = 1 + \frac{2\mathrm{R}}{\pi \mathrm{r}}\sum_{\mathrm{n}=1}^{\infty}\frac{(-1)^{\mathrm{n}}}{\mathrm{n}}\sin\frac{\mathrm{n}\pi\mathrm{r}}{\mathrm{R}}\exp\left(\frac{-\mathrm{D}\mathrm{n}^2\pi^2\mathrm{t}}{\mathrm{R}^2}\right) \tag{5.45}$$

(Note: equation 5.45 derived in reference [18] contains a typo and is missing the 1/r term.) If M_t denotes the total amount of diffusing substance which has entered the sphere at time t and M_∞ is the corresponding quantity after infinite time, then:

$$\frac{M_t}{M_\infty} = -\int_0^t D\left(\frac{\partial C}{\partial r}\right)_{r=R} dt \Big/ -\int_0^\infty D\left(\frac{\partial C}{\partial r}\right)_{r=R} dt \tag{5.46}$$

From equation 5.45, when x = R, the following is obtained:

$$\frac{\partial C}{\partial x} = -\frac{6}{\pi^2}\sum_{n=1}^{\infty}\frac{1}{n^2}\exp\left(\frac{-Dn^2\pi^2 t}{R^2}\right) \tag{5.47}$$

By substituting 5.47 into 5.46 and integrating,

$$\frac{M_t}{M_\infty} = 1 - \frac{6}{\pi^2}\sum_{n=1}^{\infty}\frac{1}{n^2}\exp\left(\frac{-Dn^2\pi^2 t}{R^2}\right) \tag{5.48}$$

The corresponding solution can then be rewritten as::

$$\frac{M_t}{M_\infty} = 6\left(\frac{Dt}{R^2}\right)^{\frac{1}{2}}\left\{\pi^{-\frac{1}{2}} + 2\sum_{n=1}^{\infty} ierfc\left(\frac{nR}{\sqrt{(Dt)}}\right)\right\} - 3\frac{Dt}{R^2} \tag{5.49}$$

With the assumptions that diffusion of cations/anions, electrons/holes, vacancies or other species are the rate-limiting step for the conversion of maghemite into magnetite, the fractional conversion can be found. The M_t / M_∞ ratio for spherical geometry may be approximated by:

$$\frac{M_t}{M_\infty} = 6\pi^{-\frac{1}{2}}\left(\frac{Dt}{R^2}\right)^{\frac{1}{2}} - 3\frac{Dt}{R^2} \tag{5.50}$$

By dividing both sides by t, the following relation is obtained:

$$\frac{M_t}{M_\infty}\times\frac{1}{t} = 6\pi^{-\frac{1}{2}}\left(\frac{D}{R^2}\right)^{\frac{1}{2}}\times\frac{1}{t^{\frac{1}{2}}} - 3\frac{D}{R^2} \tag{5.51}$$

Plotting M_t /M_∞*(1/t) vs $t^{(-1/2)}$ yields a linear dependence with a slope equal to $6\pi^{-\frac{1}{2}}\left(\frac{D}{R^2}\right)^{\frac{1}{2}}$ and a y intercept equal to $3\frac{D}{R^2}$. By fitting experimental data, with known grain

size and assumed grain boundary width, the lattice diffusion coefficient D can then be obtained.

The appropriateness of planar or spherical diffusion models depend on multiple parameters relevant to different time intervals. Three general kinetic regimes may be envisaged when considering different diffusion models associated with a heterogeneous material such as a polycrystalline oxide.[18] The following derivations and diffusion models were obtained from reference [18].

The first kinetic regime, referred to here as type A, can be observed under relatively high annealing temperature, and/ or relatively long annealing times, and/ or in materials with a relatively small grain size. For this regime, the lattice diffusion length needs to be slightly larger than the spacing between grain boundaries as indicated by the following equation:

$$\sqrt{\mathrm{Dt}} \geq \frac{\delta}{0.8} \tag{5.52}$$

The diffusion fringes around neighboring grain boundaries overlap and atoms can diffuse both through the grains and along grain boundaries. This results in an almost planar diffusion front with a penetration depth proportional to $t^{1/2}$ as in a homogeneous medium.[18]

A type B kinetic regime can be present for relatively low temperatures, and/or relatively short annealing times, and/or in materials with sufficiently large grain sizes. This regime considers a lower lateral leakage from the grain boundaries than for a regime of type A. The lateral leakage is limited to distances smaller than the grain size and the boundaries can be considered as isolated. The conditions for type B kinetics are:

$$s\delta \ll \sqrt{\mathrm{Dt}} \ll \mathrm{d} \tag{5.53}$$

where δ is the grain boundary width (assumed to be 0.5 nm for this work), s is the grain boundary segregation constant for foreign atoms segregating on the grain boundary (assumed to be 1), D is the lattice diffusion constant, and d is the crystallite size. (Note: the segregation factor is often inversely proportional to the solubility limit of the segregant at the measured temperature and can often be assumed to equal to 1 in the case of self-diffusion.[18])

The type C kinetics regime corresponds to conditions where the lattice diffusion is negligible and diffusion takes place only along the grain boundaries. This regime can be found at sufficiently low temperatures and/ or very short diffusion times and/ or large grain boundary area fractions. The conditions for type C kinetics are:

$$\sqrt{\mathrm{Dt}} \ll s\delta \tag{5.54}$$

For poly and nanocrystalline materials, the three regimes A, B, and C can be further divided to subregimes based on the interrelations between characteristic length scales. Figure 125 shows the six main diffusion sub regimes and the relative values of characteristic lengths that define each subregime (Lattice diffusion length = L_L; grain boundary width = sδ/2; grain boundary diffusion length = L_{gb}; and grain size = d). Depending on the starting crystal size, materials may pass through different diffusion subregimes as time increases and temperature and grain size remain constant. Table 16 shows expected transitions for coarse-grained, fine-grained, and ultra-fine-grained materials.[18]

For ultrafine-grained materials, the grain boundary diffusion length can be larger than the grain size and the diffusion mechanism can be proceed from C → C' → B_2'→ A. Diffusion starts in the C regime as the lattice diffusion length (L_L) is smaller than the

grain boundary width (sδ/2) and the grain boundary diffusion length (L_{gb}) is less the grain size (d). As time increases, the grain boundary diffusion length becomes greater than the grain size ($L_{gb} > d$). The C diffusion regime then transitions to the C' diffusion subregime after some time t_o. This approximate transition time can be estimated from the condition $L_{gb} = d$ or when $t_o = d^2/D_{gb}$.[18]

The transition from C' to B_2' occurs when the lattice diffusion length becomes greater than the grain boundary width ($L_L > s\delta/2$) and the effective grain boundary length

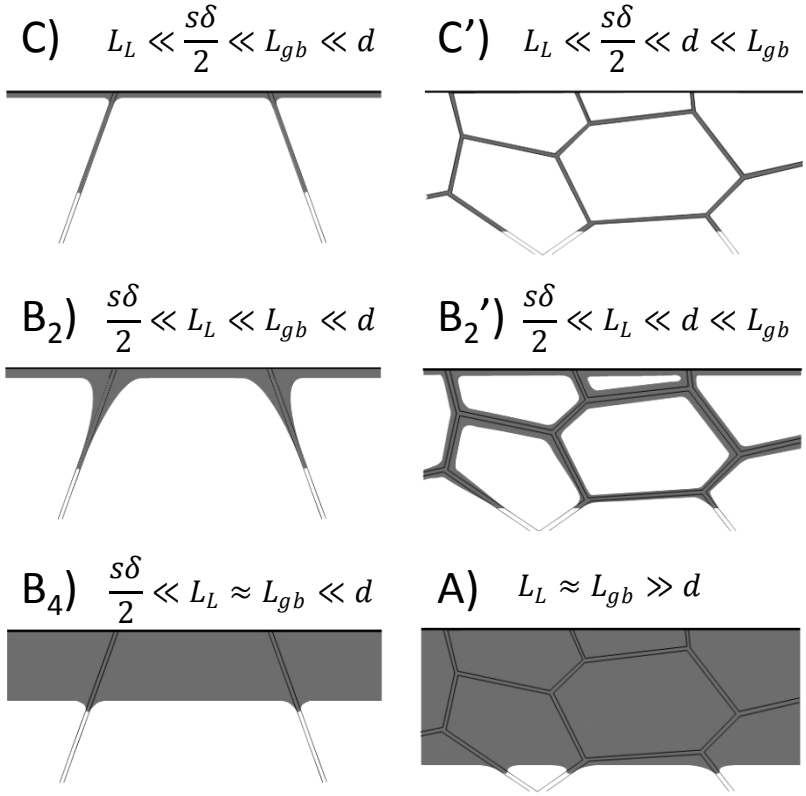

Figure 125: Six main diffusion sub regimes (C, C', B_2, B_2', B_4 and A) and the characteristic lengths that define each subregime (Lattice diffusion length = L_L; grain boundary width = sδ/2, grain boundary diffusion = length L_{gb}; and grain size = d).[18]

Table 16: Sequences of diffusion regimes and subregimes in polycrystals with different crystal sizes at a fixed temperature.

Class of Polycrystal	Sequence of diffusion regimes in time
Coarse-Grained	$C \rightarrow B_2 \rightarrow B_4 \rightarrow A$
Fine-grained	$C \rightarrow B_2 \rightarrow B_2' \rightarrow A$
Ultrafine-grained	$C \rightarrow C' \rightarrow B_2' \rightarrow A$

exceeds the average grain size ((L_{gb} > d). The main characteristics of diffusion in this regime are that: i) it is independent of grain shape, ii) diffusion fringes form around the grain boundary that do not overlap, and iii) a transition from $L_{gb}^{C} \propto \sqrt{t}$ to $L_{gb}^{C} \propto t^{1/4}$ penetration rate law.[18] Eventually the lattice diffusion lengths will exceed the grain size and the diffusion kinetics should then be described by the A regime.[18]

For the reduction of nanocrystalline maghemite into magnetite, three regimes may be envisioned. The first one, associated with type C followed by type C' consists of a planar (1D) diffusion problem. The second case involves type B_2' and A kinetics. The third case consists of an approximate spherical diffusion problem, similar to that of oxidation/reduction of spherical nano particles. The M_t / M_∞ ratio should initially be proportional to $\sqrt{t}$ if C or C' are the dominating regime and has been derived earlier as shown in equation 5.35. If diffusion transitions into the second regime, the M_t / M_∞ ratio should initially be related to $t^{1/4}$ if B_2' is the dominating regime followed by $\sqrt{t}$ dependence in the A regime. In the third region, the M_t / M_∞ ratio should be proportional to $\sqrt{t} - t$ and has been derived earlier as shown in equation 5.50. (Note: the derivation for the $t^{1/4}$ dependence in the B_2' regime can be found in reference [21].) The point at which the diffusion transitions between region one, two, and three will depend on the film thickness, relative rates of grain boundary and lattice diffusion constants, and the grain boundary diffusion paths. For a thin enough film, the grain boundary may become fully reduced, preventing the onset of the second diffusion regime (regime B_2' and A), and then transitioning directly to the spherical diffusion regime 3. While regimes C and A may also occur, the time scale needed to monitor regime C might be too small to measure

with a QCM and the grain boundaries may be fully reduced before regime A is reached. Figure 126 shows a graphical representation of the three diffusion regimes.

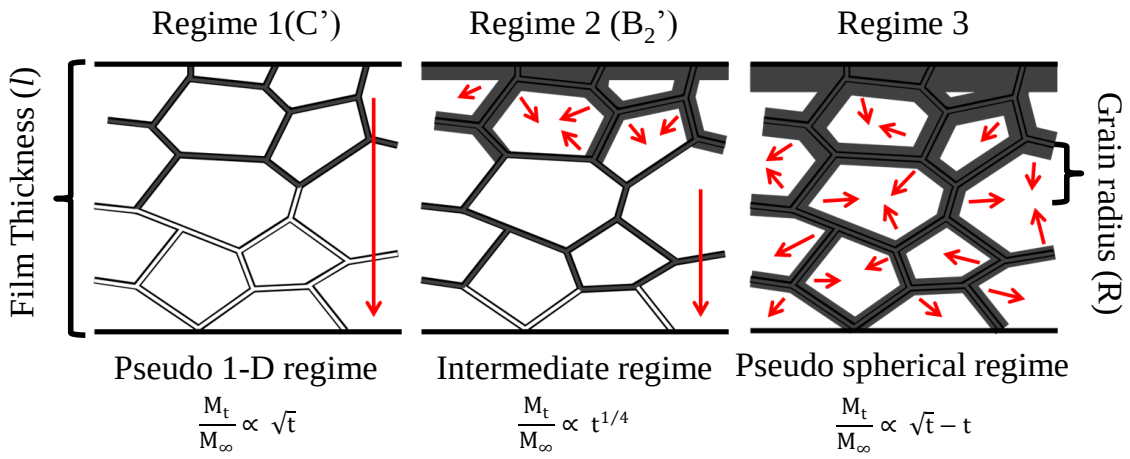

Figure 126: Schematic of proposed diffusion regimes in the reduction of maghemite into magnetite.

5.4. *Experimental procedures*

5.4.1. QCM analysis

A QCM-D, E4 system from Biolin Scientific (Västra Frölunda, Sweden) was used to study the layer-by-layer deposition of iron (III) isopropoxide and the hydrazine reduction kinetics of deposited Fe-O films. For the LbL deposition, fluid was pumped from a solution reservoir into a flow module containing the sensor. Next, the fluid was removed from the sensor region, by a down-stream peristaltic pump (Model: ISM935C, Ismatec, IDEX Corporation, IL, USA), and into a waste beaker. An in situ LbL deposition process was used to study the deposition rate of iron (III) isopropoxide (Alfa Aesar, Ward Hill, MA USA) SSG coatings. Silicon-coated quartz sensors were exposed to anhydrous 2-propanol (>99.8% purity, Acros Organics, Geel, Belgium), followed by 0.0125 M Fe(III) isopropoxide solution in IPA, IPA, a 40/60 volume ratio of water/IPA

mixture, and then IPA for one coating cycle. The silicon-coated sensors were coated by exposure to 10 deposition cycles in the manner described above.

For analyses of hydrazine reduction kinetics of Fe-O films, an open cell and titanium flow module were used at an elevated temperature 65°C and 65°C-90°C, respectively. The open cell module allowed for a rapid deposition of a thick layer of Fe-O (200-500 nm) while simultaneously monitoring the frequency shift caused by the coating. Samples were generated by pipetting 15 µl of 1 mM iron (III) isopropoxide solutions into the 5 ml chamber above the sensor which was kept at a constant temperature of 65°C. The isopropanol was then evaporated after 5 min leaving behind a Fe-O coating on the surface. This process was repeated 15 times for each sensor. The coated silicon sensors were then placed in a titanium flow chamber in a high temperature module and heated to 90°C, 83.8°C, 77.5°C, 71.3°C, or 65°C. The resonance frequency for each sample was base-lined in degassed DIW with a flow rate of 0.5 µl/s. A 20 mL solution of 0.07 wt% hydrazine (N_2H_4, 35 wt%, Sigma Aldrich, MO, USA) solution in degassed DIW was then used to reduce the Fe-O coating with QCM monitoring of the reaction kinetics. The reduction process was continued until the change in frequency over time became equal to the detection limit of the frequency shift of the QCM (change of 1 Hz per min). At this time, the reduction from maghemite to magnetite was considered complete and the time/ frequency values were used to evaluate the reduction kinetics.

QCM-D measures the frequency shift and dissipation of a piezoelectric quartz crystal as the surface is reacted with a solution. The measured resonance frequency will increase or decrease with the removal or addition of mass, respectively, and the

dissipation factor (D) represents the sum of all energy losses per crystal oscillation, providing an indication of film rigidity.[22]

Shifts in the fundamental resonance frequency (i.e., 1) and its harmonics (i.e., 3, 5, 7, 9, and 11) were monitored simultaneously. These corresponded to the 5, 15, 25, 35, 45, and 55 MHz frequencies, respectively. Dissipation from each harmonic was acquired, simultaneously, with the resonance frequency shifts. The area of sensitivity for each harmonic frequency varied from a sensing area so large that noise from O-rings holding the sensor in place made detection (1^{st} harmonic) to an area so small that, after a nm of a coating had been applied, the detection sensitivity was lost (13^{th} harmonic). The 3^{th}, 5^{th}, and 7^{th} harmonics, corresponding to the 15, 25 and 35 MHz frequencies, respectively, were selected as the best compromise between these two extremes. All evaluations of film growth (i.e., frequency shift versus number of cycles) utilized only the 3^{rd}, 5^{th}, and 7^{th} harmonics. Only the 5^{th} harmonic was utilized in the analyses of the iron oxide kinetics.

5.4.2. Coating Surface Morphology

The morphologies and thicknesses of the as deposited iron oxide thin films were evaluated with a field emission scanning electron microscope (1530 FEG SEM, LEO / Carl Zeiss SMT, Ltd., Thorn-wood, NY USA) and a scanning probe atomic force microscope (Dimension 3000 SPM equipped with a Nanoscope III Controller, Veeco Instruments, Inc., Plainview, NY USA)

5.4.3. Phase and Grain Size Determination

To study the phase and grain size of Fe-O coating/material, 25 ml of iron (III) isopropoxide (2.5% w/v in isopropanol) precursors were hydrolyzed with 25 ml of DIW in solution and dried in ambient air at 70°C for 24 h. The dried samples when either: left as is, or subjected to various thermal treatments. Samples were fired in ambient air using a tube furnace (Lindberg / Blue M, NC, USA,) with a ramp rate of 3°C min^{-1} to 250°C, 275°C, and 300°C and held at this temperature for 1 h, 4 h, or 10 h to allow for possible grain coarsening and to monitor possible phase transitions.

Thermogravimetric (TG) analyses (Netzsch STA 449C, Wolverhampton, UK) was used to determine the oxidation state of hydrolyzed sol-gel derived powders before and after hydrazine reduction, as well as that of commercially-purchased 325 mesh Fe_2O_3 (Alfa Aesar 99%) and 325 mesh Fe_3O_4 (Alfa Aesar 97%). Samples were fully reduced using a heating rate of 5°C min^{-1} up to 1000ºC in a flowing (flow rate of 50 cm^3min^{-1}) gas mixture of 2% H_2 and 98% Ar. The change in mass from loss of oxygen was used to determine the initial Fe/O ratio. The total sample mass was ~ 0.5 g for all measurements.

The phase identification for the microwave reacted pollen samples were evaluated at room temperature using X-ray diffraction (XRD) analyses. XRD analyses were conducted on a diffractometer (X'Pert Pro Alpha-1, PANalytical B.V., ALMELO, Netherlands) with $Cu_{K\alpha 1}$(1.5405980 Å) radiation emanating from a 1.8 kW ceramic X-ray tube with a copper anode (45 kV, 40 mA) through an incident beam Johansson monochromator (PANalytical) and detected by an X'Celerator detector. The incident beam optics were outfitted with 0.04 rad soller slits, a 2° fixed anti-scatter slit, a programmable divergence slit set to 5.5 mm irradiated length, and a 10 mm mask. The

diffracted beam optics were outfitted with a 5.5 mm anti-scatter slit and 0.04 rad soller slits placed before the X'Celerator detector. Each pattern was produced with a summation of 40 identical 30 minute scans conducted with Bragg-Brentano geometry and a step size of 0.017° 2θ ranging from 20° to 90° 2θ. The minimum setting for Pulse Height Discrimination (PHD) for the X'Celerator detector was increased to from 36 to 42 to help discriminate between the diffracted signals and fluorescence photons from the Fe atoms.[23] Diffraction specimens were dispersed on a quartz (cut 6° from (0001) orientation) low background specimen support (GEM dugout, PA, USA) via pipetting of an aliquot of IPA/powder slurry onto the specimen support and allowing the IPA to evaporate.

The average crystallite size (ACS) was determined using the HighScore Plus software (PANalytical B.V, Almelo, The Netherlands) with a profile fit function. A Pseudo-Voigt profile fit function was used, in conjunction with a Williamson Hall plot, to determine the grain size of a given film. The profile fit function allowed for each single peak to be characterized by position and height, width and shape (along with being described by a function of 2θ). A detailed explanation of the fitting process is provided in section 3.3.6.

5.5. *Results and Discussion*

5.5.1. SSG Coating Deposition Study

In situ studies of the Fe (III) isopropoxide LbL SSG process were performed with QCM-D to understand film growth, in terms of frequency shift as a function of number of cycles, and the relative rates of chemisorption for each process step. This study was

conducted at a constant temperature of 18°C to avoid the temperature dependent frequency response of the quartz crystal resonator. Such frequency changes could interfere with measuring the coating growth as a function of number of cycles. Secondly, maintaining an operational temperature slightly below the stock solution/laboratory temperature (20°C) helped avoid the formation of bubbles when the fluid contacted the sensor. Such bubble formation would inhibit acquisition of the coating growth kinetics.

A representative QCM plot for a single coating cycle is presented in Figure 127. The frequency shift as a function of time after the iron (III) isopropoxide exposure exhibited no appreciable change after the first 3 minutes (~180 seconds) of incubations so the incubation was terminated after a total exposure of 15 minutes. This suggested that the surface reaction was completed within the first few minutes of the precursor incubation and longer incubations were not needed.

After the samples were incubated with iron (III) isopropoxide, they were rinsed with anhydrous isopropyl alcohol. (Note: the iron (III) isopropoxide precursor solution was comprised of 12.5 mM iron (III) isopropoxide in IPA.) The slight increase in

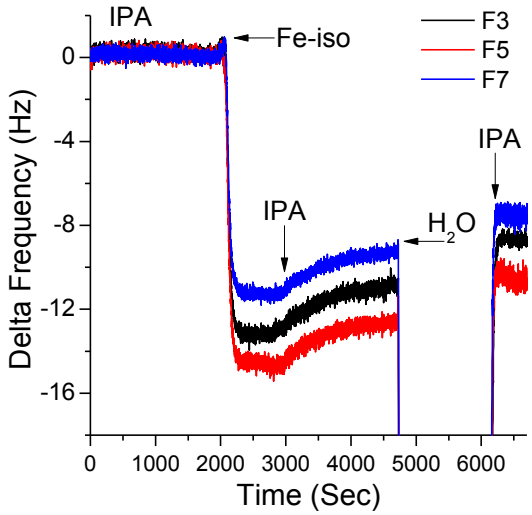

Figure 127: QCM plot of the Fe-isopropoxide SSG process revealing the frequency change of the 3rd, 5th, and 7th overtone for a single coating cycle

frequency upon IPA exposure was attributed to the removal of any excess iron (III) isopropoxide precursors that were physisorbed to the surface.

During the hydrolysis step (i.e., incubation with 40 vol% isopropyl alcohol and 60 vol% DIW), the frequency dropped on the order of 180 Hz due to the change in density/ viscosity between anhydrous isopropyl alcohol and the isopropyl alcohol/water mixture. The harmonic splitting (changes in ΔF between overtones) that occurred as a result of the changes in bulk fluid properties (i.e., viscosity and density) upon the water/hydrolysis step was not noticeable for the iron (III) isopropoxide/IPA transition because of the similarity in bulk fluid properties. That is, 12.5 mM iron (III) isopropoxide behaved almost identically to the anhydrous isopropyl alcohol. After the sensor stabilizes from the sudden change in viscosity, no detectable change in frequency was observed. After the final rinse with anhydrous isopropyl alcohol, the baseline reverted back to a slightly higher frequency then before the start of the hydrolysis step. This increase in frequency indicated a loss in mass, which was consistent with the cartoon representation shown in Figure 128. During the hydrolysis steps, the pendant alkoxide groups were replaced with lower mass hydroxyl groups (Figure 128 ii and iii). This loss of mass was significantly less than the mass gained (or resonance frequency lost) upon deposition of the iron (III) isopropoxide precursors, as seen in Figure 127.

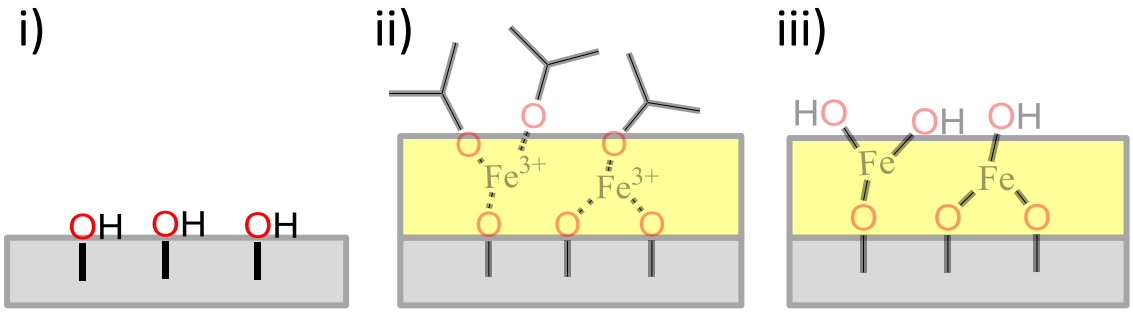

Figure 128: Schematic of a QCM substrate: i) before the coating process, ii) after iron (III) isopropoxide incubation, and iii) after hydrolysis pendant alkoxide surface groups.

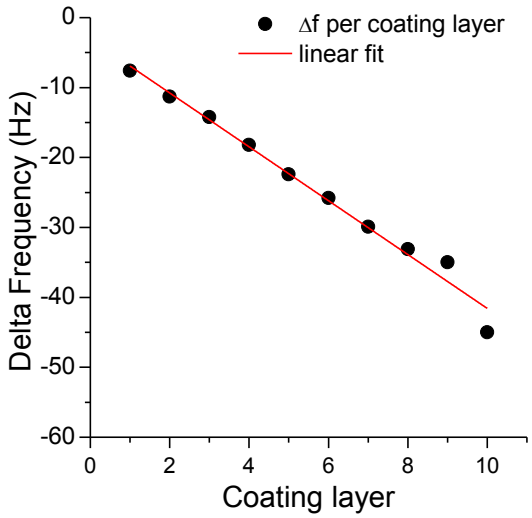

Figure 129: QCM plot of the iron (III) isopropoxide SSG processing revealing the frequency change of the 5th overtone as a function of the number of coating cycles

The layer-by-layer nature of the deposition process was studied by repeating a typical coating cycle multiple times. The change in frequency from the onset of iron (III) isopropoxide exposure through the anhydrous isopropyl alcohol rinsing step that occurred after hydrolysis was used to track each coating cycle. Figure 129 shows the frequency changes thought 10 iron (III) isopropoxide SSG coating cycles. An excellent linear fit (R^2 value of 0.98) was made with the data giving an average frequency shift per deposition cycle of -3.85 ± 0.18 Hz. These results were consistent with previous studies on SSG deposition [24, 25] and agreed with the TGA results described in sections 2.4.4. and 2.4.7.

Unfortunately, in order to utilize quartz crystal microbalance (QCM) analyses to evaluate the kinetics of layer-by-layer surface sol-gel deposition, in a manner analogous to surface sol-gel deposition on hydroxyl-rich sporopollenin (discussed in Chapters 2-4), a planar quartz crystal containing a continuous pollen-like sporopollenin coating was needed. Unfortunately, since the work of Dominguez and colleagues, who identified the molecular components that comprise sporopollenin,[26] no protocol has been developed

for the deposition of a pollen-like sporopollenin layer on synthetic substrates, such as quartz. Hence, such QCM analyses of surface sol-gel deposition on sporopollenin based coatings are not presently possible.

However, thick Fe-O coatings can be deposited directly by depositing and hydrolyzing precursors on the sensors without rinsing away the excess precursors. Using an open cell module heated to 65°C, an excess amount (well beyond one monolayer) of iron isopropoxide could be pipetted directly onto the sensor surface while simultaneously monitoring the change in resonance frequency caused by this deposition. An AFM scan of a scratched QCM sensor (Figure 130), generated by pipetting 15 µl of a 1 mM iron (III) isopropoxide solution into the 5 ml chamber above the sensor, followed by evaporation of the isopropanol, and repeating 15 times, can be seen in Figure 130. By comparing AFM-measure film thickness (Figure 131) to the measured frequency change during coating (~2000 Hz), a relation between the frequency shift and the film thickness (in Hz and nm) was obtained. From Figure 131 and QCM data, a 7.7 ± 0.4 Hz per nanometer relation was found. This would indicate that each SSG layer was on the order of 0.5 nm thick, which was consistent with previous QCM studies that indicated that between ~0.5 nm to 5.0 nm were deposited with each coating layer.[24]. SE micrographs of a QCM sensor coated so as to yield a ~1700 Hz change (coated by bulk deposition of iron (III) isopropoxide onto a QCM substrate) can be seen in Figure 132. The top of the sensor, Figure 132 a), exhibited a crack-free surface and looked similar to the AFM results shown in Figure 130. The fracture cross-section shown in Figure 132 b) revealed good contact between the ~50 nm SiO_2 surface layer and Fe-O coating with no cracks or delamination's visible.

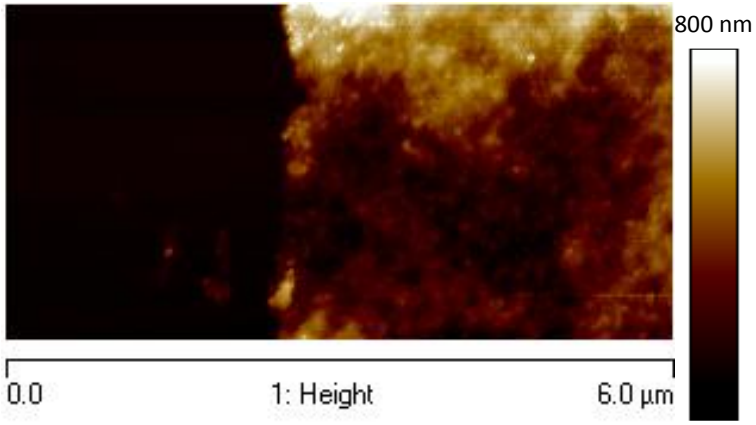

Figure 130: AFM scan of a scratched Fe-O coated QCM sensor showing the uncoated sensor on the left and the coated sensor on the right.

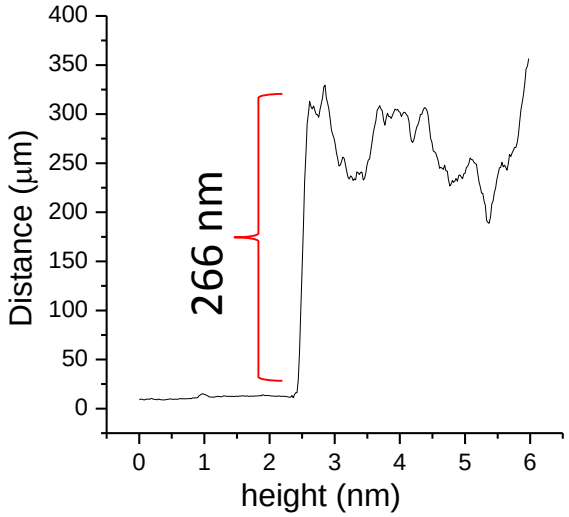

Figure 131: AFM step height evaluation of the coating thickness.

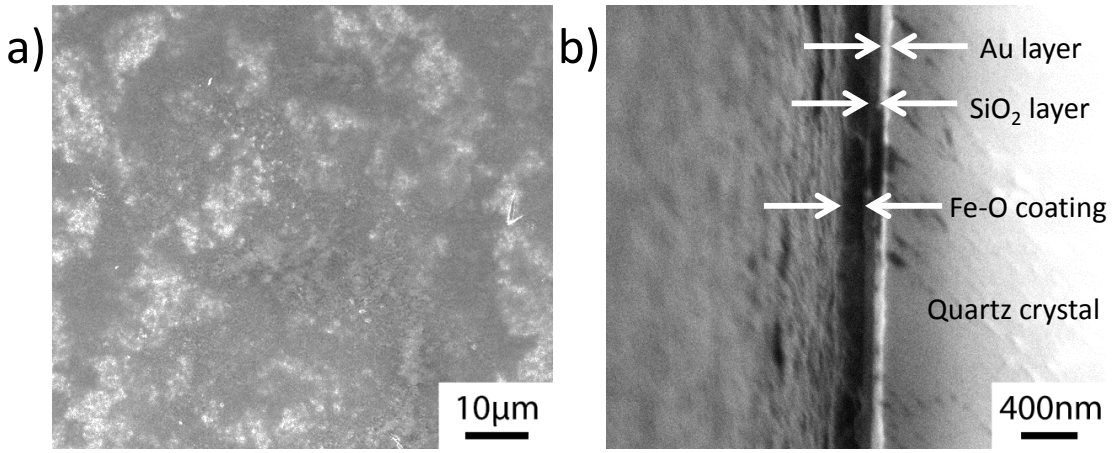

Figure 132: SEM images of: a) the surface of a QCM sensor coated with Fe-O and b) fracture cross-section of the coated sensor. The arrows in b) reveal the Fe-O layer on the external surface, the SiO_2 layer, and the Au layer on a QCM quartz crystal.

5.5.2. Phase and Grain Size Analyses

In order to determine the oxidation state and phase of the iron in the coating before and after hydrazine reduction, TG, HRTEM, and XRD analyses were used. With TG analysis, it was possible to measure the mass lost when the iron oxide was fully reduced. For maghemite (γ-Fe_2O_3), the residual mass should have been 69.6% of the starting mass upon complete reduction to elemental iron. For magnetite (Fe_3O_4), the residual mass upon complete oxide reduction should have been 72.0% (Table 17). The difference of 2.4% is well within the sensitivity of TG analysis and could be used to determine the difference between these phases. Hydrolyzed iron isopropoxide precursors were reacted in the hydrazine solution at 65°C for 24 h for subsequent TG analyses in the 2%H_2/98%Ar. Control samples of commercially-purchased oxide powders of both γ-Fe_2O_3 and Fe_3O_4 were also examined by such TG analyses. Figure 133 shows the TGA plots for both the commercially-purchased oxide powders and the precursor-derived samples, and Table 17 provides the residual mass % for all four samples along with

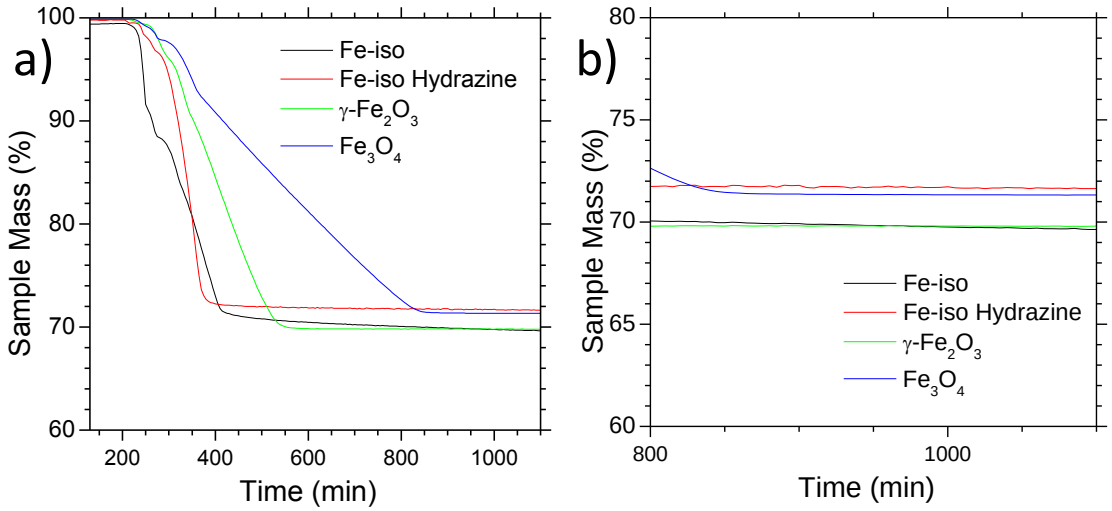

Figure 133: TG analyses plots showing the mass lost upon complete reduction of samples to Fe in a 2%H_2/98%Ar atmosphere for hydrolyzed Fe (III) isopropoxide specimens (Fe-iso), hydrazine reduced hydrolyzed iron (III) isopropoxide specimens (Fe-iso hydrazine), and bulk powders of γ-Fe_2O_3 and Fe_3O_4.

Table 17: Calculated and experimental data for residual mass for samples completely reduced into elemental iron.

Phase	Calculated residual mass	Bulk powder residual mass	Fe-isopropoxide Residual mass
Fe_2O_3	69.6%	69.9%	69.9% (hydrolyzed)
Fe_3O_4	72.0%	71.4%	71.7% (reduced with hydrazine)

calculated residual mass values. From TG analyses, it was clear that the as-coated oxide was fully oxidized (Fe_2O_3) and the hydrazine-reacted samples were in a partially-reduced state consistent with magnetite (Fe_3O_4).

XRD analyses ware then used to determine the phase of the iron oxide coating and the grain size of the coating before hydrazine reduction and then after various thermal treatments. XRD measurements were performed on samples with no thermal treatments, or on samples heated to a peak temperature of 250°C for 10 h, a peak temperature of 275°C for 4 h, or a peak temperature of 300°C for 4 h (Figure 134). XRD analyses indicated that the samples underwent a phase transition from γ-Fe_2O_3 to α-Fe_2O_3 between 250 and 300°C. The sample treated to a peak temperature of 300°C for 4 h was

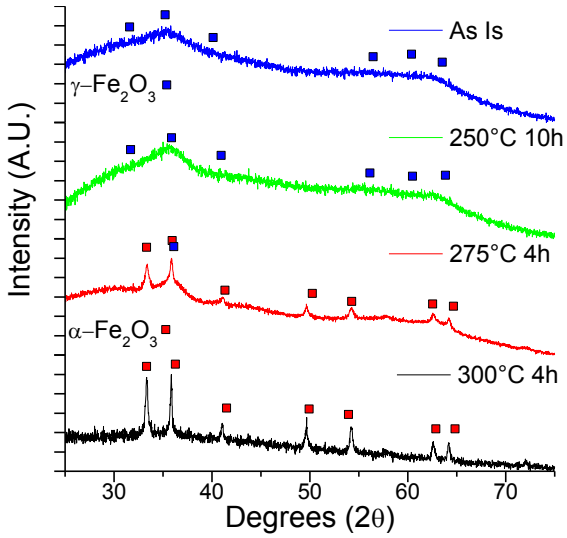

Figure 134: XRD patterns of hydrolyzed Fe (III) precursors after various thermal treatments conducted in ambient air and ambient humidity in Atlanta Georgia during the summer (~70%) with a ramp rate of 180°C/min.

comprised of α-Fe_2O_3, while the sample treated to a peak temperature of 275°C may have contained both phases. (Note: ultra-fine-grained γ-Fe_2O_3 and Fe_3O_4 were difficult to distinguish by XRD analyses.) Therefore, in order to study the reduction kinetics from γ-Fe_2O_3 to Fe_3O_4 the maximum processing temperature had to be ≤ 250°C. These results were consistent with previous work, which indicated that γ -Fe_2O_3 transformed into α-Fe_2O_3 at a temperature around ~300°C.[27]

Samples were then heat treated to 250°C for 1 h or 10 h to investigate possible maghemite grain coarsening and to investigate the impact of thermal treatments on the iron oxide coating deposited on a QCM substrate. Figure 135 shows the XRD patterns obtained from each sample with a full pattern profile fitting conducted for crystallite size analysis. The profile fit is shown in black, the calculated background is shown in green, and the difference plot between the measured and calculated plots is shown in blue. The FWHM of each peak was fitted to the Caglioti equation (shown in Figure 136) and a linear Williamson-Hall plot was then used to determine the crystallite size and microstrain for each reaction condition (Figure 137).

A Si NIST profile standard (640c) was used to calibrate the peak broadening of the samples for crystallite size and microstrain analysis. Figure 137 show the crystallite size calculated from the Williamson-Hall plot for each of the two samples showing similar results for both samples, indicating that no apparent grain growth had occurred during the 250°C/10 h thermal treatment. The crystallite size values obtained from the Williams-Hall plot (~1 nm) do not give interpretable values, with the measured crystallite sizes being of the same order as to that of the lattice parameters of maghemite (2.49 nm x 0.83 nm x 0.83 nm). For Scherrer analysis to be valid, crystals comprised of multiple unit

cells (5-10 unit cells) are required. Microstrain analysis indicated that all samples had negative strain values and it was then assumed that that the primary cause of peak broadening was due to a fine crystallite size. The lack of apparent grain growth was also consistent with a previous report of no grain growth in maghemite at temperatures below 300ºC.[20] In addition to the lack of apparent grain growth, a modest thermal treatment of 250ºC for 1 h was found to cause mud cracking and delamination of the film from the

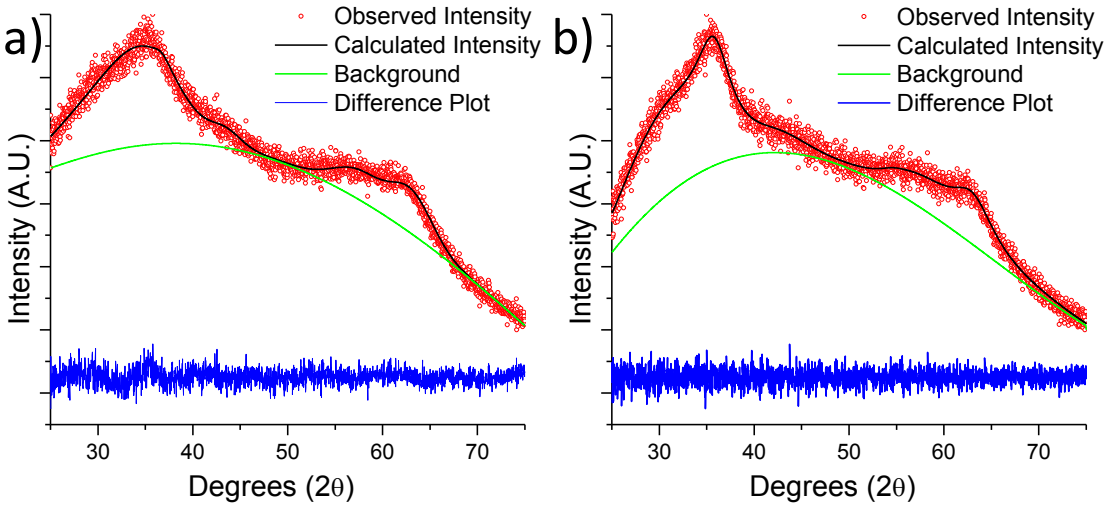

Figure 135: Pseudo-Voigt profile fit (black line) and background (green line) of the measured X-ray diffraction patterns (red circles) with the differences between the two plots shown in blue for the iron oxide precursor: a) as precipitated and b) heat treated to 250ºC for 10 h.

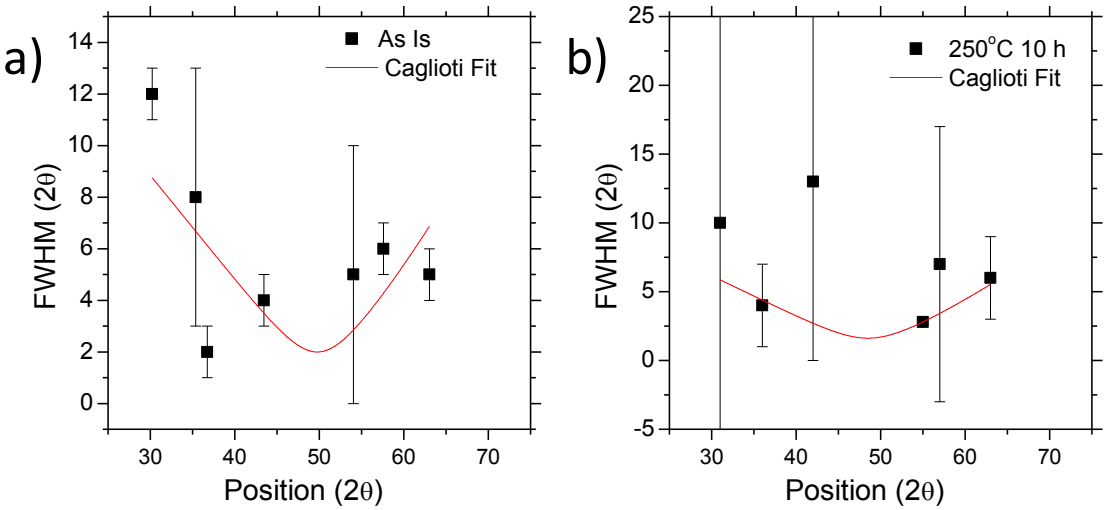

Figure 136: Caglioti fit to the FWHM values of each diffracted peak for: a) a sample with no thermal treatment and b) a sample heat treated to 250ºC for 10 h.

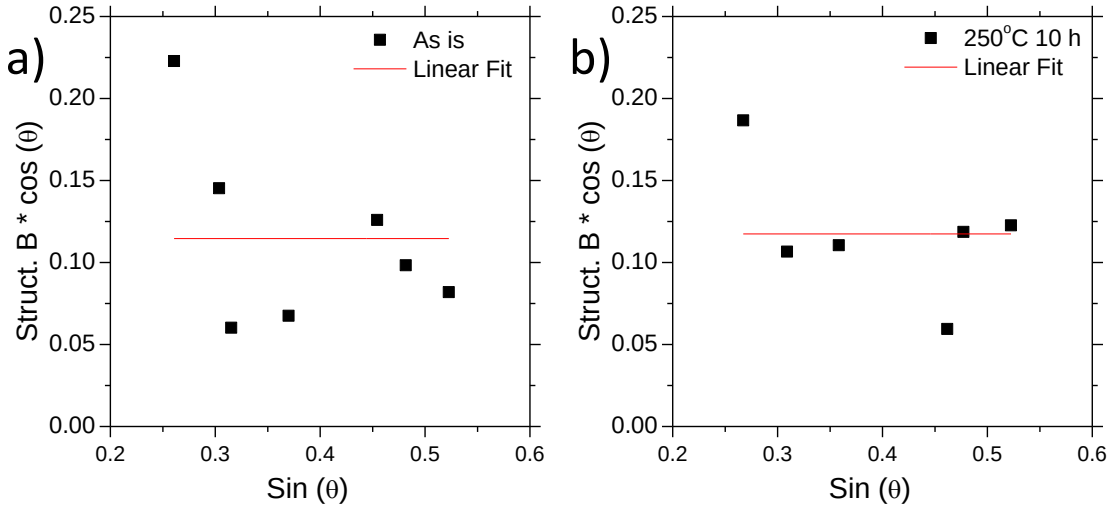

Figure 137: Williamson-Hall plots used to calculate the crystallite size for each firing temperature. The crystallite sizes were found to be: a) ~1 nm for samples with no thermal treatments and b) ~1 nm for samples fired at 250ºC for 10 h.

substrate as shown in Figure 138. The combination of the phase change that occurred around 300ºC, the lack of apparent grain growth for long thermal treatments at 250ºC (10 h), and delamination of the film with thermal treatments prevented experimental determination of the role of grain size on the kinetic mechanism of maghemite reduction.

Because XRD methods were not able to determine the grain size of the as-deposited oxide coating, HRTEM analysis was preformed to evaluate the grain size before and after hydrazine reduction. HRTEM images (Figure 139 and Figure 140)

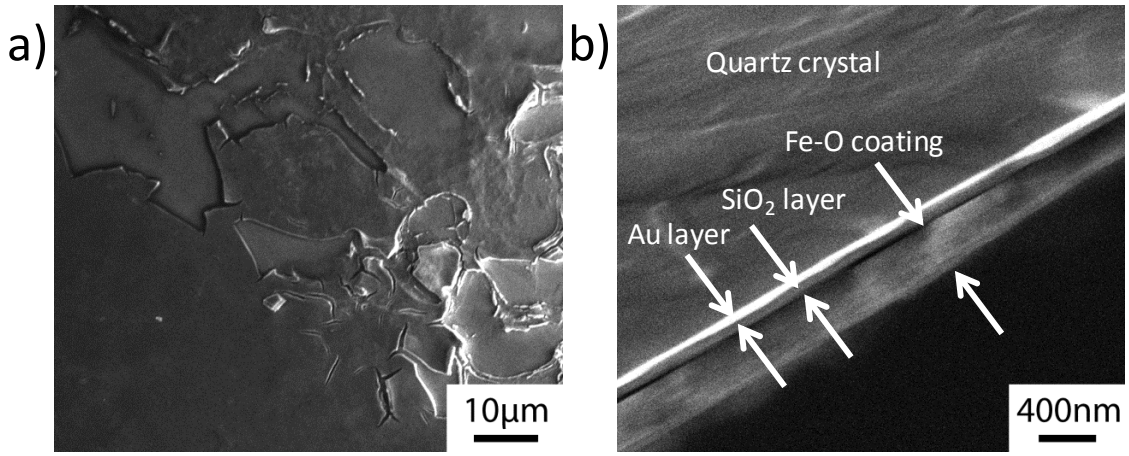

Figure 138: SEM images of a) the surface of a QCM sensor coated with Fe-O and b) fracture cross-section of the coated sensor after heating to 250ºC for 1 h. The arrows in b) reveal to the Fe-O layer on the external surface, the SiO_2 layer, and the Au layer on a QCM quartz crystal.

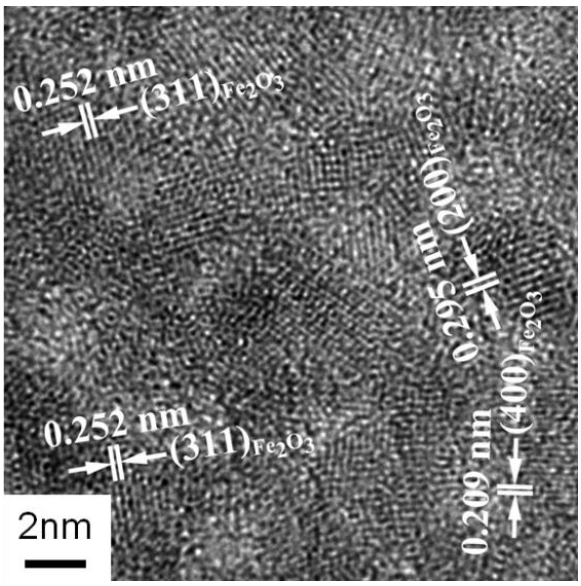

Figure 139: High resolution TEM images of the Fe-O coating on *H. Annuus* pollen grains applied with 40 SSG cycles.

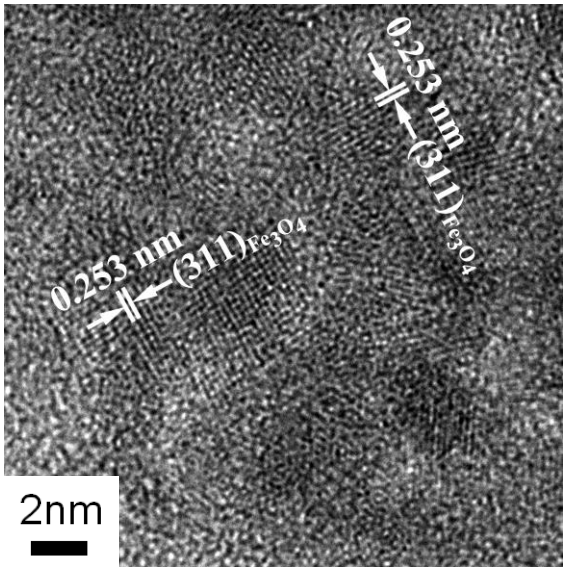

Figure 140: High resolution TEM images of the Fe-O coating on *H. Annuus* pollen grains applied with 40 SSG cycles after hydrazine reduction at 65°C for 24 h.

revealed that the coating was comprised of crystals on the order of 3 - 5 nm in size. Lattice fringe spacing's from the (311), (100), and (200) planes are indicated in Figure 139 for the as-coated samples. Lattice fringe spacing's from the (311) plane are indicated for the hydrazine-reduced sample. These nano sized grains would only accommodate 2-6

unit cells in each grain and so it is not surprising that XRD analyses were not sensitive enough to measure these values.

5.5.3. Kinetic Analyses of Maghemite Reduction with Hydrazine

The following kinetic analyses of the reduction of maghemite was used to evaluate the rate limiting step(s) of this process. Quartz crystal microbalance (QCM) experiments where performed samples at five different reaction temperatures (65.0°C-90.0°C) with samples reacted at 71.3.0°C-90.0°C discussed in section 5.5.4. Representative QCM reduction plots can be seen below in Figure 141 for samples reacted from the as-coated state at 65.0°C. (Note: QCM curve plots were converted from ΔF to % reacted by dividing by the maximum frequency shift value obtained for each sample. The experiments were stopped, and a maximum value was obtained, when the change in ΔF over time matched the instrument drift of 1 Hz per min and the samples were then assumed to be fully reacted.) Two regions were observed in the data indicating that more than a single reaction or diffusion regime may have been operative: i) an initial region with a relatively steep slope, and ii) a second region with a gradually reducing slope.

To examine rate-limiting steps and possible grain boundary-affected regimes present at different time scales, characteristic diffusion lengths were calculated from values reported in the literature. Sidhu et al.[10] determined an Arrhenius relation for the diffusion of iron through maghemite as magnetite oxidized in air at temperatures of 190-220°C. Similarly, Tang, et al.[9] found an Arrhenius relation for the assumed diffusion of iron through maghemite as magnetite oxidized in a basic (pH 12-13) aqueous environment at 24-80°C. Using the Arrhenius equation, $D = D_o exp\left(\frac{-E}{RT}\right)$, the chemical

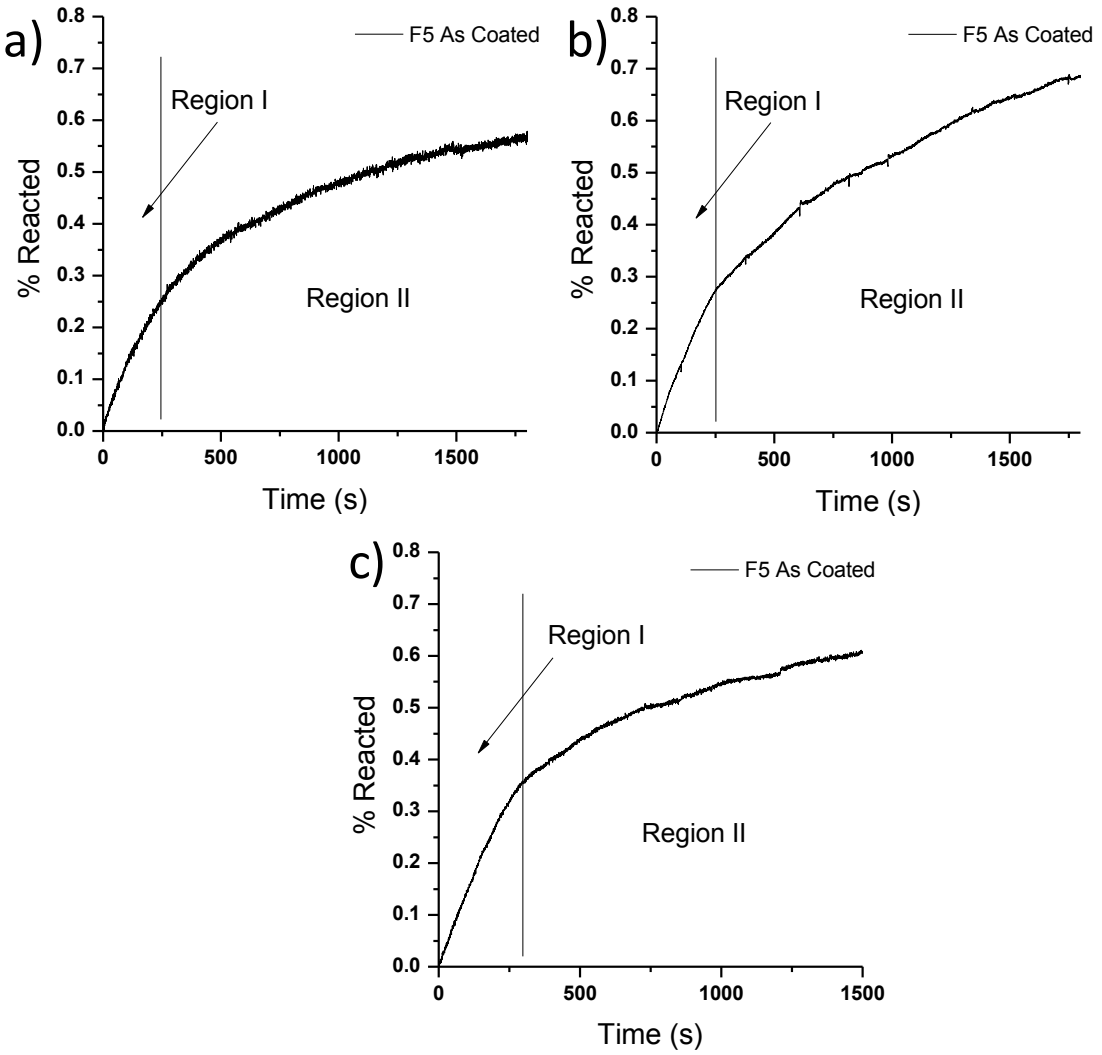

Figure 141: Three different QCM plots obtained from QCM sensors prepared in a similar manner and reacted in the as-coated state at 65.0°C

diffusion constants at 65°C were then calculated to be $9.04*10^{-18}$ cm^2/s [10] and $1.90*10^{-18} cm^2/s$[9] respectively. An effective lattice diffusion length over time can then be approximated using the following relation:[18]

$$L_{Lattice} = \sqrt{Dt} \tag{5.55}$$

where $L_{Lattice}$ is the lattice diffusion length, D is the lattice diffusion constant, and t is time. By comparing the lattice diffusion length with the grain boundary width sδ/2, a first order approximation can be made to determine when a transition from type C to type B kinetics may occur. When the diffusion length is longer than the grain boundary width,

type B kinetics may dominate. Figure 142 reveals the lattice diffusions lengths at 65°C derived from Tang, et al.(black) and Sidhu, et al. (red) compared to the grain boundary width δ values between 0.5 nm and 1 nm (shaded box) and a grain boundary segregation (s) value of 1. Below the dashed box, type C kinetics is expected to dominate, while type B kinetics should dominate above the box. The transition period should take place inside the box and depends on both the diffusion constants and grain boundary width. Based on the air oxidation kinetic (red curve) data [9], the C to B transition should occur between 150 s and 370 s after the reaction commences, while for aqueous oxidation (black curve) data [10], the time frame is between ~330 s and ~1330 s.

In addition to the lattice diffusion length, the grain boundary diffusion length is another characteristic distance that can be used to help distinguish between different diffusion regimes. Oxygen self-diffusion constants in α-Fe_2O_3 and a $NiCr_2O_4$ spinel structure determined between 1200-1600°C have been previously reported ($2.73*10^{-12}$ cm^2/sec and $1.33*10^{-12}$ cm^2/sec = extrapolated self-diffusion constants to 65°C for α-Fe_2O_3 and $NiCr_2O_4$, respectively) and were used as an initial reference point to help approximate the appropriate time scales for different diffusion subregimes.[28] The grain

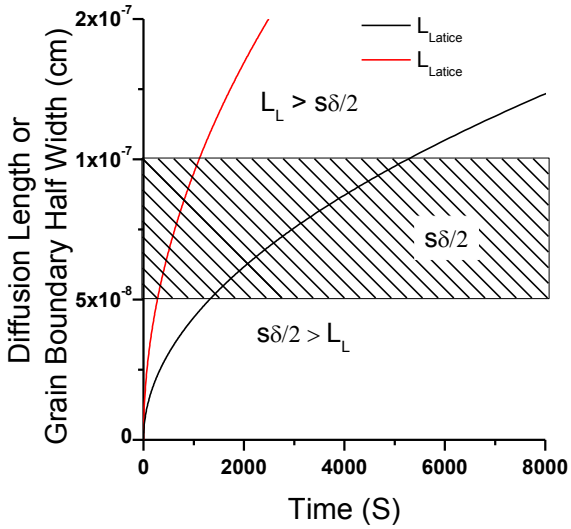

Figure 142: Lattice diffusion length at 65°C plotted as a function of time. The black curve was calculated from D_{Fe} values from reference [9], and red curve was obtained from D_{Fe} values from reference [10]. The grey box represents a grain boundary half-width between 0.5 nm and 1.0 nm.

boundary diffusion lengths in the B and C regimes can be calculated using the following two equations:[18, 21]

$$L_{gb}^{B} = \sqrt{\frac{sD_{gb}\delta}{(4D)^{1/4}}}t^{1/4} \tag{5.56}$$

$$L_{gb}^{C} = \sqrt{D_{gb}t} \tag{5.57}$$

where L_{gb}^{B} [21]is the grain boundary diffusion length in regime B, L_{gb}^{C} is the grain boundary diffusion length in regime C, s is the segregation factor (in this case for oxygen or oxygen vacancies segregation at the grain boundaries) and is assumed to be 1, D_{gb} is the grain boundary diffusion constant, δ is the gain boundary width, D is the lattice diffusion constant, and t is time.

Equations 5.56 and 5.57 have been plotted as a function of time and with the diffusions lengths compared to different grain sizes in Figure 143. When the grain boundary diffusion length is larger than the grain size, a transition from the C to C' or B_2 to B_2' diffusion regime may occur. For fine-grained material, the transition times from B_2 to B_2' may be too short to measure with a QCM (~0.005 sec for 20 nm gain size

material). Similarly, for ultrafine-grained material, the C to C' transition occurs within 3 sec for 20 nm grain size materials and may also happen too quickly for accurate measurement with a QCM. The samples in this study have grain sizes in the range of 3-5 nm and the transition times for both B to B' and C to C' may occur at even shorter times. From the reference diffusion values and the temporal limitations of a QCM, the transition from C to C' does not appear to be detectable for ultrafine-grained (<20 nm) material and the C to B_2 to B_2' transitions should also not be detectable for fine-grained material. Therefore, a $\sqrt{t}$ (equation 5.35) to $t^{1/4}$ (reference [21]) to $\sqrt{t}$ (equation 5.35) M_t / M_∞ dependence should be observed with the C' to B_2' to A transitions for ultrafine-grained (diffusion transitions showed in Table 16) material, and a $t^{1/4}$ to $\sqrt{t}$ (equation 5.35) M_t / M_∞ dependence observed with the B_2' to A transitions for fine-grained material (diffusion transitions showed in Table 16).

To test the rate-limiting mechanism at the start of the reaction process, linear fits were made to the as-coated QCM data vs. t, $t^{1/2}$, and $t^{1/4}$. A linear rate would be consistent with a rate-limiting step related to liquid phase diffusion, a liquid/solid interfacial

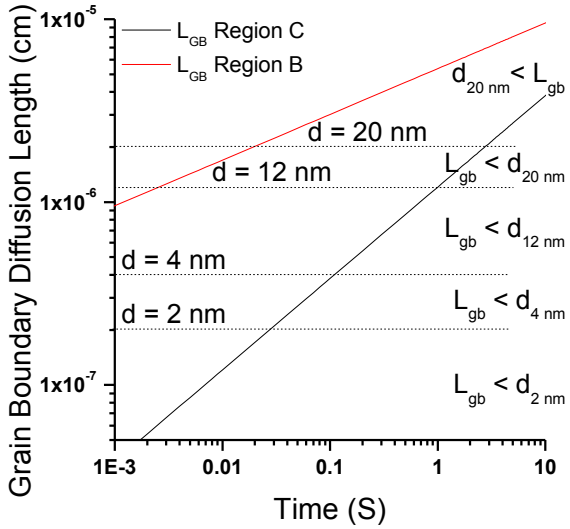

Figure 143: Oxygen grain boundary diffusion lengths at 65°C as a function of time for samples in the B and C regimes.

reaction, or a solid/solid interfacial reaction. A parabolic fit would mean that the ultrafine-grained model (equation 5.35) could be used to describe the diffusion process and $\alpha\, t^{1/4}$ relation would mean the fine grain model could be used to describe the diffusion process.[18]

Representative linear, parabolic, and quartic power fits to the region I portion of the data are shown below in Figure 144 and the fitted data along with R^2 and χ^2 values are listed in Table 18 for all three sensors. (Note: χ^2 values were obtained using $\chi 2 = \sum_{i=1}^{\infty} \frac{(O_i - E_i)^2}{E_i}$, were i is a given data point, O_i is an observed value, and E_i is the fitted value.) For each sample, identical time intervals were used to compare the linear, parabolic, and quartic power fits. The time at which the diffusion transitioned from region 1 to region 2 is discussed in the ensuing pages and shown in Figure 146. All samples were fitted for the same transition time. While all fits were relatively good, with R^2 values greater than 0.9, the parabolic fits had the lowest χ^2 values of all three curve fittings with values in the range of 0.151 to 0.00356. The high R^2 values, for all samples and fits, could be related to the relatively large number of data points fitted (over 600), and visual as well as numerical inspection needed to be performed to estimate the best fit. The parabolic relation had the highest R^2 values, lowest χ^2 values, and the best apparent visual agreement with the experimental data. The linear fits and quartic power fits had χ^2 values in the range of 3.494 to 0.193 and 0.554 to 0.400 respectively, which were larger than the χ^2 values for the parabolic fits. The linear fits started to deviate from the measured data near the end of regime 1 times, while the quartic power fits had significant divergence at intermediate times.

The second growth region may be expected to be governed by one of two mechanisms. For a thick-enough film, the diffusion regime may be expected to transition from a $\sqrt{t}$ to a $t^{1/4}$ time dependence due to a transition from C' to B_2' diffusion regimes. However, if the film is thin enough for the grain boundaries to become fully reduced before the lattice diffusion length becomes larger than the grain boundary width, a spherical diffusion model may dominate. A linear dependence was not anticipated to take place in the second growth region as the rate-limiting step for serial steps shown in

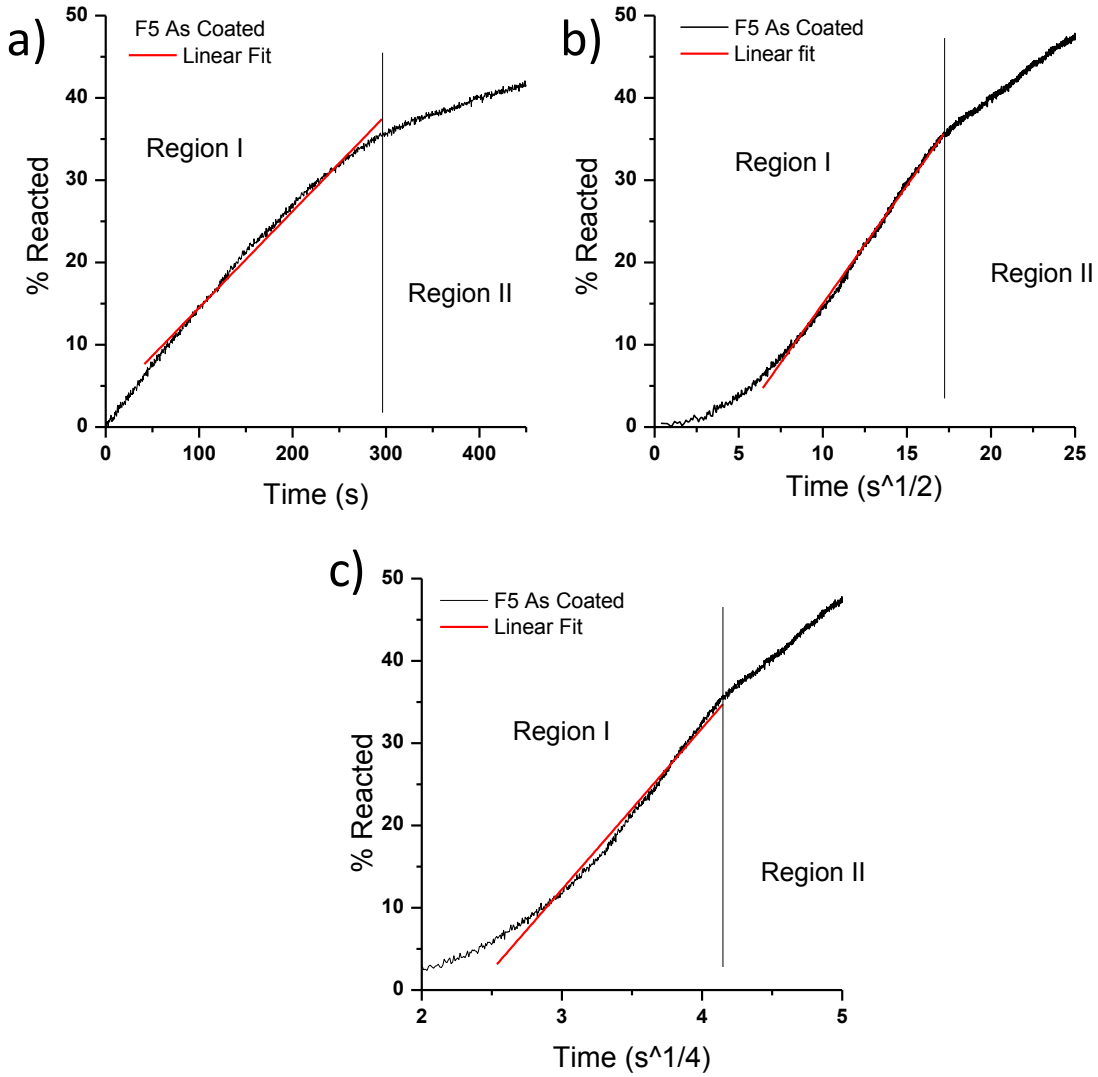

Figure 144: a) Linear, b) parabolic, and c) quartic power fits for the same time intervals to the region I kinetics for as coated QCM data obtained at 65°C

Table 18: Linear, parabolic, and 4th power fits, R^2 and, χ^2 values for region I of as coated QCM data conducted at 65°C

Fitted rate law	Fit	R^2	χ^2
	QCM sensor 1		
Linear: αt	$Y= 0.00117*t + 0.0281$	0.9919	3.494
Parabolic: αt^2	$Y= 0.0205*t^{1/2} – 0.0744$	0.9943	0.107
Power: αt^4	$Y= 0.134*t^{1/4} – 0.2892$	0.9881	0.407
	QCM sensor 2		
Linear: αt	$Y= 0.00109*t + 0.0136$	0.9943	0.211
Parabolic: αt^2	$Y= 0.0262*t^{1/2} – 0.139$	0.9987	0.00356
Power: αt^4	$Y= 0.153*t^{1/4} – 0.347$	0.960	0.400
	QCM sensor 3		
Linear: αt	$Y= 0.00119*t + 0.0208$	0.9892	0.193
Parabolic: αt^2	$Y= 0.0286*t^{1/2} – 0.136$	0.9959	0.151
Power: αt^4	$Y= 0.192*t^{1/4} – 0.452$	0.9859	0.554

Figure 119 generally was expected to transition from reaction controlled to diffusion-controlled with increased time, not the reverse.

Linear, parabolic, parabolic + linear, and quartic power fits to the region II portion of the data are shown in Figure 145 for a single representative QCM sensor and the fitted data, R^2, and χ^2 values for all three sensors are listed in Table 19. While all fits were relatively good, with R^2 values greater than 0.9, the parabolic + linear law yielded the best fit. Similar to the fitting in region I, the high R^2 values could be related to relatively large number of data points fitted (over 6,000) and visual, as well as numerical, inspection needs to be performed to evaluate the best fit. The parabolic + linear relation had the highest range of values for R^2 (0.9962 to 0.9983), and the lowest range of values

for χ^2 (0.0008 to 0.0018), and the best visual agreement with the experimental data. The linear fits, despite the high range of R^2 values (0.9093 to 0.9214), did not visually match the data well and noticeably deviated from the data at both short and long times. The χ^2 values for the linear fits were significantly larger than all the other fits with values between 105.2 and 9.392. The parabolic fits matches the data better than the linear fits, with modest deviations at both short and long times, but had higher χ^2 values (2.940 to 9.170) compared to the parabolic + linear fits. The quartic power fits have noticeable divergence at low times and also have χ^2 values (0.8908 to 2.753) much greater than the parabolic + linear growth fits. From the fitted data, it may be surmised that the second growth regime was controlled by a parabolic + linear model of the diffusion process. The parabolic + linear growth law suggests that the diffusion mechanism transitions from diffusion regime C (Figure 126 regime 1) to a spherical model (Figure 126 regime 3) after the grain boundaries have been fully reduced and before the start of type B_2' diffusion. (Note: the boundary between region I and region II was set to the time at which the parabolic + linear fit started to deviate from the experimental data by greater than 0.05, as shown in Figure 146)

To validate the different diffusion regimes, diffusion constants were obtained from the experimental data and compared to previously-reported values of diffusion in maghemite and spinel-like structures. For region I, the 1-D parabolic diffusion front model derived in section 5.3. (equations 5.35 and 5.37) was used to determine the grain boundary diffusion constant.

$$\frac{M_t}{M_\infty} = 2\pi^{-\frac{1}{2}}\left(\frac{D_{eff}t}{l^2}\right)^{\frac{1}{2}} \tag{5.35}$$

$$D_{eff} = fD_{gb} \tag{5.38}$$

Equation 5.37 below was not used, as diffusion in region C' involved little lattice diffusion (D).

$$D_{eff} = fD_{gb} + (1 - f)D \tag{5.37}$$

The difference between grain boundary diffusion and lattice diffusion was assumed to be many orders of magnitude so that the iron lattice diffusion can be neglected. The film thickness *l*, was calculated based on QCM data obtained by coating the substrate where 1 nm of coating equals ~ 7.7 ± 0.4 Hz of resonance frequency shift, as discussed in section

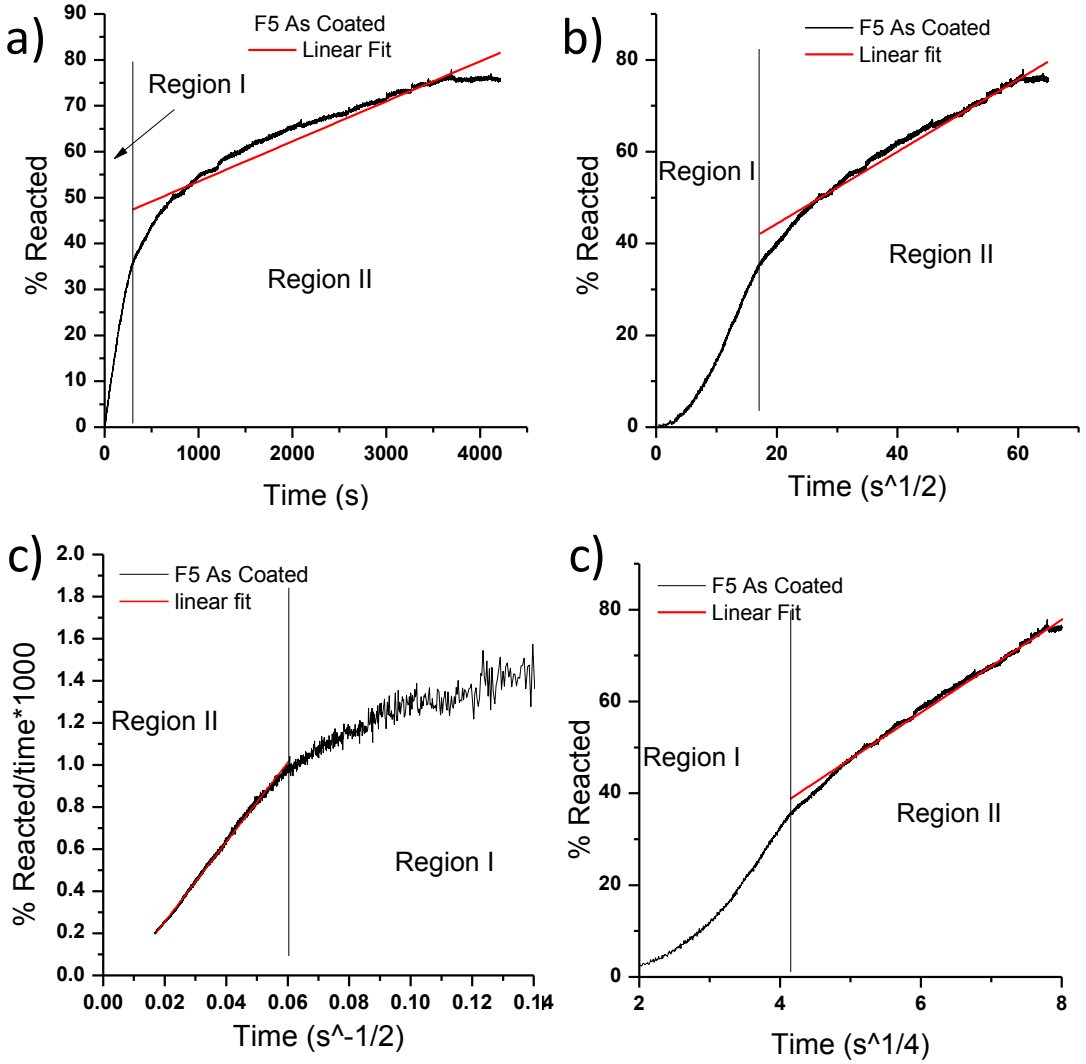

Figure 145: a) Linear, b) planar parabolic, c) spherical parabolic, and d) 4th power fits to the region II for as coated QCM data conducted at 65.0°C

Table 19: Linear, parabolic, and 4th power fits, R^2 and, χ^2 values for region II of as coated QCM data conducted at 65.0°C

Fitted rate law	Fit	R^2	χ^2
	Sensor 1		
Linear: αt	$Y= 8.72E\text{-}5*t + 0.448$	0.9145	56.12
Parabolic: $\alpha t^{1/2}$	$Y= 0.00917*t^{1/2} + 0.175$	0.9848	3.111
Parabolic + linear: $\alpha t^{1/2}+t$	$Y*t= 0.0189*t^{-1/2} - 1.23E\text{-}4$	0.9984	0.0008
Power: $\alpha t^{1/4}$	$Y= 0.114*t^{1/4} - 0.170$	0.9919	0.8908
	Sensor 2		
Linear: αt	$Y= 1.40E\text{-}4*t + 0.383$	0.9093	105.2
Parabolic: $\alpha t^{1/2}$	$Y= 0.0139*t^{1/2} + 0.0835$	0.9857	9.170
Parabolic + linear: $\alpha t^{1/2}+t$	$Y*t= 0.0193*t^{-1/2} - 8.52E\text{-}5$	0.9962	0.0018
Power: $\alpha t^{1/4}$	$Y= 0.146*t^{1/4} - 0.289$	0.9912	2.753
	Sensor 3		
Linear: αt	$Y= 1.101E\text{-}4*t + 0.414$	0.9214	9.392
Parabolic: $\alpha t^{1/2}$	$Y= 0.00869*t^{1/2} + 0.255$	0.9758	2.940
Parabolic + linear: $\alpha t^{1/2}+t$	$Y*t= 0.0237*t^{-1/2} - 1.97E\text{-}4$	0.9983	0.0010
Power: $\alpha t^{1/4}$	$Y= 0.105*t^{1/4} - 0.0560$	0.9924	0.9575

5.5.1. For the hydrazine-reduced samples, the grain size was found to be 3-5 nm from HRTEM (as discussed in section 5.5.2.) and a simple cube-shaped grain model was used to determine the cross-sectional area percentage of grain boundaries present in the sample. The average effective diffusion value calculated from equation 5.35 using

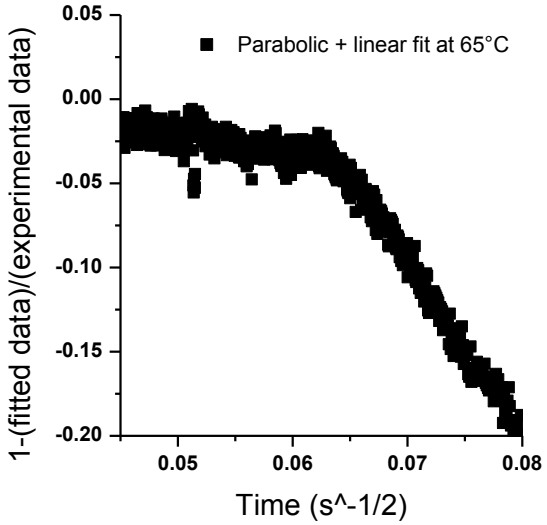

Figure 146: The difference between fitted data and experimental data are shown for parabolic + linear fits (equation 5.51) on samples reacted at 65°C

three different QCM experiments can be seen below in Table 20. Using a grain size of 4 nm, a grain boundary width of 0.5 nm and a cube-shaped grain model to determine the fraction percent of grain boundary cross-sectional area ($f = \frac{G^2-(G-\delta)^2}{G^2}$, equation 5.41), the grain boundary diffusion constant can be derived from the effective diffusion constant with equation 5.38. Table 20 and Table 21 show the average grain boundary diffusion constants calculated from the QCM data for assumed 3 nm, 4 nm, and 5 nm grains with 0.5 and 1.0 nm grain boundary widths, respectively.

Table 20: D_{eff} and D_{gb} values obtained from 3 identically conducted QCM experiments on 3 different samples at 65°C with an assumed grain boundary width of 0.5 nm. Error ranges represent ±1 standard deviation.

Gain Size	D_{eff} (10^{-12}cm^2/sec)	Area Fraction	D_{gb} (10^{-12}cm^2/sec)
3 nm	0.486 +/- 0.243	0.306	1.59 +/- 0.79
4 nm	0.486 +/- 0.243	0.234	2.07 +/- 1.04
5 nm	0.486 +/- 0.243	0.190	2.56 +/- 1.28

Table 21: D_{eff} and D_{gb} values obtained from 3 identically conducted QCM experiments on 3 different samples at 65°C with an assumed grain boundary width of 1.0 nm. Error ranges represent ±1 standard deviation.

Gain Size	D_{eff} ($10^{-12}cm^2/sec$)	Area Fraction	D_{gb} ($10^{-12}cm^2/sec$)
3 nm	0.486 +/- 0.243	0.55	0.88 +/- 0.44
4 nm	0.486 +/- 0.243	0.438	1.11 +/- 0.56
5 nm	0.486 +/- 0.243	0.360	1.35 +/- 0.67

In addition to yielding the grain boundary chemical diffusion coefficients, the percent reacted at the end of region I can also be used to validate the transition in diffusion mechanisms. The proposed transition from region I to region II is predicted to take place when the grain boundary is fully reduced and the diffusion shifts from a 1-D parabolic dependence to a spherical dependence. Therefore, the percent reacted at the end of region I should be equal to the percent of the total film volume occupied by grain boundaries in the sample. The percent reacted, (Figure 147, $f = \frac{G^3-(G-\delta)^3}{G^3}$, equation 5.55) at the end of region I, for the as-coated samples (grain size ~3-5 nm) after 65.0°C hydrazine reduction are compared to cubic grain boundary fraction approximations (an

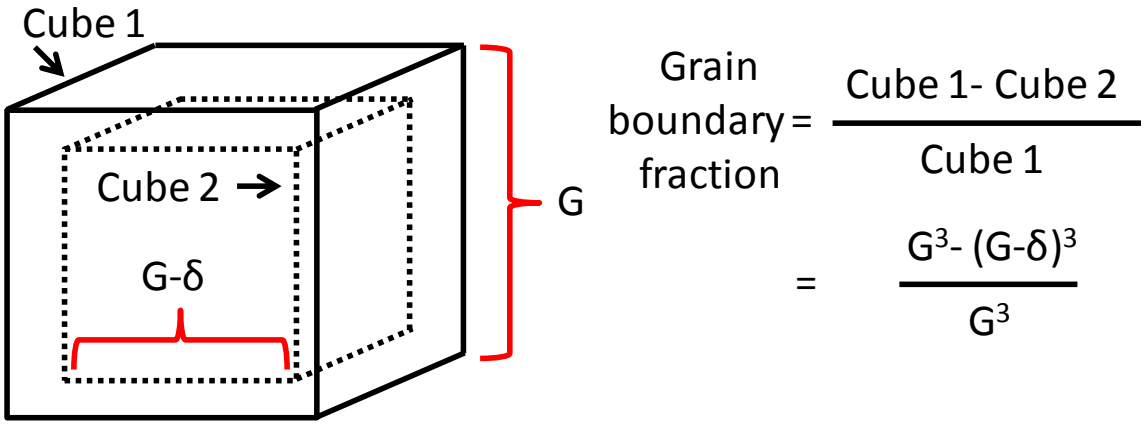

Figure 147: Schematic for calculating the grain boundary fraction for cube shaped grains with a grain boundary width of δ and a grain size of G.

assumed grain boundary with ranging from 0.5 nm to 1.0 nm) in Figure 148. The percent reacted at the time of transition from region 1 to region 2 were similar to grain boundary fraction for samples with 0.5 nm grain boundary width.

The parabolic + linear growth diffusion model was used to calculate the lattice diffusion constant for region II by fitting the data to equation 5.51.

$$\frac{M_t}{M_\infty} \times \frac{1}{t} = 6\pi^{-\frac{1}{2}} \left(\frac{D}{R^2}\right)^{\frac{1}{2}} \times \frac{1}{t^{\frac{1}{2}}} - 3\frac{D}{R^2} \qquad (5.51)$$

Grain sizes of 4 nm, or radii of 2 nm, were used to determine the diffusion constants based on the fitted data. Lattice diffusion constants determined from the slope and intercept can be seen in Table 22 and are compared to previously-reported values for iron (chemical) lattice diffusion through maghemite.

In conclusion, as-coated QCM samples with a ~4 nm grain size exhibited reduction kinetics consistent with the proposed diffusion mechanisms. During the start of the reduction process, planar 1-d parabolic grain boundary diffusion appears to be the dominating mechanism. The percent of maghemite reduced to magnetite at the end of region I matched that of the estimated grain boundary volume percentage in the sample (within 6-14% for 3 nm sized grains and complete overlap for 5 nm sized grains), suggesting that the grain boundaries are fully-reduced at the end of region I. Region II matches well to a spherical diffusion model which would indicate that each grain is being reduced from the outside in and is not governed by a 1-D planar diffusion front moving through the coating. The experimentally derived lattice diffusion constants match previously-reported values for iron diffusing through maghemite upon oxidation of magnetite via exposure to either an aqueous solution or to air.

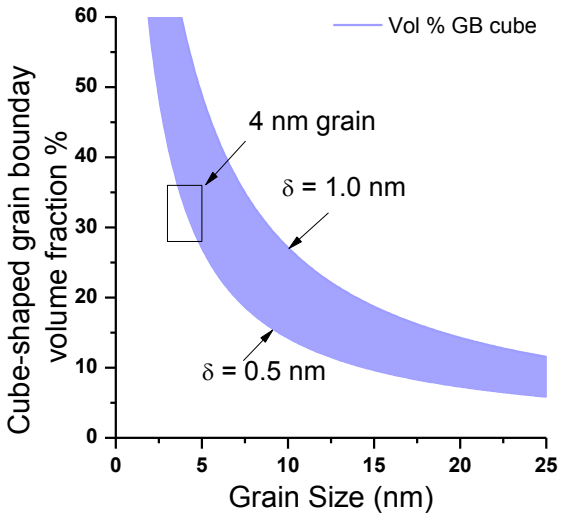

Figure 148: The black box represents the % reacted at the end of region I for as coated samples after 65°C hydrazine reduction. Blue-shaded regions represent percent grain boundary fraction for cube-shaped grains with the grain boundary width varying from 0.5 nm to 1.0 nm

Table 22: Lattice diffusion values obtained from slope and intercepts for 3 identical QCM experiments carried out at 65°C compared to reference values. Errors represent 1 standard deviation.

	D (slope) (10^{-18}cm^2/sec)	D (intercept) (10^{-18}cm^2/sec)	D - γ-Fe_2O_3 [10] (10^{-18}cm^2/sec)	D - γ-Fe_2O_3 [9] (10^{-18}cm^2/sec)
Diffusion Constant	1.49 +/- 0.41	1.74 +/- 0.82	9.04	1.90

5.5.4. Effect of Reaction Temperature on the Kinetics of Maghemite Reduction

The effect of temperature on the reduction process was investigated by performing QCM measurements at 65.0°C, 71.3°C, 77.5°C, 83.8°C and 90.0°C (Figure 149). The diffusion constants for region I were determined by fitting the data to a planar parabolic growth model (Figure 150) with equation 5.35 and using equation 5.38 to determine possible grain boundary diffusion coefficients. Table 18, Table 23, Table 24, Table 25, and Table 26 show the fitted data for samples reacted at 65.0°C, 71.3°C, 77.5°C, 83.8°C and 90.0°C, respectively.

$$\frac{M_t}{M_\infty} = 2\pi^{-\frac{1}{2}}\left(\frac{D_{eff}t}{l^2}\right)^{\frac{1}{2}} \quad (5.35)$$

$$D_{eff} = fD_{gb} \quad (5.38)$$

The grain boundary diffusion coefficient (D_{gb}) and effective diffusion coefficient (D_{eff}) data calculated from fitting QCM plots for samples reacted at 65.0°C, 71.3°C, 77.5°C, 83.8°C, and 90.0°C are listed in Table 27. At the end of region I, the extent of reduction (to magnetite) of all samples was reacted between 27 – 45%. These values matched the volume percent of grain boundaries present for samples with 4 nm sized grains as shown in Figure 151 and indicate that the transition from region I to region II occurred when the grain boundaries have been fully reacted. Unfortunately, little work has been investigated on determining the grain boundary diffusion constants for either oxygen or iron at similar temperatures. In addition, this work was unable to determine if iron or oxygen are the dominant diffusion species. However, grain boundary diffusion has been shown to occur at faster rates compared lattice diffusion for Co tracer ions in magnetite at 750°C with a D_{gb}/D_L ratio of ~10^3.[29]

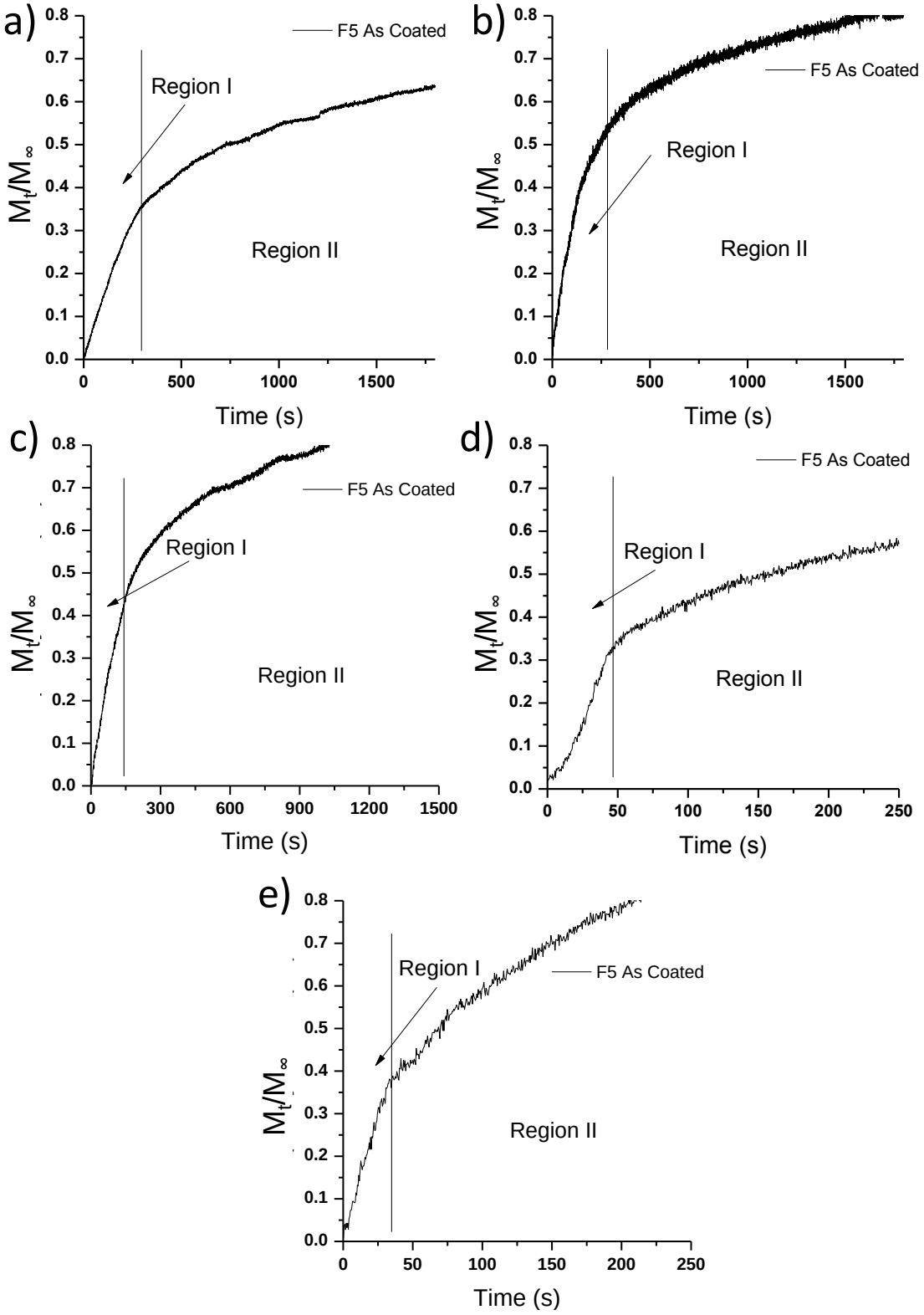

Figure 149: QCM plots of samples reacted in the as-coated state at: a) 65.0°C, b) 71.3°C, c) 77.5°C, d) 83.7°C, and e) 90.0°C

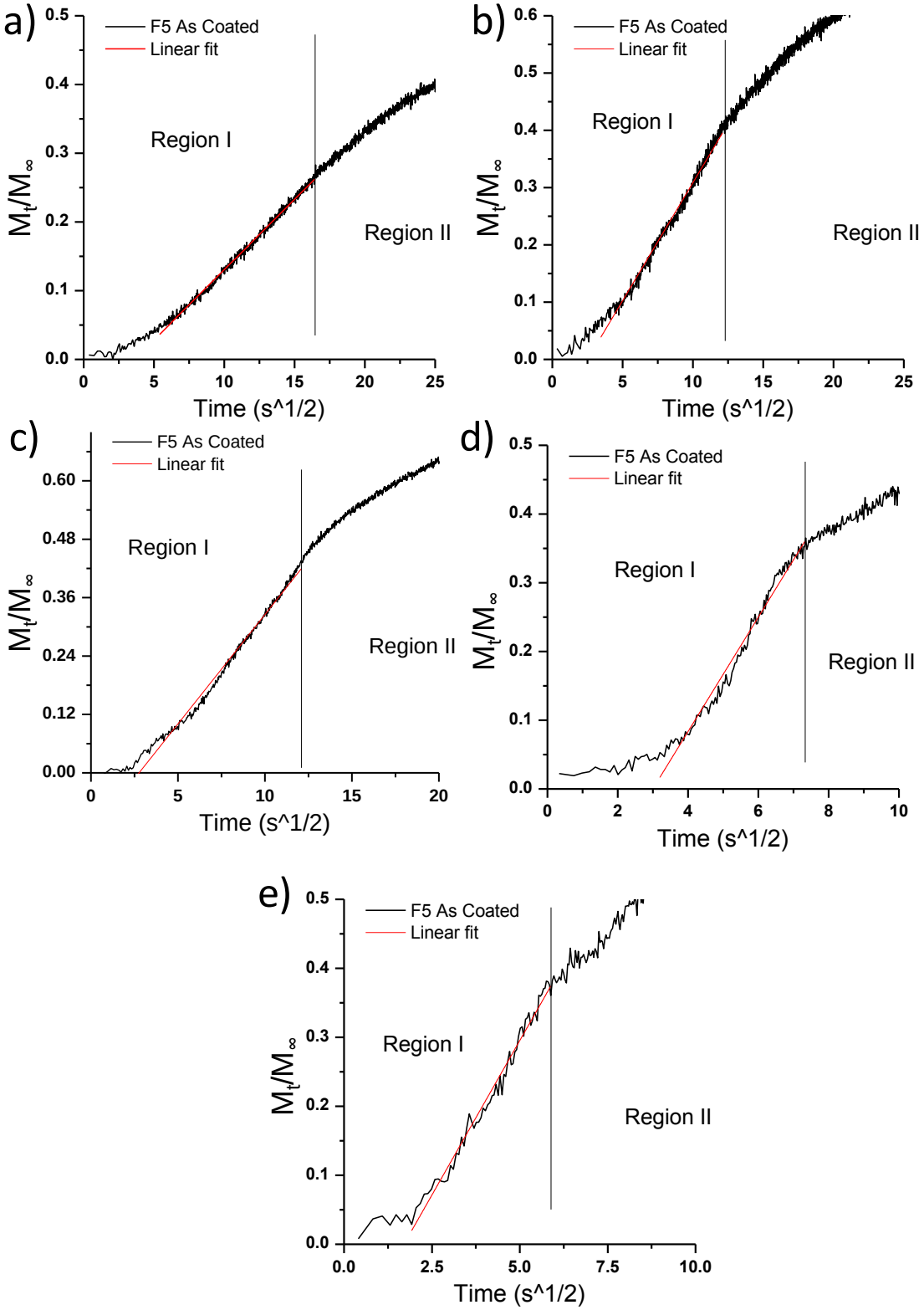

Figure 150: 1-D parabolic fits to the region I kinetics for as-coated specimens. QCM data obtained at: a) 65.0°C, b) 71.3°C, c) 77.5°C, d) 83.7°C, and e) 90.0°C.

Table 23: Linear, parabolic, and 4th power fits, R^2 and, χ^2 values for region I of as coated QCM data conducted at 71.3C.

Fitted rate law	Fit	R^2	χ^2
	QCM sensor 1		
Linear: αt	$Y= 0.001968*t + 0.04862$	0.9731	0.4803
Parabolic: αt^2	$Y= 0.03008*t^{1/2} - 0.05374$	0.9864	0.2152
Power: αt^4	$Y= 0.1572*t^{1/4} - 0.2513$	0.9696	0.5357
	QCM sensor 2		
Linear: αt	$Y= 0.002500*t + 0.05322$	0.9861	0.2047
Parabolic: αt^2	$Y= 0.04213*t^{1/2} - 0.1131$	0.9897	0.1525
Power: αt^4	$Y= 0.2380*t^{1/4} - 0.4431$	0.9806	0.3648
	QCM sensor 3		
Linear: αt	$Y= 0.002203*t + 0.02095$	0.9267	0.8205
Parabolic: αt^2	$Y= 0.03102*t^{1/2} - 0.07281$	0.9442	0.7110
Power: αt^4	$Y= 0.1599*t^{1/4} - 0.2790$	0.9334	0.7892

Table 24: Linear, parabolic, and 4th power fits, R^2 and, χ^2 values for region I of as coated QCM data conducted at 77.5°C.

Fitted rate law	Fit	R^2	χ^2
	QCM sensor 1		
Linear: αt	$Y= 0.004134*t + 0.05229$	0.9705	0.4307
Parabolic: αt^2	$Y= 0.04812*t^{1/2} - 0.07135$	0.9924	0.1033
Power: αt^4	$Y= 0.2247*t^{1/4} - 0.3254$	0.9846	1.192
	QCM sensor 2		
Linear: αt	$Y= 0.003442*t + 0.03130$	0.9895	0.0639
Parabolic: αt^2	$Y= 0.04753*t^{1/2} - 0.1243$	0.9992	0.0052
Power: αt^4	$Y= 0.2444*t^{1/4} - 0.4339$	0.9953	0.0414
	QCM sensor 3		
Linear: αt	$Y= 0.002752*t + 0.04388$	0.9891	0.1427
Parabolic: αt^2	$Y= 0.04853*t^{1/2} - 0.1592$	0.9972	0.0462
Power: αt^4	$Y= 0.2820*t^{1/4} - 0.5630$	0.9925	0.1442

Table 25: Linear, parabolic, and 4th power fits, R^2 and, χ^2 values for region I of as coated QCM data conducted at 83.8°C.

Fitted rate law	Fit	R^2	χ^2
	QCM sensor 1		
Linear: αt	$Y= 0.007520*t + 0.03129$	0.9794	0.0704
Parabolic: αt^2	$Y= 0.0205*t^{1/2} - 0.0744$	0.9850	0.0894
Power: αt^4	$Y= 0.4040*t^{1/4} - 0.7373$	0.9809	0.1688
	QCM sensor 2		
Linear: αt	$Y= 0.002109*t + 0.008226$	0.9930	0.1264
Parabolic: αt^2	$Y= 0.04857*t^{1/2} - 0.1843$	0.9861	0.2736
Power: αt^4	$Y= 0.3233*t^{1/4} - 0.7154$	0.9748	0.5372
	QCM sensor 3		
Linear: αt	$Y= 0.002993*t + 0.03441$	0.9824	0.3554
Parabolic: αt^2	$Y= 0.04540*t^{1/2} - 0.1240$	0.9880	0.2961
Power: αt^4	$Y= 0.2432*t^{1/4} - 0.4423$	0.9771	0.9665

Table 26: Linear, parabolic, and 4th power fits, R^2 and, χ^2 values for region I of as coated QCM data conducted at 90°C.

Fitted rate law	Fit	R^2	χ^2
	QCM sensor 1		
Linear: αt	$Y= 0.004738*t + 0.06376$	0.9638	.8798
Parabolic: αt^2	$Y= 0.06711*t^{1/2} – 0.1491$	0.9960	0.4592
Power: αt^4	$Y= 0.8439*t^{1/4} – 2.696$	0.9776	0.5286
	QCM sensor 2		
Linear: αt	$Y= 0.005135*t + 0.07191$	0.9599	0.2419
Parabolic: αt^2	$Y= 0.04800*t^{1/2} – 0.02295$	0.9859	0.0100
Power: αt^4	$Y= 0.1860*t^{1/4} – 0.1897$	0.9511	1.202
	QCM sensor 3		
Linear: αt	$Y= 0.01149*t + 0.01080$	0.9754	0.0293
Parabolic: αt^2	$Y= 0.08932*t^{1/2} – 0.1558$	0.9702	0.0360
Power: αt^4	$Y= 0.3466*t^{1/4} – 0.4883$	0.9614	0.0507

Table 27: Grain boundary diffusion values obtained from slope and intercepts for 5 identical QCM analyses on 3 different specimens conducted at 65.0°C, 71.3°C, 77.5°C, 83.8°C, and 90.0°C. Error ranges represent ±1 standard deviation.

Temperature	Percent Reacted	D_{eff} ($10^{-12}cm^2/sec$)	D_{gb} ($10^{-12}cm^2/sec$)
65.0°C	30 +/- 5	0.486 +/- 0.243	2.07 +/- 1.04
71.3°C	38 +/- 7	0.576+/- 0.096	7.06 +/- 3.68
77.5°C	37 +/- 5	0.824 +/- 0.052	10.1 +/- 0.64
83.8°C	38 +/- 4	1.43 +/- 0.313	17.5 +/- 3.84
90.0°C	36 +/- 3	2.53 +/- 1.10	20.9 +/- 9.09

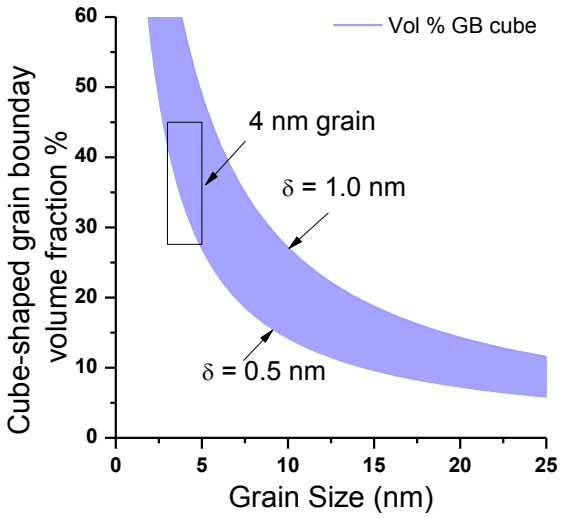

Figure 151: The black box represents the % reacted at the end of region I for as coated samples after 65.0°C-90.0°C hydrazine reduction. Blue-shaded regions represent percent grain boundary fraction for a cube-shaped grains with the grain boundary width varying from 0.5 nm to 1.0 nm.

The following Arrhenius equation was used to fit the temperature dependence of the diffusion data.

$$D = D_0 exp\left(\frac{-E}{RT}\right) \tag{5.60}$$

where E is the activation energy, R is the gas constant, T is the absolute temperature, and D_0 is the frequency factor. The activation energy and frequency factor can be calculated by obtaining a linear fit to a plot of ln(D) vs 1/T where the slope is equal to E/R and the y intercept is equal to ln(D_0). Figure 152 shows the temperature dependence of the grain boundary diffusion data fitted to the Arrhenius equation.

The effect of temperature on the diffusion coefficients in region II was also investigated by curve fitting reduction data obtained at 65.0°C, 71.3°C, 77.5°C, 83.8°C, and 90.0°C. Figure 153 shows representative plots for samples reacted at 65.0°C, 77.5°C, and 90.0°C. Tables 19, 28 29, 30, and 31 show fitted values for samples reacted at 65.0°C, 71.3°C, 77.5°C, 83.8°C, and 90.0°C, respectively. The reduction data was then

fitted to equation 5.51 and was used to calculate the lattice diffusion D in a similar fashion as discussed in section 5.5.3.

$$\frac{M_t}{M_\infty} \times \frac{1}{t} = 6\pi^{-\frac{1}{2}} \left(\frac{D}{R^2}\right)^{\frac{1}{2}} \times \frac{1}{t^{\frac{1}{2}}} - 3\frac{D}{R^2} \tag{5.51}$$

Grain sizes of 4 nm, or radii of 2 nm, were used to determine the diffusion constants based on the fitted data. The lattice diffusion data calculated from both the intercept and slope are presented in Table 32. The following Arrhenius equation was used to fit the temperature dependence of the diffusion data.

$$D = D_0 \exp\left(\frac{-E}{RT}\right) \tag{5.60}$$

where E is the activation energy, R is the gas constant, T is the absolute temperature, and D_0 is the frequency factor. The activation energy and frequency factor can be calculated by obtaining a linear fit to a plot of ln(D) vs. 1/T where the slope is equal to E/R and the y intercept is equal to $\ln(D_0)$. Figure 154 shows the temperature dependence of the diffusion constants obtained from the slope a) and y intercept b) fitted to the Arrhenius

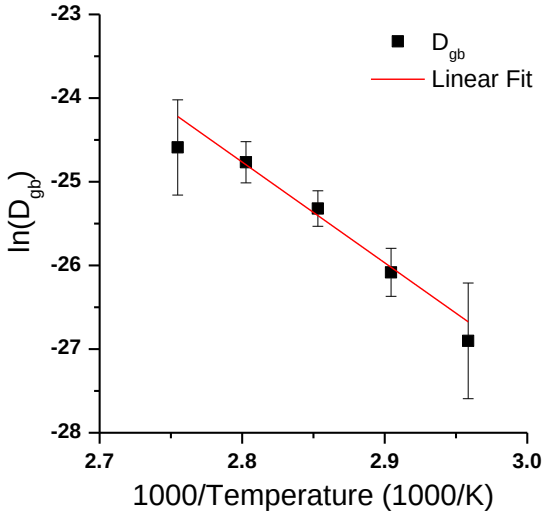

Figure 152: Arrhenius plot of the grain boundary diffusion coefficients determined from planar parabolic fits to region I.

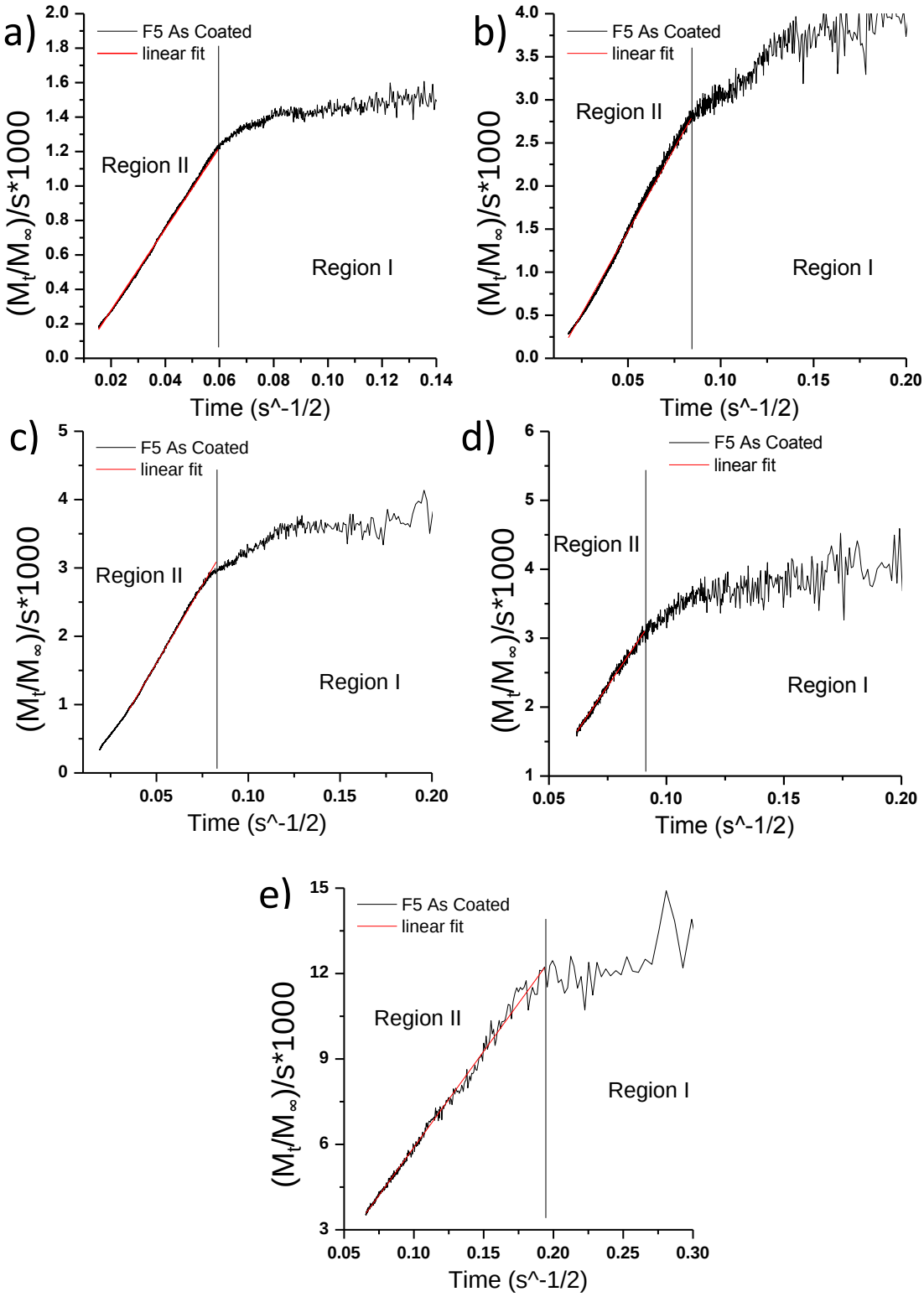

Figure 153: Parabolic + linear fits to the region II for as coated QCM data conducted at a) 65.0°C, b) 71.3°C, c) 77.5°C, d) 83.7°C and e) 90.0°C.

equation. The activation energy was found to be 20.4 +/- 3.4 kcal/mol and 16.2 +/- 4.0 kcal/mol for the slope and intercept fittings respectively, which are similar to the values obtained by Tang[9] (21.0 kcal/mol at temperatures between 24-80°C), Sidhu[10] (19.4 kcal/mol at temperatures between 170-220°C), and Colombo[30] (20 kcal/mol at temperatures 220-250°C). The theoretical value of the frequency factor, D_0, is related to the product of distance between nearest neighbors in the lattice (2.05×10^{-8} cm for magnetite[10]) and the mean molecular velocity (3×10^{4} cm/sec [10]) divided by 3, which is equal to 2.05×10^{-4} cm^2/sec.[10] The frequency factor, D_0, calculated from the fitting the diffusion data obtained from the slope was found to be $3.28 \times 10^{-5} cm^2$/sec. This value was similar to reported values by Tang[9] (7.2×10^{-5} cm^2/s) and Sidhu[10] (3.16×10^{-5} cm^2/s).

Using the D_0 and E values for iron lattice diffusion through maghemite provided by Tang[9] and Sidhu[10], diffusion constants can be calculated and compared to the average diffusion value obtained from the slope and intercept for this work at 65.0°C, 71.3°C, 77.5°C, 83.8°C, and 90.0°C, as is shown in Figure 155. Both sets of values agree reasonably well with the diffusion constants obtained with the QCM (i.e., the values are within an order of magnitude of each other). However, the diffusion constants obtained by Tang, et al, corresponding to temperatures of 24 to 80°C, matched the values obtain from this work better than those of Sidhu [10]. This work and the work of Tang, et al.[9] were conducted in an aqueous reducing or oxidizing environment, respectively, and at similar temperatures (24-80°C), while the work of Sidhu, et al.[10] was conducted in a dry oxidizing environment at slightly higher temperatures (190-210°C).

Table 28: Linear, parabolic, and 4th power fits, R^2 and, χ^2 values for region II of as coated QCM data conducted at 71.3°C.

Fitted rate law	Fit	R^2	χ^2
	Sensor 1		
Linear: αt	$Y= 3.132E\text{-}4*t + 0.3152$	0.9592	0.7390
Parabolic: $\alpha t^{1/2}$	$Y= 0.01408*t^{1/2} + 0.1664$	0.9755	0.2918
Parabolic + linear: $\alpha t^{1/2}+t$	$Y*t= 0.03114*t^{-1/2} – 4.072E\text{-}4$	0.9947	0.0005
Power: $\alpha t^{1/4}$	$Y= 0.1302*t^{1/4} – 0.1296$	0.9755	0.1682
	Sensor 2		
Linear: αt	$Y= 1.183E\text{-}4*t + 0.5750$	0.8689	12.79
Parabolic: $\alpha t^{1/2}$	$Y= 0.0091*t^{1/2} + 0.418$	0.9504	5.148
Parabolic + linear: $\alpha t^{1/2}+t$	$Y*t= 0.03847*t^{-1/2} – 4.474E\text{-}4$	0.9957	0.0009
Power: $\alpha t^{1/4}$	$Y= 0.1517*t^{1/4} – 0.0948$	0.9751	2.120
	Sensor 3		
Linear: αt	$Y= 1.133E\text{-}3*t + 0.1019$	0.8459	0.8819
Parabolic: $\alpha t^{1/2}$	$Y= 0.0314*t^{1/2} – 0.116$	0.8723	0.7244
Parabolic + linear: $\alpha t^{1/2}+t$	$Y*t= 0.03001*t^{-1/2} – 5.603E\text{-}3$	0.9898	0.0684
Power: $\alpha t^{1/4}$	$Y= 0.2318*t^{1/4} – 0.5379$	0.8833	0.6595

Table 29: Linear, parabolic, and 4th power fits, R^2 and, χ^2 values for region II of as coated QCM data conducted at 77.5°C.

Fitted rate law	Fit	R^2	χ^2
	Sensor 1		
Linear: αt	$Y= 2.842E\text{-}4*t + 0.5085$	0.8444	6.3802
Parabolic: $\alpha t^{1/2}$	$Y= 1.415E\text{-}2*t^{1/2} + 0.3472$	0.9284	2.921
Parabolic + linear: $\alpha t^{1/2}+t$	$Y*t= 0.04782*t^{-1/2} – 7.183E\text{-}4$	0.9979	0.0010
Power: $\alpha t^{1/4}$	$Y= 0.1355*t^{1/4} – 0.03164$	0.9621	1.517
	Sensor 2		
Linear: αt	$Y= 5.486E\text{-}4*t + 0.3441$	0.9389	0.6998
Parabolic: $\alpha t^{1/2}$	$Y= 0.01994*t^{1/2} + 0.1731$	0.9808	0.1808
Parabolic + linear: $\alpha t^{1/2}+t$	$Y*t= 0.04058*t^{-1/2} – 5.788E\text{-}4$	0.9962	0.0001
Power: $\alpha t^{1/4}$	$Y= 0.1658*t^{1/4} – 0.1660$	0.9929	0.0418
	Sensor 3		
Linear: αt	$Y= 1.101E\text{-}4*t + 0.414$	0.9214	0.7932
Parabolic: $\alpha t^{1/2}$	$Y= 0.001762*t^{1/2} + 0.2757$	0.9700	0.3385
Parabolic + linear: $\alpha t^{1/2}+t$	$Y*t= 0.04555*t^{-1/2} – 6.714E\text{-}4$	0.9986	0.0002
Power: $\alpha t^{1/4}$	$Y= 0.1591*t^{1/4} – 0.007850$	0.9840	0.1740

Table 30: Linear, parabolic, and 4th power fits, R^2 and, χ^2 values for region II of as coated QCM data conducted at 83.7°C.

Fitted rate law	Fit	R^2	χ^2
	Sensor 1		
Linear: αt	$Y= 2.790E\text{-}4*t + 0.4794$	0.8354	2.956
Parabolic: $\alpha t^{1/2}$	$Y= 0.01235*t^{1/2} + 0.3547$	0.9245	1.325
Parabolic + linear: $\alpha t^{1/2}+t$	$Y*t= 0.05559*t^{-1/2} – 1.20E\text{-}3$	0.9969	0.0898
Power: $\alpha t^{1/4}$	$Y= 0.1111*t^{1/4} – 0.1116$	0.9601	0.6497
	Sensor 2		
Linear: αt	$Y= 5.636E\text{-}4*t + 0.4769$	0.8956	1.792
Parabolic: $\alpha t^{1/2}$	$Y= 0.02584*t^{1/2} + 0.1886$	0.9261	1.253
Parabolic + linear: $\alpha t^{1/2}+t$	$Y*t= 0.04199*t^{-1/2} – 3.352E\text{-}4$	0.9783	0.0020
Power: $\alpha t^{1/4}$	$Y= 0.2447*t^{1/4} – 0.3867$	0.9374	1.061
	Sensor 3		
Linear: αt	$Y= 3.640E\text{-}4*t + 0.3417$	0.7256	0.0797
Parabolic: $\alpha t^{1/2}$	$Y= 0.01000*t^{1/2} + 0.2736$	0.7475	0.0733
Parabolic + linear: $\alpha t^{1/2}+t$	$Y*t= 0.05051*t^{-1/2} – 0.001478$	0.9885	0.0003
Power: $\alpha t^{1/4}$	$Y= 0.07390*t^{1/4} – 0.1376$	0.7576	0.0703

Table 31: Linear, parabolic, and 4th power fits, R^2 and, χ^2 values for region II of as coated QCM data conducted at 90.0°C.

Fitted rate law	Fit	R^2	χ^2
	Sensor 1		
Linear: $\alpha\ t$	$Y= 9.395E\text{-}4*t + 0.5106$	0.9399	0.289
Parabolic: $\alpha\ t^{1/2}$	$Y= 3.067E\text{-}2*t^{1/2} + 0.2685$	0.9616	0.1604
Parabolic + linear: $\alpha\ t^{1/2}+t$	$Y*t= 6.834E\text{-}2*t^{-1/2} - 1.247E\text{-}3$	0.9920	0.0007
Power: $\alpha\ t^{1/4}$	$Y= 0.2446*t^{1/4} - 0.2150$	0.9681	0.1218
	Sensor 2		
Linear: $\alpha\ t$	$Y= 1.037E\text{-}3*t + 0.3441$	0.9053	0.5337
Parabolic: $\alpha\ t^{1/2}$	$Y= 0.02714*t^{1/2} + 0.17436$	0.9490	0.2807
Parabolic + linear: $\alpha\ t^{1/2}+t$	$Y*t= 5.389E\text{-}2*t^{-1/2} - 9.638E\text{-}4$	0.9935	0.0009
Power: $\alpha\ t^{1/4}$	$Y= 0.1926*t^{1/4} - 0.1633$	0.9646	0.1910
	Sensor 3		
Linear: $\alpha\ t$	$Y= 2.307E\text{-}3*t + 0.3354$	0.9700	0.4479
Parabolic: $\alpha\ t^{1/2}$	$Y= 0.04987*t^{1/2} + 0.08424$	0.9938	0.0888
Parabolic + linear: $\alpha\ t^{1/2}+t$	$Y*t= 0.06743*t^{-1/2} - 8.469E\text{-}4$	0.9951	0.0010
Power: $\alpha\ t^{1/4}$	$Y= 0.3182*t^{1/4} - 0.4131$	0.9942	0.0884

Table 32: Lattice diffusion values obtained from slope and intercepts for 5 identical QCM analyses of 3 different sensors conducted at 65.0°C, 71.3°C, 77.5°C, 83.8°C, and 90.0°C. Error ranges represent 1 standard deviation.

Temperature	Diffusion Constant	
	$D_{Lattice}$ (slope) ($10^{-18}cm^2/sec$)	$D_{Lattice}$ (intercept) ($10^{-18}cm^2/sec$)
65.0°C	1.49 +/- 0.41	1.74 +/- 0.82
71.3°C	4.27 +/- 1.26	5.69 +/- 0.38
77.5°C	6.99 +/- 1.13	8.74 +/- 0.94
83.8°C	8.62 +/- 2.33	13.40 +/- 7.96
90.0°C	14.23+/- 3.65	14.23 +/- 4.85

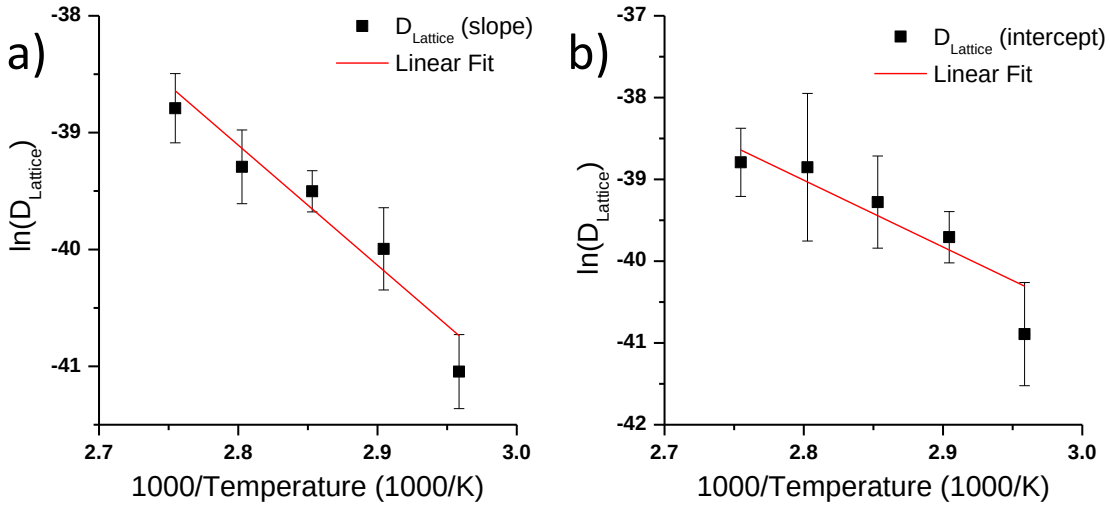

Figure 154: Arrhenius plot of the lattice diffusion coefficients determined from the a) slope and b) y intercept.

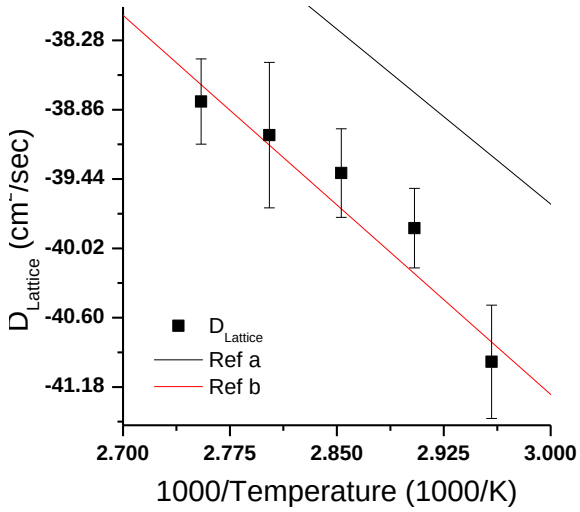

Figure 155: Lattice diffusion constant measured from QCM data (black dots) compared to ref. a, [10] (red line) and ref. b, [9] (black line).

The suggested diffusion mechanism for kinetic region II predicts that the reduction rate will depend on the size of crystals in the coatings, with shorter reduction times needed for smaller crystals. While it was not possible to generate samples with controlled and varied grain sizes, it was possible to compare the reduction times needed in this study with oxidation times presented elsewhere. Tang, et al.[9] found that nano crystals with 9 nm diameter required oxidation times between three months at 24°C to 3 h at 80°C. Similarly, Murad, et al.[31] showed that, for magnetite particles of 100 nm – 300 nm diameter, complete oxidation at room temperature required over a year. For even larger grained samples, Sidhu, et al.[10] did not detect any appreciable signs of room temperature oxidation within year. While this work has evaluated the reduction of maghemite into magnetite as opposed to the reverse, the same type diffusion mechanism seems to be describing both cases (i.e., iron lattice diffusion through magnetite upon maghemite reduction in the second kinetic region of the present work, and iron lattice diffusion through maghemite upon oxidation of magnetite). The 3-5 nm sized coatings in

this study at 83.8°C took less than 1 h to fully react, which was less time than previously reported for oxidation of 9 nm grain size magnetite at 80°C.

5.6. *Concluding Remarks*

In summary, the reduction of maghemite thin films to magnetite upon exposure to a reducing hydrazine solution has been studied with the use of a QCM. A two-part diffusion model was developed to describe the diffusion process at both short times (< 10 min at 65°C) and long times (> 10 min at 65°C). At short times, experimental revealed that the reduction rate followed a 1-D parabolic growth rate that was consistent with grain boundary diffusion. The diffusion mechanism may be described by either mechanism I (illustrated in Figure 117) or mechanism II (illustrated in Figure 118) and the diffusion pathway for regime 1 in Figure 126.

At longer times, the inward diffusion of iron cations through the lattice was found to be the rate-limiting process and this rate was governed by a parabolic + linear growth model. The diffusion models and activation energies matched those of Tang, et al. and Sidhu, et al. which indicated that both the region II reduction of maghemite to magnetite and the oxidation of magnetite to maghemite occur by a similar process. The reduction process in region II may be described by mechanism II illustrated in Figure 118 and the diffusion pathway for regime 3 in Figure 126. These results are consistent with the reverse reaction in which magnetite oxidation is believed to occur through outward diffusion of iron cations for both aqueous and dry oxidation.[9, 10]

5.7. ***References***

[1] X. Liu, J. Shaw, J. Jiang, J. Bloemendal, P. Hesse, T. Rolph, *et al.*, "Analysis on variety and characteristics of maghemite," *Science China Earth Sciences,* vol. 53, pp. 1153-1162, 2010/08/01 2010.

[2] R. Dronskowski, "The Little Maghemite Story A Classic Functional Material," *Adv. Funct. Mater.,* vol. 11, 2001.

[3] R. M. Cornell and U. Schwertmann, *The Iron Oxides*: Weinheim: VCH Verlagsgesellschaft, 1996.

[4] R. Grau-Crespo, A. Y. Al-Baitai, I. Saadoune, and N. H. D. Leeuw, "Vacancy ordering and electronic structure of γ-Fe_2O_3 (maghemite): a theoretical investigation," 2008.

[5] F. Bourgeois, P. Gergaud, H. Renevier, C. Leclere, and G. Feuillet, "Low temperature oxidation mechanisms of nanocrystalline magnetite thin film," *Journal of Applied Physics,* vol. 113, pp. -, 2013.

[6] F. Bourgeois, P. Gergaud, H. Renevier, C. Leclere, and G. Feuillet, "Low temperature oxidation mechanisms of nanocrystalline magnetite thin film," *Journal of Applied Physics,* vol. 113, p. 013510, 2013.

[7] U. Colombo, G. Fagherazzi, F. Gazzarrini, G. Lanzavecchia, and G. Sironi, "Mechanism of Low Temperature Oxidation of Magnetites," *Nature,* p. 1036, 1968.

[8] B. Gillot, A. Rousset, and G. Dupre, "Electrical conductivity of $(Fe^{2+}Al^{3+}{}_{2-x}Cr^{3+}{}_{x})O^{2-}{}_{4}$ spinels and defect phases γ-$(Fe^{2+}{}_{1/3}Al^{3+}{}_{2/3-y}Cr^{3+}{}_{y})O^{2-}{}_{3}$," *J. Solid State Chem.,* vol. 25, p. 263 1978.

[9] J. Tang, M. Myers, K. A. Bosnick, and L. E. Brus, "Magnetite Fe_3O_4 Nanocrystals Spectroscopic Observation of Aqueous Oxidation Kinetics," *J. Phys. Chem. B,* vol. 107, pp. 7501-7506, 2003.

[10] P. S. Sidhu, R. J. Gilkes, and A. M. Posner, "Mechanism of the Low Temperature Oxidation of Synthetic Magnetites," *J. Inorg. Nucl. Chem.,* vol. 39, pp. 1953-1958, 1977.

[11] S. Ogawa, "Oxidation Rate and Phase Diagram of Mu-Zn Ferrite Determined from the Cation Diffusion Coefficient"*Jpn. J. Appl. Phys.* vol. 6, pp. 1427.

[12] R. D. Shannon and C. T. Prewitt, "Effective Ionic Radii in Oxides and Fluorides," *Acta Cryst. ,* vol. B25, pp. 925-946 1969.

[13] O. Levenspiel, "Chemical reactor omnibook," ed Oregon State University Bookstores, 1999.

[14] J. A. Peña, E. Lorente, E. Romero, and J. Herguido, "Kinetic study of the redox process for storing hydrogen," *Catalysis Today,* vol. 116, pp. 439-444, 2006.

[15] T. Fukasawa, M. Iwatsuki, and M. Furukawa, "State analysis and relationship between lattice constants and- compositions including minor elements of synthetic magnetite and maghemite," *Analytica Chimica Acta,* vol. 281, pp. 413-419, 1993.

[16] W. A. Deer, R. A. Howie, and J. Zussman, *The Rock Forming Mineral, Non-Silicates*, 2nd ed. vol. vol 5. New York: Longmans, 1962.

[17] J. Crank, *The Mathematics of Diffusion*, second edition ed. Oxford: Claredndon Press, 1975.

[18] H. Hehrer, *Diffusion in Solids - Fundamentals, methods, Mtls, Diffusion-Controlled Processes*. BerlinHeidelberg: Springer-Verlag, 2007.

[19] J. M. Perrow, W. W. Smeltzer, and J. D. Embury, "The role of structural defects in the growth of nickel oxide films," *Acta Metallurgica,* vol. 16, pp. 1209-1218, 10// 1968.

[20] H. S. Hsu and G. J. Yurek, "Kinetics and mechanisms of the oxidation of cobalt at 600–800°C," *Oxidation of Metals,* vol. 17, pp. 55-76, 1982/02/01 1982.

[21] Y. M. Mishin and I. M. Razumovskiy, "On the Possibility of Using Fisher's Model to Describe the Difusion Width of an Interface and the Coefficient of Boundary Diffusion," *Phys. Met. Metall.*, vol. 53, pp. 120-127, 1981.

[22] F. Hook, "Development of a novel QCM technique for protein adsorption studies," Ph.D., Department of Biochemistry and Biophysics Department of Applied Physics, Chalmers University of Technology, Goteborg, Sweden, 1997.

[23] M. J. Fransen, "On The Influence of Generator and Detector Settings in X-ray Powder Diffractometry," *Adcancs in X-ray Analysis,* vol. 48, pp. 143-149, 2005.

[24] I. Ichinose, H. Senzu, and T. Kunitake, "A Surface Sol-Gel Process of TiO_2 and Other Metal Oxide Films with Molecular Precision," *Chem. Mater.*, vol. 9, pp. 1296-1298, 1997.

[25] I. Ichinose, H. Senzu, and T. Kunitake, "Stepwise Adsorption of Metal Alkoxides on Hydrolyzed Surfaces: A Surface Sol-Gel Process," *Chem. Lett.*, vol. 10, p. 831, 1996.

[26] E. Domínguez, J. A. Mercado, M. A. Quesada, and A. Heredia, "Pollen sporopollenin: degradation and structural elucidation," *Sex Plant Reprod*, vol. 12, pp. 171-178, 1999.

[27] G. Schimanke and M. Martin, "In situ XRD study of the phase transition of nanocrystalline maghemite (γ-Fe_2O_3) to hematite (α-Fe_2O_3)," *Solid State Ionics*, vol. 136-137, pp. 1235-1240, 2000.

[28] W. D. Kingery, D. C. Hill, and R. P. Nelson, "Oxygen Mobility in Polycrystalline $NiCr_2O_4$ and α–Fe_2O_3," *Journal of The .I merican Ceramic Society*, vol. 43, 1960.

[29] V. S. Stubican and L. R. Carinci, "Point Defects and Grain Boundary Diffusion in NiO and Fe_3O_4," *Zeitschrift fur Physikalische Chemie, Bd*, vol. 207, pp. 215-222, 1998.

[30] U. Colombo, G. Fagherazzi, F. Gazzarrini, G. Lanzavecchia, and G. Sironi, "Mechanisms for oxidation and reduction of iron oxide at temperatures below 450°C," *Ind. Chim. Belge. Compt. Rend.*, vol. 32, pp. 95-101, 1967.

[31] E. Murad and U. Schwertmann, "Temporal stability of a fine-grained magnetite," *Clays and Clay Minerals, ,* vol. 41, pp. 111-113, 1993.

Appendix A : **Synthesis of TiO_2 and $BaTiO_3$ Based Pollen Replicas**

A.1. ***Summary***

Three-dimensional (3-D) multicomponent $Ba_{1-x}Sr_xTiO_3$:Er, replicas of pollen microparticles have been synthesized with controlled chemistry through the use of surface sol–gel (SSG) processing and subsequent thermal of microwave hydrothermal processing. High-fidelity replication may allow for the pollen-shaped oxide microparticles to be utilized for adhesion via tailorable short-range (~10 nm) van der Waals (VDW) attraction, and longer rang electrostatic based adhesion influenced by the crystallite size and chemical composition of the replicas. Conversion of the pollen into ferroelectric ($Ba_{1-x}Sr_xTiO_3$) microparticle replicas may allow for the use of electrostatic attraction at short and long ranges (possible up to ~1 mm). The adhesion properties could be dynamical controlled by controlling the surface charge of the substrate. In addition optical photoluminescence properties can be imparted by doping the material with erbium atoms. The combination of both controlled VDW and electrostatic based adhesion and unique optical signature from erbium atoms allows for pollen 3-D nanocrystalline microparticles replicas, generated by SSG-enabled conversion process, with tunable short- and short to long-range attractive force and optical properties.

A.2. ***Introduction***

Adhesion by or on microparticles plays a critical role in a wide range of developing and mature technologies, including drug delivery, catalysis, water/chemical purification, sensing, anti-fouling coatings and membranes, semiconductor device processing, composite processing, paints, printing, and xerography.[1-10] While

predominant models and mechanistic experimental studies for under-standing adhesion have been based on smooth, spherical particles[11-17], microparticles with rough surfaces and non-spherical shapes are desired for a number of such technologies. However, the scalable fabrication of micro-particles with well-controlled surface asperities, in a variety of three-dimensional (3-D) morphologies, and with tunable chemistries to allow for controlled adhesion strength remains a difficult synthetic challenge.

Pollen is a rich sustainable source of 3-D microparticles, with complex morphologies affecting dispersion and adhesion in nature. Pollen particles come in a wide variety of 3-D shapes and surface topographies[18-23] and are produced in large and abundant quantities worldwide by plants.[24-31] Atomic force microscopy (AFM) based adhesion measurements have recently shown that for 3-D replicas comprised of ferromagnetic hematite (α-Fe_2O_3)[32] or ferrimagnetic magnetite (Fe_3O_4) may be based on crystallite size as opposed to the spine tip radius for native pollen.[33]

The purpose of this work is to dielectric properties can be used to tailor the attraction forces of 3-D biogenic microparticles though synthetic chemical processing. Applying a voltage on the targets substrate can be used to control adhesion through electrostatic forces. Native pollen particles have been converted into 3-D multi component oxides (TiO_2 and $BaTiO_3$, BT), via use of a highly-conformal surface sol-gel (SSG) coating process[34, 35]. The prepared replicas were attached to AFM cantilevers, and short- and long-range attraction forces between the replicas and substrates (Ni, Cu, Au, and mica) were evaluated with the scanning probe microscope. A reproducible increase in long range adhesion, for the BT replicas, was observed by applying a voltage

to the Ni substrates. By controlling the surface chemistry (BT vs. TiO_2) and substrate surface charge, long range attraction forces could be tuned. Although other authors have used coating or infiltration methods to chemically modify/transform pollen[36-43] and other biological microparticles[44-53] for desired (bio)chemical, optical, electrical, structural, or fluidynamic properties, the conversion of sustainable biogenic particles (like pollen) into all-inorganic 3-D replicas for the purpose of achieving controlled multimodal adhesion based applied surface charges, has not been previously investigated.

BT is of interest due to its wide use in the electro-ceramic industry from its ferroelectric properties. BT has a perovskite crystal structure and exhibits a cubic to tetragonal phase transition when cooled below its curie temperature (~120°C).[54, 55] Below the Curie temperature BT has a permanent dipole which gives the material its ferroelectric properties, high dielectric constant, and low dielectric loss. These properties make BT an attractive material for applications such: multi-layer ceramics capacitors[56-59] PTC resistors and thermistors,[60-63] and piezoelectric traducers.[64, 65] Due to the wide range of applications, extensive research has been conducted to synthesize BT into specific geometries such as, powders,[66, 67] thin films,[68, 69] nanoribbons,[70] nanorods,[71] nanosphere,[72, 73] nanotubes,[74] and nanowires.[75, 76] However limited work has been conducted on creating BT particles with controlled features in both the nano and micro scale. Previous work has used MWHT reactions to convert TiO_2 butterflies into BT retaining the general morphology of the butterfly on the macro scale.[77, 78]

As a derivative of BT, Barium Strontium Titanate ($Ba_xSr_{1-x}TiO_3$, BST), is a ferroelectric ceramic with an ABO_3 perovskite crystal structure an exhibits a Curie

temperature. The Curie temperature of BST much lower than BT at around 35 K compared to 393 K for BT.[79, 80] BST and BT form a solid-solid solution and depending on the alkaline ratio of Ba:Sr the cure temperature can be controlled. [81, 82] One of the most important Ba:Sr molar ratios is around 60:40, were the tetragonal to cubic transition occurs around 6.3 ºC.[83] In addition the dielectric constant to can be up to 3 times higher in BST than BT which should be beneficial electro static adhesion.[84] The improved properties compared to BT make BST of great interest for applications which require switches,[85] tunable phase shifters,[86-89] capacitors for tunable radio frequency and microwave devices,[90, 91] or dynamic random access memory.[92, 93]

A.3. *Experimental Procedures*

A.3.1. Template

Owing to its adherent nature and its biological replicability (i.e., sustainability), ready availability, abundance, and low cost, pollen was considered to be a desirable type of microparticle template for conversion into magnetic replicas (to enable a new modality of tailorable adhesion). Sunflower pollen (Figure 1 d, Chapter 1) has been chosen based on the overall size, shape, and wide range of features in both the micro- and nanometer range. The exine (outer layer) of pollen grains are composed of sporopollenin, a complex polymer consisting of carboxylic acids cross-linked with aliphatic chains (e.g. HOOC-$(CH_2)_n$-COOH).[94] The carboxylic acids provide an abundant amount of functional groups needed for the reaction with the isopropoxide precursors used in the SSG process. These surface groups can eliminate the need for surface modification in order to obtain conformal coatings.

A.3.2. Demineralization of Pollen Grains

Pollen grains obtained from Greer Laboratories, Lenoir, NC USA were cleaned, to remove pollenkitt, by immersion in a mixture of chloroform and methanol (3:1)[95] for 24 h, followed by deposition onto filter paper (P5, Fisher Scientific, Pittsburgh, PA USA) and drying under vacuum at 60°C for 12 h. A second immersion was conducted in 1 M hydrochloric acid (VWR, Suwanee, GA USA) for 1 h to remove residual inorganic material, followed by rinsing three times with de-ionized water and drying by vacuum aspiration at room temperature for 5 min.

A.3.3. SSG coating of Pollen Grains Process

Pollen grains were coated using 2 different coating schemes. i) The first coating scheme, Ti-O-bearing and Ba-O-bearing coatings are applied to cleaned, dematerialized pollen grains via a computer-automated (in a N_2 atmosphere glove box), layer-by-layer (LbL) SSG deposition process by:[78, 96-98] i) immersing pollen grains for 10 min, with stirring, in a solution of either 0.0125 M Ti (IV) isopropoxide (Alfa Aesar, Ward Hill, MA USA) in anhydrous 2-propanol (>99.8% purity, Acros Organics, Geel, Belgium) for the Ti-O-bearing layers or 0.0125 M Ba (II) isopropoxide (Alfa Aesar, Ward Hill, MA USA) in anhydrous 2-propanol (>99.8% purity, Acros Organics, Geel, Belgium) for the Ba-O-bearing layers, to allow for the chemisorption of a Ti-O-bearing or Ba-O-bearing layer, ii) rinsing three times with anhydrous 2-propanol followed by vacuum filtration, iii) immersion in de-ionized water (DIW), with stirring, for 5 min, to allow for hydrolysis of the chemisorbed alkoxide layer, iv) rinsing three times with anhydrous 2-propanol followed by vacuum filtration, and v) and drying by vacuum aspiration for 5 min. This process (alkoxide exposure, alcohol rinsing, water exposure, alcohol rinsing, drying) was

repeated 29 times (for a total of 30 cycles) to build up a continuous and conformal coating. The pollen particles were coated with alternating Ti-O and Ba-O layers, in a Ti-O:Ba-O ratio of 1:1, so as to achieve the desired stoichiometry for the $BaTiO_3$ perovskite. With barium incorporated into the coating, the BT replicas should have improved morphology retention compared BT synthesized by reacting barium acetate and TiO_2 replicas in a microwave hydrothermal reactor,[78] due to the decreasing effect of molar volume expansion. The alternating exposure of titanium and barium alkoxides is illustrated in Figure 156.

$BaTiO_3$ samples were also doped with strontium by adding known amounts of 0.0125 M Sr (II) isopropoxide (Alfa Aesar, Ward Hill, MA USA) with the barium precursors in solution. By controlling the Ba:Sr ratio in solution it is possible control the composition of the coating and tune the composition of $Ba_{1-x}Sr_xTiO_3$ for the maximum dielectric constant.

ii) the second coating scheme, Ti-O-bearing coatings are applied to cleaned, dematerialized pollen grains via a computer-automated (in a N_2 atmosphere glove box),

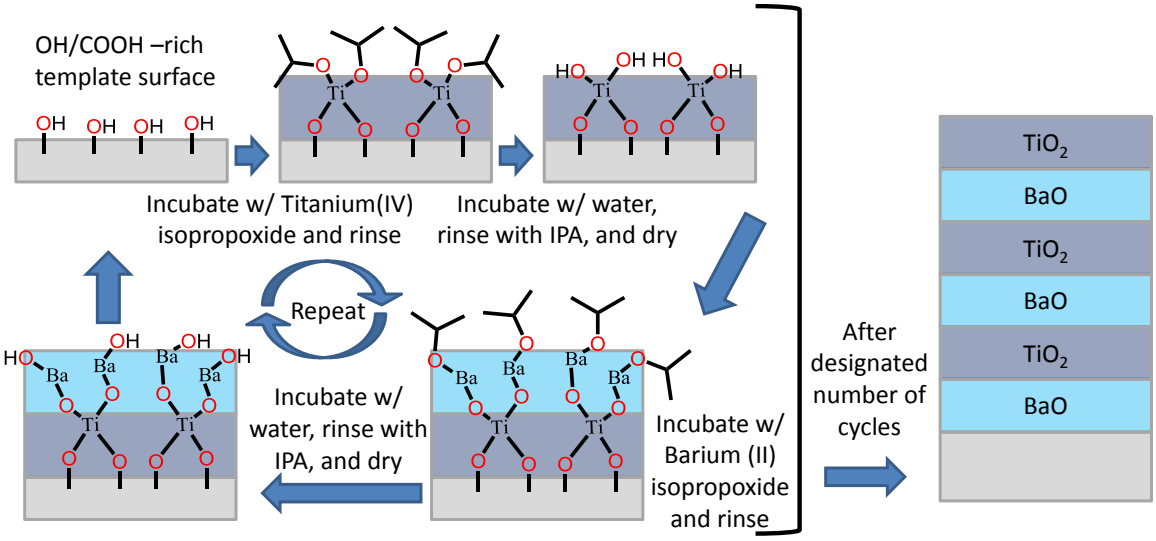

Figure 156: A schematic representation of the alternating layering surface sol-gel process utilizing titanium (IV) isopropoxide and barium (II) isopropoxide as model metal alkoxide.

layer-by-layer (LbL) SSG deposition process by:[78, 96-98] i) immersing pollen grains for 10 min, with stirring, in a solution of either 0.0125 M Ti (IV) isopropoxide (Alfa Aesar, Ward Hill, MA USA) in anhydrous 2-propanol (>99.8% purity, Acros Organics, Geel, Belgium) for the Ti-O-bearing to allow for the chemisorption of a Ti-O-bearing, ii) rinsing three times with anhydrous 2-propanol followed by vacuum filtration, iii) immersion in de-ionized water (DIW), with stirring, for 5 min, to allow for hydrolysis of the chemisorbed alkoxide layer, iv) rinsing three times with anhydrous 2-propanol followed by vacuum filtration, and v) and drying by vacuum aspiration for 5 min. This process (alkoxide exposure, alcohol rinsing, water exposure, alcohol rinsing, drying) was repeated 49 times (for a total of 50 cycles) to build up a continuous and conformal coating. The TiO_2 samples were also doped with erbium by adding known amounts of 0.0125 M Er (III) isopropoxide (Alfa Aesar, Ward Hill, MA USA) solution in 1-Methoxy 2-propanol (>99.8% purity, Acros Organics, Geel, Belgium) with the titanium precursors in solution. The solution used were created to be 5 mol% Er(III) isopropoxide with 95 mol% Ti(IV) isopropoxide solution. The By controlling the amount of Er in solution may be possible control the composition of the coating and tune the composition of $Ti_{1-x}Er_xO_2$ for the maximum optical response from the erbium dopant. The coating process of exposure of titanium and erbium alkoxides, is illustrated in Figure 157.

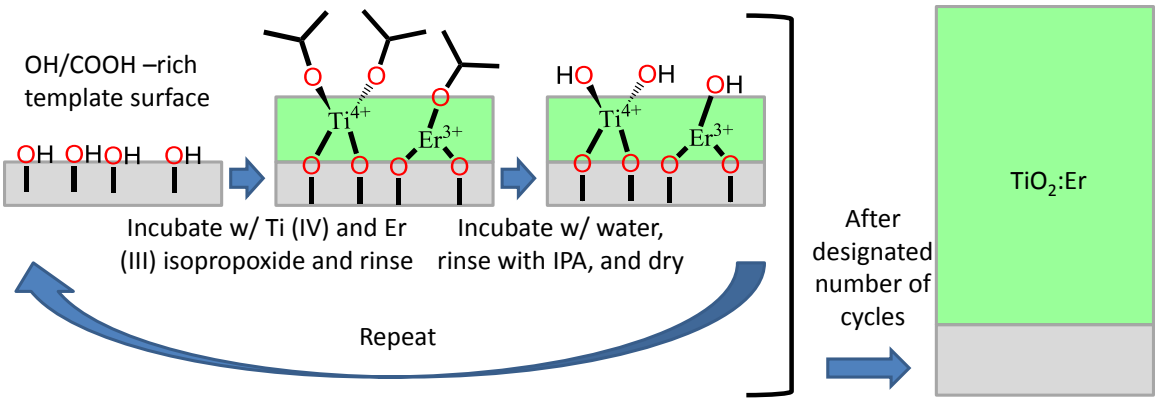

Figure 157: A schematic representation of the surface sol-gel process utilizing titanium (IV) isopropoxide and erbium (II) isopropoxide as model metal alkoxide.

A.3.4. Organic Pyrolysis and Conversion to Oxide Replicas

The Ba-O and Ti-O SSG-coated pollen particles were prepared for pyrolysis in the following manner: i) SSG-coated pollen particles suspending in IPA and then dispersed onto nickel foil (25.4 µm thick, McMaster-Carr, Cleveland, OH, USA) using a pipette, ii) SSG-coated pollen particles suspending in IPA and then dispersed onto silicon wafers (Wafernet, Inc., San Jose, CA, USA) using a pipette, and iii) SSG-coated pollen particles also placed in an MgO crucible (96.6% MgO, 2% Y_2O_3, 1.6% other, Ozark Technical Ceramics, Inc, Webb City, MO). Samples were fired in air using a tube furnace (Lindberg / Blue M, NC, USA,) with a ramp rate of 0.5°/min from 25-500°C and 3°/min from 500-1000°C then held for 2 h to allow for organic pyrolysis and oxide crystallization..

The Ti-O SSG-coated pollen particles were prepared for pyrolysis in the following manner: i) SSG-coated pollen particles suspending in IPA and then dispersed onto nickel foil (25.4 µm thick, McMaster-Carr, Cleveland, OH, USA) using a pipette, ii) SSG-coated pollen particles suspending in IPA and then dispersed onto silicon wafers (Wafernet, Inc., San Jose, CA, USA) using a pipette, and iii) SSG-coated pollen particles

also placed in an MgO crucible (96.6% MgO, 2% Y_2O_3, 1.6% other, Ozark Technical Ceramics, Inc, Webb City, MO). Samples were fired in air using a tube furnace (Lindberg / Blue M, NC, USA,) with a ramp rate of 0.5°C min^{-1} to 600°C and held at this temperature for 4 h to allow for organic pyrolysis and oxide crystallization.

A.3.5. Hydrothermal Reactions

The pyrolyzed TiO_2 and TiO_2:Er pollen replicas were reacted into $BaTiO_3$ and $BaTiO_3$:Er by the following method (illustrated in Figure 158): specimens were sealed within MWHT vessels containing a 20 mL solution of 0.125 M barium acetate and 1 M NaOH both dissolved within previously-boiled DI water. The specimens were then heated within 7 min to 220°C in microwave reaction system at a maximum power output of 1600 W and held at this temperature for 10 h to allow for complete microwave hydrothermal (MWHT) conversion into BT. After removal from the MWHT vessels, the reacted scales were washed twice for 30 min with 25 mL of 1 M acetic acid in 50 mL centrifuge tubes rotated at 30 rpm on a rotator to remove any potential $BaCO_3$ that may have formed upon opening the vessels in ambient atmosphere. The specimens were then rinsed twice with 20 mL of water, and then twice with 20 mL of IPA, followed by drying in air at 80°C for 1 hr.

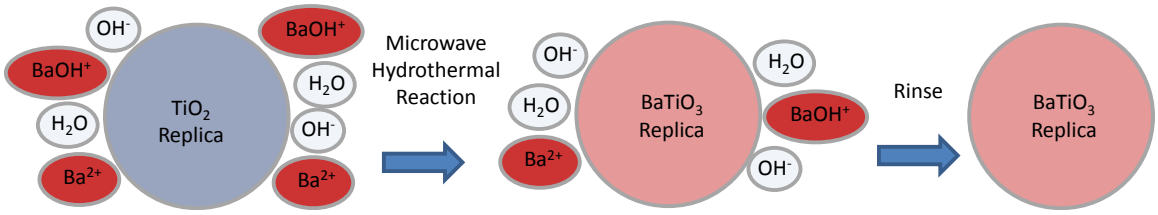

Figure 158: A schematic representation of the MWHT synthesis processes utilizing titanium pollen replicas for conversion into BT

A.3.6. Shape, Morphology and Chemical Analyses

The morphologies and spine tip dimensions of the native pollen grains, SSG-coated grains, the pyrolyzed grains, magnetite replicas, and iron replicas were evaluated with a field emission scanning electron microscope (1530 FEG SEM, LEO / Carl Zeiss SMT, Ltd., Thorn-wood, NY USA).

Elemental analysis determined by using an energy dispersive X-ray spectrometer (EDS) (INCA Model 7426, Oxford Instruments, Bucks, UK) equipped to a scanning electron microscope (1530 FEG SEM, LEO / Carl Zeiss SMT, Ltd., Thorn-wood, NY USA. X-ray photoelectron spectroscopy (XPS) was conducted (Thermo K-alpha, Thermo Fischer Scientific, Inc., Waltham, MA, USA) at a base pressure of $3x10^{-8}$ Pa using a monochromatic Al K_α source (1486.6 eV) with a spot size of 300 μm and a pass energy of 50 eV. Step sizes of 0.01 eV (high-resolution) and 1 eV (low-resolution) were used with dwell times of 50 ms at each energy value.

A.3.7. Phase and Grain Size Determination

The phase identification for the fired pollen replicas were evaluated at room temperature using X-ray diffraction (XRD) analyses. XRD analyses were conducted on a diffractometer (X'Pert Pro Alpha-1, PANalytical B.V., ALMELO, Netherlands) with $Cu_{K\alpha 1}$(1.5405980 Å) radiation emanating from a 1.8 kW ceramic X-ray tube with a copper anode (45 kV, 40 mA) through an incident beam Johansson monochromator (PANalytical) and detected by an X'Celerator detector. The incident beam optics were outfitted with 0.04 rad soller slits, a 2° fixed anti-scatter slit, a programmable divergence slit set to 5.5 mm irradiated length, and a 10 mm mask. The diffracted beam optics were outfitted with a 5.5 mm anti-scatter slit and 0.04 rad soller slits placed before the X'Celerator detector. Each pattern was produced with a summation of 40 identical 30

minute scans conducted with Bragg-Brentano geometry and a step size of 0.017° 2θ ranging from 20° to 90° 2θ. Diffraction specimens were dispersed on quartz cut 6° from (0001) low background specimen support (GEM dugout, PA, USA) via pipetting an aliquot of IPA/powder slurry onto specimen support and allowing the IPA to evaporate.

Phase identification, average crystallite size (ACS), and stoichiometry were determined using the HighScore Plus software (PANalytical B.V, Almelo, The Netherlands) using a Rietveld refinement processes with Pseudo-Voigt peak fit function. The Pseudo-Voigt function can be seen below:[99]

$$G_{jk} = \gamma \frac{C_0^{1/2}}{H_k \pi} \left[1 + C_0 1 X_{jk}^2\right]^{-1} + (1-\gamma) \frac{C_1^{1/2}}{H_k \pi^{1/2}} \exp\left[-C_1 X_{jk}^2\right] \quad \text{(A.1)}$$

where:C_0 = 4, C_1 = 4ln2, X_{ij} is related to the peak position, 2θ angle and H_k (the full-width at half-maximum (FWHM) of the k^{th} Bragg reflection) by equation A.2, and γ is a refinable "mixing" parameter of Gaussian and Lorentzian peak shapes given by equation A.3:

$$X_{ij} = \frac{(2\theta_j 2\theta_k)}{H_k} \quad \text{(A.2)}$$

$$\gamma = \gamma_1 + \gamma_2 2\theta + \gamma_3 (2\theta)^2 \quad \text{(A.3)}$$

The H_k values are then fitted to the Caglioti equation in a F WMH plot.

$$H_k = (U\tan^2\theta + V\tan\theta + W)^{1/2} \quad \text{(A.4)}$$

where U, V, and W are fitting parameters related to grain size and microstrain. A Si NIST line standard (640c) was used to determine the instrument broadening of the diffracted peaks effects the U, V, and W parameters. To determine the crystallite size the U and V parameters are set the values calibrated using the NIST standard and then calculated by refining only the W fitting parameter and using the following equation:

$$D_i = \left(\frac{180}{\pi}\right)\frac{\lambda}{(W_i - W_{std})^{0.5}} \quad (A.5)$$

The variance of the crystallite size is described by:

$$\sigma^2(D_i) = \frac{A_D^2}{4(W_i - W_{std})^3}[\sigma^2 W_i + \sigma^2 W_{std}] \quad (A.6)$$

with A_D representing the constant $180\times\lambda/\pi$. The mean error of the crystallite size is equal to the square root of the variance. The Sr content of the coating was determined by refining both the barium and strontium atomic site occupancy coefficients with Rietveld refinement process.

A.3.8. Optical Analyses

Photoluminescence spectra for BT and Eu-doped BT scales were collected by of Dimitri Deheyn, Scripps Institution of Oceanography. Photoluminescence spectra were collected with a Hyperspectral Imaging system (PARISS PHSI Model, LightForm, Inc., NC, USA, www.lightforminc.com). The system incorporated a prism-based spectrograph using a monochrome Retiga 2000R, CCD camera (QImaging, BC, Canada) to collect spectral information along rows of pixels. The system was mounted on a Nikon E800 microscope (Nikon Instruments Inc., NY, USA). Wavelength calibration was performed with a MIDL Hg^+/Ar^+ emission lamp (LightForm, Inc, NC, USA). Wavelength accuracy was recorded and verified to be better than 0.3 nm. The specimen was immersed in IPA between a glass slide and cover-glass. Each spectrum presented is representative of the major class of spectra presented in 200 acquisitions across a single specimen. Each of the 200 acquisitions was background subtracted, and each acquisition lasted 2 seconds, with no signal averaging.

A.4. *Results & Discussion*

A.4.1. $BaTiO_3$ SSG Morphology and Phase Analysis

The synthesis of BT replicas of Sunflower pollen via use of LbL SSG process has been examined using the method described in section A.3.3 in which alternating layers of Ti-O and Ba-O are applied for a total of 30 coating layers. The coated pollen particles were heated in air at 0.5°C/min to 1000°C and held for 2 h to allow for pyrolysis of the pollen template, crystallization of the Ti-O and Ba-O coatings layers, and conversion into BT. A representative secondary electron (SE) image of such a pollen replica is shown in Figure 159. With the structure able to withstand thermal treatments up 1000°C it may be possible to anneal $BaTiO_3$:Er doped samples for maximum optical response and still maintain the morphology of the starting pollen.[100]

X-ray diffraction (XRD) of such replicas (Figure 160) indicated the presence of $BaTiO_3$ as the primary crystalline phase, with a small amount of $BaSO_4$ as a secondary phase. Scherrer analysis of the (110) diffraction peak yielded an average crystallite size of 28 ± 1 nm. Energy-dispersive X-ray (EDX) analyses (Figure 161) revealed prominent peaks for barium, titanium, and oxygen, along with a distinct peak for sulfur and a weak peak for phosphorus. EDX analyses of an uncoated (but acid cleaned) sunflower pollen grain (Figure 162) indicated that the sulfur and phosphorus originated with the starting pollen. To determine whether such sulfur (in the form of $BaSO_4$) was present on the external surfaces of the $BaTiO_3$-bearing pollen replicas, X-ray photoelectron spectroscopic (XPS) analyses were conducted. While distinct peaks for Ba, Ti, O, and C (from the carbon tape substrate) were detected (Figure 163), peaks for sulfur or phosphorus were absent, which suggested that the $BaSO_4$ phase was located away from

the external surface (i.e., at/near the inner surface of the replica, where the coating had contacted the native pollen template). Hence, sulfur inherited from the starting pollen may not have a major influence on the surface dielectric properties and the associated electrostatic adhesion of the $BaTiO_3$-based pollen replicas. Both EDS and XPS analyses detected more Ba then Ti with mol ratios of 2:1 and 2.2:1 respectively. Additional samples with Ba:Ti layering ratios of 10:17 were synthesized in a similar manner as the 1:1 Ba:Ti mol ratio samples, to tune the Ba:Ti ratio of the coating. EDS of the 10:17 sample can be seen in Figure 164. EDS analysis showed that the 10:17 samples had a Ba:Ti mol ratio of 0.89:1 indicating the mols of barium and the mols of titanium deposited with each coating layer may not be the same. Ba (II) isopropoxide only has two ligands compared to the four ligands on Ti (IV) isopropoxide. From a cartoon perspective, Ba (II) isopropoxide may react with either one or two hydroxyl groups on the surface while Ti (IV) isopropoxide may react with one, two, or three hydroxyl groups. If Ba (II) isopropoxide reacts, on average, with 1.5 hydroxyl groups and Ti (IV) isopropoxide reacts, on average, with 2 hydroxyl groups, then a 1:1 coating ratio will not give a 1:1 mol ratio of Ba:Ti. A coating with an increased number of Ti-O layers is need.

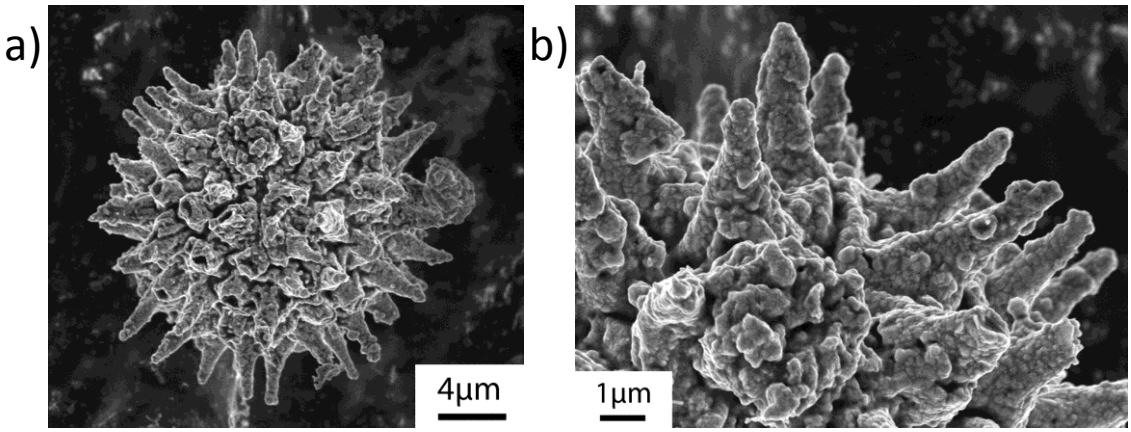

Figure 159: SE image of BT *H. Annuus* pollen replicas synthesized with a 1:1 alternating SSG layers of barium and titanium approach after firing to 1000°C for 2 h a) entire pollen grain replica b) zoomed in region of pollen grain

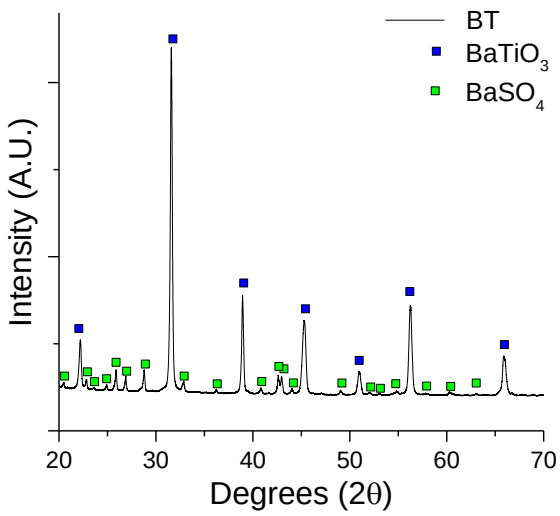

Figure 160: XRD patterns for the BT replicas synthesized with a 1:1 alternating SSG layers of barium and titanium approach after firing to 1000°C for 2 h

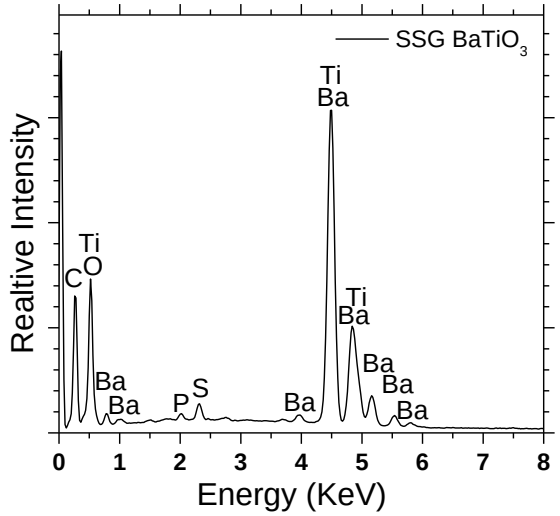

Figure 161: EDS of the BT replicas on carbon tape synthesized with a 1:1 alternating SSG layers of barium and titanium approach after firing to 1000°C for 2 h showing phosphorous and sulfur content

Further work is required to investigate different approaches to avoid such sulfur contamination in $BaTiO_3$ pollen replicas (e.g., through the use of an initial barrier coating, such as an Mg-O coating, deposited first on the pollen followed by the deposition of Ba-O- and Ti-O-bearing layers, firing, and then selective dissolution of the S-bearing MgO layer from the $BaTiO_3$). The presence of $BaTiO_3$ and $BaSO_4$, and the absence of detectable TiO_2-rich phases (e.g., $BaTi_2O_5$, $BaTi_3O_7$, $BaTi_4O_9$, $Ba_2Ti_9O_{20}$) in

the XRD pattern (Figure 160), indicated that the as-coated pollen grains were rich in barium, relative to the $BaTiO_3$ composition. This, in turn, suggested that the relative rates of chemisorption of the barium and titanium alkoxides, and/or the saturation concentrations of these alkoxides on the pollen surfaces, may be different. Future work is required to investigate the amount of material deposited with each coating cycle (QCM) and to alter the number and type of coating layers to get single phase BT pollen replicas.

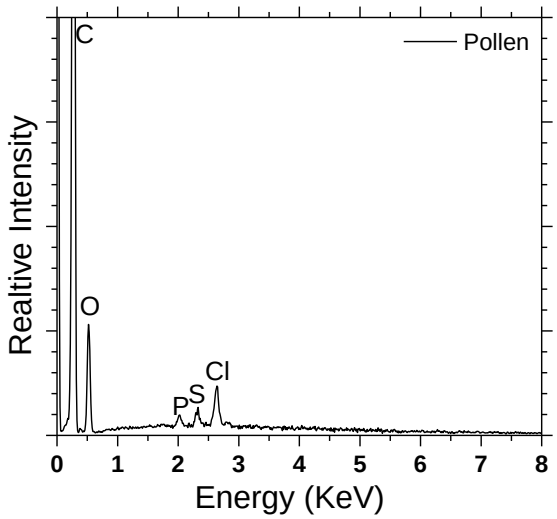

Figure 162: EDS of sunflower pollen grains on carbon tape after HCl acid wash showing phosphorous and sulfur content

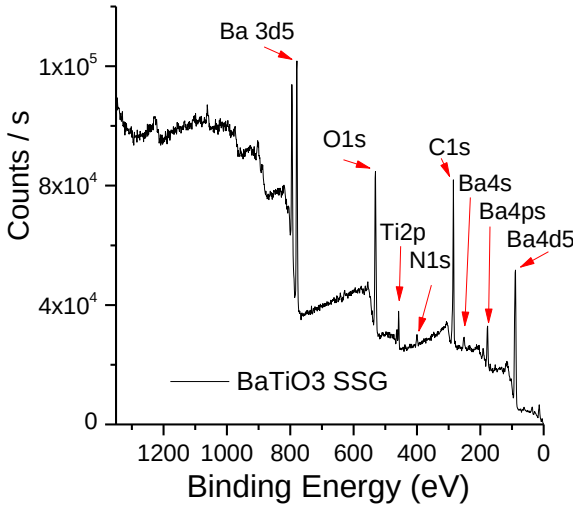

Figure 163: XPS of BT replicas synthesized with a 1:1 alternating SSG layers of barium and titanium approach after firing to 1000°C for 2 h showing no sulfur on the surface. (special thanks to Ben deGlee for obtaining the XPS spectra for this sample)

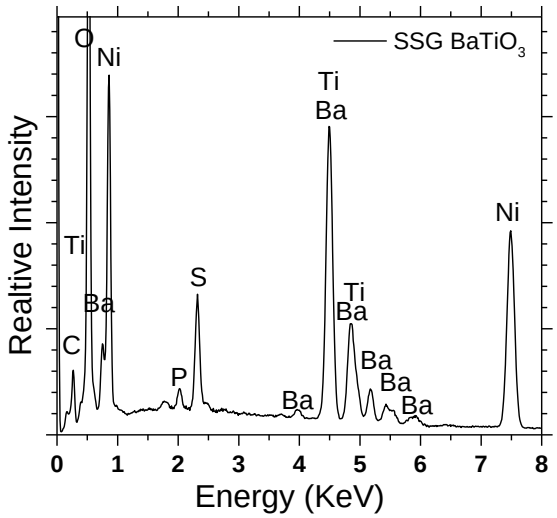

Figure 164: EDS of BT replicas on nickel foil synthesized with a 10:17 alternating SSG layers of barium and titanium approach after firing to 1000°C for 2 h showing phosphorous and sulfur content

A.4.2. Strontium Doped $BaTiO_3$ Pollen Replicas

In addition to lanthanide doping, barium titanate may substitutionally doped with strontium (i.e., by replacing some Ba with Sr). $(Ba,Sr)TiO_3$ (BST) solid solutions possess a lower Curie temperature than $BaTiO_3$.[101, 102] As shown in Figure 165, a composition of $(Ba_{0.70}Sr_{0.30})TiO_3$ possesses a Curie temperature, and an associated spike in the dielectric constant, near room temperature.[102] Such a high dielectric constant (values on the order of 104) is anticipated to allow for enhanced electrostatic adhesion. In order to allow for evaluation of the electrostatic adhesion of BST solid solutions to dielectric substrates, the LbL SSG-enabled syntheses of BST replicas of sunflower pollen has been examined.

BST pollen replicas were generated in a manner similar to SSG-derived $BaTiO_3$ replicas, except that a solution of barium and strontium isopropoxide was used (instead of just barium isopropoxide). The molar ratio of barium isopropoxide to strontium isopropoxide in this initial alkoxide solution was 6:4. After depositing a total of 30 layers

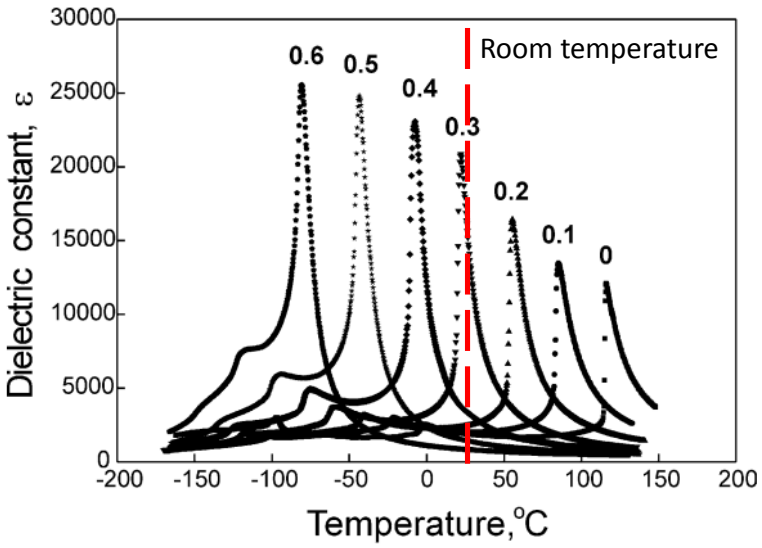

Figure 165: Dielectric property of $Ba_{1-x}Sr_xTiO_3$ ceramics sintered at 1450°C for 1 h.[102]

(involving 15 exposures to the mixed Ba-Sr isopropoxide solution and 15 exposures to the Ti isopropoxide solution), the coated pollen particles were heated in air at 0.5°C/min to 1000°C and held at this temperature for 2 h to allow for organic (pollen template) pyrolysis, crystallization of the Ti-O and Ba-O/Sr-O layers, and BST formation. After the 1000°C treatment, the BST replicas maintained the general sunflower pollen morphology, as seen in Figure 166. XRD analysis (Figure 167) indicated that a $BaTiO_3$-like perovskite compound was the predominant phase in such replicas, although a $BaSO_4$-like minority phase was also present (as was the case for the $BaTiO_3$ replicas). Scherrer analysis of the (110) diffraction peak for the BST specimens yielded an average crystallite size of 40 ± 10 nm. Closer examination of the (110) diffraction peaks (and other peaks) obtained from $BaTiO_3$ and $(Ba,Sr)TiO_3$ pollen replicas revealed noticeable peak shifting upon strontium substitution for barium (Figure 168); that is, diffraction peaks for the Sr substituted specimens were shifted to higher 2θ values (smaller d spacing), consistent with the smaller effective ionic radius of Sr^{+2} ions relative to Ba^{+2} ions. Vegard's law states that

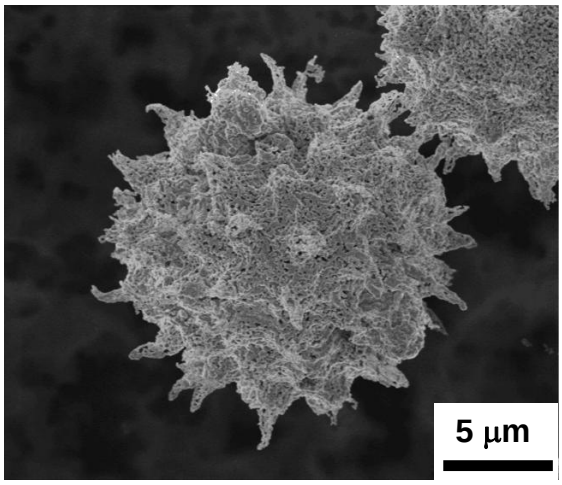

Figure 166: SE image of BST *H. Annuus* pollen replicas synthesized with a 1:1 alternating SSG layers of barium/strontium (6:4 in solution ratio) and titanium approach after firing to 1000°C for 2 h entire pollen grain replica

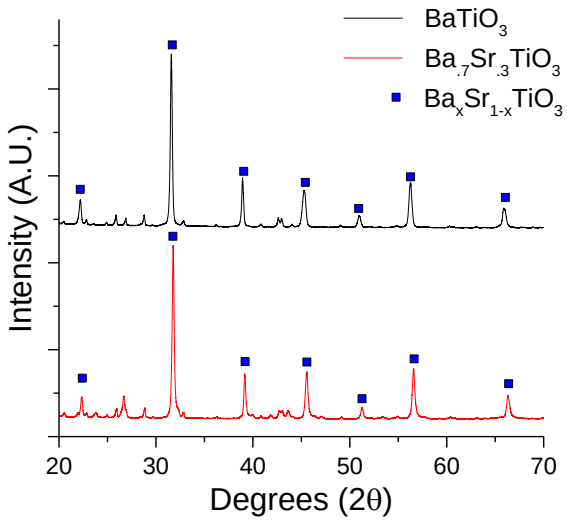

Figure 167: XRD patterns for the BT replicas synthesized with a 1:1 alternating SSG layers of barium and titanium approach after firing to 1000°C for 2 h and BST replicas synthesized with a 1:1 alternating SSG layers of barium/strontium (6:4 in solution ratio) and titanium approach after firing to 1000°C for 2 h entire pollen grain replica

the lattice parameter of a solid solution system is linear dependent on the concentration of the constituent element.

The full XRD patterns obtained from the $BaTiO_3$ and $(Ba,Sr)TiO_3$ specimens were fitted and refined via Rietveld analyses to allow for determination of the oxide composition. Table 33 reveals the Rietveld parameters used to fit the $BaTiO_3$ and $(Ba,Sr)TiO_3$ XRD patterns, as well as the calculated formula unit obtained for each

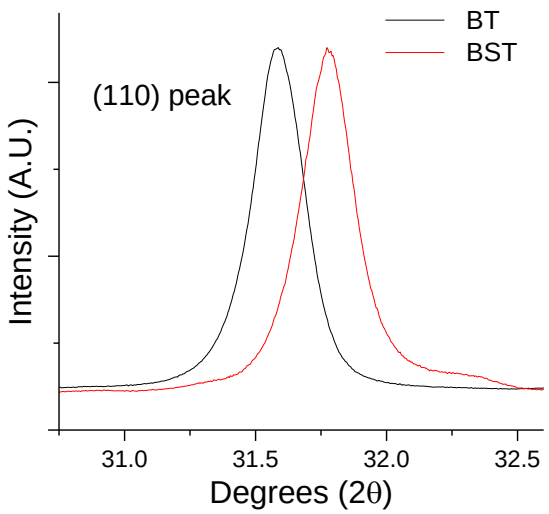

Figure 168: XRD patterns revealing the (110) diffraction peaks of $BaTiO_3$ and $(Ba,Sr)TiO_3$ pollen replicas synthesized via similar LbL SSG and thermal processes, except that a mixed Ba/Sr isopropoxide solution and a Ba isopropoxide solution were used for the syntheses of the $BaTiO_3$ and $(Ba,Sr)TiO_3$ replicas, respectively.

sample. Table 34 and Table 35 provided the calculated atomic coordinates and site occupancies for each sample. Rietveld refinement gave R values less than 5 for both samples, indicating that the refined models were in good agreement with the experimental data. The refined composition obtained for the Sr-doped specimen was $Ba_{0.69}Sr_{0.31}TiO_3$, which possessed a Ba:Sr ratio different from that of the mixed isopropoxide solution (6:4), although this XRD-derived value was quite close to the desire composition for achieving a Curie temperature near room temperature (Figure 165). This difference between the isopropoxide solution composition and the final oxide compositions suggests that the relative rates of chemisorption of the barium and strontium alkoxides, and/or the saturation concentrations of these alkoxides on the pollen surfaces, may be different. Such potential kinetic and/or thermodynamic differences could be explored in future work.

Further work needs to be done on optimizing the coating process to prevent any impurity phase from forming and to try and control the BST composition by changing the

Table 33: Rietveld refinement fitting data for $BaTiO_3$ and $(Ba,Sr)TiO_3$ sunflower pollen replicas synthesized with the LbL SSG process using 15 exposures to a barium isopropoxide solution, or a mixed barium/strontium isopropoxide solution (Ba:Sr ratio = 6:4), and 15 exposures to a titanium isopropoxide solution, followed by drying and firing in air at a peak temperature of 1000°C for 2 h.

Structure and profile data for	$BaTiO_3$ sample	$SrBaTiO_3$ sample
Formula sum	$O_{3.00}Ti_{1.00}Ba_{1.00}Sr_{0.00}$	$O_{3.00}Ti_{1.00}Ba_{0.69}Sr_{0.31}$
Formula mass/ g/mol	233.2282	217.8318
Density (calculated)/ g/cm^3	6.0246	5.7203
Space group (No.)	P m -3 m (221)	P m -3 m (221)
Lattice parameters		
a/ Å	4.0057(1)	3.98378(4)
b/ Å	4.0057(1)	3.98378(4)
c/ Å	4.0057(1)	3.98378(4)
alpha/ °	90	90
beta/ °	90	90
gamma/ °	90	90
V/ 10^6 pm^3	64.27418	63.22462
Fitting mode	Structure Fit	Structure Fit
Profile function	Pseudo Voigt	Pseudo Voigt
Background	Polynomial	Polynomial
U	0.019432	0.0580(6)
V	0.007811	0.004812
W	0.041954	0.0680(6)
Asymmetry parameter 1	0.000111	0.000111
Peak shape parameter 1	0.581912	0.534529
R (Bragg)/ %	3.14418	4.51098

Ba/Sr concentration in solution. Future work is also required to investigate the amount of material deposited with each coating cycle (QCM) and to alter the number and type of coating layers to get single phase BST pollen replicas. With samples of known composition adhesion test could then be performed to determine the effect of the

dielectric constant for electrostatic adhesion. In addition, further work needs to be conducted on doping the $BaTiO_3$ and $(Ba,Sr)TiO_3$ pollen replicas with lanthanides to generate dielectric (electrostatically-adhering) particles that also exhibit optical emission.

Table 34: Occupancy, atomic fraction (s.o.f.), coordinates and B_{iso} for $BaTiO_3$ pollen replicas

Atom	Wyck.	s.o.f.	x	y	z	Biso/ 10^4 pm^2
O	3c	1.000000	0.000000	0.500000	0.500000	0.500000
Ti	1b	1.000000	0.500000	0.500000	0.500000	0.500000
Ba	1a	1.000000	0.000000	0.000000	0.000000	0.500000
Sr	1a	0.000000	0.000000	0.000000	0.000000	0.500000

Table 35: Occupancy, atomic fraction (s.o.f.), coordinates and B_{iso} for $Ba_{X-1}Sr_XTiO_3$ pollen replicas

Atom	Wyck.	s.o.f.	x	y	z	Biso/ 10^4 pm^2
O	3c	1.000000	0.000000	0.500000	0.500000	0.500000
Ti	1b	1.000000	0.500000	0.500000	0.500000	0.500000
Ba	1a	0.69(3)	0.000000	0.000000	0.000000	0.500000
Sr	1a	0.31(3)	0.000000	0.000000	0.000000	0.500000

A.4.3. MWHT $BaTiO_3$ Morphology and Phase Analysis

Positive pollen replica containing barium titanate phase ($BaTiO_3$, BT) with preserved micro/nanostructured features in pollen grains have been created using a low temperature reaction method. The synthesis of BT replicas of Sunflower has been examined using the method described in section 6.3.3-6.3.5 in which layers of Ti-O are applied for a total of 50 coating layers followed by hydrothermal reaction into BT. The coated pollen particles were heated in air at 0.5°C/min to 600°C and held for 4 h to allow for pyrolysis of the organic content and crystallize the coating. The anatase replicas were reacted were sealed within a 100ml Teflon^{TM} containing a 20 ml solution of .125M barium acetate and 1M NaOH. The sealed samples were heated to 220°C with a ramp rate of 7mins and held at the temperature for 10 h to allow for the MWHT reaction to take place. Samples were then rinsed in 5M acetic acid for 1 h to remove any $BaCO_3$ residue formed on the surface.

The morphology and structure of the TiO_2 and $BaTiO_3$ replicas can be seen in Figure 169 and Figure 170 respectively. The $BaTiO_3$ samples preserved the general morphology of the pollen structures but did have a lower yield compared to the high temperature layer by layer process with very few pollen structures remaining intact after the microwave hydrothermal reaction. XRD analysis confirmed the sample was phase pure $BaTiO_3$ and EDS showed no major impurity elements Figure 171 and Figure 172 respectively. Scherrer analysis of the (110) diffraction peak yielded an average crystallite size of 38 ± 1. While this process can be used to synthesize the phase pure replicas, the reaction conditions need to be optimized to allow for greater morphology retention and

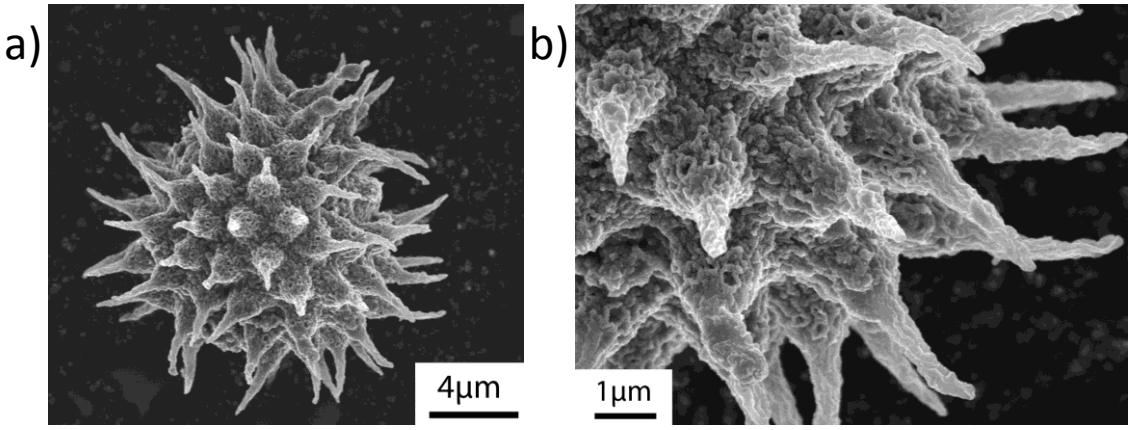

Figure 169: SE image of *Annuus* pollen replicas synthesized by applying 50 Ti-O SSG deposition cycles and pyrolysis at 600°C for 4 h.

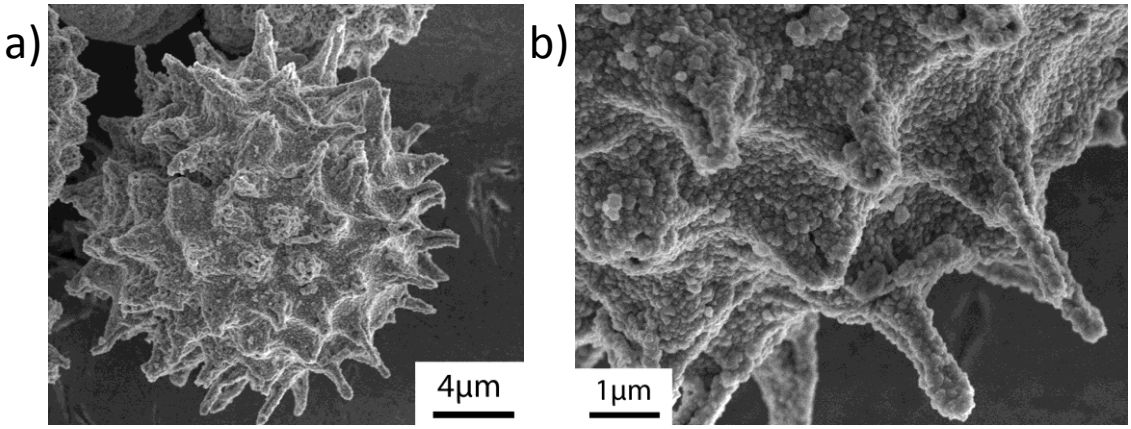

Figure 170: SE image of BT *Annuus* pollen replicas synthesized by converting pollen grains coated with 50 Ti-O SSG deposition cycles and pyrolyzed at 600°C for 4 h into BaTiO3 with the MWHT reaction process.

improved sample yield. With the current conditions only 2-3 pollen grains with intact echini were observed in each 2 h SEM session.

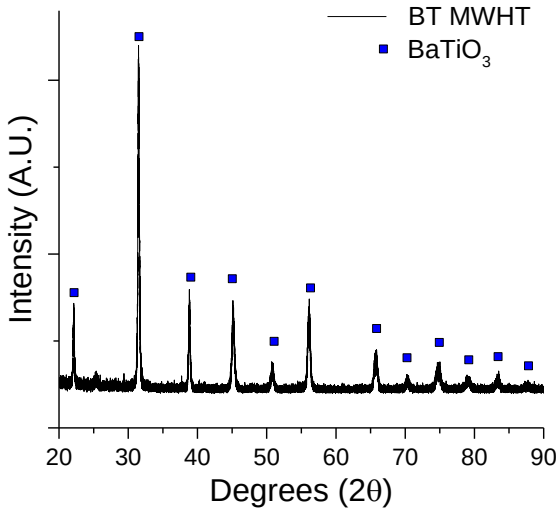

Figure 171: XRD pattern of BT *Annuus* pollen replicas synthesized by converting pollen grains coated with 50 Ti-O SSG deposition cycles and pyrolyzed at 600°C for 4 h into BaTiO3 with the MWHT reaction process.

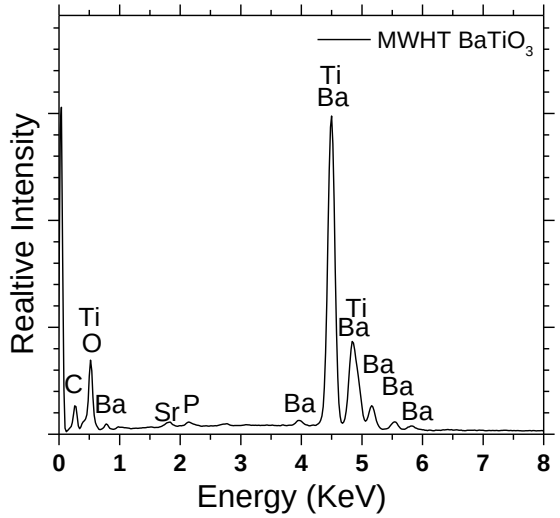

Figure 172: EDS of BT *Annuus* pollen replicas synthesized by converting pollen grains coated with 50 Ti-O SSG deposition cycles and pyrolyzed at 600°C for 4 h into $BaTiO_3$ with the MWHT reaction process.

A.4.4. Erbium Doped TiO_2 Pollen Replicas

Positive pollen replica containing barium titanate doped with erbium ($BaTiO_3$:Er, BT:Er) with preserved micro/nanostructured features in pollen grains have been created.

The shape preserving processes has been demonstrated by creating inorganic replicas of defatted Sunflower (*Helianthus annuus*) pollen grains using a layer-by-layer (LbL) surface sol-gel (SSG) technique followed by a thermal treatments to pyrolyze the organic content and to create TiO_2:Er replicas. The TiO_2:Er replicas were further reacted in a microwave hydrothermal (MWHT) reaction to also create BT:Er replicas. The synthesis of BT replicas of Sunflower has been examined using the method described in section 6.3.3-6.3.5 in which layers of Ti-Er-O are applied for a total of 50 coating layers followed by hydrothermal reaction into BT:Er.

The morphology and structure of the TiO_2:Er replicas can be seen in Figure 173. EDX analysis (Figure 174) yielded peaks for Ti, Er, and O, along with S and P peaks inherited from the starting pollen (as mentioned earlier). These Er-doped TiO_2 replicas did exhibit characteristic photoluminescent emission peaks (Figure 175), associated with the electron transitions of $^4S_{3/2} \rightarrow {}^4I_{15/2}$ at ~560 nm and $^4F_{9/2} \rightarrow {}^4I_{15/2}$ at ~670 nm, upon stimulation with 355 nm light. However, due to the high Er concentration the samples experience concentration quenching leading to limited intensity.[103] BT:Er experience 10% and 97% reduction in luminance intensities as the dopant concentration increase

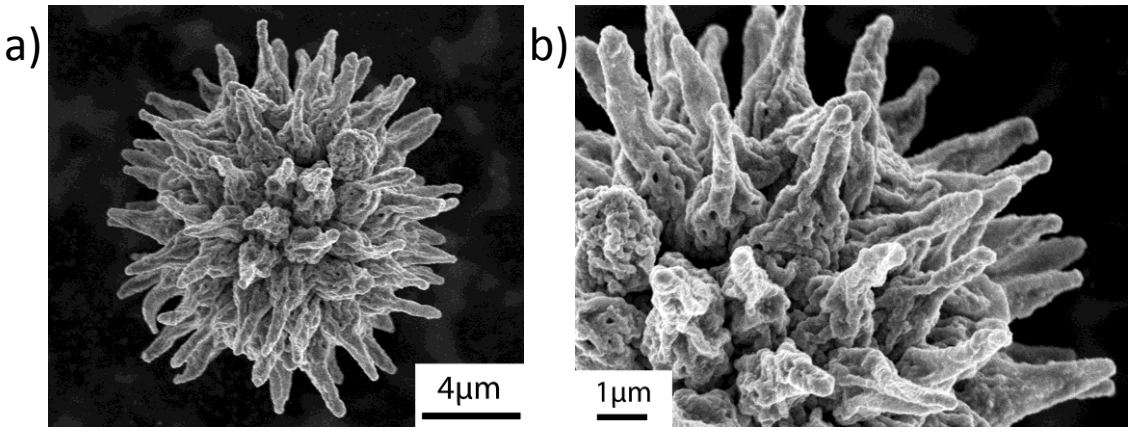

Figure 173: SE image of *Annuus* pollen replicas synthesized by applying 50 Ti-Er-O SSG deposition cycles and pyrolysis at 600°C for 4 h.

from 0.25% to 2.5% and 10% respectively.[103] In addition the low processing temperatures may be detrimental to the optical properties. $BaTiO_3$:Er doped have been found to have optimal optical output when annealed to 1000°C [100].

The BT:Er doped replicas can be seen in Figure 176. The $BaTiO_3$:Er samples preserved the general morphology of the pollen structures but have a lower yield compared to the high temperature layer by layer process. XRD and EDS, as shown in Figure 177 and Figure 178 respectively, also confirmed that the MWHT reacted samples

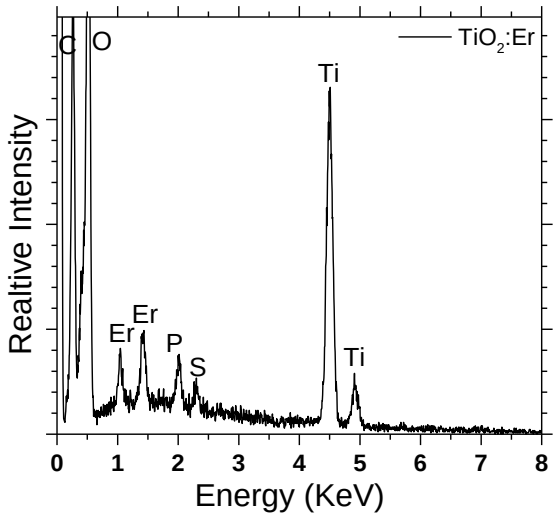

Figure 174: EDS of *Annuus* pollen replicas synthesized by applying 50 Ti-Er-O SSG deposition cycles and pyrolysis at 600°C for 4 h.

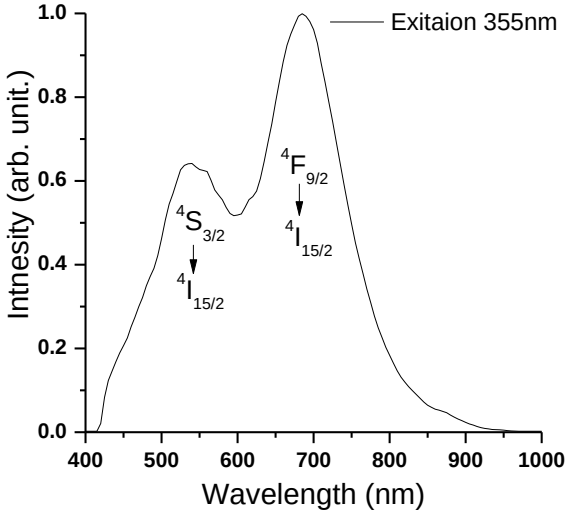

Figure 175: Photoluminescence spectra collected with 355 nm excitation of a single TiO_2:Er pollen replica via PARISS hyperspectral imaging system. Spectra courtesy of Dimitri Deheyn, Scripps Institution of Oceanography, UCSD, and Jeremy Lerner, Lightform, Inc.

were indeed $BaTiO_3$ and still contained noticeable amounts of Er. Scherrer analysis of the (311) diffraction peak yielded an average magnetite crystallite size of 51 ± 1 nm.

Future work should involve incorporating low concentrations (>.5 mol %) of erbium into the LbL SSG process. The amount of erbium deposited should be able to be adjusted until concentration quenching is prevented and maximum intensity values are obtained. From previous work it has been shown that the structure of BT replicas can be

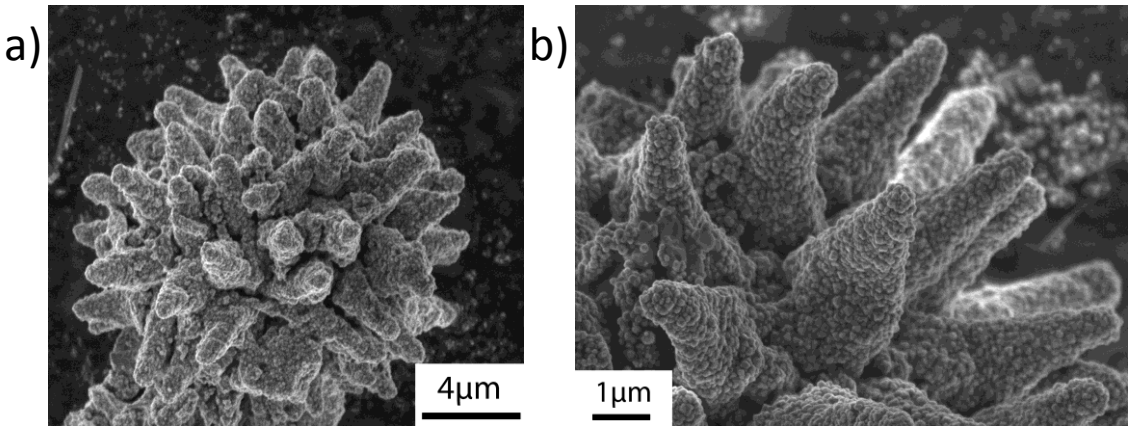

Figure 176: SE image of BT:Er *Annuus* pollen replicas synthesized by converting pollen grains coated with 50 Ti-Er-O SSG deposition cycles and pyrolyzed at 600°C for 4 h into $BaTiO_3$ with the MWHT reaction process.

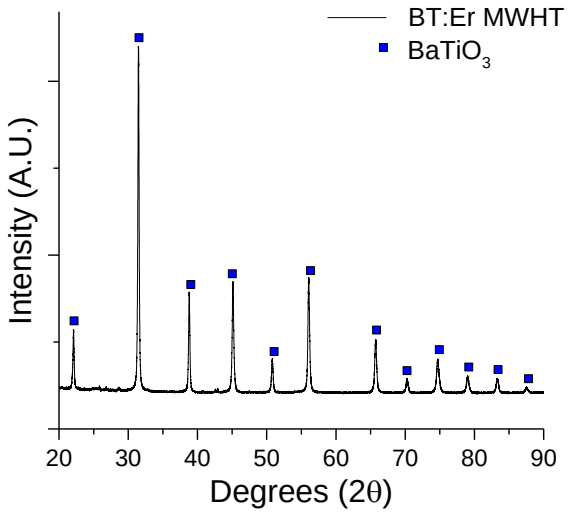

Figure 177: XRD plot BT:Er *Annuus* pollen replicas synthesized by converting pollen grains coated with 50 Ti-Er-O SSG deposition cycles and pyrolyzed at 600°C for 4 h into $BaTiO_3$ with the MWHT reaction process.

preserved with thermal treatments up 1000°C, at this temperature it may be possible to anneal BT:Er samples for maximum optical response and still maintain the morphology of the starting pollen.[100, 103]. By controlling the dopant concentration and firing temperatures, it may be possible to synthesize highly adhesive particles that exhibit photoluminescence.

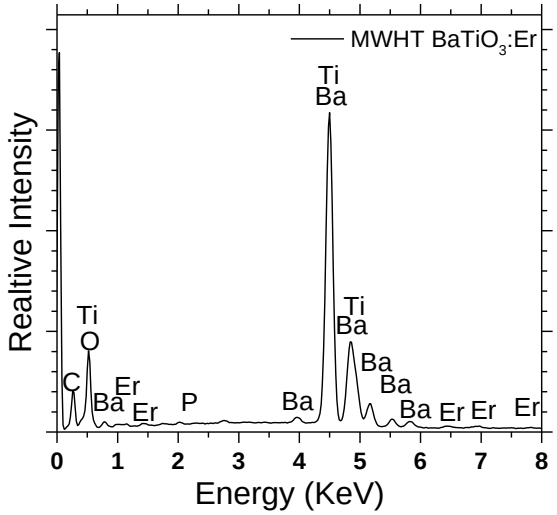

Figure 178: EDS of BT:Er *Annuus* pollen replicas synthesized by converting pollen grains coated with 50 Ti-Er-O SSG deposition cycles and pyrolyzed at 600°C for 4 h into $BaTiO_3$ with the MWHT reaction process.

A.5. *Concluding Remarks*

An automated SSG process has been developed to apply chemisorbed Ti-O and Ba-O coatings to defatted Sunflower pollen particles via alternating exposure to a Ti(IV) isopropoxide solution and water. Subsequent pyrolysis of Ti-O coated specimens yielded all-TiO_2 particles that retained the 3-D pollen shape and sharp spines, which indicated that the surface hydroxyl density of the sporopollenin on the pollen exine was sufficient as to allow for the generation of continuous chemisorbed Ti-O-bearing layers that remained inter-connected upon firing (i.e., additional amplification of surface hydroxyls was not needed). $BaTiO_3$ containing replicas were synthesized by alternating deposition

layers of Ti-O and Ba-O. The BT replicas were not phase pure but did retain the pollen shape at high temperatures (1000°C).

BST pollen replicas were generating using a SSG process and precursor solution mixed with Sr and Ba. By controlling the ratio of Ba:Sr in solution should be possible generate pollen replicas with tunable dielectric constants. In addition by doping samples with lanthanides one could generate dielectric (electrostatically-adhering) particles that also exhibit optical emission.

The SSG coating process was successfully combined with a low-temperature microwave hydrothermal reaction process to convert Sunflower TiO_2 pollen particles into phase pure $BaTiO_3$ replicas doped with the fluorescent lanthanide, Er. The SSG process was first used to apply conformal Er-Ti-O coatings to the pollen particles. Pyrolysis then yielded Er-doped TiO_2 replica particles. These thin-walled inorganic replicas were then reacted under hydrothermal conditions with barium acetate at only 220°C to form Er doped $BaTiO_3$ pollen replicas. Such complete, low-temperature hydrothermal conversion of TiO_2 replicas at only 220°C was consistent with a dissolution/reprecipitation mechanism for $BaTiO_3$ formation.

A.6. ***References***

[1] M. L. Ott and H. A. Mizes, "Atomic force microscopy adhesion measurements of surface-modified toners for xerographic applications," *Colloids and Surfaces A: Physicochemical and Engineering Aspects,* vol. 87, pp. 245-256, 8/16/ 1994.

[2] W. Richard Bowen and T. A. Doneva, "Atomic Force Microscopy Studies of Membranes: Effect of Surface Roughness on Double-Layer Interactions and Particle Adhesion," *Journal of Colloid and Interface Science,* vol. 229, pp. 544-549, 9/15/ 2000.

[3] K. Cooper, A. Gupta, and S. Beaudoin, "Simulation of the Adhesion of Particles to Surfaces," *Journal of Colloid and Interface Science,* vol. 234, pp. 284-292, 2/15/ 2001.

[4] M. A. Meitl, Z. T. Zhu, V. Kumar, K. J. Lee, X. Feng, Y. Y. Huang, *et al.*, "Transfer printing by kinetic control of adhesion to an elastomeric stamp," *Nat. Mater.,* vol. 5, p. 33, 2006.

[5] S. Mitragotri and J. Lahann, "Physical approaches to biomaterial design," *Nat. Mater.,* vol. 8, p. 15, 2009.

[6] Y. Huang, M. Liu, J. Wang, J. Zhou, L. Wang, Y. Song, *et al.*, "Controllable Underwater Oil-Adhesion-Interface Films Assembled from Nonspherical Particles," *Advanced Functional Materials,* vol. 21, pp. 4436-4441, 2011.

[7] K. E. Fischer, G. Nagaraj, R. H. Daniels, E. Li, V. E. Cowles, J. L. Miller, *et al.*, "Hierarchical nanoengineered surfaces for enhanced cytoadhesion and drug delivery," *Biomaterials,* vol. 32, p. 3499, 2011.

[8] L. Zhang, J. Shi, Z. Jiang, Y. Jiang, R. Meng, Y. Zhu, *et al.*, "Facile Preparation of Robust Microcapsules by Manipulating Metal-Coordination Interaction between Biomineral Layer and Bioadhesive Layer," *ACS Appl. Mater. Interfaces,* vol. 3, p. 597, 2011.

[9] S. Stassi and G. Canavese, "Spiky nanostructured metal particles as filler of polymeric composites showing tunable electrical conductivity," *J. Polym. Sci., Part B,* vol. 50, p. 984, 2012.

[10] I. Lee, "Molecular Self-Assembly: Smart Design of Surface and Interface via Secondary Molecular Interactions," *Langmuir,* vol. 29, p. 2476, 2013.

[11] K. L. Johnson, K. Kendall, and A. D. Roberts, "Surface Energy and the Contact of Elastic Solids," *Proc. R. Soc. London, Ser. A,* vol. 324, p. 301, 1971.

[12] B. V. Derjaguin, V. M. Muller, and Y. P. Toporov, "Effect of contact deformations on the adhesion of particles," *J. Colloid Interface Sci.,* vol. 53, p. 314, 1975.

[13] D. Tabor, *J. Colloid Interface Sci.,* vol. 58, p. 2, 1977.

[14] V. M. Muller, V. S. Yushchenko, and B. V. Derjaguin, *J. Colloid Interface Sci.,* vol. 77, p. 91, 1980.

[15] D. Maugis and H. M. Pollock, "Surface forces, deformation and adherence at metal microcontacts," *Acta Metall.,* vol. 32, p. 1323, 1984.

[16] W. A. Ducker, T. J. Senden, and R. M. Pashley, "Direct measurement of colloidal forces using an atomic force microscope," *Nature,* vol. 353, p. 239, 1991.

[17] D. Maugis, "Adhesion of spheres: The JKR-DMT transition using a dugdale model," *J. Colloid Interface Sci.*, vol. 150, p. 243, 1992.

[18] G. O. W. Kremp, *Morphologic Encyclopedia of Palynology*, 1968.

[19] J. W. Walker and J. A. Doyle, *Ann. Mo. Bot. Gard.*, vol. 62, p. 664, 1975.

[20] G. Erdtman, *Pollen Morphology and Plant Taxonomy*, 1986.

[21] S. Blackmore and S. H. Barnes, *Pollen and Spores: Patterns of Diversification*, 1991.

[22] A. Ressayre, B. Godelle, C. Raquin, and P. H. Gouyon, "Aperture Pattern Ontogeny in Angiosperms," *J. Exp. Zool.*, vol. 294, p. 122, 2002.

[23] M. Hesse, H. Halbritter, R. Zetter, M. Weber, R. Buchner, A. Frosch-Radivo, *et al.*, *Pollen Terminology: An Illustrated Handbook*, 2009.

[24] E. Horn, *Trans. Kans. Acad. Sci.*, vol. 36, p. 91, 1933.

[25] W. Grater and T. Stemen, "The plant, the pollen and the patient," *Rev. Paleobot. Palynol.*, vol. 4, p. 187, 1967.

[26] L. H. Ziska, D. E. Gebhard, D. A. Frenz, S. Faulkner, B. D. Singer, and J. G. Straka, "Cities as harbingers of climate change: Common ragweed, urbanization, and public health," *J. Allergy Clin. Immunol.*, vol. 111, p. 290, 2003.

[27] P. J. Beggs, "Impacts of climate change on aeroallergens: past and future," *Clin. Exp. Allergy*, vol. 34, p. 1507, 2004.

[28] C. A. Rogers, P. M. Wayne, E. A. Macklin, M. L. Mullenberg, C. J. Wagner, P. R. Epstein, *et al.*, "Interaction of the Onset of Spring and Elevated Atmospheric CO_2 on
Ragweed Pollen Production," *Environ. Health Perspect.*, vol. 114, p. 865, 2006.

[29] B. Fumanal, B. Chauvel, and F. Bretagnolle, "Estimation of pollen and seed production of common ragweed in France," *Ann. Agric. Environ. Med.*, vol. 14, p. 233, 2007.

[30] L. Ziska, K. Knowlton, C. Rogers, D. Dalan, N. Tierney, M. A. Elder, *et al.*, "Recent warming by latitude associated with increased length of ragweed pollen season in central North America," *Proc. Natl. Acad. Sci. U.S.A.*, vol. 108, p. 4248, 2011.

[31] M. D. Bajin, C. Cingi, F. Oghan, and M. K. Gurbuz, "Global warming and allergy in Asia Minor," *Arch. Oto-Rhino-Laryngol.*, vol. 270, p. 27, 2013.

[32] W. Brandon Goodwin, I. J. Gomez, Y. Fang, J. C. Meredith, and K. H. Sandhage, "Conversion of Pollen Particles into Three-Dimensional Ceramic Replicas Tailored for Multimodal Adhesion," *Chemistry of Materials,* vol. 25, pp. 4529-4536, 2013.

[33] H. Lin, I. Gomez, and J. C. Meredith, "Pollenkitt wetting mechanism enables species-specific tunable pollen adhesion," *Langmuir,* vol. 29, pp. 3012-3023, Mar 5 2013.

[34] I. Ichinose, H. Senzu, and T. Kunitake, "Stepwise Adsorption of Metal Alkoxides on Hydrolyzed Surfaces: A Surface Sol-Gel Process," *Chem. Lett.,* vol. 10, p. 831, 1996.

[35] I. Ichinose, H. Senzu, and T. Kunitake, "A Surface Sol-Gel Process of TiO_2 and Other Metal Oxide Films with Molecular Precision," *Chem. Mater.,* vol. 9, pp. 1296-1298, 1997.

[36] S. R. Hall, H. Bolger, and S. Mann, "Morphosynthesis of complex inorganic forms using pollen grain templates," *ChemComm,* pp. 2784-2785, 2003.

[37] Y. Wang, Z. Liu, B. Han, Z. Sun, J. Du, J. Zhang, *et al.*, "Replication of biological organizations through a supercritical fluid route," *ChemComm,* pp. 2948-2950, Jun 21 2005.

[38] S. R. Hall, V. M. Swinerd, F. N. Newby, A. M. Collins, and S. Mann, "Fabrication of Porous Titania (Brookite) Microparticles with Complex Morphology by Sol-Gel Replication of Pollen Grains," *Chem. Mater.,* vol. 18, pp. 598-600, 2006.

[39] P. Li, C. F. Zeng, L. X. Zhang, and N. P. Xu, *J. Inorg. Mater.,* vol. 23, p. 49, 2008.

[40] F. Cao and D. X. Li, "Morphology-controlled synthesis of SiO_2 hollow microspheres using pollen grain as a biotemplate," *Biomed Mater,* vol. 4, pp. 1-6, Apr 2009.

[41] X. Yang, X. Song, Y. Wei, W. Wei, L. Hou, and X. Fan, "Synthesis of spinous ZrO_2 core–shell microspheres with good hydrogen storage properties by the pollen bio-template route," *Scripta Materialia,* vol. 64, pp. 1075-1078, 2011.

[42] B. J. Thio, K. K. Clark, and A. A. Keller, "Magnetic pollen grains as sorbents for facile removal of organic pollutants in aqueous media," *J Hazard Mater,* vol. 194, pp. 53-61, Oct 30 2011.

[43] Y. Xia, W. Zhang, Z. Xiao, H. Huang, H. Zeng, X. Chen, *et al.*, "Biotemplated fabrication of hierarchically porous NiO/C composite from lotus pollen grains for lithium-ion batteries," *Journal of Materials Chemistry,* vol. 22, p. 9209, 2012.

[44] M. W. Anderson, S. M. Holmes, N. Hanif, and C. S. Cundy, "Hierarchical Pore Structures through Diatom Zeolitization " *Angew. Chem., Int. Ed.,* vol. 39, p. 2707, 2000.

[45] N. L. Rosi, C. S. Thaxton, and C. A. Mirkin, "Control of nanoparticle assembly by using DNA-modified diatom templates," *Angew. Chem., Int. Ed.,* vol. 43, p. 5500, 2004.

[46] C. S. Gaddis and K. H. Sandhage, "Freestanding Microscale 3-D Polymeric Structures with Biologically-derived Shapes and Nanoscale Features," *J. Mater. Res.,* vol. 19, p. 2541, 2004.

[47] J. Zhao, C. S. Gaddis, Y. Cai, and K. H. Sandhage, "Free-standing Microscale Structures of Zirconia Nanocrystals with Biologically Replicable 3-D Shapes,," *J. Mater. Res.,* vol. 20, p. 282, 2005.

[48] E. K. Payne, N. L. Rosi, C. Xue, and C. A. Mirkin, "Sacrificial biological templates for the formation of nanostructured metallic microshells," *Angew. Chem., Int. Ed.,* vol. 44, p. 5064, 2005.

[49] M. R. Weatherspoon, M. S. Haluska, Y. Cai, J. S. King, C. J. Summers, R. L. Snyder, *et al.*, "Phosphor Microparticles of Controlled 3-D Shape from Phytoplankton," *J. Electrochem. Soc.,* vol. 153, p. H34, 2006.

[50] D. Losic, J. G. Mitchell, R. Lai, and N. H. Voelcker, "Rapid Fabrication of Micro- and Nanoscale Patterns by Replica Molding from Diatom Biosilica," *Adv. Funct. Mater.,* vol. 17, p. 2439, 2007.

[51] U. Kusari, Z. Bao, Y. Cai, G. Ahmad, K. H. Sandhage, and L. G. Sneddon, "Formation of Nanostructured, Nanocrystalline Boron Nitride Microparticles with Diatom-Derived 3-D Shapes," *Chem. Commun.,* vol. 11, p. 1177, 2007.

[52] Z. Bao, E. M. Ernst, S. Yoo, and K. H. Sandhage, "Syntheses of Porous Self-Supporting Metal Nanoparticle Assemblies with 3-D Morphologies Inherited from Biosilica Templates (Diatom Frustules)," *Adv. Mater.,* vol. 21, p. 474, 2009.

[53] Y. Fang, Q. Wu, M. B. Dickerson, Y. Cai, S. Shian, J. D. Berrigan, *et al.*, "Protein-Mediated Layer-by-Layer Syntheses of Freestanding Microscale Titania Structures with Biologically Assembled 3-D Morphologies," *Chemistry of Materials,* vol. 21, pp. 5704-5710, 2009.

[54] C. J. Johnson, "Some dielectric and electro-optic properties of $BaTiO_3$ single crystals," *Applied Physics Letters,* vol. 7, 1965.

[55] L. Delaey, "Phase Transformations In Materials," in *Wiley-vch Verlag Gmbh*, G. Kostorz, Ed., ed Weinheim Germany, 2001.

[56] T. C. Rutt and J. A. Stynes, "Fabrication of multilayer ceramic capacitors by metal impregnation," *IEEE Transactions on Parts, Hybrids, and Packaging,* vol. 9, 1973.

[57] H. Igarashi, C. Betoh, and K. Okazaki, "Vapor-phase diffusion of metal oxides into barium titanate(IV) ceramics and its application to multilayer boundary layer capacitors," *Advances in Ceramics,* vol. 1, 1981.

[58] R. Wernicke, "Ceramic multilayer capacitors and nonlinear resistors," *Science of Ceramics,* vol. 12, 1984.

[59] H. J. Hagemann, D. Hennings, and R. Wernicke, "Ceramic multilayer capacitors," *Philips Technical Review,* vol. 41, 1984.

[60] P. D. Levett, "Properties and applications of positive temperature coefficients thermistors," *Ceramic Age,* vol. 83, 1967.

[61] J. Daniels, K. H. Haerdtl, and R. Wernicke, "The PTC effect of barium titanate," *Philips Technical Review,* vol. 38, 1979.

[62] M. Kuwabara, "Explanation for the PTCR effect in barium titanate ceramics," *Advances in Ceramics,* vol. 7, 1983.

[63] G. V. Lewis, C. R. A. Catlow, and R. E. W. Casselton, "PTCR effect in barium titanate ($BaTiO_3$)," *Journal of the American Ceramic Society,* vol. 68, 1985.

[64] L. S. Lukic, Z. Preradovic, V. Dimic, D. Stefanovic, and L. Vulicevic, "Prognosis the properties of $BaTiO_3$ ceramics for piezoelectric transducers," presented at the Sintering and Materials, Proceedings of the International Symposium on the Science and Technology of Sintering, Haikou, Peop. Rep. China, 1995.

[65] D. Stefanovic, V. Dimic, M. Radmanovic, D. Mancic, L. Lukic, and L. Vulicevic, "Synthesis of $BaTiO_3$ ceramics for piezoelectric transducers," *Science of Sintering,* vol. 28, 1996.

[66] K. Kiss, J. Magder, M. S. Vukasovich, and L. R. J., "Ferroelectrics of ultrafine particle size. I. Synthesis of titanate powders of ultrafine particle size," *Journal of the American Ceramic Society,* vol. 49, 1966.

[67] K. S. Mazdiyasni, R. T. Dolloff, and J. S. Smith II, "Preparation of high-purity submicron barium titanate powders," *American Ceramic Society,* vol. 52, 1969.

[68] A. E. Feuersanger, A. K. Hagenlocher, and A. L. Solomon, "Preparation and properties of thin barium titanate films," *Journal of the Electrochemical Society,* vol. 111, 1964.

[69] K. M. Hung, C. S. Hsieh, W. D. Yang, and Y. J. Sun, "The preparatory optimal conditions of barium titanate thin film from a hydrothermal method at low temperature," *Journal of Materials Science,* vol. 42, 2007.

[70] J. F. Scott, "Dimensional effects on ferroelectrics. Ultra-thin single crystals, nanotubes, nano-rods, and nano-ribbons," *Ferroelectrics,* vol. 316, 2005.

[71] J. H. Wei, J. Shi, Z. Y. Liu, and J. B. Wang, "Polymer-assisted synthesis of $BaTiO_3$ nanorods," *Journal of Materials Science,* vol. 41, 2006.

[72] X. Zhu, J. Zhu, S. Zhou, Z. Liu, N. Ming, and D. Hesse, "$BaTiO_3$ nanocrystals: hydrothermal synthesis and structural characterization," *Journal of Crystal Growth,* vol. 283, 2005.

[73] S. Yoon, S. Baik, M. G. Kim, N. Shin, and I. Kim, "Synthesis of tetragonal barium titanate nanoparticles via alkoxide-hydroxide sol-precipitation: effect of water addition," *Journal of the American Ceramic Society,* vol. 90, 2007.

[74] Y. Luo, I. Szafraniak, N. D. Zakharov, V. Nagarajan, M. Steinhart, R. B. Wehrspohn, *et al.*, "Nanoshell tubes of ferroelectric lead zirconate titanate and barium titanate," *Applied Physics Letters,* vol. 83, 2003.

[75] J. J. Urban, J. E. Spanier, L. Ouyang, W. S. Yun, and H. Park, "Single-crystalline barium titanate nanowires," *Advanced Materials,* vol. 15, 2003.

[76] U. A. Joshi, S. Yoon, S. Baik, and J. S. Lee, "Surfactant-Free Hydrothermal Synthesis of Highly Tetragonal Barium Titanate Nanowires: A Structural Investigation," *Journal of Physical Chemistry B,* vol. 110, 2006.

[77] J. P. Vernon, Y. Fang, Y. Cai, and K. H. Sandhage, "Morphology-preserving conversion of a 3D bioorganic template into a nanocrystalline multicomponent oxide compound," *Angew Chem Int Ed Engl,* vol. 49, pp. 7765-7768, Oct 11 2010.

[78] J. P. Vernon, N. Hobbs, Y. Cai, A. Lethbridge, P. Vukusic, D. D. Deheyn, *et al.*, "3D photoluminescent lanthanide-doped barium titanate structures synthesized by coating and shape-preserving reaction of complex-shaped bioorganic templates," *Journal of Materials Chemistry,* vol. 22, pp. 10365-10940, 2012.

[79] H. Weaver, "Dielectric properties of single crystals of $SrTiO_3$ at low temperatures," *Journal of Physics and Chemistry of Solids,* vol. 11, pp. 274-277, 1959.

[80] R. A. Cowley, "Lattice Dynamics and Phase Transitions of Strontium Titanate," *Physical Review,* vol. 134, pp. A981-A997, 05/18/ 1964.

[81] H. V. Alexandru, C. Berbecaru, A. Ioachim, L. Nedelcu, and A. Dutu, "BST solid solutions, temperature evolution of the ferroelectric transitions," *Applied Surface Science,* vol. 253, pp. 354-357, Oct 2006.

[82] C. L. Fu, C. R. Yang, H. W. Chen, Y. X. Wang, and L. Y. Hu, "Microstructure and dielectric properties of $BaSr_{1-x}TiO_3$ ceramics," *Materials Science and Engineering B-Solid State Materials for Advanced Technology,* vol. 119, pp. 185-188, May 2005.

[83] H. Abdelkefi, H. Khemakhem, G. Velu, J. C. Carru, and R. V. d. Muhll, "Dielectric properties and ferroelectric phase transitions in $Ba_XSr_{1-X}TiO_3$ solid solution," *Journal of Alloys and Compounds,* vol. 399, 2005.

[84] L. Zhou, P. M. Vilarinho, and J. L. Baptista, "Dependence of the structural and dielectric properties of $Ba_{1-X}Sr_xTiO_3$ ceramic solid solutions on raw material," *Journal of the European Ceramic Society,* vol. 19, 1999.

[85] G. Subramanyam, F. Ahamed, R. Biggers, and A. Campbell, "Design considerations for a novel coplanar waveguide based ferroelectric varactor shunt switch," *Integrated Ferroelectrics,* vol. 77, 2005.

[86] S. B. Majumder, M. Jain, R. S. Katiyar, F. W. Keuls, and F. A. Miranda, "Sol-gel derived grain oriented barium strontium titanate thin films for phase shifter applications," *Journal of Applied Physics,* vol. 90, 2001.

[87] F. Zimmermann, M. Voigts, C. Weil, R. Jakoby, P. Wang, W. Menesklou, *et al.*, "Investigation ofbarium strontium titanate thick films for tunable phase shifters," *Journal of the European Ceramic Society,* vol. 21, 2001.

[88] H. S. Kim, T. S. Hyun, H. G. Kim, I. D. Kim, T. S. Yun, and J. C. Lee, "Orientation effect on microwave dielectric properties of Si-integrated Ba0.6Sr0.4TiO3 thin films for frequency agile devices," *Applied Physics Letters,* vol. 89, 2006.

[89] X. Wang, W. Lu, J. Liu, F. Liang, and D. Zhou, "Influence of MgO on structure and low-frequency properties of $Ba_{0.6}Sr_{0.4}TiO_3$ ferroelectric ceramics," *Guisuanyan Xuebao,* vol. 32, 2004.

[90] B. Su, J. E. Holmes, C. Meggs, and T. W. Button, "Dielectric and microwave properties of barium strontium titanate (BST) thick films on alumina substrates," *Journal of the European Ceramic Society,* vol. 23, 2003.

[91] P. M. Suherman, T. J. Jackson, Y. Y. Tse, I. P. Jones, R. I. Chakalova, M. J. Lancaster, *et al.*, "Microwave properties of $Ba_{0.5}Sr_{0.5}TiO_3$ thin film coplanar phase shifters," *Journal of Applied Physics,* vol. 99, 2006.

[92] A. Kumar and S. G. Manavalan, "Characterization of barium strontium titanate thin films for tunable microwave and DRAM applications," *Surface and Coatings Technology,* vol. 198, 2005.

[93] Y. H. Xie, Y. Y. Lin, and T. A. Tang, "Characteristics of BST Thin Film Prepared by Novel Chemical Solution Deposition Method for High-Density DRAM " *Application. Integrated Ferroelectrics,* vol. 47, 2002.

[94] E. Domínguez, J. A. Mercado, M. A. Quesada, and A. Heredia, "Pollen sporopollenin: degradation and structural elucidation," *Sex Plant Reprod,* vol. 12, pp. 171-178, 1999.

[95] H. E. M. Dobson, " Survey of pollen and pollenkitt lipids - chemical cues to flower visitors," *Am. J. Bot.,* vol. 75, p. 170, 1988.

[96] M. R. Weatherspoon, M. B. Dickerson, G. Wang, Y. Cai, S. Shian, S. C. Jones, *et al.*, "Thin, conformal, and continuous SnO_2 coatings on three-dimensional biosilica templates through hydroxy-group amplification and layer-by-layer alkoxide deposition," *Angew Chem Int Ed Engl,* vol. 46, pp. 5724-5727, 2007.

[97] M. R. Weatherspoon, Y. Cai, M. Crne, M. Srinivasarao, and K. H. Sandhage, "3D rutile titania-based structures with morpho butterfly wing scale morphologies," *Angew Chem Int Ed Engl,* vol. 47, pp. 7921-7923, 2008.

[98] G. Wang, Y. Fang, P. Kim, A. Hayek, M. R. Weatherspoon, J. W. Perry, *et al.*, "Layer-By-Layer Dendritic Growth of Hyperbranched Thin Films for Surface Sol-Gel Syntheses of Conformal, Functional, Nanocrystalline Oxide Coatings on Complex 3D (Bio)silica Templates," *Advanced Functional Materials,* vol. 19, pp. 2768-2776, 2009.

[99] B. D. Cullity and S. R. Stock, *Elements of X-Ray Diffraction, 3rd ed*: Prentice-Hall, Inc,, 2001.

[100] P. Ghosh, S. Sadhu, T. Sen, and A. Patra, "Upconversion emission of $BaTiO_3$:Er nanocrystals," *Bull. Mater. Sci.,* vol. 31, pp. 461–465, 2008.

[101] S. W. Kim, H. I. Choi, M. H. Lee, J. S. Park, D. J. Kim, D. Do, *et al.*, "Electrical properties and phase of $BaTiO_3$–$SrTiO_3$ solid solution," *Ceramics International,* vol. 39, pp. S487-S490, 2013.

[102] J.-H. Jeon, "Effect of $SrTiO_3$ concentration and sintering temperature on microstructure and dielectric constant of $Ba_{1-x}Sr_xTiO_3$," *Journal of the European Ceramic Society,* vol. 24, pp. 1045-1048, 2004.

[103] A. Patra, C. S. Friend, R. Kapoor, and P. N. Prasad, "Fluorescence Upconversion Properties of Er^{3+}-Doped TiO_2 and $BaTiO_3$ Nanocrystallites," *Chemistry of Materials,* vol. 15, pp. 3650-3655, 2003/09/01 2003.

Appendix B : **Microwave Absorption Properties of Pollen Replicas**

B.1. ***Summary***

For the first time, three-dimensional (3-D) nanocrystalline all-oxide, replicas of pollen microparticles have been synthesized with tailored multimodal (bioenabled and synthetic) adhesion via use of a scalable, highly conformal surface sol–gel (SSG) coating process. High-fidelity replication allowed the pollen-shaped oxide microparticles to be utilized for adhesion via tailorable short-range (~10 nm) van der Waals (VDW) attraction, with the magnitude of such VDW-based adhesion influenced by the nanoscale topography of surface features retained by the replicas. Conversion of the pollen into ferrimagnetic (Fe_3O_4) microparticle replicas allowed the use of magnetic attraction at short and long ranges (up to ~1 mm). By selecting pollen particles with particular surface features and by SSG-enabled conversion of such pollen into 3-D nanocrystalline replicas composed of an appropriate type and amount of magnetic oxide, adhesive microparticles with tunable short- and long-range attractive forces can be generated.

B.2. ***Introduction***

Microwave absorbing materials, such as Magnetite (Fe_3O_4, a ferromagnetic material), have been heavily studied in recent years, due to their military and civilian applications such as stealth defense systems,[1, 2] microwave interference protection,[3] and microwave darkroom[4]. Most research has focused on one dimensional (1D) magnetic nanocrystals,[3, 5-8] nanorods,[9] 2D films,[10-13] and 3-D spheres.[14] While more recent work has focused shape related properties by synthesizing α-Fe_2O_3 dendritic micro-pine[15] followed by thermal conversion into γ-Fe_2O_3, Fe_3O_4 and Fe.[16] The

particle geometry and the volume fraction of magnetic particles in a host material (paraffin wax), as shown with magnetite microspheres[17] as well as magnetite-coated glass microballoons[18] both influence the magnitude and frequency of minimum microwave absorption. Sol-Gel methods have also been used to fabricate bulk, gelled, crystallized nickel ferrite samples exhibiting similar MWA behavior.[1]

The microwave absorbent properties are due to a phenomenon known as resonance absorption. The resonance absorption frequency of ferromagnetic particles due to electromagnetic can be modeled by the following equation.[19]

$$\omega_0 = \gamma\left[\left(H_z + 4*\pi + M_z + \frac{2*K_1}{M_z}\right)\left(H_z + \frac{2*K_1}{M_z}\right)\right]^{\frac{1}{2}} \qquad \text{(B.1)}$$

Where ω_0 is the frequency at which a ferromagnetic material exhibits resonance and K_1 is the first order anisotropy constant. The simplified Kittel equation can be used to calculate the natural resonance frequency of magnetic materials and is shown below:

$$f_r = \gamma H_a \qquad \text{(B.2)}$$

$\gamma = 28\text{GHzT}^{-1}$ is the gyromagnetic ratio, $H_a = 4|k_1|3\mu_o M_s$ is the effective anisotropy field, $\mu_o M_s$ is the magnetic saturation and is 0.547 for bulk Fe_3O_4, K_1 is the anisotropic coefficient and is $-9x10^3$ Jm^{-3} for Fe_3O_4. For Fe_3O_4 the resonance frequency can be calculated as f_r = 1.2 GHz.

Magnetic anisotropy is the direction dependence of a material's magnetic properties. The preferred magnetic orientation direction is called the easy direction. Magnetic anisotropy is a prerequisite for hysteresis in ferromagnetism, without directional dependence the material will be paramagnetic or diamagnetic. Magnetic anisotropy of a material is used to help determine if a magnetic material is suited for applications such as permanent magnets (high anisotropy), recording media (intermediate

anisotropy), and soft magnets (low anisotropy).[20] Magnetic anisotropy is also directly related to a materials resonance frequency, by the Kittle equation, which is important to for microwave absorbing material and antennas as the upper limit for low-loss bandwidth.[21, 22] One method for determining the magnetic anisotropy of a sample is curve fitting the high field region of a magnetic hysteresis plot using the Law of approach to ferromagnetic saturation (LAFS). For a bulk crystalline oxide the LAFS follows the following equation:

$$M(H) = M_s\left(1 - \frac{a_1}{H} - \frac{a_2}{H^2} - \frac{a_3}{H^3} - \cdots\right) + \chi_{hf}H + D\sqrt{H} \qquad (B.3)$$

or written as the differential susceptibility χ:

$$\chi = \frac{dM(H)}{dH} = M_s\left(\frac{a_1}{H^2} + \frac{2a_2}{H^3} + \frac{3a_3}{H^4} + \cdots\right) + \chi_{hf} + \frac{D}{2\sqrt{H}} \qquad (B.4)$$

Where M_S is the spontaneous magnetization, χ_{hf} is the high-field susceptibility resulting from the increase in spontaneous magnetization by the application field, D is the spin wave factor, a_2/H^2 term is caused by uniform magneto crystalline anisotropy, a_1/H is attributed to the existence of structural defects and nonmagnetic inclusions. For a ferromagnetic material with cubic crystal symmetry:

$$a_2 = \frac{8}{105}\frac{K_1^2}{M_s^2}\text{(CGS)} \qquad a_2 = \frac{8}{105}\frac{K_1^2}{\mu_0^2 M_s^2}\text{(SI)} \qquad (B.5)$$

K_1 is the first order anisotropy constant, defined by equation B.6

$$K_1' = \frac{f}{\alpha_1^2*\alpha_2^2+\alpha_2^2*\alpha_3^2+\alpha_1^2*\alpha_3^2} \qquad (B.6)$$

Where f is the unit volume of a material and α_1^2, α_2^2, and α_3^2 are the direction cosines between the magnetization vector and the edges of a magnetite crystal (modeled as a cube) [19]. For uniaxial anisotropic polycrystalline material the a_2 values are given as:

$$a_2 = \frac{4}{15}\frac{K_u^2}{M_s^2}\text{(CGS)} \qquad a_2 = \frac{4}{15}\frac{K_u^2}{\mu_0^2 M_s^2}\text{(SI)} \qquad (B.7)$$

LAFS can also be written in the following manner:

$$M(H) = \sum a_p H^p \quad \text{(B.8)}$$

$$p = n / 2, (n = -4, -2, -1, 0, 1, 2, 4), \quad \text{(B.9)}$$

$$a_0 = M_s, a_1 = \chi, a_{1/2} = D \quad \text{(B.10)}$$

In which negative exponents related to all sources of misalignment of the magnetization vector with the field. The p = -2 term involves the uniform anisotropy, while p = -1, -1/2 involves crystalline defects (vacancies, holes etc.) and other imperfections, boundaries, surface. Positive exponents correspond to the so-called paraprocess phenomena and concern the increment of the magnetization gained against the misalignment due to spin waves.

The low field region of the hysteresis curve can complicate data analysis do to demagnetization and irreversible effects and is often excluded from the fitted region. The demagnetization field has a maximum value of 0.6-.1 T. While other models are used to calculate magnetic anisotropy, such as Random anisotropy model (RAM), they are used in disordered magnetic systems, amorphous alloys, and low field regions which are not relevant for crystalline oxide material.

Pollen is a desirable type of microparticle template to use for magnetic shape anisotropy studies due, its biological replicability (i.e., sustainability), ready availability, low cost, and wide range of features in both the micro and nanometer range. Previous work has been conducted on synthesizing oxide replicas of pollen using a precursor incubations technique,[23] with hydrothermal processing,[24] and supercritical fluids.[25] This work focuses on creating iron oxide replicas via a layer-by-layer (LbL) surface sol-gel (SSG) process which allows for fine control of the thickness applied.[4]

The object of this study is to understand the effect of geometry on MWA behavior by using different pollen grains as model strucutes. While previous studies have utilized both fully dense and hollow spherical magnetite particles, irregular geometries have not been explored for MWA applications. The unique geometry of sunflower pollen is characterized by conical projections that extend from from the surface of a roughly spherical body. These projections allow pollen to have a high adherent force on many surfaces, and are of interest in MWA coating applications.[26] In contrast, pecan pollen grains have relativly shooth beach ball like geometry and will serve as a control to compare the effect of the spines.

In this study, a Sol-Gel method is used to coat grains of sunflower and pecan pollen with iron oxide coatings followed by various thermal processing to convert the coated pollen grains into Fe_3O_4 (magnetite) pollen replicas. The pollen replicas were then made into a composite using paraffin wax to measure 0MWA properties. Comparing sunflower pollen replicas, pecan pollen replicas and bulk fully dense magnetite particles of similar diameter allows for evaluation the influence of magnetite particle geometry on MWA properties.

B.3. *Experimental Procedures*

B.3.1. Template

Pollen is a desirable type of microparticle template to use due to its biological replicability (i.e., sustainability), ready availability, abundance, low cost, and wide range of features in both the micro- and nanometer range. Pollen templates will be chosen based on the overall size and shape from different plant species. The exine (outer layer)

of pollen grains are composed of sporopollenin, a complex polymer consisting of carboxylic acids cross-linked with aliphatic chains (e.g. HOOC-$(CH_2)_n$-COOH).[27] The carboxylic acids provide an abundant amount of functional groups needed for the reaction with the isopropoxide precursors used in the SSG process. These surface groups can eliminate the need for surface modification in order to obtain conformal coatings. The initial templates chosen to investigate shape dependence microwave absorption properties are Sunflower (*Helianthus annuus*) pollen grains, as shown in Figure 1 d (Chapter 1) with its spiny surface and Pecan (*Carya illinoinensis*)pollen Figure 1 a (Chapter 1) with its beach ball like geometry

B.3.2. Demineralization of Pollen Grains

Pollen grains obtained from Greer Laboratories, Lenoir, NC USA were cleaned, to remove pollenkitt, by immersion in a mixture of chloroform and methanol (3:1)[28] for 24 h, followed by deposition onto filter paper (P5, Fisher Scientific, Pittsburgh, PA USA) and drying under vacuum at 60^0C for 12 h. A second immersion was conducted in 1 M hydrochloric acid (VWR, Suwanee, GA USA) for 1 h to remove residual inorganic material, followed by rinsing three times with de-ionized water and drying by vacuum aspiration at room temperature for 5 min.

B.3.3. SSG coating of Pollen Grains Process

Fe-O-bearing coatings were applied to cleaned, dematerialized pollen grains via a computer-automated (in a N_2 atmosphere glove box), layer-by-layer (LbL) SSG deposition process by:[29-32] i) immersing pollen grains for 10 min, with stirring, in a solution of 0.0125 M Fe(III) isopropoxide (Alfa Aesar, Ward Hill, MA USA) in

anhydrous 2-propanol (>99.8% purity, Acros Organics, Geel, Belgium), to allow for the chemisorption of a Fe-O-bearing layer, ii) rinsing three times with anhydrous 2-propanol followed by vacuum filtration, iii) immersion in de-ionized water (DIW), with stirring, for 5 min, to allow for hydrolysis of the chemisorbed alkoxide layer, iv) rinsing three times with anhydrous 2-propanol followed by vacuum filtration, and v) and drying by vacuum aspiration for 5 min. This process (alkoxide exposure, 2-propanol rinsing, DIW exposure, 2-propanol rinsing, drying) was repeated for a total of 50 cycles to build up a Fe-O-bearing coating. A schematic for the SSG process can be seen in Figure 179.

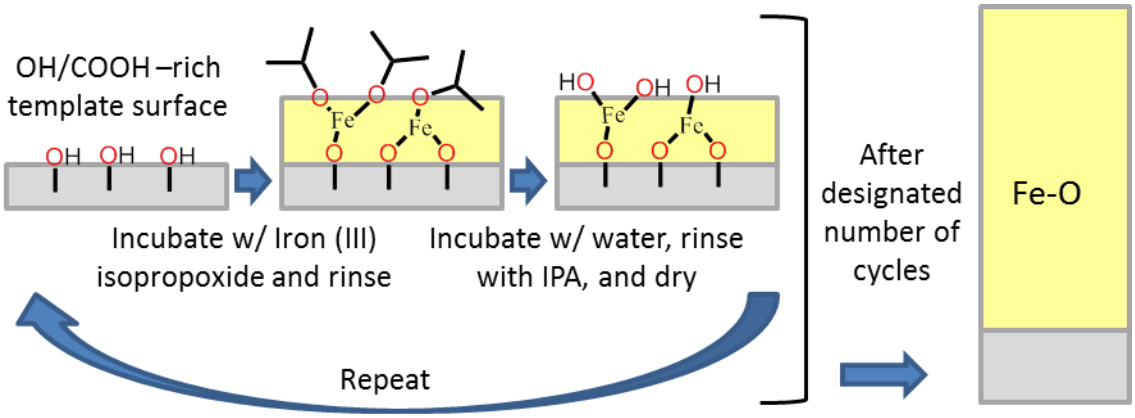

Figure 179: A schematic representation of the surface sol-gel process utilizing iron (III) isopropoxide as model metal alkoxide.

B.3.4. Organic Pyrolysis and Conversion to Magnetite

The SSG-coated pollen particles were placed in an MgO crucible (96.6% MgO, 2% Y_2O_3, 1.6% other, Ozark Technical Ceramics, Inc, Webb City, MO) for pyrolysis. Samples were fired in air using a tube furnace (Lindberg / Blue M, NC, USA,) with a ramp rate of 0.5°C min^{-1} to 600°C and held at this temperature for 4 h to allow for organic pyrolysis and oxide crystallization.

The resulting α-Fe_2O_3 hematite replicas were converted into magnetite via thermal treatment with a Rhines pack[33] powder mixture of Fe (99% purity, Acros Organics)

and Fe_3O_4 (99.95% purity, Alfa Aesar). For the Rhines pack setup an 8 in. DOM steel (0.6 max wt.% Mn, 0.04 max wt.% P, 0.05 max wt.% S) tube (1 in. dia.) was clamped and welded shut at one end. The hematite pollen replicas in the MgO crucible were removed and placed in Ni foil crucible. A nickel boat filled with 2 g of Fe and 0.5 g of Fe_3O_4 was then placed in the welded end of the tube. This amount of Fe and Fe_3O_4 powder was well in excess of that needed to partially reduce the Fe_2O_3 replicas into Fe_3O_4. 0.1 g hematite pollen replicas were placed with the Fe/Fe_3O_4 powder mixture (Fe:Fe_3O_4:Fe_2O_3 replica mole ratio = 14:14:1) inside a mild steel ampoule. The remaining open end was then clamped and welded shut in air. The sealed samples were then heated at 3°C min^{-1} to 550°C and held at this temperature for 2 h. After cooling to room temperature, the ampoules were cut open and the magnetite pollen replicas were extracted. The Rhines pack setup is illustrated in Figure 180.

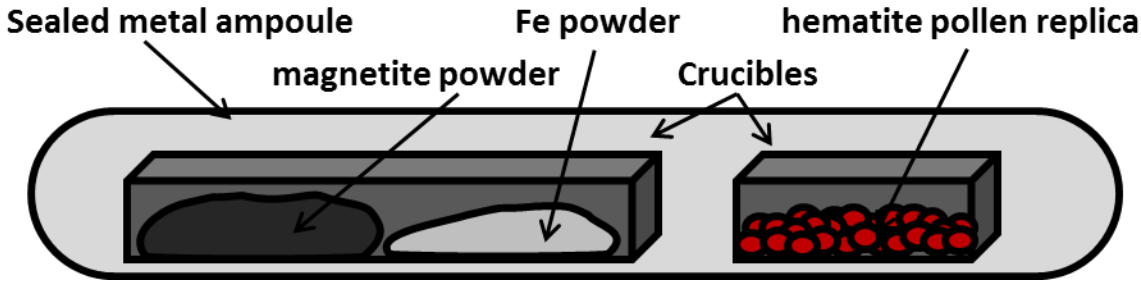

Figure 180: A schematic of the Rhines pack setup for converting hematite coatings into magnetite can be seen above. Hematite pollen replicas are placed in a sealed steal ampoule with excess Fe and magnetite powered in a 1:1 mol ratio. The sealed chamber allows for the hematite to be reduced and Fe to be oxidized until the pollen grains are converted in to magnetite.

B.3.5. Shape Morphology Analyses

The morphologies of the native pollen grains, SSG-coated grains, the pyrolyzed grains, and magnetite replicas were evaluated with a field emission scanning electron microscope (1530 FEG SEM, LEO / Carl Zeiss SMT, Ltd., Thorn-wood, NY USA).

B.3.6. Magnetic Property Measurements

Magnetic property measurements were studied using a superconducting quantum interference device (SQUID) magnetometer (Quantum Design MPMS-5S, San Diego, CA USA). The instrument sensitivity is such that it can measure changes in magnetic response up to 10^{-11}G. For sample preparation, powder samples are weighed out and recorded to the nearest tenth of a milligram. The sample is then transferred to a 0.5 mm by 1.5 mm gelatin capsule (Quantum Design, San Diego, CA USA) and immobilized by eicosane ($C_{20}H_{42}$, Arcos Organic). The sample capsule is then sealed with Kapton tape and inserted in a plastic straw (Quantum Design, San Diego, CA USA). The sample container is then taped to the end of the sample rod and inserted into the sample chamber. The Magnetic Hysteresis measurements are performed at 300 K with magnetic field going up to 7 T. When the values are plotted, magnetic saturation, remanent magnetization, and coercivity can be determined. Magnetic responses are given in units of Am^2/Kg and the coercivity field in units of Oe or G.

B.3.7. Microwave Hydrothermal Sample Preparation and Measurements

The Fe_3O_4 pollen replicas were then combined with pure paraffin wax in its liquid phase to form mixtures of 10%, 15%, and 20% pollen replicas by volume (+/- 1.0 vol. %) or 45%, 50%, and 55% (+/- 1.0 mass %) pollen replicas by mass. Control samples were also fabricated using fully dense 44 μm (ASTM 325 mesh) Fe_3O_4 particles. Since the average density of each pollen replica was not precisely known, these volume percent's were converted to mass presents in order to ensure that the same volume (i.e. same mass) of magnetite was present in the pollen replica samples and control samples meant to contain the same volume percent magnetite. These mixtures were then heated to 200^{o}C to

soften the paraffin matrix and pressed in a hollow cylindrical die to form cylindrical samples with outer diameter 2.5 mm, inner diameter .5 mm, and length 3.0 mm. For each mixture (3 control mixtures and 6 mixtures containing pollen replicas), 2 samples with these dimensions were fabricated.

These samples were then analyzed for their real and imaginary permittivity over a range of frequencies spanning from 0 Hz to 25 GHz. The methodology used was adapted from a process described by Raida et al. [34].

B.4. *Results & Discussion*

B.4.1. Pollen Shape Preservation and Coating Quality

Sunflower and pecan pollen particles were converted into iron oxide replicas via use of a computer-automated LbL SSG coating process,[29-32] as described in section B.3.3 followed by pyrolois at 600°C to convert the sample into hematite replicas. Because the exine (outer layer) of such pollen grains is comprised of sporopollenin (a complex polymer consisting of carboxylic acids and aromatic moieties cross-linked with aliphatic chains[27]), the pollen surfaces were enriched with hydroxyl groups that provided an abundance of reaction sites for the chemisorption of alkoxide precursors during the SSG coating process.[35, 36] Repeated, alternating exposure of the pollen particles to an iron (III) isopropoxide precursor and to water allowed for the LbL buildup of a conformal Fe-O-bearing coating on the pollen grains. Conversion of the hematite replicas into magnetite was conducted via use of a thermal treatment with a Rhines pack.[33] An excess powder mixture of iron and magnetite was sealed along with hematite pollen replicas within a mild steel ampoule. The ampoule was then heated to

550°C and held at this temperature for 2 h. The oxygen partial pressure established within the ampoule by the Fe/Fe_3O_4 equilibrium at 550°C (note: wüstite, $Fe_{1-x}O$, is thermodynamically unstable below 570°C[37]) allowed for complete conversion of the replica particles into phase-pure nanocrystalline magnetite (ICDD# 01-072-2303), as confirmed by XRD analysis (Figure 181).

Secondary electron (SE) images of sunflower replicas that were converted to magnetite (Fe_3O_4), using the process described in section B.3.4., along with cleaned sunflower pollen and pollen samples coated with 50 SSG coating cycles can be seen in Figure. The sunflower pollen grains were roughly spherical in shape and possessed echini (spines) of relatively high aspect ratio (height: width-at-midheight ratio of ~5:1).

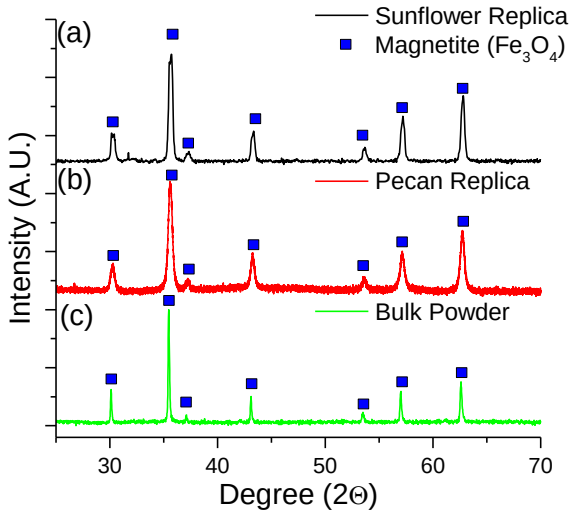

Figure 181: XRD analyses of iron oxide replicas of a) sunflower pollen and b) pecan pollen generated by exposing the pollen particles to 50 SSG LbL deposition cycles and then firing at a peak temperature of 600°C for 4 h in air, followed by sealing the resulting α-Fe_2O_3 samples, along with an excess powder mixture of Fe and Fe_3O_4 (a Rhines pack), within a mild steel ampoule and heating to a peak temperature of 550°C for 2 h, c) commercially purchased magnetite 325 mesh powder.

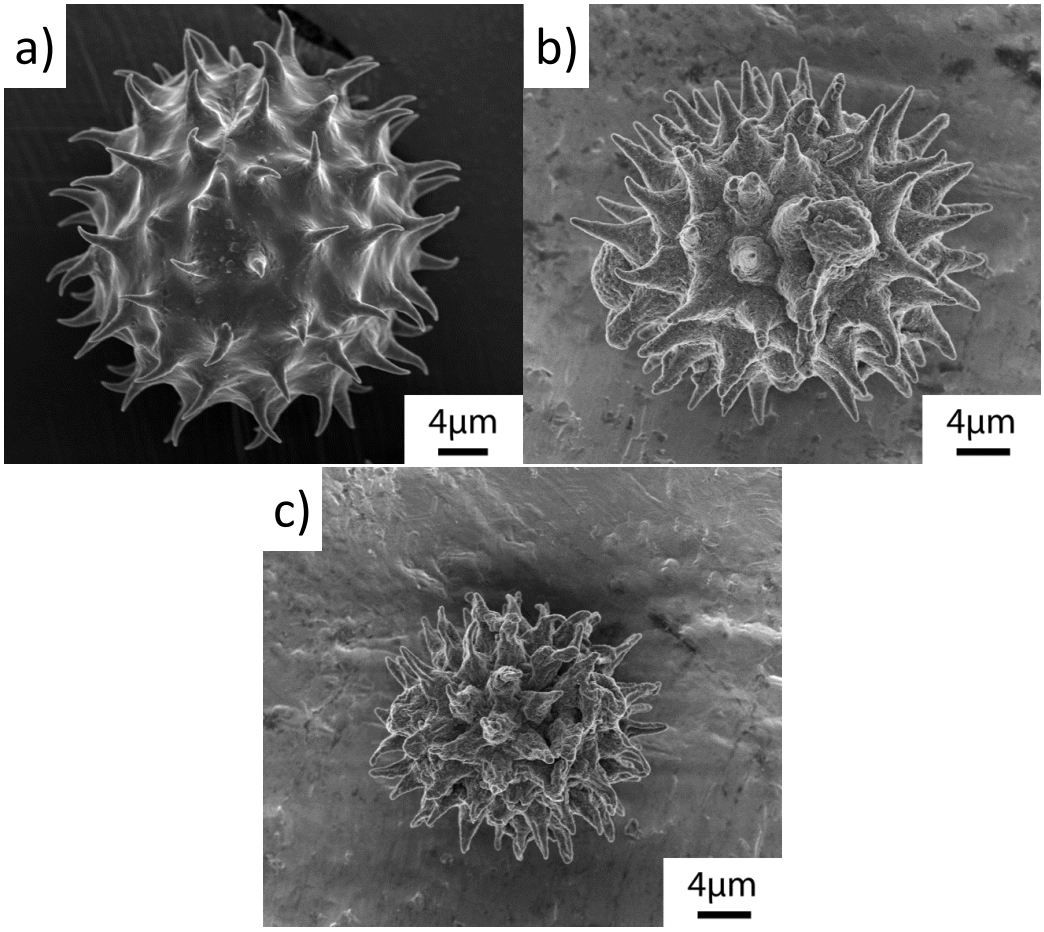

Figure 182: SE images of sunflower pollen particles at various stages of conversion into Fe_3O_4: a) a cleaned sunflower pollen grain with no coating, b) an Fe-O-coated grain after 50 SSG deposition cycles, c) an Fe_3O_4 replica after pyrolysis at 600°C for 4 h in air and partial reduction using a Rhines pack (Fe/Fe_3O_4) at 550°C for 2 h.

B.4.2. Magnetic Property Measurements

The magnetic properties of sunflower pollen Fe_3O_4 replicas were examined with a superconducting quantum interference device (SQUID) magnetometer at 300K as seen in Figure 183. The coercivity H_c, and magnetic saturation M_s values for the Fe_3O_4 replicas were determined at 300K to be 206.7 Oe, and 68.0(0.2) emu g^{-1} respectively. The H_c value was higher than that of nanoparticles with crystal sizes in the range of 4.3-55 nm (12(7)-156(7) Oe),[5] spheres with a mean diameter of 500 nm (87.4 Oe),[14] and bulk Fe_3O_4 (115-150 Oe).[6] Nanoparticles in the range of 150 nm have H_c values reported ranging from 56.5 Oe[6] up to 323(7) Oe.[5] The dendritic microspines samples have H_c

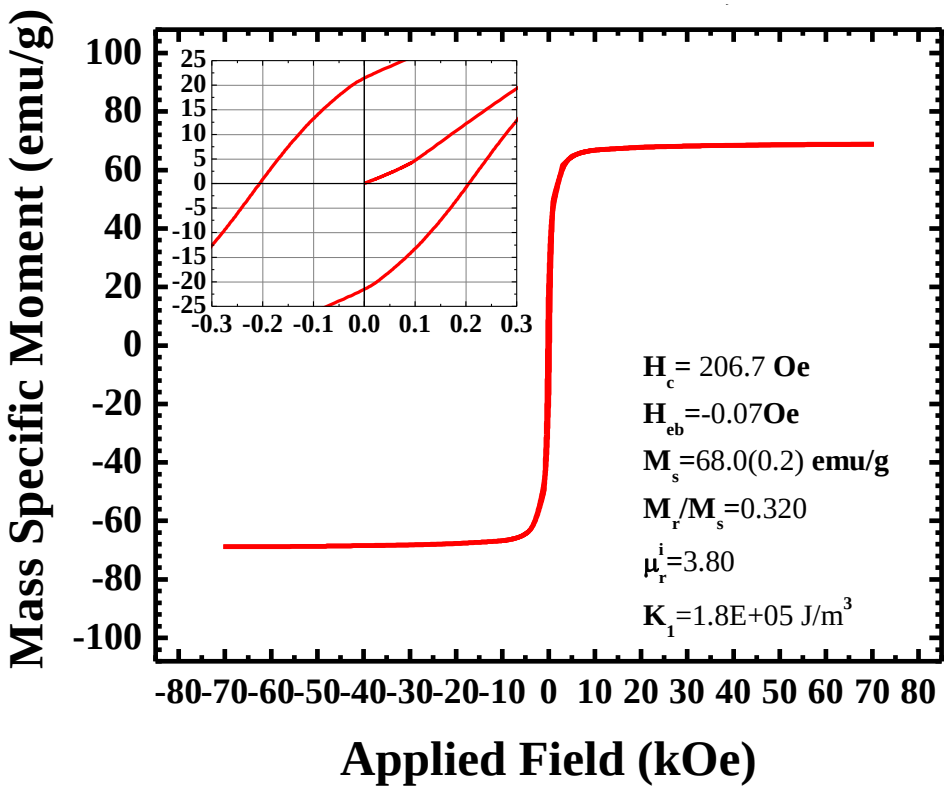

Figure 183: SQUID hysteresis plot conducted at 300K of Fe_3O_4 sunflower replicas generated using 50 layers of Fe-O SSG

values in the 270.4 Oe[16] range. Compared to the Fe_3O_4 M_s values of bulk material (92 emu g^{-1}),[20] dendritic micro pines (95 emu g^{-1}), [16] microspheres (83.1 emu g^{-1}),[14] and nanocrystals of mean diameters of ~150nm (75.4 emu g^{-1})[5, 6] the pollen replicas had lower values. In general the Ms value of nanomaterials are lower than that of the bulk and deceases with particle size.[5, 38] Nanoparticles with crystal sizes of 55 nm (65.4 emu g^{-1}), ~10 nm (60.1 emu g^{-1}), and 4.3 nm (12 emu g^{-1}) all have M_s values lower than the pollen replicas.[5] While the crystallite sizes from sheer analysis and M_s value from the pollen grains are similar to that of the 55 nm sample the particle sizes are different by 3 orders of magnitude (~23 μm vs. ~47 nm).[5] Linear correlation between particle size and M_s has been reported with γ-Fe_2O_3, suggesting that surface properties can influence

magnetic ones.[8] This could suggest that the structure of the pollen grains replicas may be affecting the M_s value.

Magnetic anisotropy was calculated by curve fitting the high field region of the hysteresis plot is using a simplified version of the Law of approach to ferromagnetic saturation as given in equation B.11:

$$M(H) = M_s\left(1 - \frac{a_2}{H^2}\right) + \chi_{hf}H \qquad (B.11)$$

Were M_S is the saturation magnetization, χ_{hf} is the high-field susceptibility resulting from the increase in spontaneous magnetization by the application field, a_2/H^2 term is caused by a uniform magnetocrystalline anisotropy. For a ferromagnet with cubic crystal symmetry the a_2 term can be defined as equation B.12.

$$a_2 = \frac{8}{105}\frac{K_1^2}{M_s^2} \qquad (B.12)$$

Were K_1 is the magnetic anisotropy constant. The measured K_1 value of 1.85E4 J m^{-3}, for sunflower pollen grains, was over an order of magnitude higher than that of the bulk (1.3-0.9E4 J m^{-3}) [5, 14, 20] and more than double that of nanoparticles (4.6E4 J m^{-3}).[5] dramatically different anisotropy values should effect the microwave absorption performance of the materials as governed by the kittle equation.

B.4.3. Microwave Absorption Measurements

MWA analysis of the pollen replica samples as well as the control samples allowed for measurements of several dielectric parameters. Of particular interest for the development of MWA materials is the reflection loss of each specimen, which indicates the measurable microwave "signature" of an object. The larger the reflection, the more "visible" the object is to microwave detectors. The reflection loss in bels for each of the

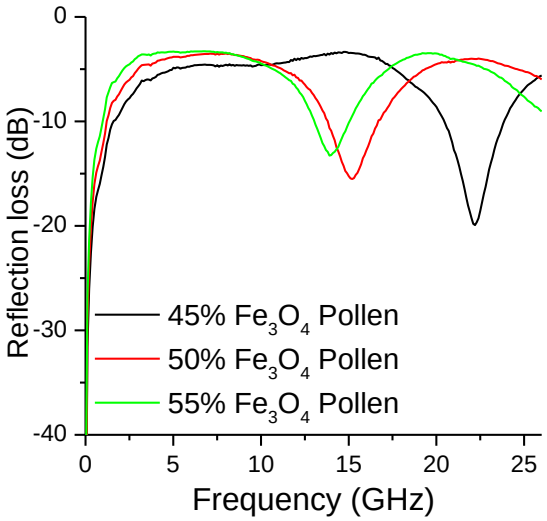

Figure 184: Reflection loss of 3mm composite made with paraffin wax and Fe_3O_4 sunflower pollen replica generated using 50 layers of Fe-O SSG with 45%, 50% and 55% mass

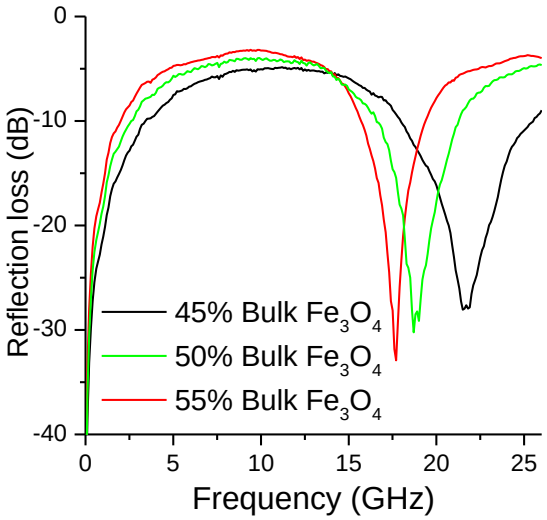

Figure 185: Reflection loss of 3mm composite made with paraffin wax and commercially purchased 325 mesh Fe_3O_4 powders with 45%, 50% and 55% mass

Fe_3O_4 pollen replica composites as well as the control samples is shown below in Figure 184 and Figure 185.

The reflection loss measurements shown in Figure 4 suggest that the microwave absorbance of Fe_3O_4 is reduced by using a sunflower pollen template to create magnetite particles of irregular geometry. While the cause for this trend is unclear, it is possible that the absorbance of individual magnetite particle depends on the contiguous length of

paramagnetic material that the electromagnetic radiation encounters. In the control specimens, the radiation passes through the same amount of magnetite as it traversed the sample. Furthermore, the bulk particles and near net-shape pollen replicas have similar dimensions: the 44 μm particle size for the control samples was selected because it was comparable to the diameter of the pollen replicas (see Figure 182). However, each particle that the radiation encountered in the control samples was fully dense and presented a greater contiguous length of ferromagnetic material over which the wave could resonate, as compared to the hollow pollen replicas whose structure was comprised of comparatively thin shells of ferromagnetic material. It was also observed that the 10 volume percent samples fabricated from magnetite powder and magnetite pollen replicas exhibited the same resonance frequency (around 21.5 GHz) while there was a significant frequency offset between the bulk control samples and replica samples at the two other compositions tested.

Further measurements of reflection loss measurements as well as other dielectric parameters are needed in order to validate these results. At present, findings suggest that near net-shaped magnetite pollen replicas, with large spined geometry, do not enhance the microwave absorbent properties of the ferromagnetic material. It is worth noting that the other unique aspects of pollen grain geometry, including the grains' prominent protrusions and high surface area to volume ratio, could lead to its use in other niche applications of near net-shaped particles composed of magnetite or other materials. Specifically, the adhesive properties of pollen grains could be utilized. It was clearly demonstrated that the SSG, firing, and reduction method here described is effective at

recreating pollen grain geometry, and this is a promising tool for future research and development.

B.5. *Concluding Remarks*

In summary, Fe_3O_4 sunflower replicas were synthesized using an LbL SSG coating process. Fitting SQUID measurements to law to approach of magnetic saturation showed that the sunflower pollen replicas had a magnetic anisotropy value an order of magnitude higher than that of bulk magnetite. Composite of paraffin wax and Fe_3O_4 with different Fe_3O_4 weight fraction were characterized for their microwave absorption properties. For both magnetite pollen samples and commercially purchased magnetite powder samples the maximum absorption frequency decreased as the weight fraction increased. The magnetite pollen samples exhibited a greater frequency shift and values closer to the bulk resonance frequency (1.2 GHz) compared to the commercially purchased powder samples. However, the maximum absorption value for the magnetite pollen replicas was noticeably lower than that of purchased magnetite. The differences between the types of samples could be related to the magnetic anisotropy values but further work is needed to validate this theory. Future work in this area should focus on creating pollen replicas with different morphologies, such as spherical in the case of pecan pollen, measure the magnetic anisotropy values of theses samples and then investigate the effective of anisotropy on the microwave absorption properties. By performing the measurements on samples that are processed in a similar manner, the effect of particle shape on both magnetic anisotropy and microwave absorption can be determined.

B.6. ***References***

[1] T. Giannakopoulou, L. Kompotiatis, A. Kontogeorgakos, and G. Kordas, "Microwave behavior of ferrites prepared via sol–gel method," *Journal of Magnetism and Magnetic Materials,* vol. 246, pp. 360-365, 2002.

[2] S. Ruan, B. Xu, H. Suo, F. Wu, S. Xiang, and M. Zhao, "Microwave absorptive behavior of ZnCo-substituted W-type," *Journal of Magnetism and Magnetic Materials,* vol. 212, pp. 175-177, 2000.

[3] P. Saini, V. Choudhary, B. P. Singh, R. B. Mathur, and S. K. Dhawan, "Polyaniline–MWCNT nanocomposites for microwave absorption and EMI shielding," *Materials Chemistry and Physics,* vol. 113, pp. 919-926, 2009.

[4] D. K. Barton, *Radar Evaluation Handbook.* New York: Artech House, 1998.

[5] G. Goya, T. Berquo, F. Fonseca, and M. Morales, "Static and dynamic magnetic properties of spherical magnetite nanoparticles," *Journal of Applied Physics,* vol. 94, p. 3520, 2003.

[6] S. Ni, S. Lin, Q. Pan, F. Yang, K. Huang, and D. He, "Hydrothermal synthesis and microwave absorption properties of Fe_3O_4nanocrystals," *Journal of Physics D: Applied Physics,* vol. 42, p. 055004, 2009.

[7] M. P. Morales, M. Andres-Verges, S. Veintemillas-Verdaguer, M. I. Montero, and C. J. Serna, "Structural effects on the magnetic properties of γ-Fe_2O_3 nanoparticles," *Journal of Magnetism and Magnetic Materials,* vol. 203, pp. 146-148, 1999.

[8] A. H. Latham, M. J. Wilson, P. Schiffer, and M. E. Williams, "TEM-Induced Structural Evolution in Amorphous Fe Oxide Nanoparticles," *J. AM. CHEM. SOC.,* vol. 128, pp. 126332-12633, 2006.

[9] S.-J. Park, S. Kim, S. Lee, Z. G. Khim, K. Char, and T. Hyeon, "Synthesis and Magnetic Studies of Uniform Iron Nanorods and Nanospheres," *J. Am. Chem. Soc.,* vol. 122, pp. 8581-8582, 2000.

[10] A. Bollero, M. Ziese, R. Höhne, H. C. Semmelhack, U. Köhler, A. Setzer, *et al.*, "Influence of thickness on microstructural and magnetic properties in Fe_3O_4 thin films produced by PLD," *Journal of Magnetism and Magnetic Materials,* vol. 285, pp. 279-289, 2005.

[11] D. T. Margulies, F. T. Parker, F. E. Spada, R. S. Goldman, J. Li, R. Sinclair, *et al.*, "Anomalous moment and anisotropy behavior in Fe_3O_4 films," *Physical Review B,* vol. 53, 1996.

[12] Y. Goryunov, N. Garif'yanov, G. Khaliullin, I. Garifullin, L. Tagirov, F. Schreiber, *et al.*, "Magnetic anisotropies of sputtered Fe films on MgO substrates," *Physical Review B,* vol. 52, pp. 13450-13458, 1995.

[13] J. Das, S. Kalarickal, K.-S. Kim, and C. Patton, "Magnetic properties and structural implications for nanocrystalline Fe-Ti-N thin films," *Physical Review B,* vol. 75, 2007.

[14] S. Ni, X. Sun, X. Wang, G. Zhou, F. Yang, J. Wang, *et al.*, "Low temperature synthesis of Fe_3O_4 micro-spheres and its microwave absorption properties," *Materials Chemistry and Physics,* vol. 124, pp. 353-358, 2010.

[15] M. Cao, T. Liu, S. Gao, G. Sun, X. Wu, C. Hu, *et al.*, "Single-crystal dendritic micro-pines of magnetic α-Fe_2O_3: large-scale synthesis, formation mechanism, and properties," *Angew Chem Int Ed Engl,* vol. 44, pp. 4197-201, Jul 4 2005.

[16] G. Sun, B. Dong, M. Cao, B. Wei, and C. Hu, "Hierarchical Dendrite-Like Magnetic Materials of Fe_3O_4, γ-Fe_2O_3, and Fe with High Performance of Microwave Absorption," *Chemistry of Materials,* vol. 23, pp. 1587-1593, 2011.

[17] S. Ni, X. Sun, X. Wang, and D. He, "Low temperature synthesis of Fe_3O_4 micro-spheres and its microwave absorption properties," *Materials Chemistry and Physics,* vol. 124, pp. 353-358, 2010.

[18] L. Xiang and P. Xiaofen, "Preparation of low-density superparamagnetic microspheres by coating glass microballoons with magnetite nanoparticles," *Materials Science and Engineering B,* vol. 135, pp. 38-43, 2006.

[19] C. Kittel, "On the Theory of Ferromagnetic Resonance Absorption," *Physical Review,* vol. 73, pp. 155-161, 1948.

[20] R. Skomski, "Nanomagnetics," *J. Phys.: Condens. Matter,* vol. 15, pp. R841–R896, 2003.

[21] C. Kittel, "On the Theory of Ferromagnetic Resonance Absorption," *Physical Review,* vol. 73, pp. 155-161, 1948.

[22] I. Tzanidis, S. Koulouridis, K. Sertel, D. Hansford, and J. L. Volakis, "Characterization of Low-loss Magnetodielectric Composites for Antenna Size Reduction," *IEEE,* 2008.

[23] S. R. Hall, H. Bolger, and S. Mann, "Morphosynthesis of complex inorganic forms using pollen grain templates," *ChemComm,* pp. 2784-2785, 2003.

[24] X. Yang, X. Song, Y. Wei, W. Wei, L. Hou, and X. Fan, "Synthesis of spinous ZrO_2 core–shell microspheres with good hydrogen storage properties by the pollen bio-template route," *Scripta Materialia,* vol. 64, pp. 1075-1078, 2011.

[25] Y. Wang, Z. Liu, B. Han, Z. Sun, J. Du, J. Zhang, *et al.*, "Replication of biological organizations through a supercritical fluid route," *ChemComm*, pp. 2948-2950, Jun 21 2005.

[26] J. P. Schaffer, *The Science and Design of Engineering Materials*, 2 ed.: McGraw Hill, 1999.

[27] E. Domínguez, J. A. Mercado, M. A. Quesada, and A. Heredia, "Pollen sporopollenin: degradation and structural elucidation," *Sex Plant Reprod*, vol. 12, pp. 171-178, 1999.

[28] H. E. M. Dobson, " Survey of pollen and pollenkitt lipids - chemical cues to flower visitors," *Am. J. Bot.*, vol. 75, p. 170, 1988.

[29] M. R. Weatherspoon, M. B. Dickerson, G. Wang, Y. Cai, S. Shian, S. C. Jones, *et al.*, "Thin, conformal, and continuous SnO_2 coatings on three-dimensional biosilica templates through hydroxy-group amplification and layer-by-layer alkoxide deposition," *Angew Chem Int Ed Engl*, vol. 46, pp. 5724-5727, 2007.

[30] M. R. Weatherspoon, Y. Cai, M. Crne, M. Srinivasarao, and K. H. Sandhage, "3D rutile titania-based structures with morpho butterfly wing scale morphologies," *Angew Chem Int Ed Engl*, vol. 47, pp. 7921-7923, 2008.

[31] G. Wang, Y. Fang, P. Kim, A. Hayek, M. R. Weatherspoon, J. W. Perry, *et al.*, "Layer-By-Layer Dendritic Growth of Hyperbranched Thin Films for Surface Sol-Gel Syntheses of Conformal, Functional, Nanocrystalline Oxide Coatings on Complex 3D (Bio)silica Templates," *Advanced Functional Materials*, vol. 19, pp. 2768-2776, 2009.

[32] J. P. Vernon, N. Hobbs, Y. Cai, A. Lethbridge, P. Vukusic, D. D. Deheyn, *et al.*, "3D photoluminescent lanthanide-doped barium titanate structures synthesized by coating and shape-preserving reaction of complex-shaped bioorganic templates," *Journal of Materials Chemistry*, vol. 22, pp. 10365-10940, 2012.

[33] F. H. Rhines, W. A. Johnson, and W. A. Anderson, *Trans. AIME*, vol. 147, p. 205, 1942.

[34] R. Tkadlek and Z. Raida, "Title," unpublished|.

[35] I. Ichinose, H. Senzu, and T. Kunitake, "A Surface Sol-Gel Process of TiO_2 and Other Metal Oxide Films with Molecular Precision," *Chem. Mater.*, vol. 9, pp. 1296-1298, 1997.

[36] I. Ichinose, H. Senzu, and T. Kunitake, "Stepwise Adsorption of Metal Alkoxides on Hydrolyzed Surfaces: A Surface Sol-Gel Process," *Chem. Lett.*, vol. 10, p. 831, 1996.

[37] H. A. Wriedt, "Iron-Oxygen Binary Alloy Phase Diagram " *J. Phase Equilib.*, vol. 12, p. 170, 1991.

[38] M. Morales, M. Andres-Verges, S. Veintemillas-Verdaguer, M. Montero, and C. Serna, "Structural effects on the magnetic properties of γ-Fe_2O_3 nanoparticles," *Journal of magnetism and magnetic materials,* vol. 203, pp. 146-148, 1999.

Vita

William Brandon Goodwin was born to Myron and Carol Goodwin, 1987 in Kijabe Kenya. He grew up with his older brother Benjamin Goodwin and younger twin sisters Lauren Reese and Merrill Durham in Kitale Kenya until the age of 11 when his family moved to Williamson County, Tennessee. He graduated from Ravenwood High School the Class of 2006. In May of 2010 Brandon graduated from the University of Tennessee, Knoxville where he earned a Bachelor's of Science degree in Materials Science and Engineering. In the fall of 2010 he joined Kenneth H. Sandhage's research group and began the Materials Science and Engineering Ph.D. program of study at Georgia Institute of Technology. Brandon is both a Boeing Fellow and a Sam Nunn National Security Fellow. Upon completion of all graduation requirements, in October 2014, Brandon will move back to Tennessee to live his wife Erin Goodwin and starting working at an academic post doctorate position at Fisk University for Prof. Arnold Burgers in research in the areas of crystal growth of scintillators and semiconductors and detector physics.